On the magnetic properties of bulk high-temperature superconductors containing an artificial array of holes

A dissertation submitted

by **Gregory P. Lousberg**

in partial fulfillment of the requirements for the degree of

Doctor of Philosophy (Ph.D.) in Engineering Sciences

January 2010

Remerciements

Bien que figurant parmi les premières pages du manuscrit, la page dédiée aux remerciements est habituellement celle que l'on rédige en dernier lieu, l'esprit libre de toute tracasserie d'ordre scientifique. Arrivé à ce stade, c'est envahi par un sentiment de soulagement et de fierté du travail accompli que j'entame la ronde des remerciements.

C'est il y a quasiment quatre ans jour pour jour que j'ai décidé, après moultes hésitations, de réaliser ma thèse de doctorat à l'Institut Montéfiore dans le domaine des supraconducteurs. Alors qu'initialement j'éprouvais quelques craintes quant aux difficultés liées à cette tâche, mes trois années de thèse se sont finalement déroulées sans encombres ni tracas, et ceci n'est certainement pas dû à moi seul ou au pur hasard; plusieurs personnes ont contribué à cette réussite, chacune à des niveaux différents.

Parce que ces trois dernières années m'ont à la fois permis de réaliser ma thèse de doctorat et de fonder un foyer avec elle, c'est avant tout Amandine que je veux remercier. Merci pour tous ces instants de vie durant lesquels j'ai pu m'échapper de ma thèse afin de mieux y replonger le moment venu. Cet équilibre a été pour moi une inépuisable source de motivation. Merci encore pour l'écoute, le réconfort et les encouragements que j'ai pu trouver à ses côtés quand la situation le demandait.

Ensuite, je tiens à remercier chaleureusement Benoit Vanderheyden et Philippe Vanderbemden, officiellement promoteur et membre du jury, mais officieusement co-promoteurs de ma thèse. Ils m'ont tous deux apporté un soutien inconditionnel vis-à-vis de la progression de mes recherches. Leur disponibilité au jour le jour n'est en rien étrangère au climat serein dans lequel j'ai pu réaliser ma thèse. Grâce à leur expertise et à leurs affinités personnelles (mesures expérimentales pour Philippe et modélisation pour Benoit), j'ai eu la chance de pouvoir parfaire mes connaissances dans ces deux domaines respectifs. Cela se traduit d'ailleurs par une thèse de doctorat jonglant entre des aspects de modélisation numérique et de caractérisation expérimentale.

Je remercie aussi Marcel Ausloos pour les nombreux conseils avisés qu'il m'a distillés tout au long de mon travail, essentiellement par email lorsque j'étais sur le point de soumettre un article. Un grand merci à Xavier Chaud, sans qui je n'aurais pu disposer de plusieurs échantillons troués ni avoir l'occasion de me rendre à Toulouse au Laboratoire National des Champs Magnétiques Intenses afin de caractériser des échantillons soumis à un champ pulsé. J'espère que les résultats tirés de cette thèse lui permettront de continuer le développement des structures trouées. Mes remerciements s'adressent aussi à Fedor Gömöry pour avoir accepté de siéger au sein de mon jury de thèse, et à Jacques Destiné pour son rôle de président du jury.

Travailler à Montéfiore, c'est aussi s'insérer dans la vie d'une équipe de recherche. J'ai eu la chance

de croiser la route de plusieurs chercheurs au cours de ces trois années. Je souhaite particulièrement remercier Jean-François Fagnard, non seulement pour ses doigts de fée vénérés par un service tout entier – et qui m'ont d'ailleurs précieusement aidé dans la réalisation des micro-bobines –, mais aussi pour son rôle d'accueil dès 7h30 du matin pour ceux qui avaient la chance de passer par les caves de Montéfiore à ce moment de la journée. Je tiens également à souligner la présence à mes côtés durant deux ans de Philippe Laurent, de son humour décapant et de son chien un peu trop bruyant... Au début de ma thèse, Samuel Denis faisait partie du service. Je le remercie pour sa gentillesse et sa sympathie. Durant ces trois années, j'ai aussi vu l'arrivée de jeunes et nouvelles recrues : Cédric, Matthieu et Etienne. Je leur souhaite beaucoup de succès dans leurs travaux de recherche et j'espère qu'une partie de cette thèse pourra leur être utile en temps voulu. Merci encore à Mohammed pour sa bonne humeur et ses talents d'organisateur de rencontres de mini-foot, même si je fus rarement de la partie.

Une équipe de recherche n'est pas seulement composée de chercheurs: elle ne pourrait tourner efficacement sans l'appui de techniciens. A cet égard, j'exprime mes plus sincères remerciements à Pascal Harmeling, sans qui je n'aurais pu réaliser si rapidement plusieurs circuits électroniques qui m'ont été utiles au cours des manipulations expérimentales. Un très grand merci également à Joseph Simon, tant pour ses précieux conseils lors des réalisations de pièces mécaniques, que pour ses fous rires communicateurs et les nombreux surnoms avec lesquels il avait l'habitude d'appeler tout le monde.

Je ne peux décemment omettre de remercier l'équipe café grâce à laquelle j'ai pu profiter tous les jours d'une pause, méritée ou pas, dans *la cuisine de Joseph*. Ces rencontres quotidiennes permettent de créer une ambiance agréable dans le service et ont contribué à l'entrain avec lequel j'ai réalisé cette thèse.

Je n'oublierai pas non plus Tom Withnell de l'Université de Cambridge pour son accueil à l'IRC où j'ai effectué quelques mesures. Merci aussi à Evert Haanappel. J'ai pu compter sur lui durant toute la préparation à distance de la campagne de 5 jours de mesure à Toulouse. J'adresse également mes remerciements à Christophe Geuzaine, Patrick Dular et Ruth Sabariego de l'Institut Montéfiore pour leur aide vitale pendant la phase d'implémentation de la méthode des éléments finis appliquée aux supraconducteurs dans le logiciel GetDP.

Pour terminer, je remercie mes parents et ma soeur Laurence pour leur soutien et leurs encouragements durant mes études et ma thèse, et surtout lors de la décision de me lancer dans celle-ci.

Abstract

In this dissertation, we investigate the macroscopic magnetic properties of bulk high-temperature superconductors (HTS) containing an array of artificial holes in view of enhancing their performances. The study involves a numerical modelling part and an experimental characterization part. In each part, novel concepts are highlighted and detailed. In particular, we develop a three-dimensional finite-element method (FEM) for calculating the magnetic field penetration in HTS where a single time-step is used in the case of a linearly varying applied magnetic field, and we probe the magnetic field in the volume of drilled samples with the help of microcoils inserted inside the holes.

The thesis starts with an introductory chapter that describes the general concept of high-temperature superconductivity and particularly draws the attention on the interests and on the synthesis of drilled structures. Then, we detail the modelling tools that are used for evaluating the magnetic properties of drilled samples. Three models are taken into account: (1) the *numerical Bean model* which is a generalization of the Bean model for arbitrary cross sections where the samples are assumed to have an infinite height; (2) a *2D finite element model* implemented in the *open source* solver GetDP for samples with an infinite height and assuming a power law relationship, that is characterized by a critical exponent n, between the electric field, E, and the current density, J; (3) a *3D finite element model* with the same equations as those of model (2), but where these are solved in a three-dimensional sample with a finite height. For large values of n, both FEM models use the properties of a slow magnetic diffusion to reduce the number of time steps. In particular, the trapped flux can be calculated with only two time-steps: during the first step, the applied magnetic flux density is increased with a constant sweep rate to a maximum value, it then decreases to zero with the same sweep rate during the second step.

The models are first used in simple geometries where they are compared to other available techniques. These are next applied to drilled samples. A systematic numerical study of the influence of the holes on the magnetic properties of the sample is reported. A single hole perturbs the critical current flow over an extended region that is bounded by a discontinuity line, where the direction of the current density changes abruptly. In samples with several holes and a given critical current density, we demonstrate that the trapped magnetic flux is maximized when the centre of each hole is positioned on one of the discontinuity lines produced by the neighbouring holes. For a cylindrical sample, we construct a polar triangular hole pattern that exploits this principle; in such a lattice, the trapped field is $\sim 20\%$ higher than in a squared lattice, for which the holes do not lie on discontinuity lines. These results are experimentally validated. Two parallelepipedic samples are drilled with two different hole lattices. The trapped magnetic flux density of these samples is characterized by a Hall probe mapping before

and after drilling holes. The sample in which the holes are aligned on the discontinuity lines exhibits the smallest magnetization drop that results from the hole drilling.

Then, we resort to a novel experimental technique using microcoils inside the holes to characterize the local magnetic properties in the volume of drilled samples. In a given hole, three different penetration regimes can be observed when the sample is subjected to an AC magnetic field: (i) the shielded regime, where no magnetic flux threads the hole; (ii) the gradual penetration regime, where the amplitude of the magnetic field scales with the applied field; and (iii) the flux concentration regime, where the magnetic field exceeds that of the applied field. A comparison of the measurements with simple models assuming an infinite height shows that the holes may serve as a return path for the demagnetizing field lines. In the case of a pulsed field excitation, that measurement technique also allows us to estimate the trapped magnetic flux density in the volume of the sample and compare it with that on the surfaces. Moreover, the penetration of a magnetic pulse from hole to hole is described in the median plane and on the surface and the differences of penetration speeds are explained.

Finally, we investigate the magnetic properties of drilled samples whose holes are filled with a ferromagnetic powder. To this aim, we use experimental techniques (Hall probe mapping techniques, together with measurements of the volume magnetization and of the levitation force between the HTS sample and a permanent magnet) and a numerical model (3D FEM) to characterize the modification of the magnetic properties resulting from the impregnation of the holes with AISI 410 ferromagnetic powder. Numerical results support the experimental observations and give clues to understand the mutual interaction between the HTS sample and the ferromagnetic powder inserted in its holes. In particular, the Hall probe mappings of the distribution of the trapped flux above the non-impregnated and impregnated samples reveal an increase of trapped flux after impregnation that is confirmed by simulations.

Version abrégée

Cette thèse est consacrée à l'étude des propriétés magnétiques des supraconducteurs massifs à haute température (SHT) contenant un réseau artificiel de trous en vue d'en optimiser les performances. Elle est basée sur des résultats provenant de modèles numériques et d'expériences menées sur des échantillons troués. Dans cette optique, nous proposons une méthode par éléments finis pour calculer la pénétration d'un champ magnétique dans un SHT, utilisant un seul pas de temps dans le cas d'un champ magnétique appliqué variant linéairement dans le temps, ainsi qu'une technique de caractérisation des propriétés magnétiques locales dans le volume des supraconducteurs troués à l'aide de micro-bobines insérées dans les trous.

En guise d'introduction, nous dressons un panorama des concepts généraux liés à la supraconductivité à haute température et détaillons l'attrait et les techniques de synthèse des structures trouées. Les méthodes numériques qui sont utilisées pour calculer les propriétés magnétiques des supraconducteurs troués sont ensuite décrites. Trois modèles sont considérés: (1) le *modèle de Bean numérique* qui est une généralisation du modèle de Bean dans des sections droites arbitraires avec des échantillons de hauteur infinie; (2) un *modèle éléments finis 2D* implémenté dans le logiciel *open source* GetDP et qui modélise des échantillons de hauteur infinie à l'aide d'une loi en puissance reliant le champ électrique, E, et la densité de courant, J, caractérisée par un exposant critique n; (3) un *modèle éléments finis 3D* qui utilise les mêmes équations que dans le modèle (2), mais qui les résout dans des échantillons de hauteur finie. Pour de grandes valeurs de n, on utilise les propriétés de diffusion lente du champ magnétique pour réduire le nombre d'itérations temporelles. En particulier, le profil de champ piégé peut être calculé en deux pas de temps: dans un premier temps le champ appliqué augmente à taux constant jusqu'à une valeur maximale, et il est ramené vers zéro dans un second temps avec le même taux de variation

Les modèles numériques sont tout d'abord testés dans des géométries simples dans lesquelles ils sont comparés à d'autres techniques disponibles. Ils sont ensuite utilisés dans des structures trouées afin de mener une étude systématique de l'influence des trous sur les propriétés magnétiques des échantillons troués. Un trou unique perturbe l'écoulement du courant critique dans une région limitée par une ligne de discontinuité où la densité de courant change brutalement de direction. Lorsque plusieurs trous entrent en jeu et que les échantillons ont la même densité de courant critique, on démontre que le champ piégé dans l'échantillon est maximisé si le centre de chaque trou se trouve sur une ligne de discontinuité. Dans un échantillon cylindrique, le réseau de trou *polaire triangulaire* exploite ce principe et permet d'augmenter le champ piégé d'environ 20% par rapport à celui d'un réseau carré dans lequel les trous ne se situent pas sur des lignes de discontinuité. Ces résultats sont vérifiés

expérimentalement. Deux échantillons parallélépipédiques sont percés par deux réseaux différents de trous. Le champ piégé au-dessus de ces échantillons est caractérisé par une cartographie par sonde de Hall avant et après perçage des trous. L'échantillon dans lequel les trous sont alignés sur des lignes de discontinuité possède la plus petite chute d'aimantation résultant de la présence de trous.

Ensuite, les propriétés magnétiques des échantillons troués sont caractérisées dans leur volume à l'aide de micro-bobines insérées dans les trous. Dans un trou donné, trois régimes de pénétration différents sont observés dans le cas d'un champ appliqué alternatif: (i) le régime de blindage dans lequel il n'y a pas de flux pénétrant le trou; (ii) le régime de pénétration graduelle où l'amplitude du champ dans le trou varie avec celle du champ appliqué; et (iii) le régime de concentration de flux pour lequel le champ magnétique dans le trou est plus grand que le champ appliqué. Une comparaison des mesures avec des modèles simples supposant un échantillon de hauteur infinie montre que les trous peuvent servir de chemin de retour pour le champ démagnétisant. Dans le cas d'une excitation par un champ pulsé, cette technique de mesure nous permet d'estimer le champ piégé en volume et de le comparer à celui en surface. De plus, la pénétration du pulse de trou en trou est décrite dans le plan médian et en surface et les différences entre les vitesses de propagation sont expliquées.

Enfin, nous étudions les propriétés magnétiques des supraconducteurs troués dont les trous sont remplis d'une poudre ferromagnétique. Dans cette optique, nous utilisons des techniques expérimentales (cartographie par sonde de Hall, mesure de l'aimantation volumique et de la force de lévitation entre un échantillon supraconducteur et un aimant permanent) et un modèle numérique (de type éléments finis 3D) pour caractériser les modifications des propriétés magnétiques induites par le matériau ferromagnétique. On observe en particulier que le champ piégé en surface de l'échantillon augmente lorsque les trous sont imprégnés par le matériau ferromagnétique.

Contents

Introduction

Discovered by Kamerlingh-Onnes in 1911, superconductors rapidly attracted the attention of the scientific community for their remarkable electrical and magnetic properties, characterized by a lack of electrical resistance to a DC current flow and a nearly perfect diamagnetism [1]. Almost one century later, the interest aroused by superconductors has not faded away and superconductivity remains a fascinating research domain, from which several new applications are still believed to emerge.

Among the promising applications, bulk high-temperature superconductors (HTS) can be used as powerful magnets. When cooled down below their critical temperature, bulk HTS can permanently trap a large magnetic flux; trapped fields of a few teslas have been measured at 77 K in bulk HTS of a few cubic centimeters [2]. Such performances cannot be attained with the traditional iron-based magnets, as their saturation flux density is of the order of 2 T. Cooling might be an issue for applications. As is the case of most HTS, the critical temperature exceeds the boiling point of liquid nitrogen, so that simple non-expensive cooling systems can be used. As a result, HTS trapped field magnets are promising alternatives to iron-based magnets.

Permanent magnets are often used in electrical rotating machines, where they act as sources of the magnetic field (either located in the stator or in the rotor) required for the electromechanical energy conversion. Their replacement by trapped field HTS magnets leads to a significant increase of the output efficiency [3]. The compact size of trapped field magnets, associated with their very large trapped flux on their surfaces, provide high torques on the shaft with a substantial gain of size and weight with respect to permanent iron-based magnets.

Moreover, HTS bulk magnets can be used in magnetic bearing systems, where they provide the means for a stable levitation between a bulk HTS and a permanent iron magnet. Such a levitation is impossible with two permanent magnets [4], unless some degrees of freedom are constrained (guided levitation). The stable magnetic levitation with HTS trapped field magnets is at the basis of several prototypes of magnetic bearing vehicles, such as a magnetic levitation train [5].

In spite of their remarkable magnetic properties, bulk HTS magnets also present drawbacks that have hindered their use in applications. Two main issues have been recently addressed in the literature: (i), the difficulty to synthesize samples of large size (> 1 cm^3) with homogeneous superconducting properties [6], and (ii), the necessity to maintain a uniform temperature when the magnet is used [7].

The first concern is related to the synthesis of HTS single domains, i.e. samples having a pseudo single crystal behaviour but containing impurities and microcracks. These are usually obtained from the top-seeded melt-grown process [8]. The superconducting properties of the single domains are

directly related to the oxygen stoichiometry which results from an oxygen annealing step taking place at the end of the synthesis process. Unfortunately, the oxygen annealing in bulk HTS is a very long step that usually creates cracks that are detrimental to the superconducting properties.

The second problem is inherent to the use of the samples in applications. When located in a motor or in a magnetic bearing system, HTS are often subjected to variable magnetic fields due to mechanical vibrations or to variations in the applied torque on the shaft [9]. The variation of the magnetic flux may lead to significant heat losses, and the resulting local temperature rise is detrimental to the superconducting properties. It is therefore of prime importance to enhance the cooling and the thermal stability of the sample.

In view of proposing a remedy to both issues, an improvement of the oxygen diffusion and of the cooling in the samples has been recently demonstrated with bulk HTS cylinders containing a lattice of holes drilled parallel to their axis [9, 10]. These are usually referred to as *drilled samples*. The holes are drilled in the initial powder before the synthesis of the sample, and, at the end of the process, the oxygen content has been shown to increase and the density of cracks to decrease with respect to the situation in a plain sample. In addition to reducing the oxygen diffusion path, the presence of the holes also offers a large heat exchange surface with the cryofluid, which improves the thermal stability.

These two improvements unfortunately occur at the expense of the magnetic properties of the trapped field magnet. The presence of the holes leads to a redistribution of the trapped flux density in the sample and reduces the trapped magnetic flux with respect to that in a sample having the same dimensions, the same critical current density and no hole.

The purpose of this dissertation is to carry out a systematic study of the magnetic properties of drilled samples, with the aim of optimizing their performances. By keeping in mind the known improvements regarding the synthesis and the thermal stability, we investigate how one can even further take advantages of the presence of the holes so as to improve the magnetic properties of drilled samples. We work simultaneously on two front lines: the numerical modelling of the magnetic properties of drilled samples and their measurements with specific experiments. The thesis is organized in six chapters:

1. **Chapter 1** is devoted to an introduction of the concepts associated with the phenomenon of superconductivity. The emphasis is put on high-temperature superconductors and their applications. In particular, the drilled structures are introduced.

2. **Chapter 2** presents the numerical methods that are used for modelling the magnetic properties of drilled samples. Two methods have been developed in this work: (1), an implementation of the Bean model in samples with an infinite height and an arbitrary cross-section, which is based on Campbell and Evett's approach [11], and, (2), a two- or three-dimensional finite-element formulation of the Maxwell equations associated with a non-linear conductivity law for the HTS. Each method is thoroughly discussed and their practical implementation is detailed. In order to check their validity, the results obtained with these methods are compared to those obtained with other techniques (analytical or numerical) in the case of simple geometries for which the solutions are well known.

3. **Chapter 3** discusses the influence of the hole lattice on the magnetic properties of the drilled samples. It exposes a systematic numerical study of the modifications of the current stream

lines and of the magnetization that are caused by the presence of the holes. Several geometries are investigated, from the simplest model consisting of a sample with an infinite height and a semi-infinite cross section that is drilled by a single hole, to the most complex situation involving a cylinder with a finite height and containing several holes arranged according to various regular patterns. The conclusions drawn from the numerical analysis are confronted to experiments.

4. **Chapter 4** investigates a characterization technique that allows us to probe locally the magnetic field inside the holes of a drilled sample with the help of sensing microcoils. The method is discussed in details and is applied to the measurement of the diffusion of an AC magnetic field in the bulk of two drilled samples. The results of the measurements are compared to those obtained with Hall probe mapping techniques. The microcoil technique is then applied to the measurement of the penetration of the magnetic flux in the bulk of the sample during a pulsed field magnetization (PFM) process.

5. **Chapter 5** studies a method for enhancing the magnetic properties of drilled samples that consists in filling the holes with ferromagnetic powder. Measurements and numerical analysis are used to assess the influence of the ferromagnetic powder on the magnetic properties of the sample, and in particular, on the trapped magnetization in the volume and on the maximum trapped flux density above its surface.

6. **Chapter 6** presents the conclusions and perspectives of this dissertation.

1

Survey of high-temperature superconductivity and related applications

Strictly speaking, superconductivity refers to a physical property of carrying an electrical current with a zero resistance. Superconductors are therefore often compared to perfect conductors across which a current flows without encountering any obstacle, and consequently, with no energy loss. However, the superconductors are not only perfect conductors, they also exhibit astonishing magnetic properties that no other material has ever possessed.

Thanks to their unique physical properties, superconductors have numerous potential applications; be it a totally new kind of application or an improvement of an existing one. The shape in which the materials are processed determines the type of applications intended. Superconductors can be released in wires, tapes, thin films, or in bulk monoliths. This latter form constitutes the main subject of the present manuscript. Tapes and wires are suited for electrical current transport, thin film technology is intensively used for superconducting electronics, whereas the bulk monoliths turn out to be very efficient trapped field magnets.

This introductory chapter offers a description of the superconductivity phenomenon, starting from the early discoveries to the most recent developments. The properties of high-temperature superconductors (HTS), together with their related applications, are then detailed, with a particular emphasis on those processed in bulk monoliths.

1.1   Discoveries of superconducting materials

The discovery of the first superconducting material is intimately linked to the research on low temperature physics, and in particular, to the breakthrough achieved in that field in 1908 by H. Kamerlingh Onnes. At that time, he succeeded to obtain a liquid phase of helium with a temperature of 4.2 K under an atmospheric pressure [1], which was the lowest ever achievable temperature on earth. Shortly after, in 1911, he made use of liquid helium to study the electrical properties of metals at very low temperatures (in a first time, he concentrated on mercury — Hg). The electrical resistance of Hg was found to drop to a non-measurable value when the sample was cooled down below a temperature of transition, called the critical temperature, T_c (see Figure 1.1). The superconductivity in mercury was discovered. The resistivity of the mercury below its critical temperature was considered to be almost zero although it was not perfectly measured as so: the measurement only indicated that its resistivity lied below the sensitivity of the most accurate devices.

Very soon, the discovery of superconductivity aroused a strong interest in the scientific community. In the following years, several other pure metals were shown to exhibit superconducting properties when cooled down below a certain temperature. Unfortunately, their critical temperature did not exceed 10 K. Cooling with liquid helium was mandatory to take benefits of these astonishing material properties. The complexity and the cost of the cooling technology with liquid helium forced the scientists to search for new superconducting materials with a larger T_c.

Figure 1.2 illustrates the evolution of the largest critical temperature through the years [12]. After the pure metal superconductors discovered in the beginning of the 20th century (Hg, Pb), a first breakthrough was realized in 1940 with the discovery of superconductivity in niobium nitride [13], NbN, that enabled wires with metallic alloys of NbTi and Nb_3Sn to be developped. Although the critical temperature of niobium alloys were not larger than 20 K, these wires, associated with a liquid helium-based cooling system, were successfully used in practical applications. Two reasons may explain the success of Ni-based superconducting wires: (i) the maximum current density carried by these wires, which was of the order of 10^{10} A/m^2 [14] at 4.2 K, allowed high field magnets to be created while there was no other alternative technology showing similar performances, and (ii) the evolution of
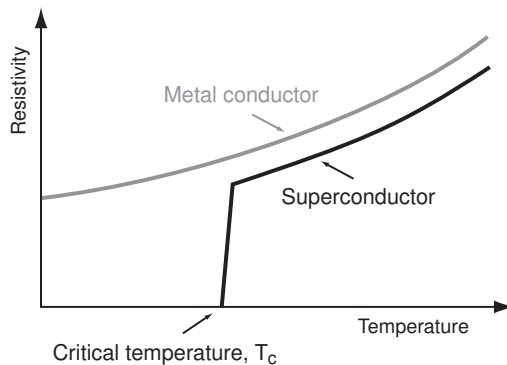
Figure 1.1: *Schematic illustration of the low temperature dependence of the electrical resistivity of a normal conductor (grey line) and of a superconductor like Hg (black line)*
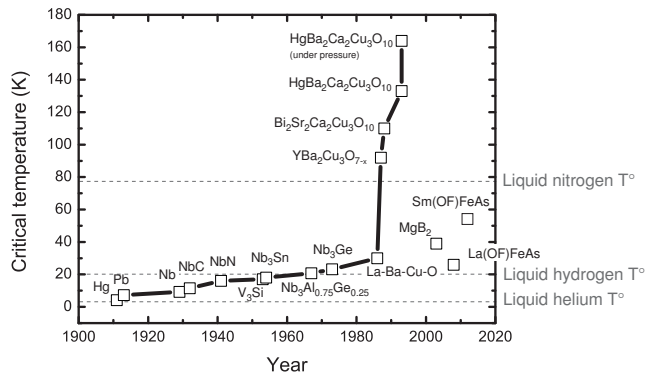
Figure 1.2: *Evolution of the critical temperature of newly discovered superconductors through years*

liquid helium-based cooling systems since 1908 made the cryogenics part more affordable than at the beginning of the century. Nowadays, these wires are still meeting a big commercial success.

Despite the discovery of the niobium-based wires, the search for a material with a higher critical temperature evolved quite slowly before 1980, as shown in Figure 1.2. The year 1986 was a turning point in that chase. During that year, G. Bednorz and K.A. Müller discovered superconductivity at 30 K in the copper oxide perovskite compound LaBaCuO [15]. This new compound having a critical temperature larger than 30 K is referred to as a *High Temperature Superconductor* (HTS). Promptly, other scientists all around the world tried to find a superconducting phase in other types of copper oxide perovskites, also known as layered cuprates. One year later, in 1987, the YBaCuO compound was shown to be superconducting at the liquid nitrogen temperature, 77 K [16].

Following the discovery of the superconductivity in YBCO at 77 K, the research on superconductivity blew up. There was a renewed interest in finding applications of superconductors that only required a cooling with liquid nitrogen (cheaper and less complex than with liquid helium) and on discovering new materials with a higher critical temperature that could even be larger than the room temperature. Figure 1.2 shows that the rapid increase of the largest T_c unfortunately ends in 1993 when the compound HgBaCaCuO was shown to have a critical temperature of 138 K under an atmospheric pressure and 164 K under a pressure of 30 GPa [17]. It still constitutes today the highest-T_c record.

Since 1993, the efforts for finding new materials with a critical temperature that is larger than 164 K have not been rewarded with the discovery of a room temperature superconductor. However, some researchers now wonder whether that quest is still necessary to increase the number of commercial applications using superconductors. It would be, for instance, more crucial to enhance the properties of the known superconductors that are already used in devices cooled with well established cooling systems. Then, in order to make them competitive with other technologies, the simplification of the processing of superconducting materials is of prime importance in view of a mass production. This simplification could be obtained either by modifying the existing process or by finding new superconducting materials with very good superconducting properties at cryogenic temperatures but whose processing is easier to carry out than that required for the copper oxide ceramics — this latter one is discussed in more details in Section 1.5. Within this philosophy, the commercial success of superconductors relies

more on achievements in material science and on the design of low-cost and high-efficient cooling systems, than on the discovery of room temperature superconductors.

This trend is confirmed by the recent evolution of the research on superconductivity. In early 2001, a Japanese group discovered that the magnesium diboride, MgB_2, was a superconductor below 40 K [18]. The simple and low-cost fabrication process of MgB_2 enables to shape the material very easily in various forms. In the same time, the development of HTS wires was progressing toward more and more efficient system with large current carrying capacity [19, 20]. Recently in January 2008, a Japanase paper reported the existence of superconductivity in iron pnictide compounds — compounds that contain elements from group V, such as arsenic, phosphorus or nitrogen [21, 22]. A transition temperature of 26 K was measured in $La(O_{1-x}F_x)FeAs$ [22], and the substitution of lanthanum atoms by samarium yields a transition temperature of $\approx$ 55 K [23]. It is believed that these materials could help unravel how high-temperature superconductivity works. All these recent discoveries tend to reinforce existing superconducting applications at cryogenic temperatures with new materials, new performances, and new theories.

1.2   Two categories of superconductors

Contrary to their literal definition, the superconductors are not only ideal conductors that carry an electrical current with a zero resistance. They distinguish themselves from perfect conductors by their behaviour when subjected to an applied magnetic field. This distinction was discovered in 1933 by W. Meissner and R. Ochsenfeld [24] with the help of an experiment during which they cooled down superconducting samples below their critical temperature in the presence of an applied magnetic field. While a perfect conductor would not modify the magnetic field lines when the temperature is lower than its transition temperature, the superconductors were found to expel the magnetic field from their volume; they became perfectly diamagnetic at $T < T_c$ — that is the Meissner effect. Figure 1.3 illustrates the expulsion of the magnetic field lines from a superconductor when the sample is cooled down below T_c in the presence of a magnetic field. The Meissner effect, together with the zero DC resistance, provides a unique definition of the superconducting state.

The Meissner effect cannot be observed with magnetic fields of arbitrary strength. If the applied field is larger than a critical field, magnetic field lines penetrate inside the superconductor. According to how the magnetic field penetrates their volume, we classify the superconductors in two types: (i) the *type-I superconductors* for which superconductivity disappears when the magnetic field exceeds the critical field, and (ii) the *type-II superconductors* where a superconducting state may coexist with magnetic field lines in the volume of the sample.

1.2.1   Type-I superconductors

Type-I superconductors return back to their normal state when the applied field exceeds their critical field H_c. The superconducting state vanishes, even if the temperature is smaller than the critical temperature. All superconducting pure metals are type-I superconductors. Typical values of $\mu_0 H_c$ lies
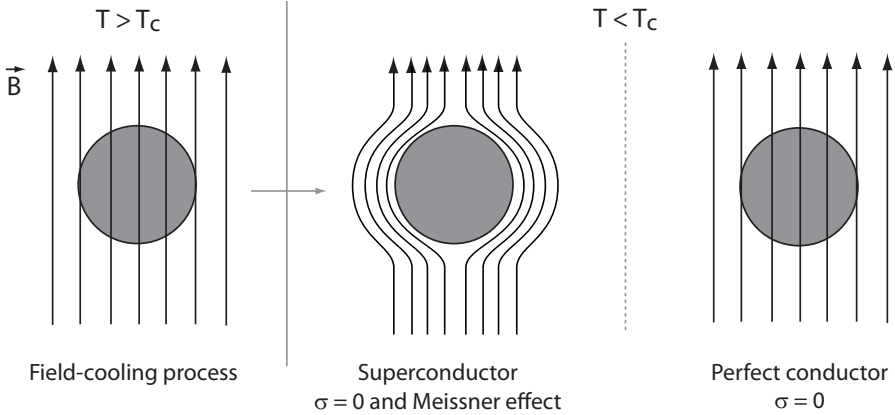
Figure 1.3: *Field-cooling process below T_c of a superconductor and of a perfect conductor (having only $\sigma = 0$). The superconductor excludes the flux lines from its volume as soon as its temperature is below T_c. That is the Meissner effect, which is not exhibited by a perfect conductor.*

within the range of $10 - 200$ mT [25] at $T = 0$ K.

A type-I superconductor is subjected to a phase transition to the normal state by increasing the applied magnetic field, in a similar manner to what occurs when the temperature exceeds T_c. Beside the critical temperature, T_c, the superconducting state is also defined by a second external parameter, namely the critical magnetic field, H_c.

A macroscopic description of the type-I superconductivity involves a two-fluid model, where *super-electrons* coexist with *normal* electrons. It was explained by F. and H. London in Ref. [26]. The density of super-electrons, n_s, is maximum when $T = 0$ K, that is n_0, and vanishes when $T = T_c$; it is given by [27]

$$n_s \;=\; n_0 \left\{ 1 - \left(\frac{T}{T_c} \right)^4 \right\}. \tag{1.1}$$

The model assumes that the repulsion of the field lines from the volume of the type-I samples is explained by the circulation of *super-electrons* in a peel of width λ all round the sample. Inside the peel, the magnetic field is governed by the following equations,

$$\mathbf{E} = \frac{\partial}{\partial t}(\Lambda \mathbf{J}) \qquad \text{and} \qquad \nabla \times (\Lambda \mathbf{J}) = -\mathbf{B}, \tag{1.2}$$

where $\Lambda = m/(n_s e^2)$, m and e are the mass and the charge of an electron. Equations (1.2) are respectively the first and the second London equation that describe both the zero DC resistance and the Meissner effect in type-I superconductors. Actually, the first London equation implies that a static current ($\partial J/\partial t = 0$) induces a zero electric field, and hence zero dissipation since the dissipation is proportional to $\mathbf{E} \cdot \mathbf{J}$. On the other hand, in the case of a time-varying current, part of the current is carried by normal electrons that dissipate energy. Moreover, the London equations, associated with the Maxwell equations, yield the diffusion equation for the magnetic flux density in the superconductor
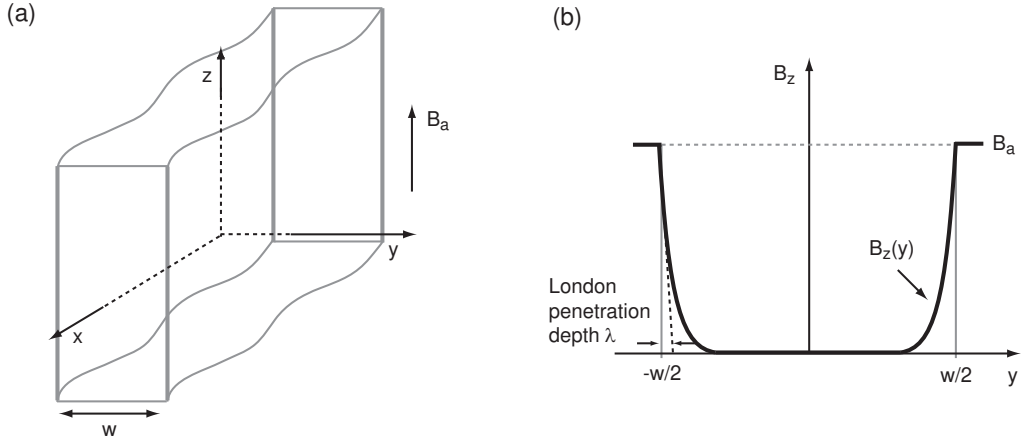
Figure 1.4: (a)- Infinite slab of superconducting material with a thickness w along the y-axis. (b)- Penetration
in the slab of a uniform applied magnetic field oriented along the z-axis.

that describes the Meissner effect,

$$\Delta \mathbf{B} \;\; = \;\; \frac{1}{\lambda^2}\mathbf{B}, \quad \text{with} \quad \lambda = \sqrt{\frac{\Lambda}{\mu_0}}, \tag{1.3}$$

where λ stands for the penetration length. The solution of Eq. (1.3) is represented in Figure 1.4
in the case of an infinite slab of width w along the y-axis, and infinitely extended along the x- and
z-axis. A DC magnetic flux density applied along the z-axis, B_a, is exponentially decaying inside the
superconducting slab (along the y-axis) within a distance of few λ. In the centre of the slab, the
magnetic flux density is almost zero.

At 0 K, the penetration depth λ_0 lies within the range of $30 - 100$ nm for type-I superconductors [12],
and tends to infinity at the transition temperature, T_c, with the following dependence [25]

$$\lambda(T) \;\; = \;\; \frac{\lambda_0}{\sqrt{1 - \frac{T^4}{T_c^4}}}. \tag{1.4}$$

Let us note that the penetration depth must be negligible with respect to the characteristic size of
the sample in order to observe the Meissner effect in type-I superconductors.

While already described phenomenologically by London in 1935, type-I superconductivity was only
explained at a microscopic scale by Bardeen, Cooper and Schrieffer in 1957 [28]. Within the framework
of their model (BCS theory), the superconductivity can be viewed as a frictionless motion within
the atomic lattice of two electrons that form a Cooper pair. Although they are subjected to a
Coulomb repulsion, two electrons may be paired with the help of an electron-phonon interaction, i.e.
an interaction between the electrons and the vibrations of the lattice.

The Cooper pairs have a characteristic size ξ, called the coherence length, whose value at $T = 0$ K
is usually few hundreds of nanometers for type-I superconductors. Contrary to the single electrons
that are subjected to the *Pauli exclusion principle* that prevent electrons from occupying the same
electronic state, the Cooper pairs act like *bosons* and condensate at a same energy level. In type-
I superconductors, the electronic state of the Cooper pairs lies at a slightly lower energy than the

unpaired electrons, with an energy gap, E_g of the order of 0.001 eV [29]. In the Cooper state, the usual collisions that lead to normal resistivity are inhibited. For temperatures such that the thermal energy is less than the energy gap E_g, the material exhibits zero resistivity. The BCS theory predicts that, due to the energy gap value, superconductivity cannot be observed at temperatures larger than approximately 30 K [28].

1.2.2 Type-II superconductors

In type-I superconductors, the transition from a superconducting state to a normal state occurs when the applied field exceeds H_c — the critical field H_c is unique. In type-II superconductors, that transition occurs in two steps through a mixed state defined by a lower and an upper critical fields, respectively called H_{c1} and H_{c2}. When the applied field H_a is larger than the lower critical field H_{c1}, the type-II materials remain in a superconducting state and are simultaneously penetrated by discretized quanta of magnetic flux, called *vortices*. Metal alloys, cuprates, MgB_2, and pnictide compounds are of type-II.

The three states of a type-II superconductor in the $H - T$ plane are illustrated in Figure 1.5 and discussed here below:

1. Meissner state ($H_a < H_{c1}$)

   The superconductor behaves in the same manner as a type-I does. In particular, the magnetic field penetrates the superconductor from its surface, over a distance roughly equal to its London penetration depth and the magnetic flux is expelled from the remaining volume of the superconductor. At $T = 0$ K, typical values for the lower critical field, $\mu_0 H_{c1}$, of type-II superconductors are 0.1 T for conventional superconductors [30], and few mT for cuprates [31].

2. Mixed state ($H_{c1} < H_a < H_{c2}$)

   In the mixed state, vortices penetrate inside the superconductor. These are columnar cylinders parallel to the applied field with a normal conducting core, having a radius equal to the coherence length ξ, and surrounded by circulating supercurrents within a distance λ, as illustrated in Figure 1.6-(a). The magnetic flux contained in a vortex is constant, that is a quantum of
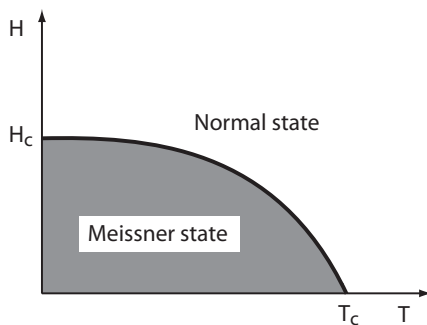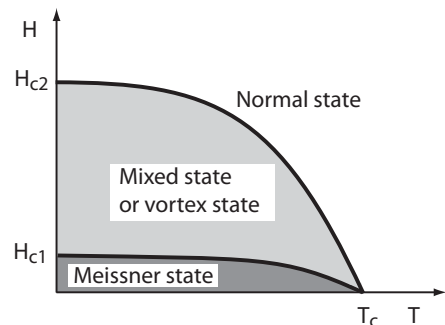
Figure 1.5: $H - T$ phase diagrams of (a) a type-I superconductor and (b) a type-II superconductor.
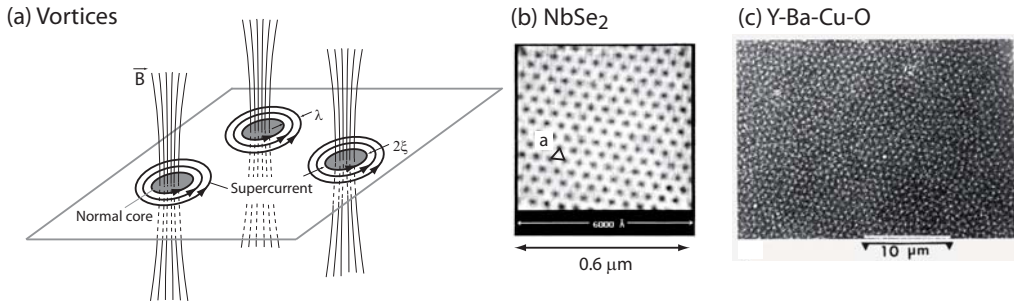
Figure 1.6: *(a)- Sketch of three vortices in a superconducting plane. The surrounding supercurrents are also represented. (b)- Magnetic decoration above a NbSe$_2$ superconductor [32] highlighting the presence of vortices (dark spots). (c)- Same experiments above a Y-Ba-Cu-O material [33]*

magnetic flux, Φ_0,

$$\Phi_0 \;=\; \frac{h}{2e}, \tag{1.5}$$

where h is the Planck constant and e is the electron charge, and hence, $\Phi_0 = 2,07.10^{-15}$ Wb. Outside the core of the vortes, the magnetic field vanishes over a distance λ due to the circulation of supercurrents.

Inside pure superconductors, i.e. samples containing no defects or impurities, the vortices are not held in a fixed position and can move freely when subjected to a non-vanishing resulting force.

The forces acting on vortices are mainly of two types. First, there is the mutual force acting between two vortices. Two vortices with magnetic field lines oriented in the same direction are subjected to a repulsive Lorentz force that drives them apart. When several vortices come into play, the vortices take an equilibrium position that minimizes their mutual interaction energy. At equilibrium, all the vortices are arranged on a triangular lattice, called the *Abrikosov* lattice [34]. Figure 1.6-(b,c) shows an Abrikosov lattice in a NbSe$_2$ and in a YBa$_2$Cu$_3$O$_{7-\delta}$ superconductor. The lattice constant a defines the density of vortices in the lattice, n_v, which is proportional to the magnetic flux density, $B = n_v \Phi_0$. When the lattice constant becomes comparable to the coherence length, the material returns to the normal state.

Second, a DC current flowing across a type-II superconductor in the mixed state exerts a Lorentz force on the vortices. For a current density **J**, that force is given by [35]

$$\mathbf{f} \;=\; \mathbf{J} \times \mathbf{\Phi}_0, \tag{1.6}$$

where $\mathbf{\Phi}_0$ is the flux quantum associated to an isolated vortex. This driving force causes the vortices to leave their equilibrium position and move as long as the current flows in the sample. Since the core of the moving vortices contains normal electrons, the induced motion of the array of vortices involves a drag force that acts on the vortices and causes energy dissipation that is detrimental for the current transport abilities of the superconductor. In order to prevent that situation from happening, impurities can be incorporated in the crystal lattice so as to pin

Table 1.1: *Characteristics of type-I and type-II superconductors*

Type-I	Type-II
Single critical field H_c	Dual critical fields H_{c1} and H_{c2}
Meissner state	Meissner state or Mixed state with quantized vortices
Generally pure elements	Metal alloys, cuprates, MgB_2 or pnictide
Low critical field	High critical field
$\xi \gg \lambda$	$\xi < \lambda$
Surface current flow for $H < H_c$	Bulk current flow for $H_{c1} < H < H_{c2}$

the vortices. Superconductors possessing pinning centres for the vortices are called *irreversible* type-II superconductors, in contrast to *reversible* type-II superconductors in which the vortices are free to move. The magnetic response of irreversible type-II superconductor exhibits an hysteretic behaviour, that is not observed with reversible type-II superconductor. That specific point is discussed further in Section 1.4.

Thanks to the very low energy dissipation when carrying a current, only irreversible type-II superconductors are used for applications, and we only consider them in this manuscript.

3. Normal state ($H_a > H_{c2}$)

   When the applied field is larger than their upper critical field H_{c2}, the material looses its superconducting properties. There are no more vortex inside its volume, the magnetic field uniformly penetrates the material. At $T = 0$ K, typical values of $\mu_0 H_{c2}$ are few dozen of T in metal alloys [25] and few hundreds of T in cuprates [2].

The penetration of the magnetic field by quantized fluxoid has been theoretically predicted by Abrikosov, whose calculations detailed in Ref. [34] were based on the Ginzburg-Landau model for superconductivity [36]. The description of that model goes beyond the scope of the manuscript, but a remarkable conclusion can be deduced from a dimensionless parameter κ, that is the ratio between the penetration depth λ and the coherence length ξ,

$$\kappa = \frac{\lambda}{\xi}. \tag{1.7}$$

This parameters illustrates in a simple way the difference between type-I and type-II superconductors: when $\kappa < 1/\sqrt{2}$, that is $\xi \gg \lambda$, the superconductor is of type-I, and when $\kappa > 1/\sqrt{2}$, that is $\xi < \lambda$, it is a type-II superconductor. A non exhaustive list of the characteristics of each type of superconductors is summarized in Table 1.1.

1.3   Critical parameters of a superconducting state

Usually, the superconducting state of a material is described in a three-dimensional (3D) phase diagram where a 3D surface defines the boundary between the normal and the superconducting phases [25],
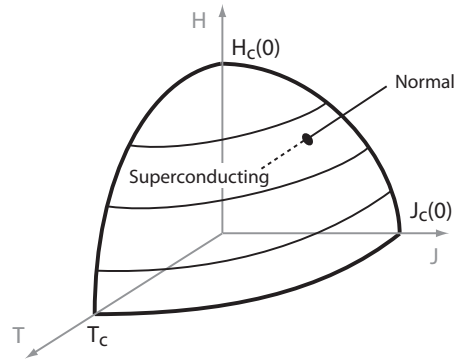
Figure 1.7: $J - T - H$ phase diagram of a type-I superconductor representing upon which conditions the superconducting state is stable.

as represented in Figure 1.7. The critical surface intersects the axis respectively at the critical current density J_c, at the critical temperature T_c and at the critical field H_c (or H_{c2} in the case of a type-II material). Each critical parameter is thus defined when both remaining ones are considered to be equal to 0.

Figure 1.7 illustrates that the temperature, the magnetic field and the current density must satisfy conditions such that the transition to/from a superconducting state occurs. In particular, for a given T and H, such that it lies in the superconducting state, a material cannot carry a current density exceeding a critical value J_c without loosing its superconducting properties. In type-I superconductors, such a transition to the normal state is explained by the breaking of all the Cooper pairs due to a large current density, that is the *depairing* critical current density. In irreversible type-II superconductors, the critical current density is defined as the current density that pulls out the vortices from the defects or impurities, that is the *depinning* critical current density. Contrary to T_c and H_c, the critical current density is not an intrinsic properties of a given superconducting material. In irreversible type-II superconductors, it depends strongly on the presence of pinning centres in the material. Two samples of same stoichiometric composition may exhibit different critical current densities.

The shape of the critical surface is representative of almost all the superconductors. Inside the volume determined by that surface, the phase diagram is however not similar for both types of superconductors. Such a difference appears clearly in the phase diagram in the $H - T$ plane represented in Figure 1.5. That two-dimensional phase diagram is a particular cut along a J-plane of the critical surface.

The analysis of the $J - T - H$ surface plays an important role for applications using superconductors. Careful attention must be drawn when designing the systems: the operating point (J, T, H) can never lie above the critical surface.

Moreover, the critical surface reveals that working at a temperature close to T_c is not very optimal; the critical current density is quite low in that region, and hence, is not convenient for applications. This partly justifies the extensive research effort that has been devoted during the recent years to the enhancement of the critical current density of HTS operating at 77 K, rather than running toward higher-T_c materials. For instance, a hypothetic room temperature material would only exhibit an

admissible critical current density for applications at lower temperatures than T_c; a cooling system would be also required to use them. Therefore, the scientists have rather chosen to strengthen the critical current density of known superconductors for which the associated cooling system is already well understood.

1.4   Magnetic properties of irreversible type-II superconductors

Irreversible type-II superconductors contain impurities and/or defects in their crystal lattice that act as traps for the vortices. These vortices are held up in place by the defects with a large attraction energy, they are said to be *pinned* in the superconductor. The displacement of the vortices needs to be triggered by an external intervention, such as a variation of the applied magnetic field or a large current flow exceeding the critical current density.

The distribution of the vortices in a superconductor with pinning centres results from an equilibrium between the forces acting on these vortices. Although the microscopic interaction between vortices is a complex problem, it is possible to describe the force balance with macroscopic quantities. The first interaction is the Lorentz force acting on the vortices due to a current flow with a density **J**. In the case of an isolated vortex, that Lorentz force is given by Eq (1.6). Let us now assume that there are n_v vortices per unit of volume, the average Lorentz force density, **F**, is therefore given by

$$\mathbf{F} \quad = \quad \mathbf{J} \times n_v \boldsymbol{\Phi}_0, \tag{1.8}$$
$$= \quad \mathbf{J} \times \mathbf{B} \tag{1.9}$$

In addition to the Lorentz force, the pinning force has also to be taken into account. In a sample with a uniform distribution of pinning centres, one can define an *average pinning force density*, F_p. That pinning force describes the minimal force density that causes a vortex motion. In other words, if the DC current density is such that $\mathbf{F} < \mathbf{F}_p$, the vortices stay pinned and the current flows in the superconductor with no energy dissipation (non-dissipative regime) ; whereas if $\mathbf{F} > \mathbf{F}_p$, the flux line lattice moves and the superconductor enters in the flux flow regime. When the force balance equation
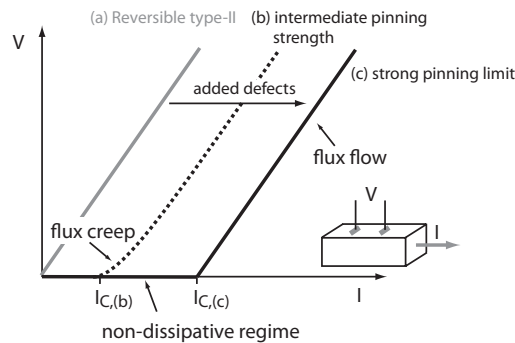

Figure 1.8: *Current-voltage relationship, as measured by the experiment sketched in the inset, in a reversible type-II superconducting bar (grey line) and in an irreversible type-II superconducting bar with an intermediate (dashed line) and a strong (solid line) pinning strength (after Strnad et al [37]).*

is satisfied $\mathbf{F} = \mathbf{F}_p$, the current density is equal to the depinning critical current density, $\mathbf{J}_c$.

The aforementioned regimes are illustrated in Figure 1.8, on which is represented the current-voltage relationship at a finite temperature in type-II superconductors with (a) no defects, (b) an intermediate pinning strength, and (c) a strong pinning, *i.e. a high density of efficient pinning centres*. The reversible superconductor (a) has a single flux motion regime with a dissipative current flowing through it; the pinning force is strictly equal to 0 and only a drag force acts on the vortices and causes energy dissipation. The material with the strong pinning (c) shows nearly an abrupt transition between the non-dissipative regime and the flux flow regime at a critical current I_c corresponding to the critical current density J_c. In the more realistic case of an intermediate pinning strength (b), a third regime is observed — the *flux creep* regime —, where the vortices are depinned from the impurities by thermal fluctuations. The Lorentz force acting on the vortex is not sufficient to make it moving, but a small amount of thermal energy is sufficient to pull out the vortex from the pinning centre.

1.4.1 Bean critical state model

In an irreversible type-II superconductor, the dynamic of a vortex is mainly governed by the force balance condition that assumes the following form,

$$\mathbf{F}_p \;\; = \;\; \mathbf{J} \times \mathbf{B}, \tag{1.10}$$

This equation brings C. P. Bean in 1962 to describe macroscopically the magnetization of the irreversible type-II superconductors with a strong pinning [38, 39]. This model, called the Bean critical state model, assumes that the distribution of the current $\mathbf{J}$, and hence of the magnetic field $\mathbf{H}$ with $\nabla \times \mathbf{H} = \mathbf{J}$, is such that the force balance condition (1.10) is satisfied everywhere in the volume of the superconductor penetrated by flux lines. Thus, the current density J can only have three values: $\pm J_c$ or 0. The sign of the current flow is such that it induces a magnetic field that opposes the variation of the applied field.

The microscopic interpretations of the critical state are the following:

1. When the superconductor is subjected to a positive (resp. negative) increment of applied field, flux lines are nucleated (resp. destroyed) at the surface of the material. The magnetic field becomes discontinuous at the surface. The large spatial variation of the magnetic field at the surface thus involves a local current density $\mathbf{J} = \nabla \times \mathbf{H}$ that is initially larger than $\mathbf{J}_c$.

2. The flux lines at the surfaces move inside the material (resp. toward the surface) until the *gradient force*, i.e. the Lorentz force due to the current induced by the curl of the magnetic field $\mathbf{J} \times \mathbf{B}$, is balanced by the pinning force $\mathbf{F}_p$

The Bean model is described by a single equation,

$$\nabla \times \mathbf{B} \;\; = \;\; \begin{cases} \pm\mu_0\mathbf{J}_c & \text{in the penetrated regions} \\ 0 & \text{in the virgin regions} \end{cases}, \tag{1.11}$$

under the following assumptions:

1. a strong pinning,
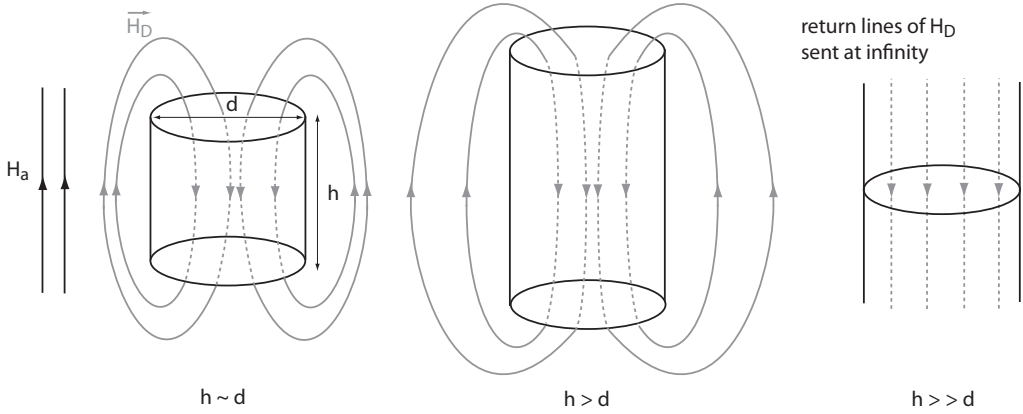
Figure 1.9: *Demagnetizing field* $\mathbf{H}_D$, *defined as* $\mathbf{H} = \mathbf{H}_D + \mathbf{H}_a$, *in cylinders of diameter d and height h, such that* $h \sim d$ *(a),* $h > d$ *(b) and* $h \gg d$ *(c) which represents a geometry of infinite height.*

2. a negligible lower critical field, $H_{c1} \to 0$,

3. a very large upper critical field, $H_{c2} \to \infty$,

4. dimensions of samples that are not negligible with respect to the penetration depth, λ,

5. a surface barrier that is neglected[1],

6. a constant critical current density in the sample.

Critical state in an infinite superconducting slab

Although the Bean model is defined by a single explicit differential equation, Eq (1.11), it is not trivial to find an analytical solution to that model in several geometries. The analytical solution of the critical state can only be determined in few ideal geometries with obvious symmetries. In particular, the Bean model can be solved analytically when the vector Bean equation (1.11) can be reduced to a single scalar equation, like in an infinite superconducting slab, of width w, subjected to a longitudinal field, as illustrated in Figure 1.4-(a).

In view of further understanding the consequences of the symmetries in such a geometry, one has to introduce the concept of the demagnetizing field, $\mathbf{H}_D$. The demagnetizing field is defined as the magnetic field created by the induced currents flowing in the superconductors, such that

$$\mathbf{H} = \mathbf{H}_a + \mathbf{H}_D. \tag{1.12}$$

The demagnetizing field lines form closed loops, as skecthed in Figure 1.9 in the case of cylinders of various heights (the situation around a superconducting slab is similar). In the infinite geometry (c), the demagnetizing field has a single component oriented along the z-axis inside the cylinder, and due to the symmetry along the z-axis, the field lines close at infinity. Moreover, the return field lines that surround the sample are sent to infinity and no longer influence the applied field at the border

---

[1] The surface barrier represents the interaction between a vortex and the surface of the superconductor that prevents the entry of a flux line or its exit from the sample. That surface barrier has only an influence at low magnetic fields [25].

of the cylinder, like in geometries with finite height. Therefore, the demagnetizing effects — i.e. the effects associated with the return lines of the demagnetizing field, and with the curvature of the demagnetizing field lines such that they form closed loops — have no influence in samples having an infinite height.

Consequently, the Bean equation simply assumes the following form in the case of the infinite slab as represented in Figure 1.4-(a),

$$\frac{dB_z}{dy} = \begin{cases} \pm\mu_0 J_c \\ 0 \end{cases}.$$ (1.13)

where J_c flows along the x-axis direction. The orientation of the current flow is such that the magnetic flux density is smaller (resp. larger) inside the slab (at least in the vicinity of the surface) than at the surface if the applied field is increasing (resp. decreasing).

To illustrate the critical state in the infinite slab, let us consider the following sequence of applied magnetic flux density at the surface of the slab: (i) $0 \rightarrow B_{max}$, (ii) $B_{max} \rightarrow -B_{max}$, and (iii) $-B_{max} \rightarrow B_{max}$. Such a sequence is usually referred to as a full magnetization cycle.

We consider each of the steps separately, and we calculate the analytical expression of the magnetic flux density profile within the slab. The corresponding profile is represented in Figure 1.10.

(i) $0 < B_a < B_{max}$, with $B_{max} > \mu_0 J_c w$
As long as $B_a < \mu_0 J_c w/2$, the slab is not fully penetrated, i.e. the current density is not equal to $|J_c|$ in all the slab, and the magnetic flux profile is given by

$$B_z = \begin{cases} B_a - \mu_0 J_c(w/2 - |y|) & \text{if} |y| \geq y_1^* \\ 0 & \text{if} |y| < y_1^* \end{cases},$$ (1.14)

$$\text{with} \quad y_1^* = \frac{w}{2} - \frac{B_a}{\mu_0 J_c}.$$ (1.15)

When B_a exceeds the penetration field $B_p = \mu_0 J_c w/2$, the slab is fully penetrated and the profile reads

$$B_z = B_a - \mu_0 J_c(w/2 - |y|).$$ (1.16)

In particular, the magnetic flux density decays linearly with a slope J_c, from the surface toward the centre of the slab. Note that the condition $B_{max} > \mu_0 J_c w$ is further explained in case (ii).

(ii) $B_{max} < B_a < -B_{max}$
Since the applied field is now decreasing, the current induced at the surface is now oriented in the opposite direction to that of case (i). The position where the current switches between the positive and the negative orientation, $\pm y_2^*$, starts from the surface and moves toward the slab centre as the applied field keeps decreasing, as long as $B_a > B_{max} - \mu_0 J_c w$. In that situation the magnetic flux profile reads

$$B_z = \begin{cases} B_a + \mu_0 J_c(w/2 - |y|) & \text{if} |y| \geq y_2^* \\ B_{max} - \mu_0 J_c(w/2 - |y|) & \text{if} |y| < y_2^* \end{cases},$$ (1.17)
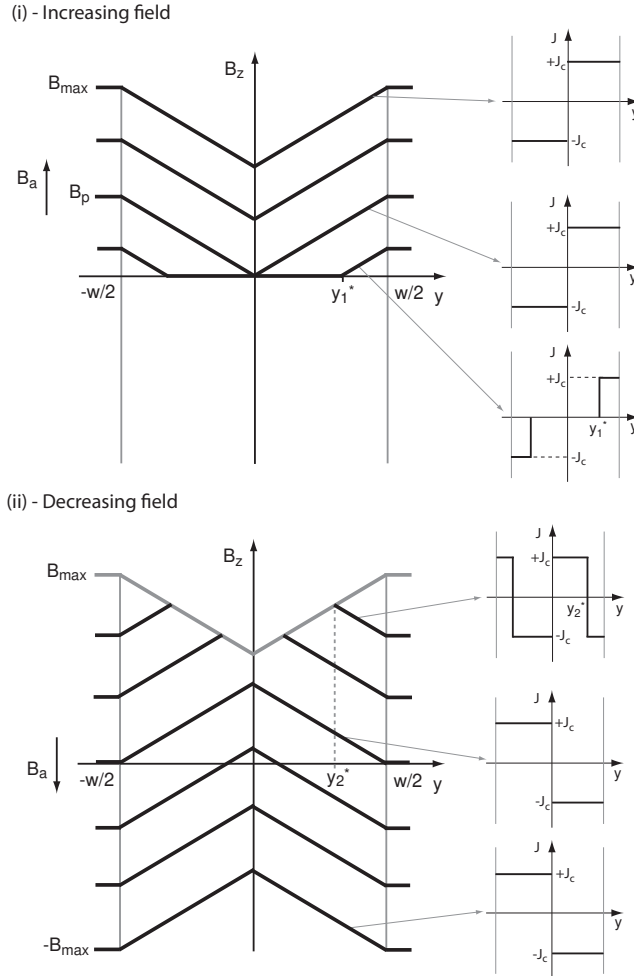
Figure 1.10: *Distribution of the magnetic flux density and of the current density in an infinite superconducting slab when the uniform applied magnetic flux density is increased from 0 to B_{max} in (i) and decreases to $-B_{max}$ in (ii). The distribution is calculated at successive increments of the applied field according to the Bean model.*

$$\text{with} \quad y_2^* = \frac{w}{2} - \frac{B_{\text{max}} - B_a}{2\mu_0 J_c}. \tag{1.18}$$

For $|y| > y_2^*$, the flux profile increases linearly from the surface toward the centre and has the opposite slope to that in case (i). Then, for $|y| < y_2^*$, the profile remains the same as when $B_a = B_{\text{max}}$ in case (i). When $B_a \leq B_{\text{max}} - \mu_0 J_c w$, the profile gets simpler:

$$B_z = B_a + \mu_0 J_c(w/2 - |y|), \tag{1.19}$$

and the current density is oriented in the same direction in a half-slab. In particular, when $B_a = 0$, there remains a positive magnetic flux density in the slab, that is the trapped magnetic flux. If the initial condition in case (i) was not fulfilled, i.e. if $B_{\text{max}} - \mu_0 J_c w < 0$, the current

(a)- Bean model - Uniform critical current density   (b)- Bean model - Field-dependent critical current density
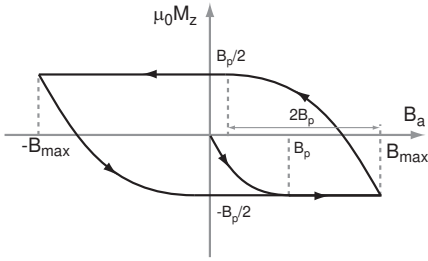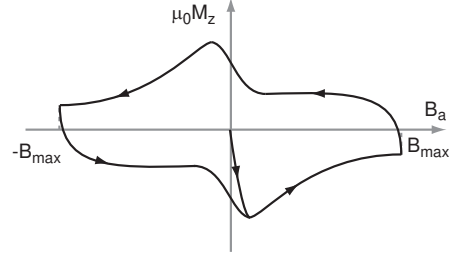
Figure 1.11: *Magnetization curve of an irreversible type-II infinite superconducting slab with a strong pinning and with, (a), a constant critical current density or, (b), a field-dependent critical current density according to Eq. (1.21).*

would not be oriented in the same direction in the half-slab when $B_a = 0$ and the trapped magnetic flux density would not have been maximum at the slab centre.

(iii) $-B_{max} < B_a < B_{max}$. That situation is symmetric to the case (ii) and leads to similar relations.

According to the description of the Bean critical state model in Figure 1.10, the vortex pinning involves a hysteretic magnetic behaviour in irreversible type-II superconductors. In particular, it is responsible for the remnant magnetic flux density observed in the case (ii). The hysteresis arises from the vortices that are only nucleated or destroyed close to the surface of the superconductor, and that do not diffuse immediately in all the sample. In the centre of the sample, the effect due to an increment of the applied field is delayed.

The full magnetization cycle described by cases (i), (ii) and (iii) is usually represented with a magnetization curve that highlights the hysteresis in the magnetic properties of the irreversible type-II superconductors. The magnetization is defined as

$$\mathbf{M}(H_a) = \frac{1}{\mu_0 V} \int \mathbf{B} \, dV - \mathbf{H}_a, \tag{1.20}$$

where $\mathbf{H}_a = \mathbf{B}_a / \mu_0$. The magnetization curve, $\mu_0 M(B_a)$, is plotted in Figure 1.11-(a). An hysteresis loop with a maximum width of $B_p = \mu_0 J_c w / 2$ is observed.

The considerations on the magnetization of irreversible type-II superconductors are based on the Bean model that simply assumes a constant critical current density. Refinements of that model are brought by the Kim's model [40], where the critical current density depends on the magnetic flux density,

$$J_c(|\mathbf{B}|) = \frac{J_{c0}}{1 + |\mathbf{B}|/B_1}. \tag{1.21}$$

An analysis of the critical state of the infinite slab, with a field-dependent critical current density can be also carried out analytically. It yields a magnetization curve with a hysteresis loop, where the magnetization does not saturate anymore at $|\mu_0 M| = B_p/2$, but exhibits two extremum values close to $B_a = 0$, as schematically represented in Figure 1.11-(b).

1.4.2 Power law model

Although the critical state model is very efficient to qualitatively describe the main features of irreversible type-II superconductors subjected to an applied magnetic field, it nevertheless fails in describing some effects associated with the dynamic of vortices in the material. Actually, the critical state model refers to a steady-state where the vortices are so efficiently pinned that their motion follows instantaneously the variations of the applied magnetic field: the critical current density has a single value such that the balance force equation (1.10) is satisfied everywhere; the time during which the driving force, $\mathbf{J} \times \mathbf{B}$, is unbalanced and the vortices rearrange between themselves is negligible.

In the critical state, the current has a single value, such that the electric field E reads

$$E(J) \quad \propto \quad \begin{cases} 0 & \text{in the regions with no vortices motion} \\ -\dfrac{dB_a}{dt} & \text{in the regions with vortices motion} \end{cases} \tag{1.22}$$

The electric field is only induced by time-variations of the applied flux density B_a. The critical state model does not take into account the thermally-activated motion of vortices, which is dissipative and implies the existence of an electric field that is different from that given by Eq. (1.22).

However, it has been already shown in Figure 1.8 that the flux creep phenomenon that occurs when the driving force is almost equal to the pinning force, $J \sim J_c$, can be observed in samples with intermediate pinning strength when the pinning energy of the vortices U becomes comparable with the thermal energy $k_B T$. That thermally induced motion of vortices is more and more important when the temperature increases. In particular, it cannot be neglected in HTS.

The flux creep in superconductors is usually observed when studying the time evolution of the magnetization of a sample [40]. The trapped magnetic flux decays with time according to a logarithmic law. The field gradient within the superconductor decays with time because of thermally activated flux motion of the vortices resulting in a relaxation of the persistent current and of the magnetization.

The thermally activated flux creep causes dissipation. The electric field associated with a vortex motion accross the pinning energy barrier with a height U is expressed in Ref. [2] as

$$E \quad = \quad E_0 \exp\left(\frac{-U(J)}{k_B T}\right), \tag{1.23}$$

where the pinning energy depends on the current density. In HTS, the observed magnetic relaxation can be understood by considering collective motion of vortices grouped into large flux bundles [41]. According to the model of collective flux creep applied to HTS oxides, as described in Refs. [42, 43, 44, 45], the activation energy in HTS depends on the current density with a logarithmic law

$$U(J) \quad = \quad U_0 \ln\left(\frac{J_c}{J}\right), \tag{1.24}$$

where J_c is the critical current density and U_0 is the pinning energy when there is no current flowing in the sample. Therefore, Eq. (1.23) yields a power-law relationship between the electric field and the current density, which is in agreement with measured data [46, 47, 48, 49, 50]. The $E(J)$ power law was introduced in 1990 by Gilchrist [46] and assumes the following form

$$E \quad = \quad E_c \left(\frac{J}{J_c}\right)^n, \tag{1.25}$$
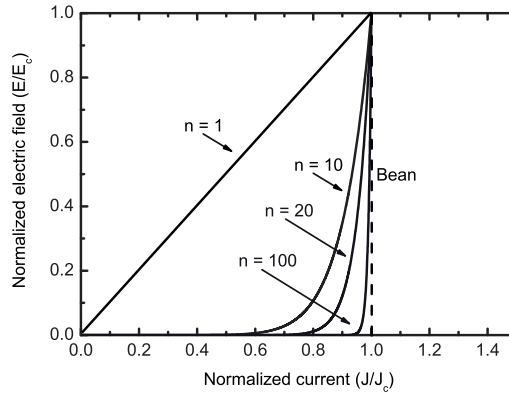
Figure 1.12: *Relation between the electric field and the current density according to the power law (1.25) with a critical exponent n equals to 1, 10, 20 and 100. The E − J relationship corresponding to the Bean model is reproduced with a dashed line.*

where $n = U_0/kT$ is a critical exponent, E_c is a critical field and J_c is the critical current density. The power law model with a critical exponent n equal to 1, 10, 20 and 100 is represented in Figure 1.12; the $E − J$ relationship corresponding to the Bean's critical state is also plotted with a dashed line. When $n = 1$, Equation (1.25) corresponds to the ohmic law, with a linear relationship between E and J. The critical exponent associated to the HTS is typically around 25. The power law model is asymptotically equivalent to the Bean model, for $n \to \infty$.

The main advantage of using a power law instead of the critical state model for calculating the magnetic flux penetration in a HTS samples is that the effects of the dissipative motion of vortices across energy barriers are taken into account. In particular, the observed dependence of the width of the hysteresis loop ΔM with the sweep rate dB_a/dt is well reproduced [51, 52]. Moreover, the power law model yields an analytical expression for the conductivity of the material, unlike in the Bean model, for which the conductivity of the superconductor is discontinuous, it is either 0 or infinite. The power law can be directly incorporated in usual numerical methods for solving the Maxwell equations in the superconductor.

1.5   A further insight on high-temperature superconducting oxides

High-temperature superconductors (HTS) relate to a family of superconducting materials whose critical temperature exceeds 30 K. Among the HTS family, the most famous materials are the copper oxide-based superconductors, or the cuprates. Discovered in 1986, the HTS oxides are now slowly leaving the research laboratories to creep into the industrial market; the workhorse of the HTS applications being the second generation of superconducting wires using YBCO coated conductors [20, 53].

The following section introduces the HTS oxides in general, describes their main characteristics and focuses particularly on the bulk monolith forms of $YBa_2Cu_3O_{7-\delta}$.

HTS are brittle ceramics containing CuO_2 layers that govern most of the HTS properties and make

the material highly anisotropic. The unit cell of a YBaCuO material is shown in Figure 1.13-(a) in both tetragonal and orthorhombic phases. The tetragonal phase, with the stoichiometry $YBa_2Cu_3O_6$, is not superconducting, as opposite to the oxygen-rich orthorhombic phase, $YBa_2Cu_3O_{7-\delta}$. We notice the presence in both phases of the copper-oxide layers separated by Ba and Y atoms. The structure of a YBCO crystal is schematically represented in Figure 1.13-(b). The layered structure along the c-axis consists of two CuO_2 planes separated by Y site. Between these layers, one find an interlayer region that corresponds to the CuO chains linked to the CuO_2 planes by a barium oxide. The superconductivity essentially takes place within the CuO_2 planes. The CuO planes may be viewed as *charge-reservoirs* which bring mobile charge inside the CuO_2 planes. In a YBCO compound, these charge reservoirs are created by adding oxygen site to a $YBa_2Cu_3O_6$ crystal that enters the compound as O^{2-} and creates the CuO chains. To maintain the charge equilibrium, electrons are removed from the copper oxide planes; the remaining holes are mobile inside the CuO_2 planes and form kinds of Cooper pairs below T_c. Such a description leads us to deduce the schematic model of the structure of all HTS oxides represented in Figure 1.13-(c).

In HTS oxides, the distance between neighbouring atoms is very different in the a, b-plane than along the c-axis; in a YBCO, it is 38 nm in the CuO_2 planes and it is 116 nm along the c-axis. That difference has a great influence on the superconducting properties of the HTS oxides, and leads to anisotropy in their properties. Even at room temperature, the electrical conductivity of these metallic oxides is much larger along the a- and b-axis, than along the c-axis.

The coherence length of HTS oxides is very small, $\xi_{a,b} \sim 15$ Å and $\xi_c \sim 4$ Å for YBCO, which is practically equal to the separating distance between two adjacent CuO_2 planes. Consequently, HTS oxides are type-II superconductors, as described by the Ginzburg-Landau theory. Moreover, the coherence length is also anisotropic. The Ginzburg-Landau theory leads to the definition of an
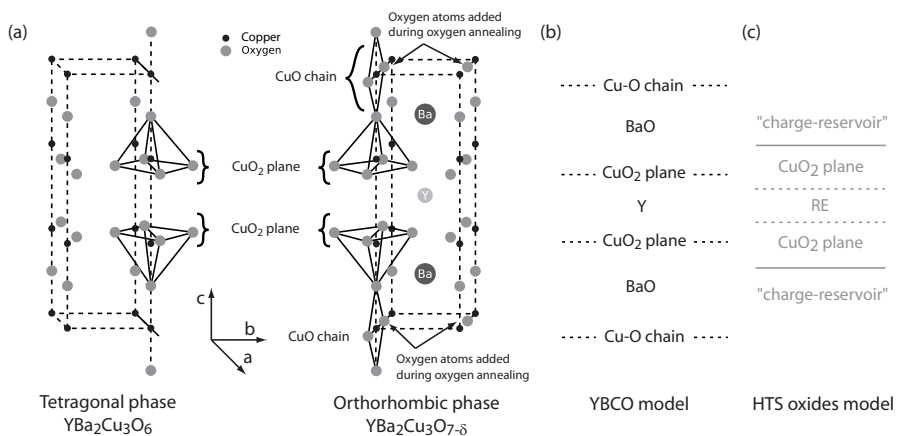
Figure 1.13: (a)- Crystallographic structure of a Y-Ba-Cu-O system arranged on a tetragonal lattice, $YBa_2Cu_3O_6$, and on an orthorhombic lattice, $YBa_2Cu_3O_{7-\delta}$. (b)- Schematic representation of a YBCO. (c)- Schematic representation of a (RE)-Ba-Cu-O system, where RE stands for a rare-earth element.
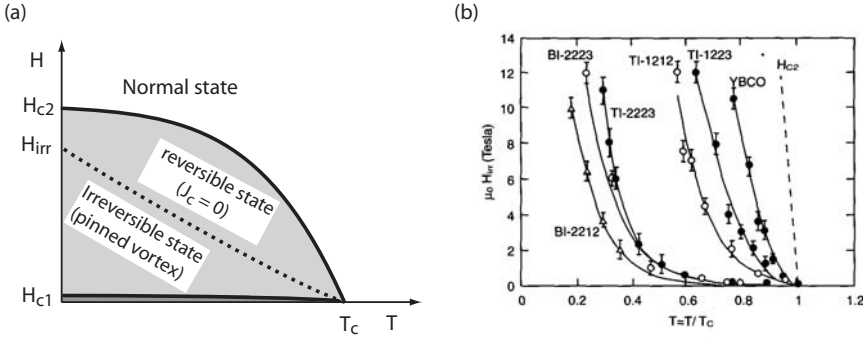
Figure 1.14: (a)- $H - T$ diagram of a HTS oxides. The vortex state is split in two parts by the irreversibility line. (b)- Irreversibility fields of several HTS cuprates, taken from Ref. [55]

anisotropy ratio, γ, such that

$$\gamma = \frac{\xi_{a,b}}{\xi_c} = \frac{\lambda_c}{\lambda_{a,b}} = \frac{H_{c2}^{//a,b}}{H_{c2}^{//c}} = \frac{H_{c1}^{//c}}{H_{c1}^{//a,b}} \quad (\gamma \geq 1). \tag{1.26}$$

In YBCO, typical values of γ are within the range $[5 - 7]$ and are rather in the range $[50 - 200]$ for highly anisotropic layered compounds like $Bi_2Sr_2CaCu_2O_{8+x}$. The anisotropy ratio mainly depends on the coupling strength between adjacent CuO_2 planes [54].

Due to the anisotropy and the small coherence length of the cuprates, the mixed state of HTS reveals some peculiar features:

(i) The transition from the non-dissipative regime to the flux flow regime due to an increase of current is broader than in the case of conventional type-II materials. As a result, large flux creep effects are observed in HTS oxides and the critical exponent n of the power law is smaller ($n \sim 25$) than that of the conventional superconductors ($n \sim 100$) [43].

(ii) An additional transition line appears in the $H - T$ phase diagram of HTS, that is called the *irreversibility line*. Below H_{c2}, there exists a magnetic field H_{irr} such that there is no more effective pinning in the HTS if $H_a > H_{irr}$. When $H_a > H_{irr}$, the pinning energy becomes comparable with the thermal energy, the vortices are depinned by thermal fluctuations and $J_c = 0$ [2]. The irreversibility line is of prime importance for applications, much more than H_{c2} governs the maximum field that maintain the pinned vortex state with no dissipation. The irreversibility line of several HTS oxides is reproduced in Figure 1.14. Note that H_{irr} is much smaller than H_{c2}, particularly in Bi-based cuprates.

(iii) The vortex lattice exhibits only a short-range hexagonal order, not a long-range order like in an Abrikosov lattice. Moreover, while the flux lines along the c-axis have a circular cross section, those along the a, b-plane have rather an elliptical cross section due to the anisotropy.

1.6   Bulk HTS materials

Among all the available forms in which high-temperature superconductors may be processed, two of them are particularly important in the framework of this thesis. These are the polycrystalline bulk monoliths and the single domains[2], both types are referred to as bulk HTS. We will come back on the other forms (wires, cables, thin films) in the last section of this chapter, when dealing with the applications of HTS.

Although great progress has been achieved in the recent years in the field of HTS thin films and tapes, several interesting applications, such as levitation systems and flywheels, remain still more efficiently realized with bulk materials. Therefore, there is still a need for developing bulk HTS materials for engineering applications.

HTS bulk materials are of mainly two types : (RE)-BaCuO, where (RE) denotes a rare earth such as yttrium and (X)-CuOCa where (X) denotes either TlBaO, HgBaO or (Bi,Pb)SrO such as in Bi-2223 which is the most common material of that type. The second type of bulk HTS has a very weak interactions between the superconducting layers. As a result, they have a smaller irreversibility field than that of (RE)-BaCuO materials and are therefore less interesting for applications involving high magnetic fields. Moreover, Bi-based materials are not processed in single crystals, but as a sintered powder, having therefore a smaller critical current density than that of single domain (RE)-BaCuO. In the present manuscript, we will mainly focus on (RE)-BaCuO bulk materials, and particularly on YBaCuO, whose processing is described in the following paragraphs.

Bulk HTS made of (RE)-BaCuO materials are typically processed in plane-parallel or in cylindrical shape, with a typical diameter that may extend up to maximum 100 mm [57], or even more with multiple seeding [58]. However, the processing of single domains with such large dimensions is very difficult and time-consuming. The bulk samples with larger dimensions are polycrystalline with numerous single domains, or grains, that are weakly coupled together [59]. The polycrystalline samples are characterized by two different current flows:

(i) the *intragranular* current that flows inside an isolated grain, without crossing the joints between the grains,

(ii) the *intergranular* current that crosses the grain boundaries.

In the case of a transport current flowing in the sample, only the intergranular current is activated. When an applied magnetic field penetrates the sample, both current types plays a role in the magnetic properties of the sample. In particular, the intergranular critical current density between naturally-occurring grain boundaries is several orders of magnitude smaller than the intragranular one, and is very sensitive to low magnetic fields [60]. As a result, the trapped magnetic flux above a cylindrical polycrystalline bulk HTS exhibits a non-axisymmetric profile with several local maxima that are observed in a Hall probe mapping experiment, provided the probe may resolve these maxima; while the trapped flux profile above a single domain has a single maximum. That difference is illustrated in Figure 1.15.

---

[2]A single domain consists of a pseudo-crystalline matrix composed of large parallel crystal plates having a common perpendicular axis. It also includes numerous defects such as microcracks or inclusions of another type of materials [56].
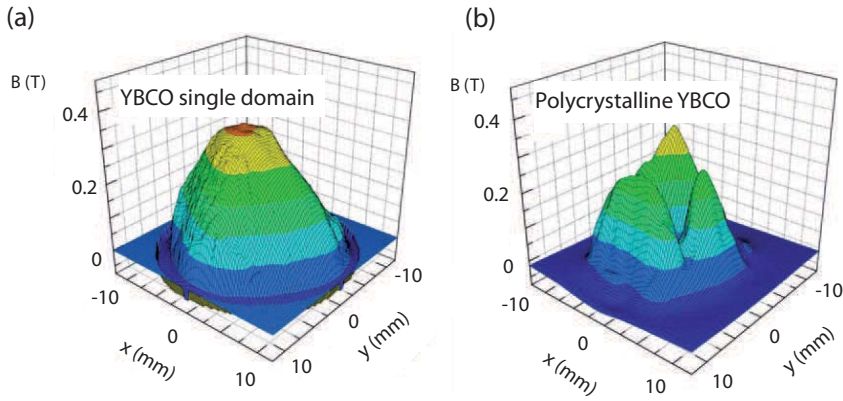
Figure 1.15: *Distribution of the trapped magnetic flux density above the sample surface of a single domain YBCO (a) and of a polycrystalline YBCO (b), taken from Ref. [61]*

In order to avoid the polycrystalline behaviour of bulk materials, the crystallographic alignment of the different grains may be forced during the processing of bulk materials, that is the texturing technique. The description of the texturing and of the processing of HTS single domains is described in the following section.

1.6.1   Processing of bulk YBCO single domains

Bulk YBCO single domains are realized with a textured crystal growth. The most common method is the top-seeded melt-textured growth (TSMG) [8, 62]. It consists in melting an initial powder mixture, containing mainly Y_2BaCuO_5 – Y211 –, by heating the mixture slightly above the peritectic temperature, $T \sim 1050°C$ [63], and then reducing slowly the temperature to solidify the $YBa_2Cu_3O_6$ – Y123 – phase with the help of a seed having a higher melting temperature, thereby ensuring the alignment of the Y123 grains (see Figure 1.16-(a)).

The texturing technique is based on the peritectic recombining reaction of Y123 from the Y211 phase and a liquid phase saturated in baryum and copper [64, 65, 66],

$$Y_2BaCuO_5 + liquide(Ba, Cu) \rightarrow YBa_2Cu_3O_6. \tag{1.27}$$

The superconducting phase $YBa_2Cu_3O_{7-\delta}$ is then obtained after an oxygen annealing of the isolating phase $YBa_2Cu_3O_6$. In order to enhance the texturing during the crystal growth, a Y211 excess is added to the initial powder mixture that acts as an yttrium tank [67]. Moreover, the smaller are the Y211 particles, the higher is the critical current density, since the Y211 particles that did not react and that are surrounded by the Y123 matrix may act as efficient pinning centres for the vortices [68, 69]. Usually, some dopants, such as Ce and Sn, are also present in the initial mixture in order to obtain fine particles of Y211 [67].

The seed that controls the crystal growth direction has a crystallographic structure that is close to $YBa_2Cu_3O_{7-\delta}$ and a higher melting point. Typically, the seed is a single crystal of $SmBa_2Cu_3O_x$ or
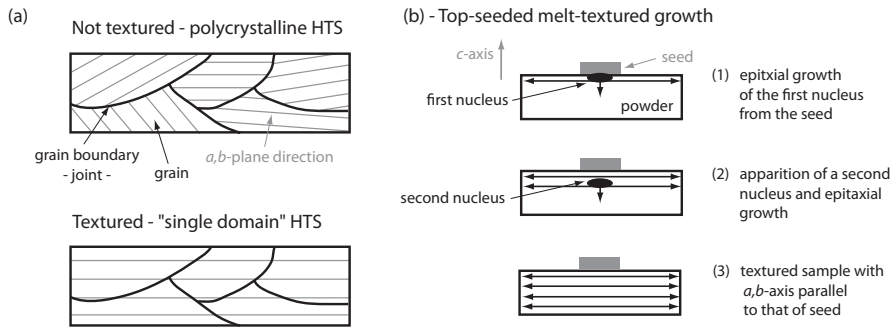
Figure 1.16: *(a)- Illustration of the difference between a non-textured polycrystalline YBCO, where the crystallographic direction of the different grains are not aligned, and a textured sample, forming a quasi YBCO "single crystal", or a single domain. (b)- Formation steps of the epitaxial crystal growth of a top-seeded melt-grown YBCO sample, from a seed located at the surface of a powder.*

$NdBa_2Cu_3O_x$ [70]. The a, b-planes of the seed are parallel to the surface of the liquid phase of Y123 such that the growth front follows these directions. The crystal growth proceeds epitaxially, layer by layer, starting from the surface that is in contact with the seed. A schematic illustration of the top-seeded melt-growth process is shown in Figure 1.16-(b).

The TSMG process allows for obtaining single domains in cylindrical shape with a diameter up to 100 mm. The melt grown samples are nevertheless subjected to numerous microcracks and macrocracks [71, 72] that impede on the superconducting properties. These cracks are either due to material contraction during the growth [73] or during the oxygen annealing [74]. Actually, the oxygen annealing modifies the crystallographic structure of the material. Y123 switches from the tetragonal phase to the orthorhombic one having a different mesh size; it causes material contractions which may generate cracks.

1.6.2   Drilling holes in bulk YBCO

The macro- and microcracks appearing in melt-grown samples mainly during the oxygen annealing degrade their superconducting properties. Besides, the oxygen annealing of large bulk samples is a long process. In order to improve the oxygen annealing process, it has been shown that a gradual oxygen annealing process may contain the gradient of the oxygen rate below the limit of crack creation [75]. However, that technique has been revealed efficient only on small samples (< 2 mm) where the oxygen has only to diffuse on a very small distance. For using that technique on large samples, it has been proposed to create an array of parallel columnar holes in the bulk material, so as to create thin walls for the oxygen diffusion [6, 10, 61, 76, 77, 78, 79].

These drilled samples are also aimed to

(i) reduce the porosity inside the bulk materials, since the holes could serve as a gas extraction conduit [80],

(ii) induce a higher critical current density,

(iii) ensure a good thermal stability in applications, since the heat exchange surface is increased as compared to a non-drilled sample.

The drilled samples are processed with the top-seeded melt-grown technique. The holes are drilled in the sintered powder before the crystal growth. In order to prevent the powder from crumbling, it is first sintered for a better mechanical behaviour. The holes are usually drilled vertically in the pellet, along the direction of the axis of the cylinder, with the help of a usual high speed drilling machine. The drills are coated with a diamond film against abrasion and have a typical diameter of $0.5 - 1$ mm. Although the holes are believed to be only useful during the oxygen annealing, these are drilled before the texturing of the material for the sake of mechanical stability. In fact, drilling holes in a brittle ceramic without breaking it, as it is done in Ref. [81], is a very difficult task that is time-consuming and may require heavy equipments, such as an ultrasonic drilling machine [82].

The first drilled superconducting single domain was successfully processed in 2004 [76]. Although initially aimed at being gradually annealed under an oxygen flow, the drilled samples still require a very long annealing time, even with a distance between holes that is smaller than 1.5 mm (diameter of the sample is ≈ 20 mm). Up to now, these were usually annealed with a classical process. Recently, it has been proposed to use a high oxygen pressure (16 MPa) for the annealing [83]. Such high pressure allows one to work at a higher temperature, and consequently, the oxygen diffusion rate in the single domain is increased. Drilled samples with a high-pressure oxygen annealing were successfully processed by X.Chaud *et al.* in Ref. [83].

Independent of the oxygen annealing process (gradual or classical), the as-obtained drilled samples possess several advantages with respect to non-drilled (or plain) samples having similar dimensions:

(i) A reduction of the porosity with respect to a plain sample, as revealed by microstructural analysis. A picture of a vertical cross section of a plain sample (1) and of a drilled sample (2) is shown in Figure 1.17-(a). The drilled sample is more dense than the plain one. In particular, a continuous distribution of pores with a typical size of 100 μm is found in the bulk of the plain sample, and not in the drilled sample. In a drilled sample, the smaller diffusion path intended for an improved oxygen annealing also allows the trapped gas to escape from the bulk.

(ii) A higher critical current density than that of a plain sample. Thanks to the reduced oxygen diffusion path, the oxygen content in a drilled sample is larger and more uniform than in a plain sample, either with the classical (non-gradual) process [6, 84] or with the high-pressure gradual one [83]; in the latter case, the drilled sample exhibits almost no crack. A comparison of the trapped flux profile of a plain (1) and a drilled (2) samples processed under the same conditions as described in Ref. [6] is shown in Figure 1.17-(b). Even if the volume of the superconducting material is smaller in the drilled sample than in the plain one, the increase of critical current density compensates that material removal. As a result, the trapped flux is larger in the drilled sample than in the plain one.

(iii) a larger heat exchange surface with the cryofluid that ensures a better thermal stability. In particular, Laurent *et al.* in Ref. [9] compares the trapped flux decay in a drilled and in a non-drilled sample that results from a small heater glued at the surface of both samples. The drilled
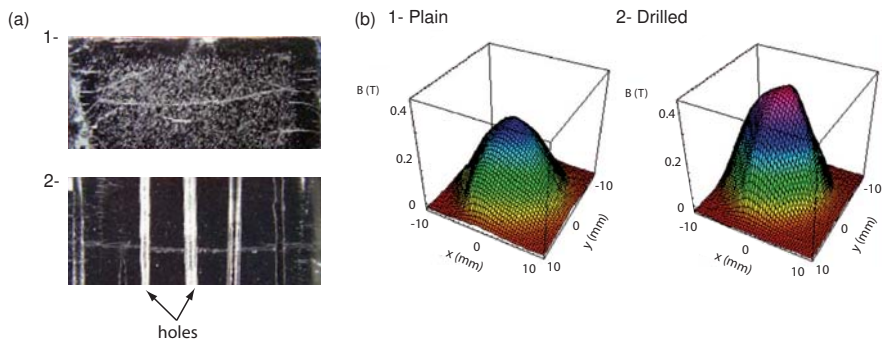
Figure 1.17: *(a)- Vertical cross section of a top-seeded melt-grown sample having no holes (top panel) or several holes along the c-axis (bottom panel), from Ref. [6]. (b)- Distribution of the trapped magnetic flux density above the sample surface of a non-drilled and a drilled top-seeded melt-grown cylindrical sample, from Ref. [6]*

sample exhibits the smallest trapped flux decay, and hence, the best thermal stability. When used in a motor, drilled samples are thus believed to suffer less from the heat generated by the motion of vortices due to magnetic flux variations.

(iv) A new way for reinforcing mechanically the sample with the help of a resin impregnation inside the holes [81, 85]. The reinforcement is very important in samples used as trapped field magnets, where huge radial Lorentz forces may break them up. It has been shown that reinforcing the samples may increase the tensile strength of (RE)-BaCuO samples (typically $20 - 30$ MPa [2]) up to 80 MPa [86].

Besides these advantages, the drilling of holes in the sintered powder also has some drawbacks. First, the crystal growth of the sintered powder is influenced by the presence of holes. When a growth front coming from the seed and propagating along the a, b-plane reaches a hole, it leads to the formation of a small closed growth subsector beyond the hole that does not disturb the Y123 crystal growth [79]. Furthermore, a Y211 layer extending along the c-axis may be observed in the neighbouring of holes, due to the formation of the growth subsector. On the other hand, if the hole lies on the boundary between two growth fronts coming from adjacent sides of the seed, it yields a more complex situation, with the formation of other growth sector boundaries extending beyond the hole; the crystal growth of Y123 is modified [79]. It is therefore strongly advised to position the seed in a hole free region and such that the growth sector boundary will not cross the holes.

Then, the presence of the holes in the sample affects its mechanical properties [87]. Calculations based on the Bean model has shown that the stresses caused by flux pinning around a central hole may increase by a factor of 2 [88].

Finally, drilling holes in a superconductor is detrimental to its magnetic properties. It was found in [89, 90] that removing superconducting matter decreases both the full penetration field and the trapped flux, provided the critical current density remains unchanged. For bulk samples, studies based on the Bean model already pointed to the magnetization drop that results from drilling holes [89, 90]. Holes also lead to macroscopic changes in the current distribution. According to the Bean model, the

current stream lines near a hole abruptly change their direction along discontinuity lines [11] and circle the hole in a region that extends far beyond the hole itself. This effect is enhanced in thin films, as the magnetic flux density displays sharp peaks at the discontinuity lines. Such macroscopic changes of the magnetic flux were observed with magneto-optical imaging of thin films having macroscopic defects [91, 92].

1.7   Applications using HTS cuprates

The discovery of high-temperature superconductivity in 1986 rose scientists' hopes for providing new and very efficient applications that could force some technological barriers and open new research horizons. For instance, the non-dissipative current flow at the liquid nitrogen temperature would solve the problem of energy losses on long-distance transmission lines; next, the large current density that may flow continuously in a closed loop of HTS cable would be used for generating large DC magnetic fields (up to several tens of teslas) that would lead to new scientific discoveries, in a similar manner as the development of ultra-sensitive magnetic probe incorporating superconducting layers does; and finally, the pinning of vortices in HTS samples enable a stable levitation between a permanent magnet and a HTS sample from which would follow the creation of levitating transportation systems.

Unfortunately, the early passions for HTS applications faded slowly away because of difficulties arising from their synthesis processes. The development of HTS applications was therefore intimately related to the progresses realized in material processing. Nowadays, the research on material science have allowed for a mass production of YBCO coated conductors that are believed to occupy a leading role for the appearance in the forthcoming years of HTS applications in the everyday's life.

The coated conductors, which represent the second generation of HTS wires, were precessed by a first generation of HTS cables made of $Bi_2Sr_2Ca_2Cu_3O_{10}$ (Bi-2223) material. HTS cables of the first generation consisted of several Bi-2223 tapes embedded in a silver alloy matrix. The tapes had a typical size of 0.2 by 4 mm, and a cable contained approximately 50 tapes [20]. These cables were able to sustain critical current densities up to 10^8 A/m^2 that allowed them to successfully meet the technical requirements of the first HTS applications. However, the much higher irreversibility field and critical current density of YBCO have always forced scientists to work towards YBCO-based HTS cables. They stroke against several processing problems, mainly due to the polycrystalline features of such materials, but they eventually developed the concept of YBCO coated conductors with unbeatable superconducting properties at the liquid nitrogen temperature. Coated conductors are made with a thin-film of a layer of $YBa_2Cu_3O_{7-\delta}$, with grain-to-grain misorientations of at maximum 5° [93, 94]. Coated conductors rely on the thin-film technology to deposit epitaxially a superconducting layer on a highly biaxially textured tape-shaped template. The nickel-textured RABiTS substrates are usually chosen [93]. Coated conductors are flexible and available in long lengths.

While the coated conductor technology is the latest released and the most discussed progress in the field of HTS, it is worth mentioning that superconducting electronics using HTS have greatly taken advantage of the development of HTS thin films. In the same spirit, advances have been also made in bulk materials processing, with, for instance, the introduction of drilled samples, as discussed in

Section 1.6.2. The applications using bulk materials become more and more efficient and feasible for industry and everyday's life.

The success of HTS applications is also dependent on the efficiency of the solutions brought to the cooling-related problems. Working with HTS requires an efficient cooling system with low thermal losses for reducing the working costs as far as possible. Actually, the main relevant aspect that will push (or not) HTS applications into the economic market is the price of the system. Even if the efficiency and the technical advantages of a HTS application are undoubtedly demonstrated, its commercial success will almost entirely depends on its market price. Therefore, the cooling price should be kept at a minimal value [95]. On the other hand, the technical features of the cooling systems, such as their sizes or their efficiency, are also decisive for the success of HTS applications. The cooling of HTS in large-scale applications is performed via a cryofluid, whereas HTS thin-films used in electronic applications are cooled by small cryocoolers. That difference must be taken into account when developing the cryosystems.

In the following section, we describe first some recent applications using HTS shaped in wires and thin films. Then, we present in more details the application domains where the bulk monoliths are intended to be used.

1.7.1 HTS wires

The HTS cables, no matter if they are of first or second generation, are used for **energy transport**. They are advantageous with respect to classical copper cables for several reasons. First, HTS cables achieve large power transmission capacity with a compact size. For instance, an aluminum alloy cable with a diameter of 30 mm carries as much energy as a YBCO coated conductors having a rectangular cross section of 2 μm by 4 mm. This is fruitful for the total cost of the cable system, and for solving the problems related to the continuously growing power requirement around big city centres. The energy transport in HTS cable occurs with low power losses. It is worth mentioning here that the electrical power is usually carried with an AC current. Although a superconductor has almost a zero DC resistance, it exhibits small losses in AC regime due to the induced motion of pinned vortices. The AC losses are still much smaller than the resistive losses measured with conventional cables. Then, transporting electrical power through HTS cables is also respectful for the environment. The low power losses allows for an energy consumption reduction at the upstream part of the power grid. Then, because the HTS cables are cooled down, and usually immersed in a continuous flow of liquid nitrogen, there is no risk of fire or burst. Finally, the magnetic field created around a cable carrying a current may be efficiently shielded by an additional superconducting layer that circle the cable. There is therefore no electromagnetic pollution around the HTS cables.

Nowadays, several prototypes of HTS cables are being installed all around the world [96, 97, 98], including the Long Island project of replacement of a 600 m-long wire by a 2G HTS wire in the commercial power grid [99]. These are conceived in order to better clarify the reliability and the stability of the HTS cables.

The unique nature of superconductors wires enables for the design of compact **fault-current limiter**

preventing from rapid increases of the current in the network [100, 101]. Actually, when the current density flowing in the superconductor becomes greater than J_c, the superconductor returns back into its normal state, whose impedance is quite high for HTS and avoid the increase of the current propagating in the network and causing damages on the connected devices. The quenching of the superconductor, i.e. the transition from the superconducting to the normal state, is reversible, provided that the heat produced by the current flowing in the high resistive state is efficiently removed from the cable.

The HTS wires may also be used as **current leads** in large superconducting coils for the generation high magnetic fields. HTS current leads substantially reduce the heat load to the cold superconducting coil made of LTS wire. The resistive losses in usual cables that electrically connect the coil to the power source generates a large amount of heat in the cold part that has to be removed by the cooling system. In particular, the LTS superconducting coils of the Large Hadron Collider (LHC) are equipped with HTS current leads [102].

Superconducting coils can be now also realized with HTS wires. The high irreversibility fields of HTS wires, on the order of 70 T for 2G wires, allows one for working with much higher magnetic fields than those achieved with LTS coils. HTS coils have therefore the potential to breach the limit of today's superconducting magnet using LTS (45 T in a hybrid magnet (resistive and superconducting) at NHMFL, Florida, USA [103]) and open opportunities for developments in magnetic resonance, particle accelerators, colliders, and fusion devices [104, 105]. Nowadays, the world-record's magnetic flux density in the centre of a 2G HTS coil is 26.8 T in a background field of 19 T and cooled down at 4.2 K [105, 106]. The coil has a very compact size with a diameter of $\sim$ 200 mm and a height of $\sim$ 150 mm.

Another use of the superconducting coils is related to electrical energy storage. The **superconducting magnetic energy systems** (SMES) transform electric energy into magnetic energy by a lossless current flowing continuously in a closed superconducting coil [107, 108]. The SMES are able to store up to tens of kJ/kg (limited by mechanical constraints) with a specific power that is typically 100 MW/kg [109], which makes them ideal candidates for power sources. By increasing the operating temperature, 2G HTS SMES require a simple refrigeration system and are cheaper than LTS SMES due to reduced exploitation and investment costs. Note however that the very fast discharge of the energy stored in HTS SMES is inappropriate for a domestic use, where the power has to be almost constant over time. HTS SMES rather aim at the compensation of the power grid deficiencies during a very short period.

Motors, transformers and generators based on 2G HTS coils are of considerable interests for applications where the weight reduction is of prime importance. In particular, the US Navy works toward lightweight small-sized HTS motors for their battleships and submarines [110]. In the same spirit, the US Air Force develops a new generation of aircrafts where the hydraulic will be completely replaced by electronics, and where HTS generators could save weight and volume together with providing a higher efficiency than classical motors [111]. Other civilian projects are also lead in different laboratories. For instance, compact and light HTS transformers are taken on board of train wagons in order to improve the welfare of the passengers (low noise) and the ecological impact (high efficiency) [112].

1.7.2 HTS thin films

Superconducting electronics constitutes maybe one of the most important field of applications for superconductors because superconducting thin-films offer technical features for electronic system that no other known material is able to reproduce. In the other domains, HTS with their unique properties aim at enhancing the performance of existing systems, and sometimes quite impressively, but rarely provide totally new kinds of applications that were not available with classical technologies.

The Josephson junctions lie at the basis of these new applications. The Josephson junctions are trilayer structures comprising two superconductors separated by an isolating or metallic material. Without any applied voltage, an electrical current is able to cross the junction by tunnel effect. When a DC voltage is applied to the junction, it induces current oscillations whose frequency lies in the range 1 GHz $- 1$ THz. Moreover, the current across the junction can be modulated with the help of a magnetic field. Both effects are referred to as Josephson effects.

The Josephson junctions are used as a voltage standard, defining physically the *volt* unit from a frequency [113]. The coupling of resonators to microwave filters is enhanced by using the low microwave losses of HTS thin films [114]. The improved coupling with much sharper frequency characteristics than conventional compact filters is used for instance in aircraft electronics [95] or in mobile phone communications systems [115].

Two junctions arranged in a closed loop constitute a superconducting quantum interference device (SQUID) sensor. The SQUIDs are the most sensitive magnetic field sensors ever realized that probe magnetic fields that are several order of magnitudes smaller than the sensitivity of conventional magnetic probes. The smallest measured magnetic flux density is of the order of 10^{-18} T after averaging few days of measurements [116]. HTS SQUIDs are believed to have an important commercial impact since they can be handled without complex cryosystems. An important aspect associated with HTS SQUIDs is their possibility to be used without the burden of a magnetic shield. To this aim, the SQUIDs measure the magnetic field gradient instead of the local magnetic field value. Mobile non-shielded HTS SQUIDs were tested successfully in biomedical [117] and geophysical applications [118]. In Josephson samplers, the fast voltage reaction of a Josephson junction when a current exceeds the critical current of the junction determines repeated signal forms with picosecond resolution [119].

1.7.3 Bulk HTS in levitation systems

The ability of bulk HTS to trap a high magnetic field that is almost constant in time makes them ideal candidates for replacing conventional permanent magnets. These classical magnets have typically a maximum magnetic flux density of 500 mT at their surface, while HTS bulk magnets can trap flux densities that are one order of magnitude larger. The world record is hold by Tomita and Murakami with over 17 T at 29 K [81]. Since stored magnetic energies and forces scale quadratically with the trapped flux density, these trapped magnets offer magnetic energies and forces of two orders of magnitude higher than conventional magnets. New classes of applications are available for permanent magnets.

Among these applications, there is a particular interest for superconducting bearing systems. The stable magnetic levitation of a bulk HTS above a permanent magnet is one of the most fascinating phenomenon associated with superconductivity. This levitation is completely passive and results from the trapping of the magnetic flux surrounding the permanent magnet by the pinned vortices. The magnet and the HTS then constitute a single body inside which all relative motions of one part with regards to the other one require the application of a force at least equal to the pinning force [2]. It is worth mentioning that no stable levitation is possible with two permanent magnets [4], unless some degrees of freedom are limited or unless it is controlled with an active feedback. The magnetic bearings using HTS levitation are found in linear transportation systems (MAGLEV train or contactless transportation system in microelectronic cleanroom), in magnetic trap systems or in flywheels energy storage.

Activation of bulk HTS trapped field magnets

In order to be used as trapped field magnets, the bulk HTS need to be magnetized. There are usually three ways for activating the magnets: the field-cooled magnetization (FC), the zero field-cooled magnetization (ZFC) and the pulsed-field magnetization (PFM), the latter technique being a part of the ZFC process.

(i) **Field-cooled (FC) magnetization**: the HTS bulk magnet is cooled down to its operating temperature in a magnetic environment. When the temperature is above T_c, the sample behaves as a non magnetic material and is fully penetrated by the magnetic field. As soon as its temperature becomes smaller than T_c, the uniform magnetic flux inside its volume reorganizes itself in vortices, each one carrying a quantum of magnetic flux. At a microscopic sale, the distribution of the magnetic flux is discontinuous, while at a macroscopic scale, it remains continuous. As usual with HTS materials, the vortices are pinned by impurities, such that there remains a trapped flux in the bulk HTS when the applied field vanishes. Because of the large flux creep observed in HTS samples, a 15 min period is needed after the external magnetic field has vanished in order to stabilize the trapped flux.

In order to fully magnetize the sample, i.e. to have a critical current density flowing in the same direction all over its volume, and hence, to trap the maximum magnetic flux, it is necessary to apply a DC uniform field whose flux density is at least equal to the maximum magnetic flux density that can be trapped in the sample — also called the penetration field B_p in Section 1.4.1. The applied magnetic flux density can be very large. For instance, the full magnetization of a (RE)-BCO single domain samples with a diameter of 20 mm and a height of 10 mm may require magnetic flux densities up to 3 T. Typically, such large flux densities are achieved with superconducting coils. These coils are bulky, heavy and usually not mobile; the HTS magnet has to be first magnetized in the facility where the coil is located and then moved toward the location where it is needed.

A FC activation is also obtained with permanent magnets located close to the HTS samples. For many samples, the use of a permanent magnet does not allow one to fully magnetize a HTS sample. A full magnetization with a permanent magnet may only be achieved in small

(RE)-BCO single domain samples, with a characteristic size smaller than 5 mm.

(ii) **Zero field-cooled (ZFC) magnetization**: the HTS sample is first cooled down below its critical temperature in a zero magnetic field environment. Then, a uniform magnetic field is applied around the sample. In a ZFC process, it is usual to apply a linearly increasing magnetic field with a given sweep rate (usually few mT/s) up to a maximum magnetic field that is larger than twice the penetration field of the sample (in order to fully magnetize the sample), followed by a linearly decaying field with typically the same sweep rate. Like in a field cooled magnetization process, the applied magnetic field is usually produced by a superconducting coil.

(ii) **Pulsed field magnetization (PFM)**: the HTS is first cooled down below its critical temperature in a zero magnetic field environment. Then, a pulse of magnetic field produced by a fast discharge of a capacitor through a copper coil is used for activating the magnet. Even if the magnetic field is applied during a very small time (typically up to hundreds of ms), the PFM enables to trap as large magnetic flux densities as those obtained with the other techniques, provided the amplitude of the pulse is twice the penetration field of the sample. As opposite to the other activation processes, no superconducting coil is required. The as-obtained gain of weight and volume of the exciting coil is very convenient for *in situ* activation of the magnets. The pulsed-field magnetization will probably be used widely in future applications using trapped field magnets.

MAGLEV train

Rising a train wagon at few centimeters above the tracks has been a challenge for engineers since decades. Since there is no contact between the car and the ground, a levitating train travels at high speeds (more than 500 km/h) with an energy consumption that is reduced with respect to that required by a conventional train; the energy in a levitating train is only necessary to overcome the air drag and maintain a constant velocity.

Magnetic levitation (MAGLEV) trains may be designed with various technologies: (i) electrodynamic suspension or (ii) stabilized permanent magnet suspension. In an electrodynamic suspension, the levitation of the cars is achieved by the repulsive force between two current coils arranged in a specific configuration. Secondary coils on the tracks that are crossed by an alternating current ensure the propulsion of the train. In the stabilized permanent magnet suspension, the levitation is ensured by the repulsive force between two magnets. The stable levitation with two permanent magnets requires a guidance or an active feedback control, that become unnecessary when using HTS trapped field magnets. HTS bulks are therefore ideal substitutes for rare-earth permanent magnets in MAGLEV trains

MAGLEV trains using a passive levitation with HTS bulk magnets are under development, in China particularly. The basic idea is to use a permanent magnet guideway and onboard HTS bulk magnets cooled down at liquid nitrogen temperature [5, 120, 121]. The permanent magnet levitation, by its nature, reduces drastically the electromagnetic drag, and hence, the power consumption. Moreover, since no current is required for levitating the train, the power supply system is less complex than that needed for the electromagnetic levitation and the line losses are reduced. The guideway magnets are

NdFeB permanent magnetic materials exhibiting a high residual magnetic field and a high coercive force. The arrangement of the permanent magnets on the guideway is also an important factor that determines the efficiency of the suspension. Although the advantages of such systems are numerous, there is still progress to be done in view of a first commercialized MAGLEV trains with bulk HTS.

Water treatment for environmental purposes

The stable levitation with HTS trapped field magnets also provides a way for magnetic separation. That technique has been successfully applied for purifying contaminated water plants in Japan [122]. HTS bulk-based systems remove aggregated ferromagnetic parts, including emulsion oil, from a water flow, by making them levitating above HTS magnets that were previously magnetized. Such a system is more compact than conventional ones and has the advantage of not having a filter to replace periodically. The disposal efficiency is close to 100 %, but the flow rate is rather limited, tens of liters per min.

Flywheels

With similar objectives than those of SMES, flywheels are energy storage systems based on the mechanical rotation of a magnetized piece. In order to reduce the energy losses during its motion, the rotating part is suspended in the air. The levitated flywheels offer several advantages for stationary applications: few maintenance services, low-noise operation and minimized losses. A flywheel behaves both like a motor, when accelerating the rotating piece for accumulating kinetic energy, and a generator, when delivering part of the kinetic energy.

In that field of applications, HTS trapped field magnets are very promising. Several HTS flywheel prototypes have already been developed [123, 124, 125]. The storage capacity ranges up to 10 kWh. Such systems are believed to be associated with windmills or solar plants, in order to deliver energy in the event of lack of wind or sunshine [2].

1.7.4   Bulk HTS used as magnetic shields

Beside constituting very efficient trapped field magnets, bulk high-temperature superconductors processed in hollow tubes may also act as magnetic screens that strongly attenuate the magnetic field at their centre. HTS shielding tubes achieve very high attenuation factors, in longitudinal (field parallel to the tube axis) as well as in transverse (field perpendicular to the tube axis) configurations. Such a dual shielding is not possible with a single high-permeability ferromagnetic tube.

The shielding mechanism is already illustrated by the description of the critical state in the infinite slab (see Section 1.4.1). When the magnetic field surrounding the slab is lower than its penetration field, the centre of the slab is not penetrated by the external field. The same effect is used in shielding tubes.

Shielding tubes consist either of $Bi_2Sr_2Ca_2Cu_3O_{10}$ sintered powder [51, 126, 127], of polycrystalline

YBCO (since the shield has to have large dimensions) [128], or even in YBCO thin films deposited on a substrate [129, 130]. Bi-2223 tubes have been shown to shield the tube centre from magnetic flux densities up to tens of mT at 77 K [51], while YBCO tubes are believed to shield a much larger magnetic flux density, especially in the case of textured YBCO.

The shielding applications with bulk YBCO do not form by themselves a part of this thesis, since drilled structures are rather intended for trapped field magnet applications. However, the shielding properties are intrinsically related to the magnetic properties of bulk HTS materials, exactly as the trapping ones are. In a magnetic environment, the inside of the holes may be preserved from magnetic field and may serve as shielding pockets.

1.7.5 Electrical rotating machines using bulk HTS elements

Bulk HTS are also intended to be used in electrical rotating machines for providing very high specific output power with very few losses. These machines are still at the primary laboratory tests, provide great power density [3] and are be very useful for typical applications where the weight reduction is of prime importance, such as in submarines [2].

In many topologies envisaged for designing an efficient electrical rotating machines based on bulk superconductors, the HTS sample is permanently magnetized parallel to its c-axis and placed in the machine rotor [3, 131]. In this configuration, the sample is likely to experience transient variations of the applied magnetic field caused by modifications of the applied torque on the shaft. The resulting vortex motion may cause large hysteresis losses and a significant temperature increase which, in turn, has a detrimental effect on the initial trapped flux [9, 132]. Drilled structures are therefore believed to improve the stability of the trapped field magnets used in rotating machines.

1.8 Summary of Chapter 1

In this first chapter, we review the basic concepts lying behind the term superconductivity and we specify the role played by the bulk drilled high-temperature superconductors in the broad range of applications using superconductivity. We particularly discuss the interest of creating an array of artificial holes in bulk YBCO superconductors for enhancing its synthesis. The pattern of holes separated by very thin walls favors the oxygen diffusion process in the superconductor. As a result, the oxygen annealing, required for the transition of the crystal structure to its superconducting phase, is enhanced, and provides critical current densities, and hence trapped magnetic flux densities, in drilled samples that are substantially larger than in plain samples processed similarly. The drawbacks of the drilled structures are also described. The presence of holes impedes the growth front propagation and perturbs the current stream lines that have to circle the holes. These observations prepare the ground for the study and the optimization of the magnetic properties of the drilled bulk HTS that is reported in this manuscript.

The applications of HTS are then described. We particularly point out the features of bulk drilled HTS that are of prime importance in applications, such as the trapped magnetic flux or the magnetization

process. We are now able to target more precisely the study of the magnetic properties of drilled structures in the perspective of trapped field magnet applications.

2

Numerical methods for the modelling of the magnetic properties of drilled bulk high-T_c superconductors

Drilling holes in the pellet of a YBCO powder has several advantages regarding the synthesis of the superconductor, as well as its mechanical and thermal properties. However, the removal of superconducting volume is detrimental for the magnetic properties of the sample, as the current stream lines in drilled bulk HTS are modified with respect to those of a plain sample. It is therefore of prime importance to model these current stream lines and the modification they induce on the magnetic properties of the superconducting sample[1].

This chapter introduces several models and methods for calculating the current stream lines and the magnetic field distribution in samples with artificial holes. These models are intensively used in the following chapters to study the influence of the holes, of their sizes and of their arrangement on the magnetization of the drilled samples and to explain the measurement results.

2.1 Different strategies for modelling the magnetization of HTS drilled samples

In a series of geometric configurations of samples with a high level of symmetry, e.g. a cylinder subjected to an applied field with an axial symmetry, the current flows azimuthally, i.e. its direction is known *a priori* for symmetry reasons. In such cases, it is possible to reduce the three-dimensional (3D) model to an axisymmetric 2D model. Such a simplification is however not possible when considering

---
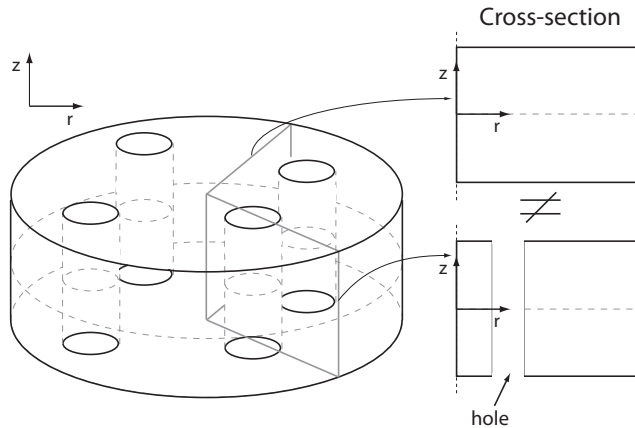
Figure 2.1: *Geometry of a drilled sample with two particular cross sections in the* (r, z)-*plane.*

drilled samples, since these samples are three-dimensional (3D) bodies having no particular symmetry that can be used to reduce the dimension of the model, as shown in Figure 2.1.

Calculating a three-dimensional magnetic field distribution in HTS is notoriously difficult [135, 136]. In the limit of strong pinning, the magnetic flux distribution can be described with the concept of the critical state, introduced by C.P. Bean [38]. The critical state assumes that the current density has a constant magnitude and flows perpendicular to the local field lines, since the magnetic force exerted on the vortices only depends on that component [136]. However, for some configurations where either the sample or the source of the field has no particular symmetry, such as those including holes in the sample cross section, the critical state model must be modified in order to properly describe the time evolution of the component of the current density that is parallel to the local magnetic field [136]. This problem was recently solved in very simple geometries, but the generalization to arbitrary geometries is still not established.

However, in drilled samples, we expect that modelling the longitudinal currents only yields second-order corrections to the magnetic field distribution calculated with a model neglecting them for several reasons. First, the flux distribution near the median plane of the sample is not affected by longitudinal currents, since the current lines are expected to lie in the plane and thus to be perpendicular to the local flux lines. Then, close to the sample surface, the radial component of the magnetic flux density that may be parallel to the critical current density in the regions of influence of the holes still remains very small in samples for which the height is comparable to the diameter. Finally, when considering global quantities, such as the magnetization of the sample, the effects of the longitudinal current are averaged and thus become negligible since they are expected to only have impact close to the cylinder surfaces. Therefore, we believe that the first-order approximations of the magnetic field distribution neglecting the longitudinal currents may lead to *qualitative* conclusions regarding the influence of the hole lattice on the magnetic properties of the drilled samples.

At the same time, the critical state concept fails in reproducing the magnetic relaxation effects observed in HTS samples. These effects are more important in HTS than in conventional type-II superconductors, particularly at the temperature of liquid nitrogen (77 K) [48, 137, 138]. It is

thus necessary to take them into account for accurately describing the magnetic properties of HTS samples. Numerical methods as those introduced by Campbell [139, 140, 141, 142] or those involving the minimization of the magnetic energy [143, 144], which are however applicable to 3D geometries, are not well suited for modelling the flux creep in the superconductor. We use instead the $E - J$ power law with a finite critical exponent, as described by Eq. (1.25).

Considering these remarks, this thesis aims at making progress toward a 3D modelling of the magnetic properties of drilled HTS samples, by taking into account the flux creep and the demagnetizing effects, while neglecting those related to the longitudinal currents. The modelling of the magnetic properties of HTS samples by taking into account the demagnetizing effects and a finite n-value remains however still a delicate problem, and the results obtained with a model combining a 3D geometry and the highly non-linear resistance of HTS must be discussed with a carefully. Consequently, we adopt a step-by-step strategy to move toward the 3D model.

(i) First, we start with a hypothetical geometry of drilled samples having an infinite height, for which we develop a numerical model to solve the Bean critical state. The model is based on the approach of Campbell and Evetts [11] as regards the propagation of the flux front in superconductors of arbitrary cross section.

(ii) Then, we build a model for calculating the magnetic properties of samples with an infinite height, an arbitrary cross section, and a finite value of the critical exponent n in the $E - J$ power law. Several numerical methods are available to calculate the magnetic field penetration in HTS with a power law conductivity: finite-difference approximation in cylinders [145], Green's function approach in cylinders [135] or in tubes [126], and finite element method (FEM) with so-called A-ϕ formulations [146, 147], T-Φ formulations [148, 149], or unconstrained H-formulations [150, 151].

In this thesis, we adopt a finite-element formulation implemented in the *open source* numerical solver GetDP [152, 153, 154] for several reasons. The choice of a FEM formulation is mainly motivated by the robustness provided by this method when considering highly non-linear problems and its flexibility with respect to a change of geometry. As opposed to commercial softwares such as Flux2D/3D or COMSOL Multiphysics, GetDP is an open source code widely available and well documented.

(iii) Finally, we study geometries with a finite height with the help of a 3D FEM model. The approach is validated for an axisymmetric problem — the magnetic field penetration in hollow cylinders of finite height — where the results of the 3D FEM model are compared with those obtained with a Green's function approach [126].

Let us finally note that the three methods that are discussed in the following sections are not intended to be used with drilled geometries only. These methods are general and may also serve for calculating the magnetic properties of various HTS samples with various geometries and external sources of magnetic field. In particular, we propose a single time-step iteration for calculating the magnetic field penetration in HTS samples subjected to a linearly increasing (or decreasing) magnetic field in order to drastically speed up the numerical calculations. This strategy can be generalized outside the framework of this thesis.

2.2   Bean critical state in samples with an arbitrary cross section and an infinite height

As a first step toward a 3D model of the magnetic properties of drilled bulk HTS, we neglect demagnetization effects and focus on superconducting samples that are infinitely long. Figure 2.2 shows, (a), a sample with a rectangular cross section, and, (b), a sample with a semi-infinite cross section containing a circular hole of radius R located at a distance D from the border. The cross section lies in the $x - y$ plane. We further assume that the applied magnetic field, H_a, is oriented along the z-axis and is uniform. Its amplitude is such that $H_{c1} \ll H_a \ll H_{c2}$. We further assume strong pinning and neglect the surface barrier effects. Under these assumptions, the distribution of the magnetic field in the sample cross section is described by the Bean model [38], which reads

$$\frac{dH_z}{d\ell}(P) = \begin{cases} 0 \\ \pm J_c \end{cases} \tag{2.1}$$

where J_c is constant, while ℓ represents the distance traveled by the flux front to reach a given point, P.

Let us illustrate the procedure to determine the distance ℓ with the help of the two examples shown in Figure 2.2. For reaching a point P_1 located inside the rectangular cross section, the flux front may come from one of the four outer boundaries. Four values for the distances ℓ are possible, $\ell = d_1, d_2, d_3,$ or d_4. How can we determine which one corresponds to the distance traveled by the flux front to reach the point P_1? To answer this question, we rely upon an observation made by Campbell and Evetts [11] regarding the motion of flux fronts in samples with an infinite height within the framework of the critical state. As the external field is increased from 0 to a finite value H_a, the flux front nucleates along the external borders. The flux front propagates toward the non-penetrated regions at a uniform speed, so that the magnetic flux moves in the direction perpendicular to the front
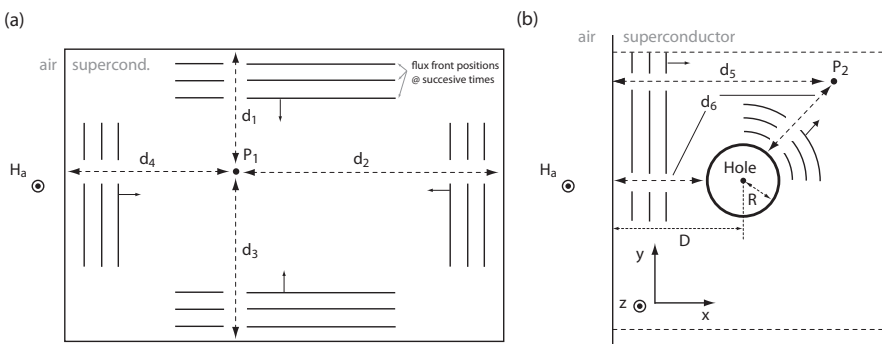
Figure 2.2: *Sketch of an infinitely long sample with (a) a rectangular cross section, and (b) a semi-infinite cross section drilled by a single hole of radius R located at a distance D from the border. In sample (a), four paths (with distance d_1, d_2, d_3 and d_4) are available for the flux front to reach point P_1. In sample (b), the flux front can reach the point P_2 by following two paths: directly from the border, with a path length d_5, or via the hole, which acts as a radial source, yielding a path length d_6.*

(represented by a solid arrow in Figure 2.2). Hence, the points along the flux front are located at a fixed length $\ell = H_a/J_c$ from the border. When the sample is fully penetrated the flux front does not propagate anymore. As a result, the point P is first reached by the part of the flux front coming from the closest border. The distance ℓ that has to be incorporated into Eq. 2.1 is the shortest one among all the available paths, i.e. $\ell = d_1$.

When a point P is at an equal traveling distance for two or more penetration paths, it belongs to a *discontinuity line*, or *d-line*. A discontinuity line separates two regions that are first penetrated by two different parts of the flux front. In a rectangular cross section, these lines correspond to the bisections of the edges of the cross section.

In the sample having a hole in Figure 2.2-(b), let us consider a point P_2 located at a distance $d_5 > D$. For reaching it, the flux front can travel along two paths: it can reach P_2 directly from the border, with a path length d_5, or via the hole which acts as a *radial source* of magnetic field [11], with a total path length d_6. As for the point P_1 in the rectangular cross section, we assume that the flux front travels along the shortest path. In samples of infinite height, the magnetic field, and hence the magnetic flux density, inside a hole is constant and equals to its value in the superconductor, at the border of the hole.

The magnetic field, $H = H_z$, at a given point P in an arbitrary cross section can then be calculated by determining the length, ℓ, of the shortest path that reaches P and by evaluating

$$H = H_a - J_c\, \ell. \tag{2.2}$$

In practice, we build a rectangular meshing grid on the sample cross section which is uniform along the x- and y-directions, with respective grid sizes of Δ_x and Δ_y along both axis. We calculate the magnetic field H_i at all the points P_i of the grid with the help of Eq. (2.2). The magnetization of the sample is then given by

$$M \quad = \quad \frac{1}{S}\int H\, dS - H_a \sim \frac{1}{S}\sum_{P_i} H_i \Delta_x \Delta_y \tag{2.3}$$

where S is the sample cross section. This model is referred in this manuscript to as the *numerical Bean model*.

In order to validate our numerical approach for solving the critical state, we consider a sample with an infinite height and a rectangular cross section of length $2a$ and width a. It corresponds to a classical geometry in which the critical state has already been discussed and solved in Ref. [155, 156]. The distribution of the current stream lines in the sample cross section obtained with the numerical Bean model described here above is reproduced in Figure 2.3-(a). The current stream lines are similar to the lines of constant magnetic field [11], and hence to the lines of constant perpendicular distance from the border. As a result, they can be viewed as the successive positions of the flux front that penetrates the sample from the borders toward the centre. The current lines are parallel to the closest border, and thus exhibits a rectangular shape with wedges aligned on the discontinuity lines where the current abruptly changes its direction. These points are aligned along four discontinuity lines that are represented by grey lines in Figure 2.3-(a).

The magnetization curve of the rectangular sample with an infinite height and calculated with Eq. (2.3)
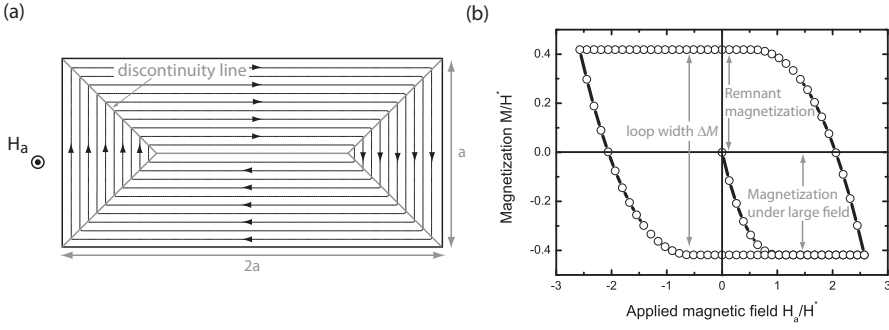
Figure 2.3: *(a)- Current stream lines in a rectangular sample with an infinite height calculated with the numerical model dedicated for solving the critical state in samples of infinite height and arbitrary cross section. The cross section has a length 2a and a width a. The applied magnetic field is such that the sample is fully penetrated, $H_a < H^*$. The discontinuity lines are represented by grey lines. (b)- Magnetization curve of the rectangular sample. The magnetization and the applied field are given in units of H^*.*

is reproduced in Figure 2.3-(b), where the penetration field H^* is given by $H^* = J_c a/2$. The grid size is taken as $\Delta_x = \Delta_y = a/50$. We notice that the magnetization under large fields is equal to the remnant magnetization. In particular, the width of the magnetization loop is

$$\Delta M \;\; = \;\; 0.84 H^*. \tag{2.4}$$

In a rectangular cross section with dimensions $a \times b$ $(a < b)$, the analytical expression for the width of the magnetization loop is given by

$$\Delta M \;\; = \;\; \left(1 - \frac{a}{3b}\right) H^*. \tag{2.5}$$

In the situation where $b = 2a$, one gets $\Delta M = 5/6 H^*$. This value is consistent with that obtained with the numerical model.

2.3   Finite-element method for the modelling of HTS

The second step toward the 3D model of the magnetic properties of drilled HTS consists in introducing the $E(J)$ power law (1.25) in the model of samples with an infinite height. The power law yields an analytical relationship between the electric field and the current density, so as to be incorporated directly in the Maxwell equations and solved with classical resolution scheme, such as finite-element, finite-difference or Green methods.

In this thesis, we use the finite-element method for the reasons discussed in Section 2.1. Within the FEM framework, the approximate solution of a problem is chosen among linear combinations of basis functions so as to minimize the residual of the differential equations of the problem − that is the weak solution. The basis functions are constructed on the meshing grid, that is defined for a specific geometry, such that they only have a non-zero value on few elements of the grid.

2.3.1 Equations describing the magnetic field penetration in HTS samples

The description of the magnetic field penetration in HTS is based on the magneto-quasistatic approximation of the Maxwell equations [157],

$$
\begin{cases}
\nabla \times \mathbf{E} & = & -\dot{\mathbf{B}} \\
\nabla \times \mathbf{H} & = & \mathbf{J} \\
\nabla \cdot \mathbf{B} & = & 0.
\end{cases}
\tag{2.6}
$$

The lower critical field, H_{c1}, is neglected against the applied field, so that the material follows the constitutive law, $\mathbf{B} = \mu_0 \mathbf{H}$. We introduce the vector potential $\mathbf{A}$ and the scalar potential ϕ, through

$$
\nabla \cdot \mathbf{B} = 0 \;\;\Rightarrow\;\; \mathbf{B} = \mathbf{B}_{\text{self}} + B_a(t)\mathbf{e}_z = \nabla \times \mathbf{A} + \nabla \times \mathbf{A}_a,
\tag{2.7}
$$

$$
\nabla \times \mathbf{E} = -\dot{\mathbf{B}} \;\;\Rightarrow\;\; \mathbf{E} = -\frac{\partial \mathbf{A}}{\partial t} - \frac{\partial \mathbf{A}_a}{\partial t} - \nabla \phi,
\tag{2.8}
$$

where the magnetic flux density is split into two contributions: the uniform applied magnetic flux density, $B_a(t)\,\mathbf{e}_z$, which points along the z-axis, and the reaction magnetic flux density, $\mathbf{B}_{\text{self}}$, which is produced by the currents induced in the HTS sample. In cylindrical coordinates, the vector potential corresponding to the uniform applied magnetic flux density is given by $\mathbf{A}_a = -r/2\, B_a(t)\,\mathbf{e}_\theta$. Note that our method is not limited to the particular type of uniform exciting field pointing along the z-direction. For being used with other forms of applied fields, $\mathbf{B}_a(t)$ and $\mathbf{A}_a$ need to be modified accordingly. The choice of the gauge used for the definition of the vector potential is linked to the practical implementation of the FEM, and will be discussed in the Section 2.3.2.

Introducing the potentials $\mathbf{A}$ and ϕ allows one to reduce the magneto-quasistatic Maxwell equations to the only Ampere's law that reads

$$
\nabla \times \nabla \times \mathbf{A} - \mu_0 \sigma(\mathbf{A}, \phi)\left(-\dot{\mathbf{A}} - \dot{\mathbf{A}}_a - \nabla \phi\right) \;\; = \;\; 0,
\tag{2.9}
$$

where the electrical conductivity σ is calculated from the power law (1.25), as

$$
\sigma(\mathbf{E}) \;\; = \;\; \frac{J_c}{E_c^{1/n}}\left(|\mathbf{E}|\right)^{\frac{1-n}{n}}
\tag{2.10}
$$

$$
\Rightarrow \sigma(\mathbf{A}, \phi) \;\; = \;\; \frac{J_c}{E_c^{1/n}}\left(|-\dot{\mathbf{A}} - \dot{\mathbf{A}}_a - \nabla \phi|\right)^{\frac{1-n}{n}}.
\tag{2.11}
$$

In order to solve Eq. (2.9), together with the constitutive laws $\mathbf{B} = \mu_0 \mathbf{H}$ and $\mathbf{J} = \sigma(\mathbf{E})\mathbf{E}$, $\mathbf{A}$ and Φ must be defined on the contour Γ of the working domain Ω. Two types of boundary conditions are available:

1. *Dirichlet conditions*, or essential conditions, that specifies the values of the unknowns on Γ.

2. *Neumann conditions*, or natural conditions, that specifies the values of the normal derivative of the unknowns along Γ.

Moreover, the system also requires an initial condition on the unknowns. Note that there are no boundary conditions that are imposed on the hole surface since the equations are also solved inside the volume of the hole (or surface in a 2D model) that is assumed to have a negligible conductivity

σ with respect to that of the HTS. The continuity conditions at the superconductor/hole interface are guaranteed by choosing an appropriate basis of interpolating functions for the unknowns. This particular point is further detailed in Section 2.3.2.

Given appropriate boundary and gauge conditions, Eq. (2.9) is sufficient to describe the electromagnetic behaviour of HTS in the A-ϕ formulation [146, 158, 159]. Conversely to an analytical method in which the Ampere's law (2.9) is solved for every locations in the domain under consideration, the FEM is based on solving globally that equation in the domain, such that the obtained solution converges *on average* to the exact solution, but not locally. This weak solution is said to converge to the exact solution in terms of a minimization of the Galerkin residual of the equation. The residual of the Ampere's equation is defined as

$$\mathcal{R} \equiv \nabla \times \nabla \times \mathbf{A} + \mu_0 \sigma(\mathbf{A}, \phi) \left(\dot{\mathbf{A}} + \dot{\mathbf{A}}_a + \nabla \phi \right). \tag{2.12}$$

The Galerkin residual minimization method consists in approximating $\mathbf{A}$ and ϕ in terms of a linear combination of basis functions, $\mathbf{A}_i$ and ϕ_j, that are known *a priori*,

$$\mathbf{A} = \sum_{i=1}^{M} a_i \mathbf{A}_i \qquad \text{and} \qquad \phi = \sum_{j=1}^{N} b_j \phi_j, \tag{2.13}$$

where M and N are linked to the meshing elements and are detailed in Section 2.3.2. The basis functions have a compact support − they have a non-zero value only in small volume (or surface) surrounding a meshing element (hence the term *finite-element*) − and satisfy the Dirichlet boundary conditions on the external contour of the domain, Γ.

Then, for a given set of basis functions, the residual of Eq (2.9) is projected in the basis defined by $\mathbf{A}_i$ and $\nabla \phi_j$ and it is minimized in the sense of Galerkin theory when it is orthogonal to that basis, that is

$$\int_\Omega \left\{ \nabla \times \nabla \times \mathbf{A} - \mu_0 \sigma(\mathbf{A}, \phi) \left(-\dot{\mathbf{A}} - \dot{\mathbf{A}}_a - \nabla \phi \right) \right\} \cdot \mathbf{A}_i d^3 \mathbf{r} \quad = \quad 0 \quad \text{for all } \mathbf{A}_i \tag{2.14}$$

$$\int_\Omega \left\{ \nabla \times \nabla \times \mathbf{A} - \mu_0 \sigma(\mathbf{A}, \phi) \left(-\dot{\mathbf{A}} - \dot{\mathbf{A}}_a - \nabla \phi \right) \right\} \cdot \nabla \phi_j d^3 \mathbf{r} \quad = \quad 0 \quad \text{for all } \phi_j, \tag{2.15}$$

where $\mathbf{A}$ and ϕ are given by Eq. (2.13). These are the weak forms of the Ampere's equation (2.9). Note that there are $M + N$ independent equations for $M + N$ unknown coefficients. The system is thus well determined.

For the sake of convenience, let us introduce the following notations for the volume and surface integrals

$$(u, v) = \int_\Omega u(\mathbf{r}) v(\mathbf{r}) d^3 \mathbf{r} \qquad \text{and} \qquad < u, v > = \int_\Gamma u(\mathbf{r}) v(\mathbf{r}) d\mathcal{C}, \tag{2.16}$$

and let us consider the following Green identities [160] for reducing the order of Eqs. (2.14)-(2.15)

$$(\mathbf{u}, \nabla v) + (\nabla \cdot \mathbf{u}, v) \quad = \quad < v, \mathbf{n} \cdot \mathbf{u} > \tag{2.17}$$

$$(\mathbf{u}, \nabla \times \mathbf{v}) - (\nabla \times \mathbf{u}, \mathbf{v}) \quad = \quad < \mathbf{u} \times \mathbf{n}, \mathbf{v} >, \tag{2.18}$$

where $\mathbf{u}$ and v, as well as their first derivatives with respect to the three spatial coordinates x,y,z have an Euclidean norm whose square is integrable in the compact Ω delimited by the contour $\mathcal{C}$.

With the help of Eqs.(2.17)-(2.18), the second order derivative terms appearing in Eqs. (2.14)-(2.15) are integrated by parts,

$$(\nabla \times \mathbf{A}, \nabla \times \mathbf{A}_i) - <\mathbf{B}_{\text{self}} \times \mathbf{n}, \mathbf{A}_i > + \mu_0 \left(\sigma(\dot{\mathbf{A}} + \dot{\mathbf{A}}_a + \nabla \phi), \mathbf{A}_i \right) \;=\; 0, \qquad (2.19)$$

$$(\sigma \dot{\mathbf{A}}, \nabla \phi_j) + (\sigma \dot{\mathbf{A}}_a, \nabla \phi_j) + (\sigma \nabla \phi, \nabla \phi_j) + <\mathbf{n} \cdot \mathbf{J}, \phi_j > \;=\; 0, \qquad (2.20)$$

where $\sigma = \sigma(\mathbf{A}, \phi)$. Note that Eq. (2.20) corresponds to the weak form of $\nabla \cdot \mathbf{J} = 0$ [161]. The weak forms defined by Eqs. (2.19)-(2.20) only includes first order derivatives, such that piecewise linear functions may be used as basis functions for $\mathbf{A}$ and ϕ.

In order to deduce this weak formulation, no assumption on the dimension of the working domain Ω was made. It means that Eqs. (2.19)-(2.20) are valid in a 2D as well as in a 3D geometry. The differences between 2D and 3D models appear when implementing these equations in the numerical solver.

In the A-ϕ formulation, as described here above, only the Ampere's equation is solved weakly in the domain Ω (in the sense of minimizing the Galerkin residual). The Faraday's equation, $\nabla \times \mathbf{E} = -\dot{\mathbf{B}}$, and $\nabla \cdot \mathbf{B} = 0$ are verified everywhere in the domain Ω. Consequently, in an A-ϕ formulation, the magnetic flux density and the electric field are said to be strongly known, unlike the magnetic field and the current density that are weakly solved. That is the reason why we use the A-ϕ formulation in this thesis. It yields a divergence-free magnetic flux density, which is the quantity that is directly available in experiment.

Other FEM formulations of the Maxwell equations can be also used for modelling the properties of HTS. They differ in the electromagnetic quantities ($\mathbf{E}$, $\mathbf{B}$, $\mathbf{H}$ or $\mathbf{J}$) that are strongly solved. For instance, the T-Φ formulation is often used for calculating the current in HTS wires or tapes since it offers a strong knowledge of the current density and can be coupled easily with circuit equations [148, 149]. Similarly, H-field formulation also yields a strong knowledge of the current density [162]. A formulation with the diffusion equation for the electric field [163] is rather convenient for a strong knowledge of the magnetic field. Each of the available formulations has its pros and cons and the choice of a particular formulation mainly depends on the type of quantities intended to be strongly known from the simulations, and on the availability of these formulations in the solver adopted for implementing the FEM.

2.3.2 Implementation and computation of the finite element model

We describe in this section the practical implementation of the system of coupled equations defined by Eqs. (2.19)-(2.20). This implementation is performed using the *open source* environment of GetDP [152, 153, 154]. GetDP (General Environment for the Treatment of Discrete Problems) is a freeware realized by P.Dular and C.Geuzaine in the framework of an academic research in the Department of Electrical Engineering and Computer Sciences (Montefiore Institute) of the University of Liege.

Definition of the geometry and of the meshing

In order to describe the geometry of the working domain, one must distinguish between the two-dimensional and the three-dimensional models.

In the 2D model, a sample with an infinite height and an arbitrary cross section is considered. Equations (2.19)-(2.20) are not only solved in the superconducting material, but also in the surrounding environment which is assumed to behave almost as vacuum, with $\mathbf{B} = \mu_0\mathbf{H}$ and $\sigma_0 = 10^{-10}$ S/m. The non-zero value of the conductivity is required for numerical convergence in the case of domains with multiple connexity [161]. Note that it is possible to check *a posteriori* that the conductivity of the surrounding environment is indeed negligible with respect to that of the superconducting material when penetrated by a magnetic field, $\sigma_0 \ll \sigma(\mathbf{A}, \phi)$. The surrounding environment extends up to infinity where the boundary conditions are imposed. The implementation of infinite boundary conditions can be done in one of two ways. A first possibility is to draw a circle with a radius that is much larger than the characteristic size of the sample cross section and whose perimeter is used for imposing the boundary conditions. This procedure drastically increases the amount of meshing elements and thus the size of the matrices to be treated. In order to deal with a finite number of meshing elements while extending the meshing to infinity, a Jacobian transformation can be used to send the outer contour of a circular shell to infinity [164]. The shell has an inner radius that is slightly larger than the characteristic size of the sample (typically twice). The boundary conditions defined on the external contour mathematically correspond to those imposed at infinity.

In the 3D model, samples of arbitrary shapes can be treated[2]. These are also surrounding by an almost vacuum environment, with a magnetic permeability μ_0 and a conductivity σ_0. Similarly to the 2D model, a spherical shell is constructed around the sample, with a radius which is almost twice as large as the characteristic size of the sample, and its outer surface is sent to infinity by a Jacobian transformation [164]. Moreover when the sample exhibits a symmetry on both sides of its median plane – as it is the case for all the samples that are simulated in the manuscript –, only half of the geometry is represented in order to reduce the size of the meshing. In this case, the median plane serves as an external surface where appropriate boundary conditions (such as the perpendicularity of $\mathbf{B}$) are imposed in order to account for the symmetry of the sample.

The geometry of the problem is defined using a dedicated software Gmsh [165, 166], which is a 3D meshing generator. The structure is constructed using basic geometric elements (lines or circle arcs); the surfaces and the volumes are defined on that basis. The definition of the geometry includes the superconducting structure and the surrounding air environment. The meshing is built automatically from the geometry definition. We use triangle (2D) or tetrahedric (3D) meshing elements. The characteristic size of the meshing elements is defined on each basic geometrical elements.

Examples of working domains for the 2D FEM (a) and the 3D FEM (b) models are represented in Figure 2.4. A superconducting hollow cylinder, or a tube, with an infinite height, together with the

---

[2]While it can be used with arbitrary geometries, one has to be aware that the 3D model does not take into account the effects associated with components of the current that are parallel to the applied magnetic field. When the symmetry of the geometry does not ensure a perpendicularity between the current and the magnetic field, results must be discussed with great care.
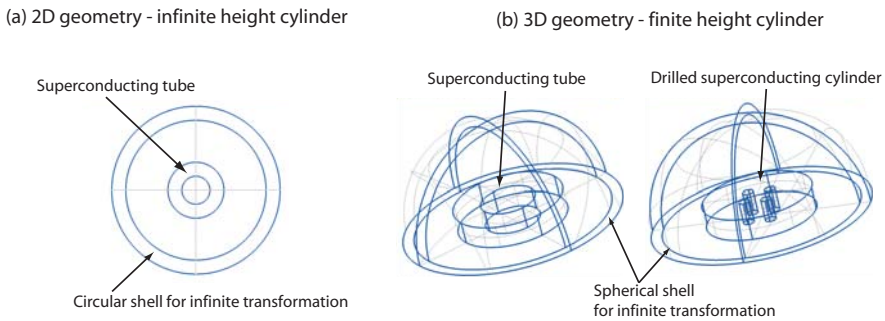
(a) 2D geometry - infinite height cylinder   (b) 3D geometry - finite height cylinder

Figure 2.4: *(a)- Definition of the 2D geometry for the simulation of a superconducting tube with an infinite height. The circular shell used for the infinite transformation is also indicated. The boundary conditions are imposed on the external circumference. (b)- Definition of the 3D geometry for the simulation of a superconducting tube (left) and a superconducting drilled cylinder (right) with a finite height. The spherical shell for imposing the boundary conditions at infinity is also indicated. For symmetry reasons, only half of the cylinder is represented.*

surrounding environment and the circular shell for the boundary conditions are shown for the 2D model. The examples of 3D geometries consist of a superconducting tube and of a drilled superconducting cylinder. The spherical shell and the median plane are also represented.

The size of the meshing is a key parameter for the calculation time. It is moreover limited by the amount of RAM memory available on a single processor. The numerical algorithms that are used for solving the equations with GetDP are still not available in parallel environment. The calculations have to be performed on a single processor, with its own physical memory. On a personal computer with 2Gb of memory, the maximum number of meshing nodes that can be treated is approximatively 200 000 for the problem defined by Eqs. (2.19)-(2.20). By using the computer cluster NIC3 of the *Service Général d'Informatique* (SEGI) from the University of Liege, the maximum size of RAM can reach up to 32 Gb on a single processor, which allows one for treating much more nodes but also increases drastically the calculation time. The switch toward a parallel environment for solving the problem with GetDP will probably reduce the calculation time and allow for dealing with larger meshings.

Basis function

Within the framework of FEM, the solutions $\mathbf{A}$ and ϕ of Eqs. (2.19)-(2.20) are approximated in terms of a linear combination of basis functions $\mathbf{A}_i$ and ϕ_j. The basis functions $\mathbf{A}_i$ are vectorial fields, and the functions ϕ_j are scalar fields.

The electric potential is represented by a sum of first-order nodal functions. The functions are defined piecewise. They are equal to 1 on a single node of the meshing, linearly decreases to 0 in the elements adjacent to the node and is set to 0 in the other meshing elements. The coefficient b_j associated with the node function in (2.13) corresponds to the value of the unknown electric potential on a meshing node. Such a choice of basis functions ensures the continuity of ϕ from elements to elements. A typical node function is represented in Figure 2.5-(a).
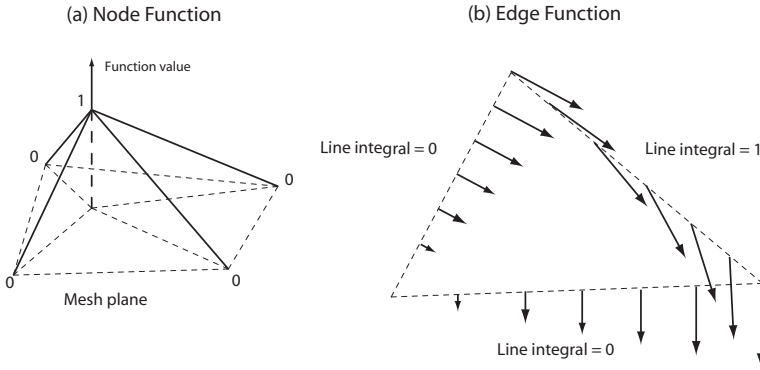
Figure 2.5: *(a)- Node function corresponding to the central node of the meshing partition. (b)- Vectorial edge function corresponding to one of the edge of the meshing element. For clarity, the function is only represented on the edges of the meshing element.*

The functional space for the vector potential is composed of vectorial edge functions of the first order. These functions are defined on a triangle element of the meshing grid such that the line integral of their tangential component is equal to 1 along a given edge $\mathcal{C}_i$ and 0 along the other edges $\mathcal{C}_j$ and $\mathcal{C}_k$. A schematic representation of an edge function is shown in Figure 2.5-(b). The vector field is orthogonal to two edges and varies linearly inside the element (not shown for clarity). There exists three edge functions per triangle elements.

The coefficient a_i corresponding to the edge function appearing in Eq. (2.13) thus corresponds to the value of the line integral of the unknown vector potential along $\mathcal{C}_i$, that is

$$ a_i \;=\; \int_{\mathcal{C}_i} \mathbf{A} \cdot \mathbf{d}\ell \; . \tag{2.21}$$

The line integral of the vector potential around a meshing element $\partial\mathcal{C}$ defined by the edges $\mathcal{C}_i$, $\mathcal{C}_j$ and $\mathcal{C}_k$ is thus given by

$$ \oint_{\partial\mathcal{C}} \mathbf{A} \cdot \mathbf{d}\ell \;=\; \int_{\mathcal{C}_i} \mathbf{A} \cdot \mathbf{d}\ell + \int_{\mathcal{C}_j} \mathbf{A} \cdot \mathbf{d}\ell + \int_{\mathcal{C}_k} \mathbf{A} \cdot \mathbf{d}\ell \; . \tag{2.22}$$

Using Eq. (2.21), one obtains

$$ \oint_{\partial\mathcal{C}} \mathbf{A} \cdot \mathbf{d}\ell \;=\; a_i + a_j + a_k \, . \tag{2.23}$$

The edge functions ensure the continuity of the line integral of $\mathbf{A}$ along an edge between elements sharing that same edge. As a result, the continuity of the normal component of the magnetic flux density $\mathbf{B}$ through the surface of adjacent elements is ensured.

Gauge conditions

In order to be univocally defined, the vector potential $\mathbf{A}$ needs to be restricted to a given gauge. To this aim, we use a spanning tree technique [167, 168]. It consists in making the vector potential
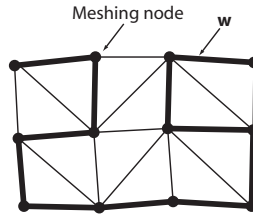
Figure 2.6: *Example of a tree used in the spanning tree technique and constructed on an arbitrary meshing.*

orthogonal to a set of vector **w** whose field lines are not closed. In order to define **w**, a tree is built on the edges of the meshing. The tree is a set $\widehat{A}$ of edges which connects all the nodes of the meshing without forming closed contours. In a meshing with N points, there are $N-1$ edges in the tree. A pair of nodes can only be connected by a single way on the tree. The vector set based on the edges of the tree $\widehat{A}$ has no closed field lines and is referred to as **w**. Hence, the gauge condition reads

$$\mathbf{A} \cdot \mathbf{w}_i \quad = \quad 0 \quad i = 1, \ldots, N-1 \tag{2.24}$$

where $\mathbf{w}_i$ is a unit vector parallel to a mesh of the tree (see Figure 2.6). Associated to the edge functions that are already perpendicular to some edges, as defined in the above paragraph, the spanning tree technique simply consists in forcing some coefficients a_i to vanish when their related edge functions $\mathbf{A}_i$ is not already perpendicular to the edge of the tree, so as to decrease the total number of unknown coefficients.

Operation

The weak formulations of the differential equation governing the magnetic field penetration in the cylinder are solved weakly by minimizing the residual obtained with a series of chosen basis functions. For each projection on the basis functions, the weak equation (2.12) is reduced to a non-linear scalar equation for the unknown coefficients a_i and b_j.

Since the applied magnetic field varies with time, we use a step-by-step temporal resolution with a backward Euler scheme, which has a good stability and a high convergence rate even with very large time steps [169]. The convergence and the stability of this method have already been demonstrated in the context of HTS in the case of a E-formulation [163]. In our formulation, the implicit resolution required at each step generates a system of equations which are non-linear, because of the conductivity law of Eq. (1.25). This non-linearity is treated with a fixed point iteration technique [170], which consists in updating at each iteration step the value of the unknowns appearing in the non-linear terms of Eqs. (2.19)-(2.20) with the solution found at the previous iteration. The as-obtained linear system of equations yields a matrix that has to be inverted. The matrix is composed of a very large number of elements among which only a few have a non zero value (sparse matrix). Therefore we use in GetDP the GMRES iterative solver that is very efficient for inverting such matrices [171]. The non-linear loop is run until the relative difference between two consecutive solutions, e_n, is smaller than a predefined criterion, whose value is discussed in Section 2.4.

Contrary to a Newton-Raphson scheme, the fixed point iteration does not require the calculation of
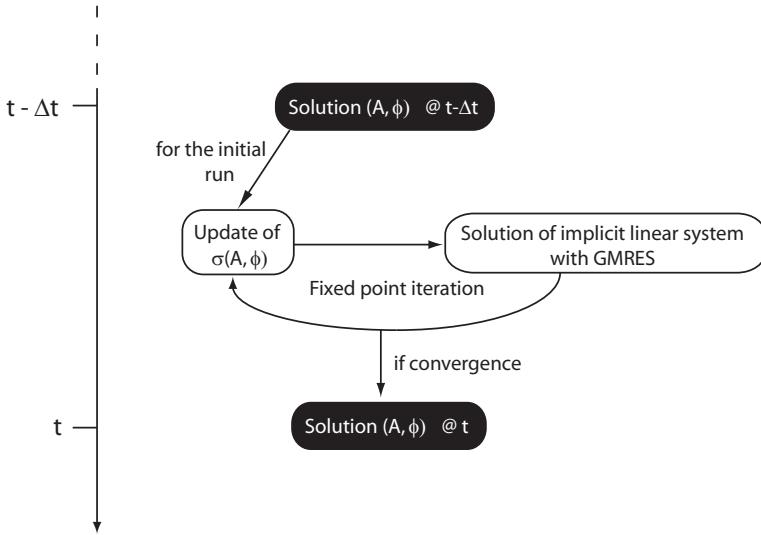
Figure 2.7: *Fixed point iteration loop used for the time resolution of the FEM formulation.*

the Jacobian of the functions (2.19)-(2.20), which may lead to modify the power law conductivity $\sigma(E)$ because of infinite derivatives when $E = 0$ [172]. While the Newton-Raphson scheme might lead to a faster convergence, the implementation of the fixed point method is much easier and does not require an excessive number of iterations (on average, there are approximately 10 non-linear iterations per time step).

Figure 2.7 represents the sequence of operations to be executed during a given time step. Let us assume that the solution $(\mathbf{A}, \phi)$ is known at time $t - \Delta t$. At the beginning of the time step t, this solution is used for updating $\sigma(\mathbf{A}, \phi)$ and the resulting linear system is then solved with the GMRES iterative solver. The solution of this linear system is then used for updating $\sigma(\mathbf{A}, \phi)$. The new linear system is solved again, until the convergence criteria of the fixed-point iteration loop is fulfilled. The solution $(\mathbf{A}, \phi)$ is then used for the next time-step.

2.3.3   FEM with a single time-step iteration for applied fields varying with a constant sweep rate

To our knowledge, in the FEM for the modelling of HTS properties that have been suggested so far [146, 147, 148, 149, 150, 151], the computation time-step Δt was chosen much smaller than the timescale characterizing the simulated external excitation. Such a choice can however be largely improved in the case of an excitation varying linearly with time by using a *single* time-step. Our argumentation is two-fold. First, from the point of view of the physics involved, one knows that the diffusion of vortices is strongly reduced as the pinning becomes stronger or the temperature fluctuations become weaker. Thus, for large critical exponents *n*, the motion of vortices can only be induced by applying an external flux variation, so that the time behaviour of the magnetic response is expected to be mainly dictated by the excitation sweep rate, not by creep effects. The second part

of our argumentation stems from the numerics involved. The time-differential equation (2.19) that is solved with the backward Euler scheme [169] has a generic form that reads $\partial u / \partial t = g(u)$ where u is a function of A. With this method, the temporal derivative at time t is approximated at first-order, yielding the implicit equation

$$\frac{u_t - u_{t-\Delta t}}{\Delta t} = g(u_t).$$

(2.25)

Such a scheme has been shown to yield a truncature error proportional to the second time derivative, $e_t \approx \partial^2 u / \partial t^2 \, \Delta t + O(\Delta t^2)$ [169]. Again, in the limit of large n and with an external field applied as a ramp, we expect the second time derivative of the magnetic response to be small, as the timescale of that response is dictated by that of the excitation, which varies here linearly with time. These arguments suggest that larger Δt can be used, and in the extreme case, a single time-step might be used.

In the following of this chapter, we will only concentrate on linearly varying excitation and we will compare two different choices for the time integration of the field from instant *zero* to a predetermined instant, t_1: in the first choice, the integration is carried out in a succession of small time steps of duration $\Delta t \ll t_1$; in the second choice, the equations are iterated in a single time-step, with $\Delta t = t_1$. These two choices will be compared in a number of situations in order to validate the single time-step approach.

2.4   Validation of the 2D FEM model using a single time-step iteration

We first apply the 2D FEM for calculating the Bean critical state in a HTS tube (inner radius b and outer radius a) subjected to an axial field varying linearly with time, in the limit of infinite height. This is a geometry for which the current density flows in the cross section plane and is everywhere perpendicular to the local magnetic field. Analytical solutions are known in such a geometry, from the Bean model (2.1). The goal of this section is to compare the results obtained with the two-dimensional FEM to an analytical solution in order to validate our approach and to asses the interest of the single time-step iteration.

According to Eq. (2.1), the magnetic flux density in a tube of infinite height subjected to a uniform applied field is linearly decaying along the tube radius in the superconducting wall of thickness $w = a - b$, and remains uniform in the non-superconducting regions. In particular, the magnetic flux density in the tube is given by

$$B_{\text{Bean}}(r) \;\; = \;\; \begin{cases} B_a - \mu_0 J_c (a - r) & b \leq r \leq a, \\ B_a - \mu_0 J_c (a - b) & 0 < r < b. \end{cases}$$

(2.26)

In practice, in order to compare the magnetic flux profile obtained with the Bean critical state model to that obtained with the $E(J)$ power law, we assume a large value of n, $n = 100$, and a linearly varying applied flux density, with a sweep rate equal to $\dot{B}_a \in [1 \text{ mT/s}, 100 \text{ mT/s}]$, as already discussed in Ref. [173].

We now consider the critical state of a superconducting tube of infinite height. The tube has an external radius $a = 10$ mm and an internal radius $b = 5$ mm. The critical current density is assumed

to be independent of the magnetic field, and is equal to $J_c = 2 \ 10^7$ A/m^2. The critical state is simulated with the 2D FEM model and compared to the analytical solutions of the Bean model. The $E(J)$ power law is considered with $n = 100$ and $E_c = 10^{-4}$ V/m. The external field is applied with a constant sweep rate, $\dot{B}_a = 10$ mT/s. The penetration field of the tube H_p, is given by $H_p = J_c(b-a) = 10^5$ A/m, which corresponds to a flux density, $\mu_0 H_p = 125.6$ mT.

In Figure 2.8-(a), the magnetic field profile is plotted along the diameter of the tube for an external induction $B_a = 10$, 50, 100, 150, and 200 mT. FEM simulations are run with different choices of time-steps: dashed lines show the results of simulations with multiple small time-steps $\Delta t = 1$ s, stopping at either $t_1 = 1$, 5, 10, 15 and 20 s; solid lines show results from single time-step simulations, where $\Delta t = t_1$ is fixed to either 1, 5, 10, 15, or 20 s. The choice of the the end criterion for the fixed point iterative loop is empirically fixed at $e_r = 5.10^{-2}$ for the multiple time-steps simulation and $e_r = 2.10^{-3}$ for the single time-step method, so as to obtain a solution that has reached its asymptotic value at the end of the loop.

It can be observed that in each case the profile of the magnetic field in the superconductor is linear. It closely follows the result of the Bean model. To further quantify the results, we define the average deviation from the Bean model as

$$\widetilde{\Delta B} = \frac{1}{2a} \int_{-a}^{a} |B_{\text{FEM}} - B_{\text{Bean}}| dr, \tag{2.27}$$

where B_{FEM} stands for the FEM results. Figure 2.8-(b) shows the average deviation in the FEM method using a single time-step (filled circles) and in that using multiple time-steps (open squares). Both methods produce almost the same deviation as long as the magnetic field has not fully penetrated the wall of the tube, or for $B_a < B_p = 125.6$ mT. For $B_a > B_p$, the deviation obtained with the multiple time-step approach first increases abruptly and then has a value around 3 mT. The single time-step method, on the other hand, leads to a deviation which peaks at about 2.5 mT at $B_a = 130$ mT and then decreases at larger fields to be less than 2 mT at $B_a = 200$ mT.
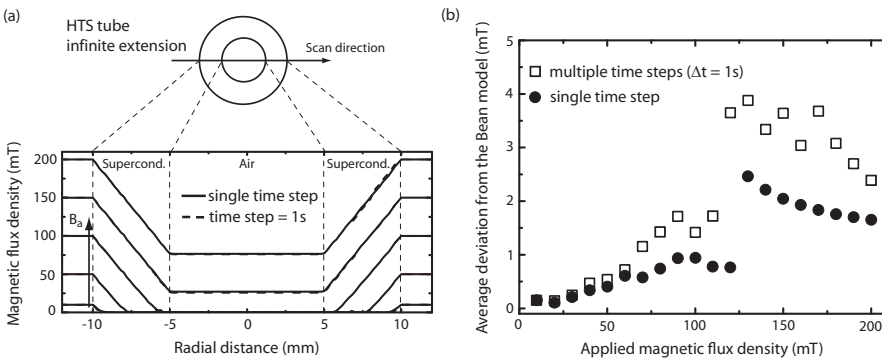
Figure 2.8: (a) Profile of the magnetic flux density along the tube diameter, as calculated with the FEM with a single time-step (solid lines) and with multiple time-steps, $\Delta t = 1$ s, (dashed lines). The exponent n is equal to 100 so as to approach the critical state. The magnetic flux density is applied with a constant sweep rate of 10 mT/s. The profiles are shown for $B_a = 10$, 50, 100, 150, and 200 mT. (b) Average deviation $\widetilde{\Delta B}$ from the Bean model, as a function of B_a, for the single time-step method (filled circles) and for the multiple time-step method (open squares).

Overall, the single time-step method, as well as the multiple time-step one, give a solution which is close to the Bean prediction, with a relative difference that stays below 5%. However, the single time-step result is computed in a relatively short calculation time with respect to a multiple time-step method. For example, the 20 single time-step simulations of Figure 2.8-(b) take less than half a day on a dual-core 2.8 GHz processor with 2 Gb of memory, whereas the multiple time-step approach with $\Delta t = 1$ s and $t_1 = 20$ s takes almost 3 days on the same computer.

2.5 Validation of the 3D FEM model using a single time-step iteration

2.5.1 Magnetic flux profile in a HTS tube with a large critical exponent

We now turn to the case of a superconducting tube of finite height subjected to a uniform axial field. The tube has an external radius of 10 mm, an internal radius of 5 mm, and a height of 8 mm (see Figure 2.9). The external field is applied with a constant rate $\dot{B}_a = 10$ mT/s and raises up to $B_a = 200$ mT. Here again, we assume $n = 100$. The critical current density, J_c and the critical electric field, E_c, have the same values as for the tube with an infinite height.

Even if the tube geometry may be solved with a 2D axisymmetric model, the FEM approach is carried
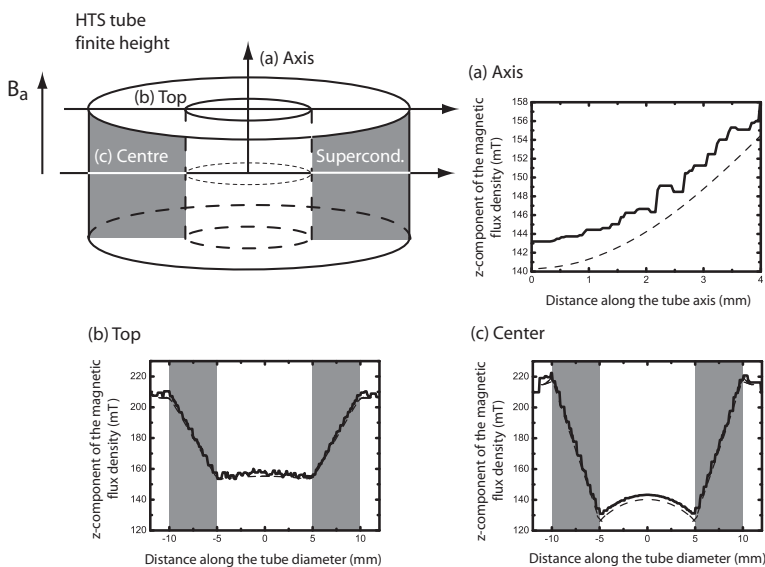
Figure 2.9: *Sketch of the HTS tube (outer radius 10 mm, inner radius 5 mm, and height 8 mm) and magnetic flux profiles along the axis (a), a diameter in the top surface (b) and in the median plane (c), as represented by the arrows. The arrows indicate different scan directions for plotting the magnetic flux profile. The external field is applied with a constant sweep rate of $\dot{B}_a =10$ mT/s, and raises up to $B_a =200$ mT. The flux penetration problem is either solved with the FEM single time-step method (grey solid lines and $\Delta t = 20$ s), or with Brandt's method with multiple time-steps (black dashed lines and $\Delta t = 5\ 10^{-4}$ s), both assuming $n =100$.*
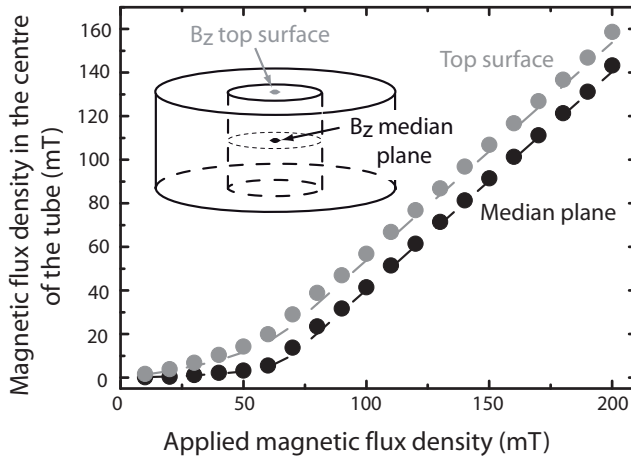
Figure 2.10: *Magnetic flux density calculated at the centre (median plane - black - or top surface - grey -) of a HTS tube with the FEM single time-step method (circles) and with the Green's function method (dashed lines and $\Delta t = 5\ 10^{-4}$ s). The external field is applied with a ramp of constant rate $\dot{B}_a = 10$ mT/s and increases up to 200 mT. FEM single time-step method are shown for different choices of the time-step: $\Delta t = 1,\ldots,20$ s. The inset shows the location where the magnetic flux density is calculated.*

on a 3D mesh with a single time-step method ($\Delta t = 20$ s), so as to validate the method. Only half of the tube is meshed, and vanishing conditions on the tangential component of B are imposed in the median plane. The FEM results are compared with those of the Green's function method of Brandt [126, 174] (see Appendix A for details). The time-step used for the Brandt's algorithm is fixed at 5×10^{-4} s to ensure convergence.

The z-component of the magnetic flux density is probed along three different directions [see Figure 2.9: (a), the tube axis, (b), a diameter at the top surface, and (c), a diameter on the median plane]. Solid lines show the FEM results and dashed lines show those obtained with Brandt's method. It can be observed that solid lines exhibit step-like features, whereas dashed lines are smoother. This difference can be traced back to the low meshing density adopted in the FEM method. Even though only half of the tube is meshed in 3D, the maximum number of available nodes with 6 Gb RAM (200 000) is still too small[3] to obtain a smooth curve after linear interpolation, unlike in Brandt's method.

Despite this observed difference, one can see that the results of both methods are in good agreement. In particular, on the linescan along direction (c) (Figure 2.9-(c)), we observe a magnetic flux density on the outer wall of the tube that is slightly larger than $B_a = 200$ mT. This is caused by the demagnetizing field, which was absent in the results obtained with samples of infinite height. Inside the superconducting wall, the magnetic flux density decreases linearly; in the central part of the tube, it remains at a low level, but exhibits variations due again to the demagnetizing field.

Figure 2.10 shows the z-component of the magnetic flux density calculated at the centre of the cylinder, B_{centre}, in the median plane (black) and on the top surface (grey), as a function of the

---

[3]In a parallel computing environment, the 3D meshing could be more refined.

external field B_a. The dashed lines show the results of the Green's function approach. Circles show the FEM results in a single time-step approach, with different choices of the time-step ranging between $\Delta t = 1$ s and 20 s. Here again, the agreement between both methods is excellent, demonstrating the relevance of a single time-step iteration in a FEM approach.

The total calculation time for obtaining the results of Figure 2.10 is larger for the 3D FEM method than for Brandt's method, because a 3D meshing is used for the FEM and a 2D axisymmetric meshing is used for Brandt's method. However, we remind the reader that the purpose of this section was to evaluate the accuracy of the 3D FEM in a case where comparisons could be made with existing methods, while keeping the method explicitly in a 3D geometry. We could of course optimize the FEM code for this particular case by considering an axisymmetric 2D meshing.

2.5.2 Domain of validity of the single time-step method

We have seen in Sections 2.4–2.5 that the FEM method with a single time-step produces accurate results in the large n limit ($n = 100$). The purpose of this subsection is to analyze the accuracy of the method at lower n-values and establish its sensitivity to the sweep rate of the external field. Mastering these two factors is essential to make comparisons with experiments.

We estimate the error of the FEM single time-step method on the basis of the magnetic field produced at the centre of the tube with a finite height (the tube considered in the previous subsection), either in its median plane or on its top surface. The external field is ramped with a fixed rate $\dot{B}_a$ up to
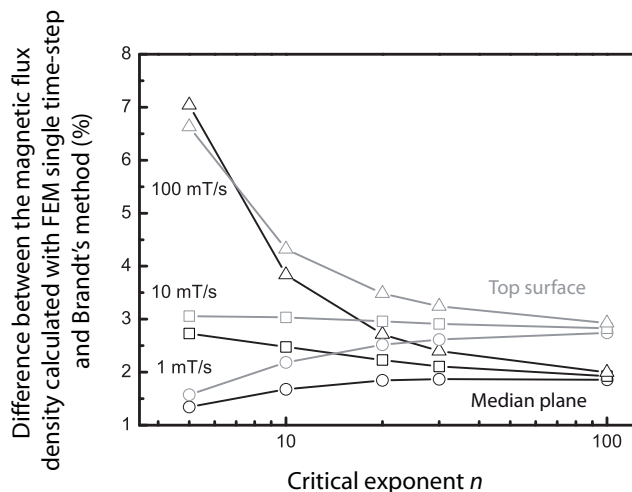
Figure 2.11: *Difference between the magnetic flux density at the centre of the HTS tube, as calculated by the FEM single time-step method and the Green's function method (with multiple time steps $\Delta t = 5 \; 10^{-4}$ s) either in the median plane (black lines) or on the top surface (grey lines). The magnetic field is applied as a ramp with a sweep rate of 1 mT/s (circles), 10 mT/s (squares), and 100 mT/s (triangles). The applied magnetic flux density is ramped up to B_a =200 mT. The exponent n varies from 5 to 100.*

$B_a = 200$ mT. The error is then evaluated as the absolute difference between the results of the single time-step FEM and the Brandt's method. Figure 2.11 shows the error (in %) as a function of the exponent n, varying from 5 to 100, and the sweep rate $\dot{B}_a$, taken as 1 mT/s (circles), 10 mT/s (squares), or 100 mT/s (triangles).

In the large n limit ($n = 100$), the error remains small — below 2 % (resp. 3 %) in the median plane (resp. on the surfcae) — and is fairly independent of the sweep rate. This limit practically corresponds to the critical state, which is uniquely determined by the external conditions and is independent of the magnetic history of the sample, i.e. the sweep rate of the external field in this case. Provided convergence is guaranteed, the FEM approach should thus produce the critical state solution. The discrepancy between the situations in the median plane and on the surface is attributed to the non-uniform meshing used in the FEM simulations which has a smaller characteristic length close to the median plane than on the top surface. The opposite limit of low n-values shows a much larger sensitivity to the sweep rate and a larger spread in the error. Here, these results should be considered as qualitative only, as the Green's function method itself has an error that grows in this limit, so that our estimate of the FEM error becomes questionable in this regime. For intermediate values of n, the error remains low and weakly sensitive to the sweep rate: e.g., for the experimentally relevant value for melt-textured YBCO at 77 K, $n = 20$ [50], the error is below 4 %. This demonstrates that the single time-step method is useful for simulating the magnetization of HTS with finite n-values.

2.6   Summary of Chapter 2

This chapter introduces three different numerical models that are used in this thesis for calculating the magnetic field penetration in drilled samples. These models are of increasing complexity. The simplest one, based on the Bean model, neglects the flux creep and the effects associated with the finite height of the samples. Both finite-element models (two-dimensional and three-dimensional) incorporate flux creep in the form of an $E - J$ power law; the 2D model neglects the finite height effects, while the 3D model takes them into account. The calculation load required by each model is obviously proportional to its complexity. The Bean model is solved in few minutes in MatLab and the FEM models in few hours within the GetDP environment. However, when considering the finite-element method, we propose for large values of n ($n > 20$) and for linearly varying applied fields to use the properties of a slow magnetic diffusion inside the HTS to reduce the number of time steps. In particular, the penetration of a linearly increasing applied field can be calculated with only a single time-step. Such a technique may also be applied for calculating the trapped flux: during the first step, the applied magnetic flux density is increased with a constant sweep rate to a maximum value, it then decreases to zero with the same sweep rate during the second step.

3

Influence of the holes and of their arrangement on the magnetic properties of bulk HTS

Since it removes superconducting materials, drilling holes in bulk HTS samples may alters their magnetic properties. In this chapter, we study how and by how much the magnetic properties are affected by the presence of the holes, with the help of both numerical modelling and experiments[1].

The modification of the magnetic properties incurred in drilled samples have already been considered in the framework of other studies. These ones have reported that drilling holes in a bulk cylinder reduces its bulk magnetization, provided its critical current density remains unchanged [89, 90]. The drilled cylinder exhibits a lower magnetization than that of the plain cylinder. Although the main consequences of drilling holes on the magnetic properties have been described in these papers, they do not thoroughly reviewed, to our knowledge, the mechanisms that are responsible for the observed magnetization drops. Understanding, for instance, the influence of the relative position of the holes in a two-hole sample would bring essential informations regarding the optimal arrangement when several holes are arranged on a given lattice in the sample.

The aim of this chapter is to provide an exhaustive study of the magnetic properties of drilled samples, with modelling and experimental results. We first consider samples consisting of a semi-infinite plane having a single boundary and an infinite height. Such a geometry allows one to understand the effects of the holes on the current stream lines, without dealing with the more delicate effects associated with the edges of the cross section and with the finite height. Then, we review the magnetic properties of semi-infinite samples containing several holes and discuss the possibility of maximizing the trapped

---

magnetic flux in samples where several holes arranged on a optimal lattice. Various regular hole patterns are detailed in samples with an infinite height and a semi-infinite or a circular cross section. Then, samples with a finite height are considered. The influence of the demagnetizing effects is discussed in cylindrical samples.

In samples with an infinite height, the magnetic field distribution is calculated with both the numerical Bean model described in Section 2.2 and the FEM described in Section 2.3. FEM simulations with a critical exponent of, (i), $n = 100$ (strong pinning) and, (ii), $n = 25$ (typical value for YBCO) are compared to the numerical Bean model in order to, (i), validate the FEM simulations in the limit of strong pinning $n = 100$, and, (ii), study whether the value of the critical exponent modifies the predictions obtained in the limit of a very strong pinning. Conversely, the samples with a finite height can only be treated with FEM simulations. The results obtained with FEM in samples with an infinite height are therefore used as a reference so as to assess the effects associated with the finite height of the sample.

In the last part of this chapter, we demonstrate with an experiment carried on parallelepipedic drilled samples that the trapped magnetic flux depends on the hole lattice and that it is possible to maximize it with a proper arrangement of holes. These conclusions are supported by results from the numerical models.

Three particular magnetic quantities are considered in this chapter for evaluating the magnetic properties of the samples: (i) the magnetization of a given sample that is subjected in the zero field cooled state to an applied field, H_a, (ii), the remnant magnetization that is obtained when the same sample is initially magnetized above twice its penetration field before the applied field returns to zero, and (iii), the maximum trapped flux density in a given cross section. For samples with a finite-size cross section, both magnetizations (i) and (ii) actually have the same magnitude (they have opposite signs, however), provided that the critical current density is assumed to be field-independent and that the applied field in situation (i) is larger than twice the penetration field. Such equivalence cannot be found for samples with a semi-infinite cross section, as they are never fully penetrated.

3.1   Samples of infinite height with a single hole

3.1.1   Preliminary case : a sample with a slab hole

To get a first grasp of typical magnetic flux profiles in drilled samples, we first consider a semi-infinite plane of infinite height drilled by a slab hole. This particular geometry is represented in Figure 3.1-(a). The cross section lies in the $x - y$ plane and the sample is infinitely extended along the z-direction. The slab hole has a width $2R$ in the x-direction and is infinitely extended along the y and z directions. The sample is subjected to a uniform applied field parallel to the z-axis. The dashed line at the distance a from the external border indicates the spatial domain in which the magnetization is calculated.

Applying the Bean model to that sample with a constant critical current density J_c and subjected to a uniform applied field is straightforward. The magnetic field decays linearly from the external border
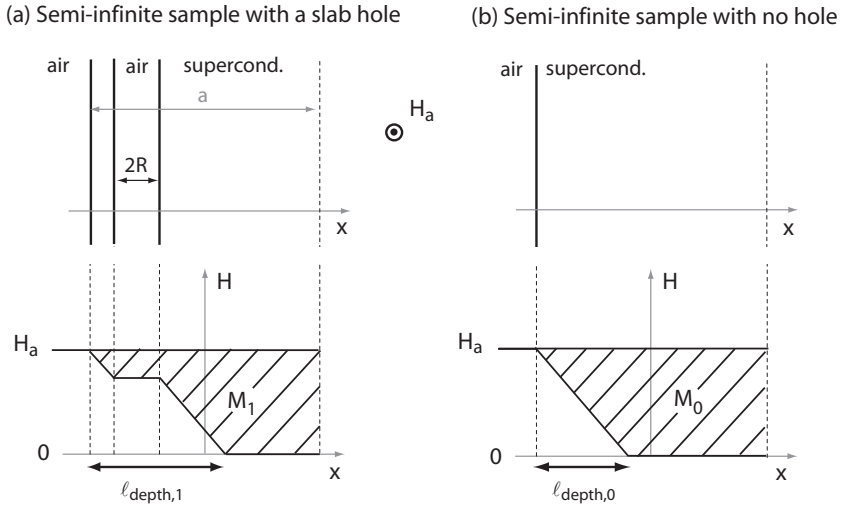
Figure 3.1: *Magnetic field distribution in a semi-infinite superconducting plane, with (a) and without (b) a slab hole. The distribution is calculated with the Bean model. The hatched surface area represents the magnetization for the region extending from the border to the dashed line located at a distance a from the border.*

with a slope J_c, penetrates the hole, where it remains constant along the thickness $2R$, and finally decreases linearly with the coordinate x. For comparison, the situation in a sample with no slab hole is depicted in Figure 3.1-(b). One directly observes that the effect of the slab hole is to increase the penetration length ℓ_{depth}, as $\ell_{\text{depth},1} > \ell_{\text{depth},0}$. As a result, the magnetization of the drilled sample, M_1, defined here as $M_1 = 1/a \int_0^a H dx - H_a$, is smaller than that of the plain sample, M_0. The presence of the slab hole thus induces a magnetization drop.

This simplified model shows that the flux front tends to penetrate further the sample with a hole, since the magnetic field does not decay inside the hole. The magnetization of the drilled sample is consequently reduced (in absolute value).

Note that this particular hole geometry is highly idealized and is discussed here for didactical purposes. It is discussed in this paragraph for teaching purposes. Apart from this exception, this thesis only focuses on circular holes. The circular hole geometry is the most feasible in terms of machining and reproducibility. Other hole geometries could also be considered, but their practical realization would be very difficult or even impossible.

3.1.2   Sample with a circular hole

We now turn to the situation of a sample with a semi-infinite cross section drilled by a single circular hole of radius R centered at a distance D from the border. The sample is moreover assumed to have a uniform and field-independent critical current density J_c. Again, the sample, initially in the ZFC condition, is subjected to a magnetic field H_a oriented perpendicular to the cross section. In this

geometry, the field distribution is two-dimensional, i.e. it varies inside the cross section, but remains constant along the vertical coordinate z.

Current lines

The critical state in the one-hole sample is first calculated with the help of the numerical Bean model. Following the main principles of that algorithm described in Section 2.2, the magnetic field can reach a given point by two distinct penetration routes, (i) either directly from the external border, or (ii) via the hole that acts as a radial source of magnetic field. Two regions may be identified: one for which the direct penetration from the border has the shortest path, and one for which the radial penetration via the hole has the shortest path. Hence, the boundary between these regions is characterized by the equality of path lengths,

$$ x \;\; = \;\; D + r - 2R, \tag{3.1} $$

where x is a cartesian coordinate along an axis that is perpendicular to the external boundary and r is the distance from the hole centre to the point where we determine the path lengths (see Figure 3.2). We thus find that the boundary defined in Eq. (3.1) is the locus of points for which the difference between the distance to the external boundary and that to the hole centre is equal to a constant, $D - 2R$. This locus is a parabola whose vertex is located at $(x, y) = (D - R, 0)$, whose directrix runs along $x = D - 2R$, and whose focus lies at $(0, D)$. In cartesian cooordinates, the parabola equation
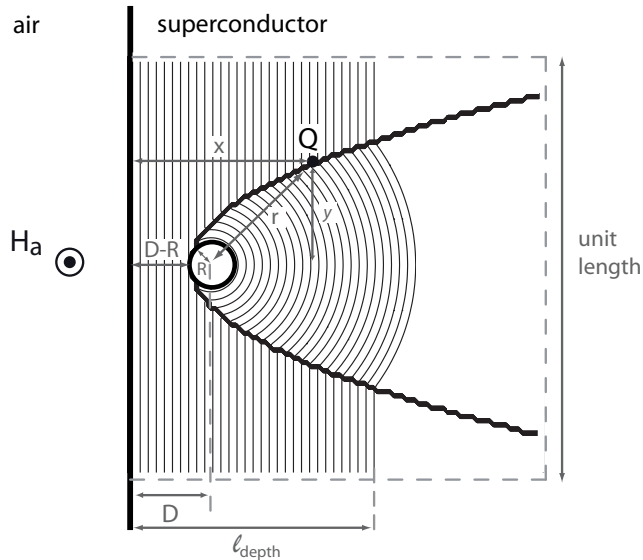
Figure 3.2: *Simulated current lines (or constant magnetic field lines) in a sample with a semi-infinite cross section and a single hole. The calculation is based on the numerical Bean model. The hole has a radius R =0.05 and is located at a distance D =0.2 from the border. Here, the unit length corresponds to the length of one of the segments of the dashed contour. The applied magnetic field is such that the penetration depth is given as ℓ_{depth} =0.6.*

reads

$$x = \frac{y^2}{4R} + D - R. \tag{3.2}$$

It is plotted as a thick line in Figure 3.2 for the case of a hole of radius $R = 0.05$ located at a distance $D = 0.2$ from the border. Note that the unit length corresponds to the length of one of the sides of the square delimited by the dashed grey lines; all the distances are normalized to this length.

Equation (3.2) also characterizes the current discontinuity line. As explained in Chapter 2, the current stream lines can be constructed from the contour lines of constant magnetic field, i.e. lines for which the shortest penetration length from the border is constant. These lines follow straight segments outside the parabola, where the distance to the border is the shortest, and arcs of circle inside the parabola, where the penetration path through the hole is the shortest. The current lines abruptly change their direction on the parabola. Figure 3.2 shows the current lines obtained when the field is applied in the zero field cooled state and is raised to a finite H_a. In the particular case shown, the applied field corresponds to a penetration length $\ell_{depth} = 0.6$. In particular, the current density is effectively tangent to the hole border.

Magnetization of the one-hole sample and influence of the hole radius

Due to the symmetry of the problem the magnetization of the one-hole sample of Figure 3.2 is defined as

$$M = \frac{1}{\mu_0 S} \int_S B dS - H_a = \frac{1}{\mu_0} \mathcal{B} - H_a \tag{3.3}$$

with $S = 1$ is the cross section of a square of unit length, and $\mathcal{B}$ is the average value of the vertical component of the magnetic flux density, B, in that cross section.

The relative magnetization drop incurred by the drilled sample is then given by

$$\frac{\Delta M}{|M_0|} = \frac{|M_0 - M_1|}{|M_0|}, \tag{3.4}$$

where M_1 is the magnetization of the one-hole sample and M_0 is that of a sample having the same dimensions and critical current density and containing no hole. The calculations are carried over a square of unit side length. In the particular case considered here, the applied field is given as $H_a = J_c \ell_{depth} = 0.6\, J_c$. These choices guarantee that the flux does not extend further than $x = 1$ in the influence region of the hole.

In the one-hole sample, the magnetization can be calculated either numerically, with the numerical Bean model and with the 2D FEM, or analytically. The analytical calculations, that are only affordable in the specific case of the one-hole sample, are based on the distribution of the magnetic field inside and outside the parabola of Eq. (3.2) that reads

$$\begin{cases} B = B_a - \mu_0 J_c x = \mu_0 J_c (\ell_{depth} - x), & \text{outside the parabola} \\ B = B_a - \mu_0 J_c (D - R) - \mu_0 (r - R) = \mu_0 J_c (\ell_{depth} - r - D + 2R), & \text{inside.} \end{cases} \tag{3.5}$$
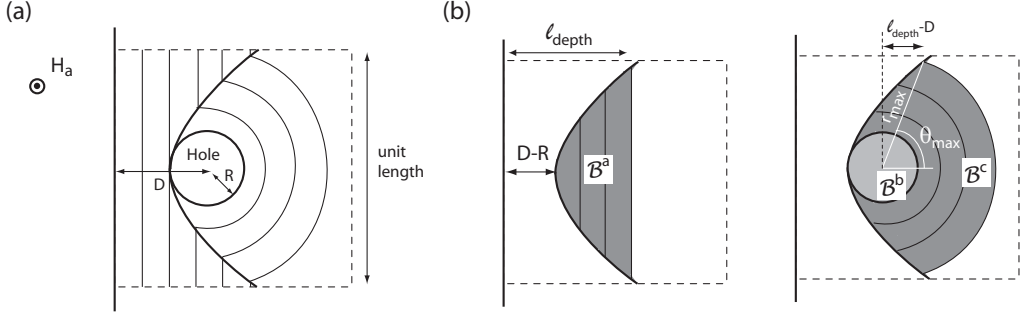
Figure 3.3: (a) Sketch of the current line in a sample with a semi-infinite cross section drilled by a hole of radius R and located at a distance D from the border. (b) Geometrical representation of the surface where we calculate the magnetic flux for the magnetization difference ΔM.

In order to calculate analytically the magnetization drop, the magnetization difference ΔM is decomposed as

$$M_0 - M_1 \quad = \quad \frac{1}{\mu_0} \left(\mathcal{B}^a - (\mathcal{B}^b + \mathcal{B}^c) \right) \tag{3.6}$$

where $\mathcal{B}^{a,b,c}$ are respectively the average magnetic flux evaluated in the grey areas represented in Figure 3.3-(b). The three contributions are

$$\mathcal{B}^a \quad = \quad \frac{1}{S} \int_{D-R}^{\ell_{depth}} \int_{-2\sqrt{Rx-Dx+R^2}}^{2\sqrt{Rx-Dx+R^2}} B(x) \, dy \, dx, \tag{3.7}$$

where $B(x) = \mu_0 J_c(\ell_{depth} - x)$,

$$\mathcal{B}^b \quad = \quad \frac{1}{S} \int_0^{2\pi} \int_0^R \mu_0 J_c(\ell_{depth} - (D-R)) r \, dr \, d\theta, \tag{3.8}$$

$$= \quad \mu_0 J_c \frac{\pi R^2}{S} (\ell_{depth} - (D-R)), \tag{3.9}$$

and

$$\mathcal{B}^c \quad = \quad \frac{2}{S} \left\{ \int_0^{\theta_{max}} \int_R^{r_{max}} B(r) r \, dr \, d\theta + \int_{\theta_{max}}^{\pi} \int_R^{r_{parabola}} B(r) r \, dr \, d\theta \right\}, \tag{3.10}$$

where $B(r) = \mu_0 J_c(\ell_{depth} - r - D + 2R)$. The integrals in the right side are carried in polar coordinates, with the origin fixed at the centre of the hole. In these coordinates, the parabola equation is given as

$$r_{parabola} \quad = \quad \frac{2R}{1 - \cos\theta}. \tag{3.11}$$

The flux front intersects the parabola at an angle θ_{max} that is defined by

$$r_{max} \quad = \quad \frac{2R}{1 - \cos\theta_{max}} \tag{3.12}$$

with

$$r_{max} = \ell_{depth} - D + 2R. \tag{3.13}$$

Figure 3.4: *Magnetization drop in a sample with one hole and a semi-infinite cross section, as a function of the hole radius. The sample geometry is represented in Figure 3.2. The sample is limited to a unit surface for the calculation of the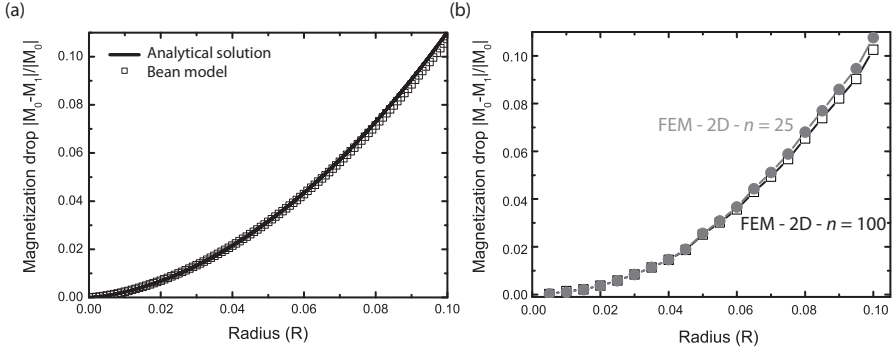 magnetization. The applied magnetic field is $H_a = 0.6\ J_c$. The magnetization is calculated analytically (solid line in (a)), with the numerical Bean model (open squares in (a)) and with the 2D FEM - n = 100 (open squares in (b)) - and - n = 25 (filled circles in (b)).*

Carrying the angular integrals (3.10), we arrive at

$$\mathcal{B}^c \quad = \quad \frac{2\mu_0 J_c}{S}\left\{\int_R^{r_{max}} \theta_{max}(\ell_{\text{depth}} - r - D + 2R)r\,dr \right. \tag{3.14}$$

$$\left. +\mu_0 \int_R^{r_{parabola}} (\pi - \theta_{max})\,(\ell_{\text{depth}} - r - D + 2R)r\,dr\right\} \tag{3.15}$$

where $\theta_{max} = \arctan\left\{2\sqrt{R(\ell_{\text{depth}} - D + R)}/(\ell_{\text{depth}} - D)\right\}$. The integral over r is computed numerically.

A series expansion around $R = 0$ of $\Delta M = |M_0 - M_1|$ yields

$$\frac{\Delta M}{|M_0|} \quad = \quad \frac{\mu_0 J_c}{|M_0|S}\left(\frac{32}{9}\sqrt{R^3(\ell_{\text{depth}} - D)^3} + O(R^{5/2})\right), \tag{3.16}$$

$$= \quad 0.97\left(\frac{R}{\ell_{\text{depth}}}\right)^{3/2} + O\left(\frac{R}{\ell_{\text{depth}}}\right)^{5/2}. \tag{3.17}$$

This is not a trivial result! One could have naively expected that the magnetization drop roughly scales either as the area of the hole, $\Delta M \propto R^2$, or as the area of the region delimited by the parabola, $\Delta M \propto \sqrt{R}$. From Eqs. (3.16), we conclude that an intermediate situation occurs, with $\Delta M \propto R^{3/2}$. Note that the magnetization drop does not depend on the critical current density.

The calculated magnetization drop is compared to the results provided by the numerical methods. Figure 3.4-(a) shows the relative magnetization drop, $\Delta M/|M_0|$, as a function of the hole radius R (the analytical result is shown with solid lines, the numerical Bean model is plotted with square symbols). The analytical results and those obtained with the numerical Bean model are in perfect agreement. Figure 3.4-(b) also shows the magnetization drops obtained with the 2D FEM method, with $n = 100$ (black open squares) and $n = 25$ (grey filled circles) in the same sample.

For the FEM methods, the semi-infinite sample is approximated by a squared section taken out from a larger rectangular sample of infinite height. One of the borders of the section coincides with the

external border of the rectangular sample, and the current density flows parallel to that external border in the section when there is no hole inside. All the distances are normalized to the length of the squared section. The applied magnetic field $H_a = 0.6\ J_c$ is such that the flux front lies in this squared section. The magnetic field distribution is calculated with the single time-step method and $\dot{B}_a = 1$ mT/s. Moreover, the critical current density is assumed to be field-independent and is equal to $J_c = 2\ 10^7$ A/m^2. Note however that the relative magnetization drop is expected to be independent on the value of J_c, provided that J_c is constant and uniform in the sample, as calculated above.

We observe that the calculated drops by FEM are coherent with Eqs. (3.17). The 2D FEM method in the strong pinning limit ($n = 100$) provides magnetization drops that are slightly smaller than those obtained analytically or with the numerical Bean model. That difference is attributed to the unavoidable error associated to the finite-element method.

However, the comparison of the FEM calculations with $n = 100$ and $n = 25$ tends to show that the larger is the flux creep, the larger seems the magnetization drop. Given the numerical errors affecting both results, this latter conclusion must be handled carefully.

While not shown here, the behaviour of the current density in the vicinity of a discontinuity line is also different when the $E - J$ model is taken into account. Actually, for finite values of n, the current density may have different values around J_c, unlike in the critical state model where it is only 0 or J_c. As a result, the sharp bend of the current density observed across the discontinuity lines within the framework of the critical state is smoother with finite values of n. The current density is no longer strictly discontinuous with finite values of n, but the variations of the current direction still remains very sharp when $n = 25$.

3.2   Samples with an infinite height and several holes

3.2.1   Samples with two holes

As a second step, we consider a sample with a semi-infinite cross section and two holes. Both holes have the same radius $R = 0.05$ and are separated by a constant distance $d = 0.2$. The first hole is placed at a distance $D = 0.2$ from the border. Again, the semi-infinite surface is limited to a square whose edges have a unit length. We vary the angular separation θ between the holes and study the interactions between the regions of influence of the holes; their interaction should depend on whether the centre of the second hole lies inside or outside the parabolic influence region of the first hole. We work in polar coordinate and take the origin at the centre of the first hole. The coordinates of the second hole are given by (r, θ) with $r = d$. The discontinuity line produced by the first hole has the equation

$$r_{parabola} \quad = \quad \frac{2R}{1 - \sin\theta}. \tag{3.18}$$

Thus, the centre of the second hole lies on the parabola when $r_{parabola} = 0.2$, and hence when $\theta = 30°$.
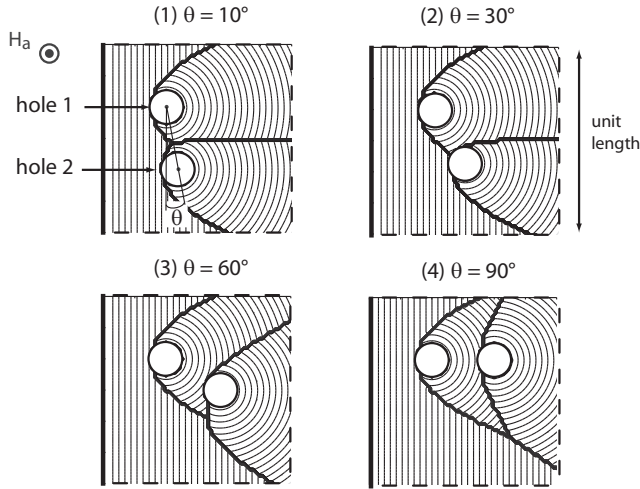
Figure 3.5: *Simulation (numerical Bean model) of the current lines in a sample with a semi-infinite cross section and with two holes. The holes have a radius R =0.05. The unit length corresponds to the side of the square delimited by the dashed lines. The first hole is located at D =0.2 from the border. The separation distance between the holes is constant, d =0.2. The second hole is located at θ =10° (1), θ =30° (2), θ =60° (3) and θ =90° (4). The thick lines represent the discontinuity lines.*

Figure 3.5 shows the current lines for four different angular positions θ calculated with the numerical Bean model. For $\theta = 10°$, the centre of the second hole is located outside the influence region of the first hole. A new discontinuity parabola appears around the second hole. The two parabolic curves merge between the holes and form a common discontinuity line. This last line corresponds to the locus of points for which the difference between the distances to each hole centre is equal to a constant; the discontinuity line is therefore a branch of a hyperbola. When θ increases further, the second hole is pushed away from the border and, for $\theta = 30°$, enters the influence region of the first hole. Again, each hole produces a parabolic discontinuity line and both lines merge into a branch of hyperbola. As the second hole goes deeper in the region of influence of the first one, the hyperbola opens up. The surface of the combined region of influence of the holes increases with θ and reaches a maximum for $\theta = 90°$.

We evaluate the magnetization drop induced by the second hole as

$$\frac{\Delta M}{|M_1|} = \frac{|M_1 - M_2|}{|M_1|},$$

(3.19)

where M_1 is the magnetization for the sample with hole 1 only, and M_2 is that for the sample with holes 1 and 2. We can evaluate this expression either by following the numerical methods exposed in Chapter 2, or with analytical calculations. However, analytical calculations rapidly become tedious when several holes are involved; we will thus restrict ourselves to numerical results from now on. The magnetization drop is plotted in Figure 3.6 as a function of the relative angular position of the holes. It is calculated either with the numerical Bean model (a) or with the 2D finite-element methods (b) with $n = 100$ and $n = 25$, $\dot{B}_a = 1$ mT/s, and $J_c = 2 \ 10^7$ A/m^2. All numerical results show similar trends. For small θ, the magnetization drop decays as the angle is increased. This result follows from the fact
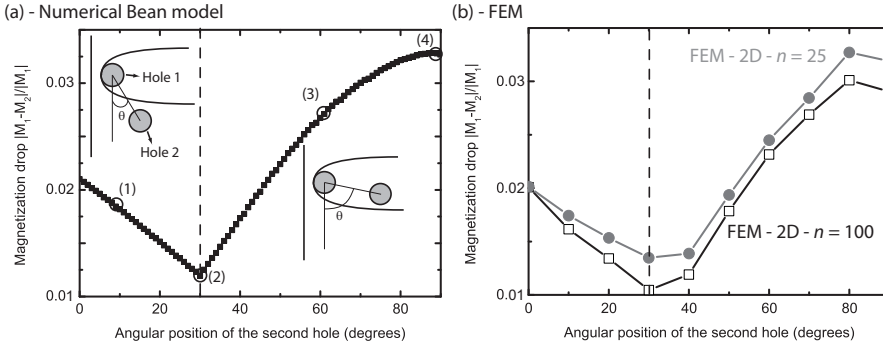
Figure 3.6 : *Magnetization drop in a sample with two holes and a semi-infinite cross section, as a function of the relative angular position of the holes. It is calculated (a) with the numerical Bean model and (b) with the 2D FEM with n =100 (open squares) and with n =25 (filled grey circles). The angular positions (1), (2), (3) and (4) correspond to the situations in Figure 3.5. See text for geometrical details.*

that the second hole is pushed away from the border as θ increases; the hole is thus penetrated by a lower magnetic flux and its effect is reduced. By contrast, for large angles, $\Delta M/|M_1|$ increases with θ because the influence region of the second hole becomes larger. Hence, the optimal position of the centre of the second hole is right on the discontinuity line of the first hole: the magnetization drop is minimum for $\theta = \theta_{opt} = 30°$. Although the results are not shown, we have also studied the situation with a fixed relative angular position and a variable separation distance and found similar conclusions.

We should notice that the results obtained with the numerical Bean model are smoother than those obtained with FEM. It is attributed to the numerical errors affecting the FEM results. Moreover, the influence of the critical exponent is negligible in the conclusions drawn for this analysis. The use of the numerical Bean model is therefore particularly recommended in these very simple cases.

Some insight on these results can be gained by examining how the flux penetrates the system. The flux front near the second hole is sketched in Figure 3.7 for $\theta = \theta_{opt} = 30°$ (a), $\theta < \theta_{opt}$ (b), and $\theta > \theta_{opt}$ (c). We can observe that the flux front reaches the second hole tangentially in all cases. However, for $\theta = \theta_{opt}$, the flux front is tangent to the second hole simultaneously in the region inside

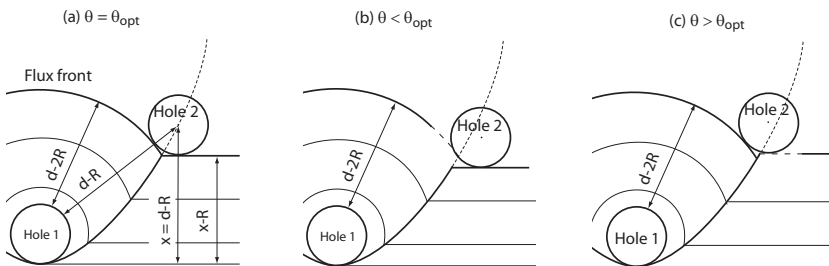**Figure 3.7** : *Sketch of the flux front tangent to hole 2 for angular positions $\theta = \theta_{opt}$ (a), $\theta < \theta_{opt}$ (b), and $\theta > \theta_{opt}$ (c). The dashed parts are the remnant flux front in the influence region of the second hole.*

the discontinuity parabola produced by the first hole (circular front) and in the region outside the parabola (straight front). The simultaneous penetration from the two regions appears to be necessary for reducing the effects of the second hole on the magnetization of the sample.

3.2.2   Samples with three holes

We now turn to adding a third hole to the optimized two-hole pattern of Figure 3.7-(a), where the first hole is again located at $D = 0.2$ away from the external border and the centre of the second hole lies on the discontinuity parabola of the first one, at a distance $d = 0.2$. The three holes have a radius $R = 0.05$. The third hole is located at a constant distance $d = 0.2$ from the second hole. Adding a third hole reduces again the magnetization of the sample. The magnetization drop, when $H_a = 0.6\ J_c$ is now given by

$$\frac{\Delta M}{|M_2|} = \frac{|M_2 - M_3|}{|M_2|},$$

(3.20)

where M_2 is the magnetization of a sample containing only the first two holes, and M_3 is the magnetization for a sample containing three holes.

Figure 3.8 shows the magnetization drop, $\Delta M/|M_2|$, as a function of the angular position of the third hole; the inset shows the configuration of the holes. The magnetization drop is calculated either (a) with the numerical Bean model or (b) with the 2D FEM with $n = 100$ (open squares) and $n = 25$ (filled circles); the other parameters for the FEM are similar to those used in Section 3.2.1. Again, the different models show similar behaviours for the magnetization drop. The centre of the third hole can be located in three different regions: region A, a region that is not affected by holes 1 and 2, and regions B and C, that respectively correspond to the influence regions of hole 2 and hole 1. Consider first that hole 3 lies in region A. As θ increases, the magnetization drop, $\Delta M/|M_2|$, decays because the distance of hole 3 from the border decreases (such a behaviour was already observed with the two-holes pattern). The magnetization drop is minimum when the centre of hole 3 lies on the discontinuity parabola of the hole 2, separating regions A and B. If θ increases further, hole 3
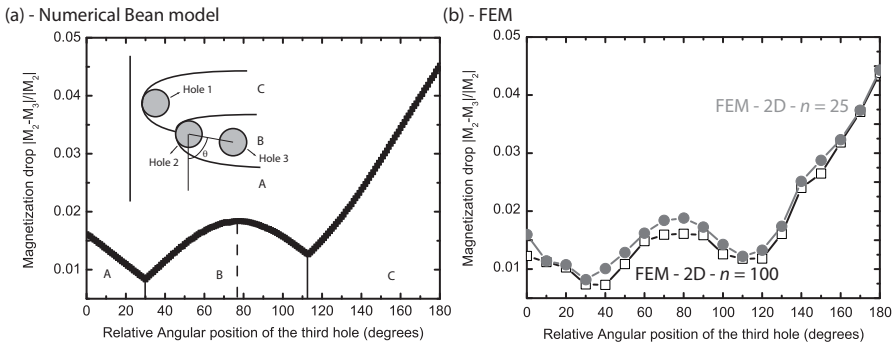

Figure 3.8: *Magnetization drop in a sample with three holes and a semi-infinite cross section, as a function of the relative angular position between the second and the third hole. It is calculated by the three methods of Figure 3.6. The first hole has a radius R =0.05 and is located at a distance D =0.2 from the border. See text for details of the geometry*

enters region B, and $\Delta M/|M_2|$ increases again, to reach a maximum when the centre of hole 3 reaches the remnant parabola of hole 1 (this line does not appear as a discontinuity line in the current line distribution). Then, $\Delta M/|M_2|$ decreases until hole 3 reaches the boundary between regions B and C (this discontinuity line is a hyperbola). As it continues through region C, $\Delta M/|M_2|$ increases again. We can thus conclude that the magnetization drop is minimized each time the centre of the hole is located on a discontinuity line. Note however that the values of $\Delta M/|M_2|$ on a minimum are not equal; the lowest value of $\Delta M/|M_2|$ is achieved when hole 3 is placed on the boundary between regions A and B.

3.3   Influence of the types of lattice in samples of infinite height

3.3.1   Samples with a semi-infinite cross section

The analysis of samples containing two or three holes reveals that the relative position between the holes is an important factor that affects the magnetic properties of the drilled samples. When several holes are drilled, they are usually arranged on a regular pattern. In such samples, the relative position between these holes depends on the type of pattern that is chosen.

Therefore, we apply the results of the previous sections to construct a lattice containing many holes. Let us first compare the magnetization for two lattices. The first lattice is a square lattice, where a line of equidistant holes (separated by a distance d) parallel to the external boundary is reproduced periodically every distance d in the direction perpendicular to the border. The second lattice is obtained from the square lattice by shifting every other row by half the length of a unit cell, leading to a
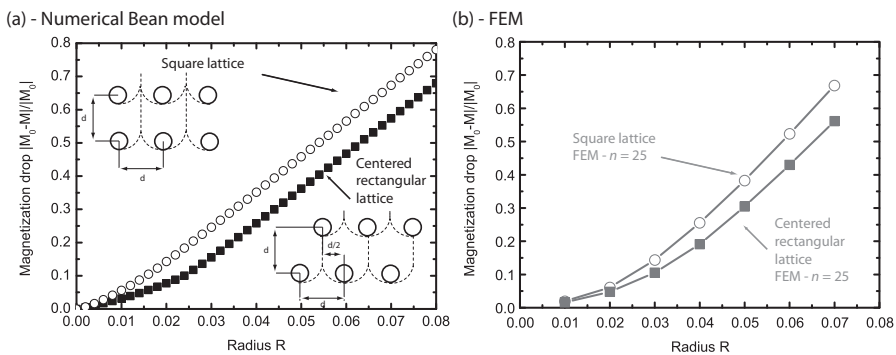
Figure 3.9: *Magnetization drop (as compared to a sample with the same geometry and without holes), as a function of the hole radius in a sample with a semi-infinite cross section (limited to a square of unit length) with two different lattice configurations. The drop is calculated with the numerical Bean model (a) and with the 2D FEM with n =25 (b). The open circle symbols correspond to a square lattice with a lattice constant d =0.2 and the filled square symbols refer to a centered rectangular lattice with the same lattice constant. The insets show the lattices. The number of holes for a given radius is the same in each lattice. The applied magnetic field is H_a =0.6 J_c. The centered rectangular lattice produces the largest magnetization.*

particular realization of a centered rectangular lattice. The two lattices are represented in the insets of Figure 3.9-(a). Since we are working with semi-infinite cross sections, we work in a square of unit length, which we arbitrarily choose to contain five rows of holes. The holes have a common radius, R, and the lattice constant is fixed at $d = 0.2$. Note that the hole density is equal in both lattices.

The magnetization drop is defined as

$$\frac{\Delta M}{|M_0|} = \frac{|M_0 - M|}{|M_0|},$$

(3.21)

where M is the magnetization of the sample and M_0 stands for the magnetization for a sample with the same geometry and J_C but without holes. The applied field is chosen to be $H_a = 0.6\ J_c$ so that the flux front stays within the square of unit length. $\Delta M/|M_0|$ is plotted as a function of the hole radius in Figure 3.9. Whether the calculations are carried out with the numerical Bean model or with the 2D FEM ($n = 25$), we find that the centered rectangular lattice produces a smaller magnetization drop than the square lattice. Although not shown, we checked that this result is independent of the hole separation distance d. This result naturally follows from the conclusions of the previous sections: in the centered rectangular lattice, the holes are located on the discontinuity parabola of the neighbouring holes and the magnetization is maximized (in absolute value).

3.3.2   Samples with a circular cross section

Consider next infinitely long samples with a circular cross section. These samples have a geometry which is more realistic for bulk HTS applications. Moreover, calculations on infinitely long geometries describe well the magnetic properties in the median plane of a cylinder with a finite height, provided its height h is large with respect to its diameter D [126, 174].

We found earlier that in a centered rectangular lattice, the holes were placed on the discontinuity lines of the neighbouring holes. This placement helped increasing the magnetization. However, this result is not necessarily valid in circular cross sections, because of the flux front geometry. The flux front is now circular, and as the flux penetrates the sample, the critical currents flow around concentric circular trajectories. Such a geometry is not compatible with the symmetry imposed by a centered rectangular lattice. The current lines in a circular sample with a centered rectangular hole pattern are represented in Figure 3.10-(a). One can observe for instance that the hole indicated by the arrow is not located on a discontinuity line.

We can construct another lattice, that uses the circular shape of current lines, and place the holes on discontinuity lines. Figure 3.10-(b) shows such a realization, which we name a "polar triangular lattice". The holes are positioned on concentric layers separated by a distance d. Inside each layer, the holes have a common angular separation. Furthermore, the holes are shifted every other layer by half their angular separation. This ensures that the holes are located on discontinuity lines.

By comparison with the square lattice, one could also define a polar square lattice where the hole angular position is not shifted from one layer to the next. The polar square lattice, the polar triangular lattice, the square lattice and the centered rectangular lattice are represented in a sample with a circular cross section in Figure 3.10-(c).
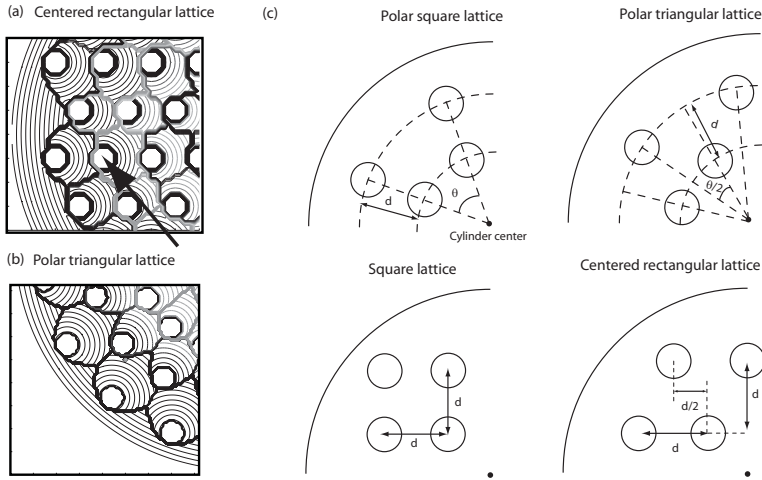
Figure 3.10: (a) Simulation of the current lines in a sample with a circular cross section and a centered rectangular hole lattice. The arrow indicates a hole which is not located on a discontinuity line. (b) Simulation of the current lines in a sample with a circular cross section and a polar triangular hole lattice. (c) Lattice patterns under consideration in samples with a circular cross section.

The four lattices of Figure 3.10-(c) are incorporated into a cylinder of infinite height and having a diameter of 20 mm. The lattice parameters are chosen in a such way that the total diameter of the holes is kept constant, so as to fix the total surface of heat exchange. The square and the centered rectangular lattices contain each 24 holes with a radius of 1 mm. The polar lattices contain two layers of 10 holes with a radius of 1 mm and a central layer with 10 holes with a radius of 0.4 mm. The four samples are represented in Figure 3.11-(a). The trapped magnetizations M are calculated in each sample with the numerical Bean model and with the 2D FEM in two time-steps ($n = 25$): one for increasing the applied flux density to $B_a = 2\mu_0 J_c a \approx 503$ mT at $\dot{B}_a = 1$ mT/s, and another one for decreasing the applied field to 0 with the same sweep rate. These results are compared to the trapped
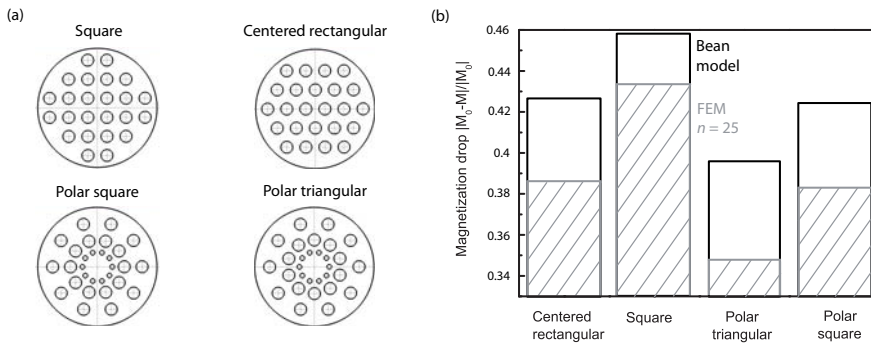
Figure 3.11: (a) Drilled samples of infinite height with a circular cross section and holes arranged in four different lattices. See text for geometrical details. (b)- Magnetization drop in the drilled samples (with respect to a plain one), as calculated with the numerical Bean model (black) and with the 2D FEM with n = 25 (grey).

magnetization M_0 of a sample having the same diameter and containing no hole; the corresponding magnetization drops are shown in Figure 3.11-(b). We find that the sample with the polar triangular hole lattice, which aligns holes of each layer on the discontinuity lines produced by the previous layers, has the smallest magnetization drop, and hence the highest trapped flux.

Although not shown here, the FEM calculations with $n = 100$ yield magnetization drops that differ at maximum by 1% from those obtained with $n = 25$.

3.3.3 Influence of a field-dependent critical current density

Hitherto, the critical current density in the superconductor has been assumed to be uniform and field-independent. We now consider the case of a field-dependent J_c in order to know whether the conclusions of the previous paragraph are modified.

We consider four drilled samples similar to those of Figure 3.11-(a). The critical current density is assumed to depend on the magnetic flux density according to the Kim's law [40],

$$J_c(B) = \frac{J_{c0}}{1 + B/B_1},$$ (3.22)

where B_1 is the flux density for which J_c is half of its initial value at zero field, J_{c0}. B_1 usually depends strongly on the material properties. In Bi-based bulk superconductors, it is usually low and the critical current density varies strongly around the maximum trapped flux density of the sample. In YBCO, B_1 is often larger than in Bi-based samples and the variations of the current density are smaller in the trapped flux profile. Both situations are investigated in this paragraph. We consider three values of B_1. Large variations of the critical current density in the flux profile are obtained with $B_1 = 0.25B_p$, where B_p is the penetration field of the plain sample, $B_p = \mu_0 J_c a$. Conversely, small variations are
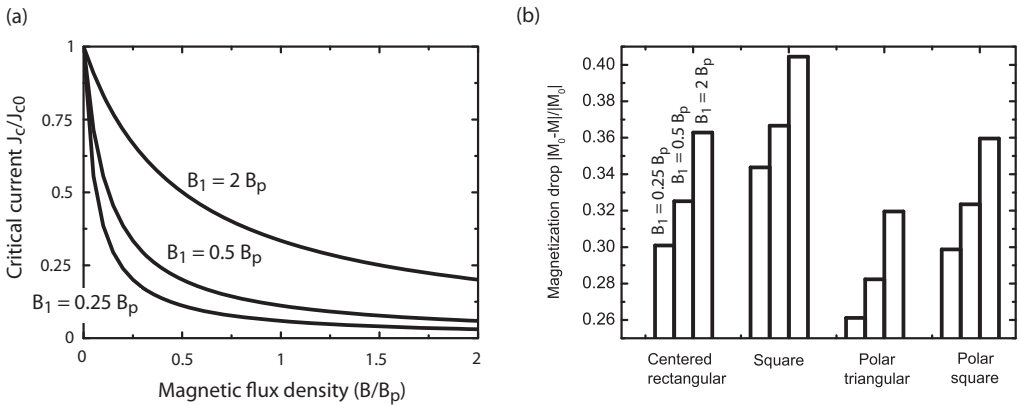
Figure 3.12: (a)-Dependence of the critical current density on the magnetic flux density, according to the Kim's law with $B_1 = 0.25B_p$, $B_1 = 0.5B_p$ and $B_1 = 2B_p$. The penetration field corresponds to that of a plain sample of circular cross section having the same dimensions as those of Figure 3.11, $B_p = 251$ mT. (b)- Magnetization drop in the drilled samples of Figure 3.11 calculated with the field-dependent critical current density presented in (a).

simulated with $B_1 = 2B_p$, and an intermediate situation is considered with $B_1 = 0.5B_p$. These three situations are represented in Figure 3.12-(a) where the critical current density is plotted as a function of the magnetic flux density.

The calculations of the flux profile in the samples with the three different field-dependences of the critical current density are carried out with the 2D FEM ($n = 25$, $J_{c0} = 2 \ 10^7$ A/m^2). Note that it would have been also possible to use the numerical Bean model, but a complete modification of the code would have been mandatory, while it was not required with the FEM code. Figure 3.12-(b) shows the calculated magnetization drops (with respect to that of a plain sample having the same dimensions and critical current density) in the four lattices of Figure 3.11-(a) and with the three different dependences. It is observed that the polar triangular always yields the smallest drop, independent of the type of field-dependences.

Moreover, the values of the magnetization drops vary with B_1. In a given sample, the constant critical current density (see Figure 3.11-(b)) produces the largest drop, this drop is smaller when the flux profile exhibits large variations of the critical current density ($B_1 = 0.25B_p$). When the holes are drilled in the superconductor, the maximum trapped flux density is reduced as compared to that of the plain sample. On the other hand, in the case of a field-dependent J_c, this reduction of B_{max} is accompanied by an increase of the critical current density with respect to its value in the plain sample. That explains the smaller drops observed in drilled samples with a large field-dependence of the critical current density.

3.4   Influence of the demagnetizing effects

The samples of infinite height considered in Sections 3.1-3.3 allow one to readily assess the effects of the holes on the magnetic properties, but they do not accurately reproduce the more realistic situation of typical drilled samples whose height L is of the order of the diameter D [76, 77, 78, 82]. In particular, the distribution of the magnetic flux density in the median plane is not close to that of a sample with an infinite height when $L \sim D$; the demagnetizing effects cannot be neglected anymore in such samples [126, 174]. In order to study the influence of the demagnetizing effects, we consider in this section 3D FEM calculations of the magnetic properties of drilled cylinders having a finite height.

3.4.1   Cylindrical samples of finite height with one hole

We first concentrate on a sample containing a single hole, as represented in Figure 3.13-(a). The cylinder has a radius of 10 mm and a height of 8 mm. The centre of the single hole is located at 2.5 mm from the border and has a radius of 1.5 mm. The sample is assumed to have a field-independent critical current density, $J_c = 2.10^7$ A/m^2, and a critical exponent of $n = 25$. We consider that the sample is subjected to a uniform applied flux density of 300 mT. The magnetic field distribution is solved with the single time step 3D FEM, with $\dot{B}_a = 1$ mT/s. The magnetic field distribution along the sample diameter crossing the centre of the hole is reproduced in the median plane and on the top surface respectively in Figure 3.13-(b) and (c). The magnetic field distribution along that same diameter in
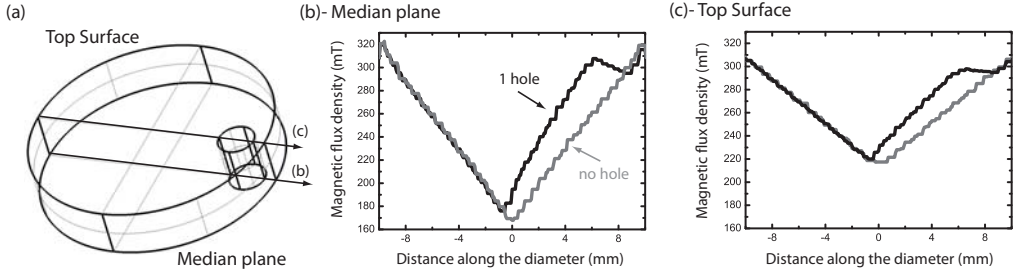
Figure 3.13: *(a)- Cylindrical sample with one hole (half of the sample is represented). See text for the geometrical details. The arrows show the diameters on which the flux profiles (b) and (c) are represented. (b)- Magnetic flux profile along arrow (b) in the median plane of the sample that is subjected to a uniform applied flux density of B_a =300 mT (black line). The profile in a plain sample having the same dimensions and J_c is reproduced with a grey line. (c)- Magnetic flux profile along arrow (c) at the top surface of the drilled (black line) and plain (grey line) samples.*

a sample having the same dimensions and no hole is also reproduced as a reference, with grey lines.

Starting from $r = 10$ mm and as far as we have not reached the hole ($r > 9$ mm), the magnetic flux profile in the median plane of the one-hole sample is similar to that of the sample with no hole, no matter it is in the median plane or on the top surface. In particular, we observe that the magnetic flux density at the sample outer edge is larger than the applied field. There is a flux concentration due to the return lines of the demagnetizing field that are oriented outside the superconductor in the same direction as the applied field. In the hole, the magnetic field is no longer uniform, contrarily to what happens in samples with an infinite height. It increases as one gets closer to the sample centre. We believe that it is a consequence of the return lines of the demagnetizing field that cross the hole. The presence of the hole induces a shift between both flux profiles in the superconductor when $r < 6$ mm. Moreover, the spatial variations of B are larger in the one-hole sample than in the plain one. The magnetic flux profile in the one-hole sample no longer reaches its minimum value at the sample centre, but at $r \approx -1$ mm. For $r < -1$ mm, the profile is similar in both samples.

Note that the minimal value of the magnetic flux density in the median plane of the plain sample is $B_{min} \approx 165$ mT. That value in the plain sample is larger than the estimate based on the Bean critical state applied to a plain sample with an infinite height and the same cross section, $B_{min} = B_a - \mu_0 J_c r = 49$ mT. The difference between the Bean model's estimate and the calculated B_{min} in the sample with a finite height is attributed to the finite value of n and to the demagnetizing effects that reduce the spatial variations of the magnetic flux density with respect to those of a sample of infinite height. Moreover, since the hole offers it a return path, the demagnetizing field less affects the spatial variations in the one-hole sample for $-1 < r < 6$ mm.

3.4.2   Cylindrical samples of finite height with several holes

As observed in Figure 3.13, the return lines of the demagnetizing field play a crucial role in the magnetic flux profile in samples of finite height whose radius is larger or approximately equal to their height. It is responsible for the flux concentration at the sample outer edges, for the non-uniform field inside the holes, and for the smaller spatial variations of the magnetic field with respect to those found in a sample of infinite height. However, these effects do not necessarily lead to reconsider the conclusions on the influence of the hole arrangement in drilled sample of infinite height.

Actually, let us consider the four lattice types of Figure 3.11-(a) and let us incorporate them in cylindrical samples with a radius of 10 mm and a height of 8 mm. These drilled samples are shown in Figure 3.14-(a). The trapped magnetic flux density in the drilled samples is calculated with the 3D FEM in two time-steps, with the same parameters as in Section 3.3. The obtained flux profile along the diameter in the top cross section [see black arrow in Figure 3.14-(a)] is represented in Figure 3.14-(b). The dashed curve corresponds to the trapped flux profile in a cylinder having the same dimensions and material parameters, but containing no hole. The flux profiles exhibit steps, resulting from the number of meshing elements used in 3D simulations, as was already observed in Section 2.5. It can be observed that the maximum trapped magnetic flux density is smaller in the drilled samples than in the plain one.

Table 3.1 lists the values of the maximum trapped magnetic flux density in the top cross section and in the median plane, as well as the results obtained with the 2D-FEM (with the same parameters) for infinite drilled cylinders having the same cross sections. The drops of trapped flux with respect to those of the plain sample are also indicated. In all cases, the maximum trapped magnetic flux density is obtained with a polar triangular lattice, with a value higher by $\approx$ 40% with respect to that obtained in a centered rectangular lattice. This result is almost independent of the cross section where it is
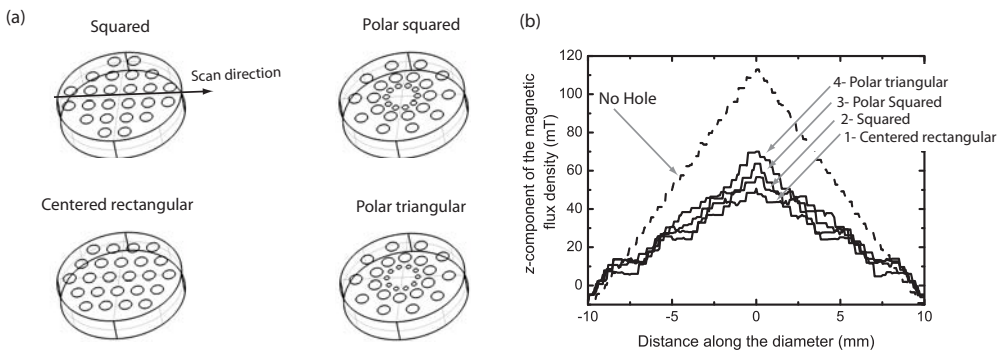
Figure 3.14: (a)- Four drilled cylinders (radius 10 mm, height 8 mm). The hole patterns are similar to those of Figure 3.11-(a). (b) - Trapped magnetic flux profile along the cylinder diameter, as calculated with the FEM two time-steps method, with a sweep rate of 10 mT/s and n = 25. The profile is represented in the top cross section of the cylinder. The dashed line corresponds to the flux profile in a cylinder without holes, also calculated with the FEM two time-step method.

B_{max}	3D - Top		3D - Centre		2D	
No hole	112.9 mT		176.6 mT		225.8 mT	
Polar triangular lattice	70.05 mT	37.9%	112.7 mT	36.2%	137.9 mT	38.9%
Polar squared lattice	63.6 mT	43.7%	97.7 mT	44.7%	120.9 mT	46.4%
Square lattice	56.7 mT	49.8%	87.8 mT	50.3%	110.8 mT	50.9%
Centered rectangular lattice	50.6 mT	55.2%	76.4 mT	56.7%	101 mT	55.3%

Table 3.1: *Maximum trapped magnetic flux density in cylinders of finite height, as calculated in the top cross section (3D - top) and in the median plane (3D - centre), and in cylinders of infinite height obtained with the 2D FEM.*

calculated and agrees with the theoretical predictions based on the Bean model. The demagnetizing effects only affect the values of the maximum trapped flux density. They are found to be smaller in the finite height samples than in the cylinders of infinite height with the same hole lattice, whereas the relative drops of maximum trapped flux are of similar magnitudes.

The above results are based on the comparison of a plain sample and a drilled sample that have the same critical current density. In other words, we only assess the modifications of the current stream lines induced by the presence of the holes, by considering that the current density remains unchanged. However, in practical situations, it is important to remind oneself that the first advantage of drilling holes is to be able to increase the oxygen content in the sample, and hence to increase the critical current density. The overall consequence of drilling holes thus results from a compromise between the increase of critical current density and the magnetization drop induced by the modification of the current stream lines and by the loss of superconducting material. While in this section we have only considered the second factor, the first factor has been experimentally shown to be dominant [6, 83].

3.5 Measurements of the magnetization drop resulting from the drilling of a pattern of artificial holes

In Section 3.4, we show with modelling arguments that the hole arrangement is a key parameter for reducing the magnetization drop inherent to the drilling of holes in a HTS bulk sample. We now present and discuss, on the basis of the above modelling results, an experiment which aims at assessing the influence of the hole pattern on the magnetic properties of the drilled samples. For this purpose, we perform Hall probe mapping measurements on drilled and plain samples and the experimental results are then compared to the numerical results obtained with the three models presented in Chapter 2: (1), the numerical Bean model, (2), the 2D FEM model with a finite value of n, and (3), the 3D FEM model.

3.5.1   Sample preparation

In most cases considered so far [9, 10, 61, 76, 77, 78, 79, 83, 84, 85], drilled samples were obtained from Y211-preform where the holes had been arranged *before* the synthesis of the Y123 phase. This approach makes the assessment of the different hole arrangements difficult, since the critical current densities may differ appreciably from one sample to another even though they are processed similarly. We thus follow a different approach and consider bulk YBCO samples that are drilled *after* their synthesis. This technique allows us to compare the trapped magnetic flux in every sample before and after drilling the holes. Provided the microstructure of the sample has not been affected by the drilling process, one can make the reasonable assumption that the critical current density is unchanged and consider the sole effect of the modification of the current stream lines on the magnetic properties of the sample.

The plain samples are extracted from a top-seeded melt-grown YBCO bulk cylinder that was synthesized at CRISMAT (Caen, France). The cylinder has a diameter of 22 mm and a height of 16 mm. With the help of a wire saw, two rectangular samples are cut out as sketched in Figure 3.15. The resulting samples have a length of 8.6 mm, a width of 6.6 mm, and a height of 4 mm.

In each sample, six holes with diameter 1 mm are drilled along the *c*-axis. To prevent the superconducting ceramics from breaking during the drilling process, an ultrasonic drilling machine is used. In order to avoid effects associated with the finite side lengths of the samples, the six holes are made in the trapezoidal sector delimited by the grey dashed lines shown on Figure 3.15. For each sample, this sector lies in the rectangular cross section and is delimited by one long edge of the cross section, a segment of its longest median, and two lines which start at the corners with a 45 degree angle. This choice is motivated by the critical state configuration found in a non-drilled sample of similar dimensions subjected to a magnetic field applied along the *c*-axis. In this case, the two boundaries at 45 degrees are placed where the current stream lines change abruptly their direction, whereas they flow parallel to the long edge within the trapezoidal sector (these boundaries are discontinuity lines) [155, 156]. Thus, the holes are drilled in a sector where the current lines are initially parallel to one another, a situation which is close to that considered in the previous theoretical models of

(1) Cut of two rectangular samples out of a bulk cylinder

(2) Drilling of two different hole patterns
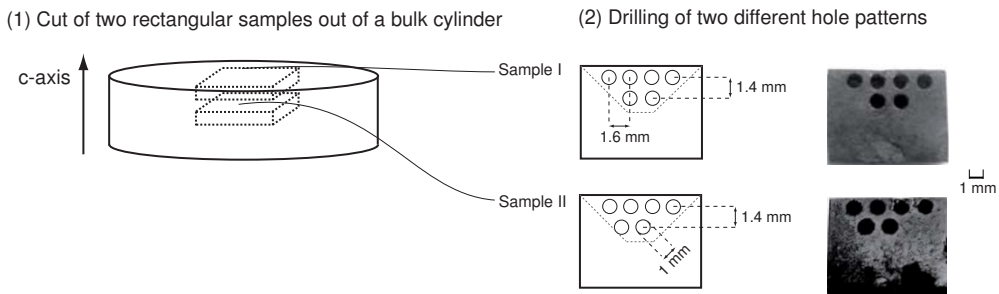
Figure 3.15: *(1)- Extraction of two rectangular YBCO samples out of a cylindrical one, with the help of a wire saw. (2)- Sketch of the hole patterns drilled in the samples and pictures of the samples after the drilling process.*

Sections 3.1-3.3.

For each sample, two series of holes (containing 4 and 2 holes, respectively) are made along parallel lines. The hole separation along a line is 1.6 mm and the lines are separated by 1.4 mm. The two holes on the second line can be arranged in two different ways: (I) either they are aligned with the holes of the first line and form the beginning of a *rectangular lattice*, or (II), the holes are shifted with respect to those of the first line by half a separation (0.8 mm) and start forming a *centered rectangular lattice*. In this latter case, the centres of the holes of the second line are in fact placed on the discontinuity lines associated with the holes of the first line. A picture of the two samples obtained after the drilling process is shown in Figure 3.15-(2).

3.5.2   Measurements

The trapped magnetic flux density above the sample surface is measured in a Hall probe mapping experiment, by moving a miniature probe fixed to a motor-driven xy micro-positioning stage over the sample surface [9, 61]. The Hall probe is sensitive to the component of the local field which is perpendicular to the surface. Its active area is 0.05×0.05 mm^2 and its distance from the sample surface is 0.5 mm. The Hall probe is moved across the top surface with a step size of 0.5 mm in x and y directions. In addition, we also measure the maximum trapped magnetic flux density directly

Figure 3.16: *Distribution of the trapped magnetic flux density at $\approx$0.5 mm above the sample surface of Sample I and Sample II, before (a) and after (b) drilling the holes.*

on the surface. We bring the Hall probe in close contact with the sample and move it slightly around the sample centre until the maximum reading is found.

The samples are magnetized with a field-cooling process during which the samples, initially at room temperature, are immersed in liquid nitrogen in a uniform magnetic flux density of 300 mT created by a large copper coil. The field-cooling process 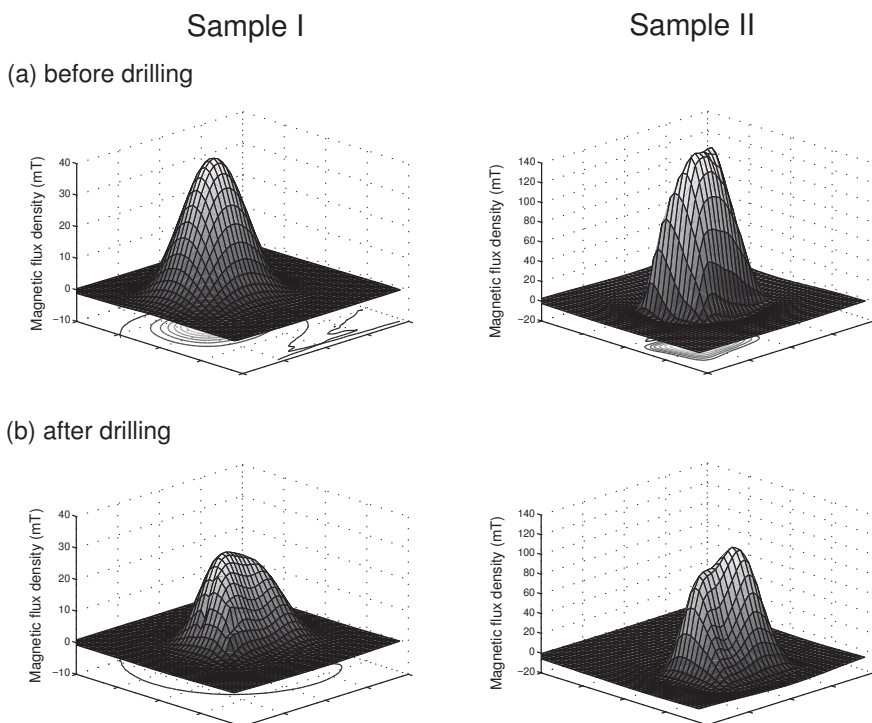lasts 5 min, and the characterization of the trapped field starts 15 min after the applied magnetic field has been switched off, so that magnetic relaxation effects are negligible.

The distribution of the trapped magnetic flux density 0.5 mm above the top surface of Sample I — left panels — and Sample II — right panels — are shown in Figure 3.16, respectively before drilling, (a), and after drilling, (b). In Sample I, the trapped magnetic flux density has a single maximum at $B_{\text{trapped}}^{\text{max}} \approx 40$ mT before drilling; after drilling, the maximum field drops to $B_{\text{trapped}}^{\text{max}} \approx 25$ mT. In Sample II, a larger maximum trapped flux density is found before drilling, with $B_{\text{trapped}}^{\text{max}} \approx 130$ mT; it reduces to $B_{\text{trapped}}^{\text{max}} \approx 100$ mT after drilling. The relative drop of the maximum trapped flux density is found to be the largest in Sample I. It can also be observed that, in addition to reducing the trapped flux, holes also modify its distribution with the largest effects near the maximum.

3.5.3   Discussion

The measured drops of trapped flux in the drilled samples are compared to the simulation results. The same set of parameters are used for drilled and plain samples. They are fixed as follows. First, the critical current density is assumed to be uniform and field-independent. Its value is chosen such that model (3) − 3D FEM − reproduces well the value of the maximum trapped flux density that is measured on the top surface of each plain sample. This gives $J_c = 4.1\ 10^7$ A/m^2 for Sample I and $J_c = 8.8\ 10^7$ A/m^2 for Sample II. Second, for the $E - J$ power law in models (2) and (3), the critical exponent n is taken as $n \approx 25$, a typical value for YBCO bulk samples [175].

Unlike the experiments where the samples are magnetized with a field-cooling process, the simulations reproduce a zero field-cooling process, and hence require a maximum applied field larger than that used in the experiments. In order to fully magnetize the samples, even those with an infinite height, the maximum value of the applied magnetic flux density is chosen at 1 T and the sweep rate is equal to 1 mT/s. Let us first compare the distributions of the trapped flux measured above the surface of the drilled samples with that calculated with the 3D FEM model. Figure 3.17 shows the measured trapped flux distribution at 0.5 mm above the surface in the bottom panels and the numerical predictions in the top panels, for each sample. Note that in the experimental results, the holes cannot be resolved because of the distance between the Hall probe and the surface of the samples. In Sample I, the simulated distribution of the trapped flux is symmetric, with a maximum trapped flux density occuring at the centre of the cross section. This distribution deviates from the experimental mapping (bottom left panel), where the maximum trapped field is found to be slightly shifted to the left of the centre. The agreement between the calculated and the measured distributions is much better for Sample II, where the maximum of the trapped flux is found to be shifted to the right of the centre in both the experimental mapping and the simulated distribution.
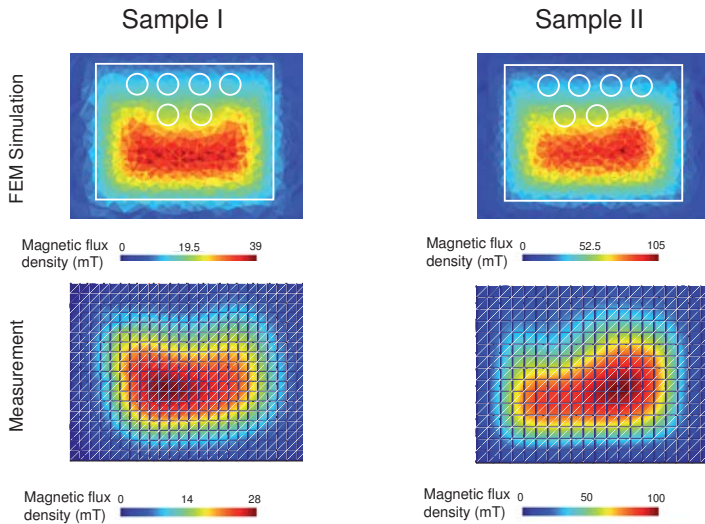
Figure 3.17: *Two-dimensional trapped magnetic flux distributions at ≈0.5 mm above the sample surface of the drilled samples I and II. The top panels correspond to the simulation results with the 3D-FEM model and the bottom panels to the measurements.*

The measurement of the trapped flux distribution at a finite distance above the sample surface can be affected by a systematic error in the distance between the Hall probe and the sample surface that cannot be reproduced accurately in simulations. It is thus interesting to compare the maximum trapped flux densities when the probe is in contact with the sample. Table 3.2 reports the simulated and the measured maximum trapped flux density in samples I and II, before and after drilling.

The maximum trapped flux density is simulated in the median plane of the samples with models (1),

Table 3.2: *Comparison of the maximum trapped magnetic flux density in samples I and II*

Sample I	Median plane			Top surface	
Rectangular lattice	Bean model	FEM - 2D	FEM - 3D	FEM - 3D	Measurement
Before drilling	169 mT	137 mT	95 mT	61 mT	60 mT
After drilling	126 mT	104 mT	75 mT	46 mT	33.7 mT
Relative drop	25%	24%	21%	25%	44%
Sample II	Median plane			Top surface	
Centered rectangular lattice	Bean model	FEM - 2D	FEM - 3D	FEM - 3D	Measurement
Before drilling	358 mT	310 mT	244 mT	154 mT	155 mT
After drilling	291 mT	253 mT	207 mT	130 mT	120.7 mT
Relative drop	19%	18%	15%	16%	22%
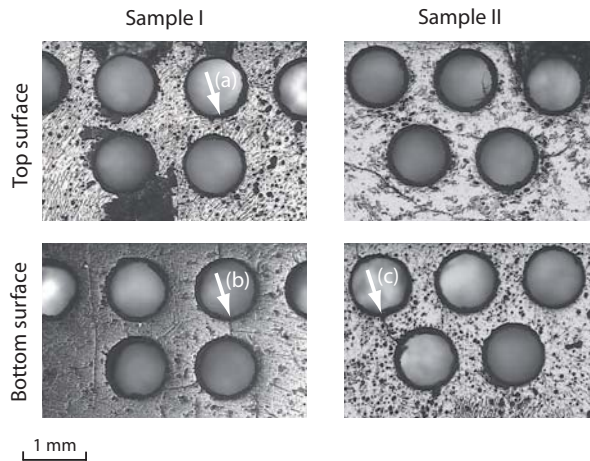
Figure 3.18: *Micrographs of the bottom and top surfaces of Sample I and II after the drilling of the holes.*

(2) and (3) and on the surface with model (3). It is found that the maximum trapped flux density is in each case the largest with the Bean model, the flux creep and geometrical effects bringing additional drops of trapped flux. Further, although the drops in magnetic flux density are of different magnitudes in each model, the relative drops calculated by these models are found to be nearly equal, about 23 % for Sample I and 17% for Sample II. These results indicate that the centered rectangular lattice is the configuration with the smallest drop in the trapped flux, as was already found in samples with different cross sections in Section 3.3-3.4.

Experimentally, the measured maximum magnetic flux density is found to drop by 44% in Sample I, and by 22% in Sample II. On the one hand, the smallest relative drop that is observed in Sample II is well reproduced by simulations, which confirms the previous theoretical results discussed in Sections 3.3 and 3.4. It should be noted that the simple 2D models, while not absolutely suitable for samples under consideration in this study, already yield a reasonable estimate of the relative drop that is measured at the surface of Sample II. For Sample I, on the other hand, the numerical simulations fail in describing the large measured drop.

Given the discrepancy between theory and experiment for Sample I, the large observed magnetic field drop cannot be only due to a reorganisation of the current lines after drilling. Presumably, drilling holes has also affected the microstructure of the sample. Figure 3.18 shows optical microscope pictures of top and bottom surfaces of samples I and II after drilling. The arrows (a) and (b) show a crack between two neighbouring holes in Sample I. This crack is found on both surfaces and has probably be produced during drilling. Its position is consistent with the shift to the left observed in the maximum of the field distribution in Figure 3.17. By contrast, Sample II presents a crack on one of its sides (arrow (c)) but not on the other, so that the drilling process appears to have preserved most the microstructure of this sample.

3.6   Summary of Chapter 3

In this chapter, the magnetization drop induced by the removal of superconducting material in drilled samples is studied numerically, with the models described in Chapter 2, and experimentally. Different hole arrangements are considered.

We first focus on the modelling of the magnetization of drilled samples and compare the drilled samples to plain ones having the same dimensions and critical current density. We show that discontinuity lines are attached to a single hole and take the form of parabola in the case of a one-hole sample with an infinite height and a semi-infinite cross section. In that geometry, the dependence of the hole radius on the magnetization drop of the drilled sample of infinite height is calculated analytically, with the numerical Bean model, and with the 2D FEM model. The results given by each of the methods are consistent and indicate that the loss in magnetization scales neither with the surface of the hole ($\propto R^2$), nor with the surface of its parabolic region of influence ($\propto \sqrt{R}$), but as a surface of intermediate size, that is as $R^{3/2}$. In samples with two and three holes, one must resort to simulations in order to calculate the magnetization drop. They demonstrate that the holes should always be located on discontinuity lines of their direct neighbours so as to maximize the magnetization.

When several holes are drilled in a bulk sample, the optimal lattice arrangement is the one that aligns the holes on the discontinuity lines. It depends on the sample cross section: we obtain the largest magnetization with a centered rectangular hole lattice in samples with a semi-infinite cross section, and with a polar triangular lattice in samples with a circular cross section. The demagnetizing effects associated with the short length samples do not modify that conclusion.

Then, the modelling results are confronted to experiments. To this aim, we consider two synthesized plain samples with the same dimensions and made six holes in each, according to two different arrangements. In Sample I, the holes are placed on a rectangular lattice, and in Sample II, they form a centered rectangular lattice. The measurement of the trapped flux density above the sample surfaces shows that the drilled samples trap a smaller magnetic flux than a sample with no hole. Sample II with the centered rectangular lattice exhibits the smallest relative drop of the maximum trapped magnetic flux, as expected from modelling results. The experiment demonstrates that the hole arrangement is a key parameter for optimizing the trapped magnetic flux density in drilled samples.

4

A novel experimental technique for characterizing the penetration of the magnetic field in drilled samples

The magnetic characterization of bulk (RE)BCO samples is essential for the prediction of their behaviour and efficiency when used in specific devices, such as those introduced in Chapter 1[1]. Magnetic characterization methods for bulk superconducting samples can be divided in two categories: (i) *volume measurements*, i.e. probing a magnetic response that is averaged over the volume of the sample, or (ii) *surface measurements*, i.e. measuring the distribution of the magnetic field at the surface of the sample. The first category of methods includes DC magnetization measurements [178, 179] and AC susceptometry [9, 180, 181, 182]. The second category involves measuring the distribution of the magnetic field above the surface of the material, either by scanning a miniature Hall sensor over the sample surface [183, 184], or by using an array of (fixed) Hall sensors [185]. In these experiments, the samples are either subjected to a uniform applied magnetic field, for flux penetration characterization, or permanently magnetized, for trapped flux measurements. Variants also consist in using a small permanent magnet that magnetizes the sample locally during the scanning process (the so-called *magnetoscan* technique [186, 187, 188]), or scanning the surface with a miniature coil system generating an AC magnetic field and detecting the local inductive response [189]. The magnetic signal obtained in *surface measurements* can be then used to estimate physical quantities of practical interest, e.g. the critical current density [178, 179, 190, 191] or the levitation forces [192]. Since melt-processed materials may also contain numerous defects that impede the current flow (cracks, subgrain boundaries, oxygen deficient regions, . . .), the measurements are also of prime importance to assess the sample homogeneity, to locate cracks or multiple superconducting grains and their deleterious influence on the material performances [186, 192, 193].

---

[1]Part of the materials presented in this chapter are published in G P Lousberg *et al*, *Supercond. Sci. Technol., 22, 125026* (2009) [176], and in G P Lousberg *et al*, *Supercond. Sci. Technol., 22, 045009* (2009) [177].

The drilled structures offer an alternative method for characterizing the magnetic properties of bulk HTS that is based on a local probing of the magnetic flux variations with coils inserted *inside* the holes. The method combines the advantages of the *volume* and *surface* measurements. In particular, it allows one to gather pieces of information on the local penetration in the bulk of the sample, which are not available with classical techniques.

In order to use this novel experimental technique, magnetic flux variations have to be induced in the samples. An efficient way of producing a time-varying magnetic field surrounding the sample is to deliver an AC current through a copper coil. The resulting AC magnetic field has a single frequency component, and the induced voltage in the microcoil can be measured accurately with a lock-in amplifier [194, 195]. The microcoil technique combined with an AC field may potentially be very effective in assessing both the extrinsic superconducting properties of the sample and the effects of the microstructure of the material, for instance by studying the diffusion of a low-frequency AC magnetic-field.

However, the novel method is not restricted to AC excitations, it may also be used with pulsed magnetic fields for instance, in view of characterizing the penetration of the magnetic pulse in the bulk of the sample. This topic is nowadays of prime importance, mainly because the pulsed-field activation appears to be the most efficient method for an *in situ* magnetization of bulk trapped field magnets. However, because of the fast motion of vortices it induces, this activation method involves intricate mechanisms for flux diffusion. In order to better grasp the flux motion and optimize the resulting trapped flux, many experiments aim at characterizing the pulse diffusion in the sample via *surface measurements*. They involve either (i) the acquisition of the waveform $B(t)$ during the pulse with Hall probes glued on the surface of the sample [196, 197, 198], or (ii) a Hall probe mapping realized after the application of the pulse [198, 199, 200]. However, none of these methods is able to provide direct information on the flux penetration and/or trapping in the bulk of the superconductor.

Interpreting the results from a pulsed field experiment is still a delicate task that must be handled with care. It is important to clearly distinguish the particular effects associated with the pulsed-field activation, e.g. the flux jumps or the temperature rise, from the peculiarities inherent to the experimental technique, e.g. calibration issue or microcoil positioning in the present case. The results obtained with AC fields help us to better understand these effects related to the experimental method.

The purpose of this chapter is two-fold: (1) describe the microcoil technique and discuss the details of its implementation and (2) present the results of the measurements of the magnetic field threading the holes of a drilled sample subjected to either an AC magnetic field or a pulsed magnetic field. Two drilled samples are used for the experiments. The results are correlated with DC Hall probe scans on the surfaces of the samples.

4.1   Description of the method

The magnetic field in drilled melt-textured samples is probed inside the holes with the help of microcoils, made of a single layer of 10 turns of fine insulated copper wire ($\phi = 50$ μm) tightly wound on an insulating Teflon cylinder with a diameter of 0.5 mm. An example of a single microcoil is shown
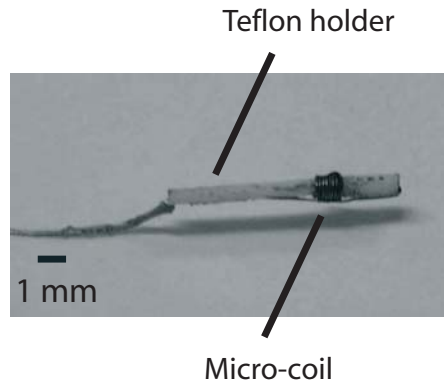
Figure 4.1: *One of the microcoil inserted in the holes of the drilled YBCO sample. The coil consists of 10 turns of insulated copper wire with a diameter of 50 µm. The wire is wound on an insulating cylinder whose diameter is 0.5 mm.*

in Figure 4.1. Since the electromotive force (emf) appearing across each coil probes the magnetic flux variations averaged over the coil volume, we use a number of turns (10) that is small enough to ensure a good spatial resolution, while yielding a measurable signal. The microcoils are either positioned symmetrically with respect to the median plane of the sample (centre coil), or placed at less than 1 mm from the top or bottom surfaces of the sample (surface coil). In order to reduce the number of insertion steps of the microcoils inside the holes, both surface and centre coils may be wound on the same Teflon holder.

The wires connecting the microcoils to the measuring devices are finely twisted together in order to reduce a spurious inductive pick-up. The emf of the microcoils is measured either:

(1) by both (i) a SR560 low-noise preamplifier followed by a TDS 2012B digitizing oscilloscope in order to record its waveform and (ii) a Perkin Elmer 7260 lock-in amplifier in order to characterize its fundamental harmonic. The latter technique can only be used with AC magnetic field. The lock-in amplifier requires a stable reference signal. In commercial systems as well as those reported in the literature [178, 201, 202], it is a common practice to take as a reference the voltage drop across a precision resistor placed in series with the magnet coil. In the present case, however, this procedure cannot be used because the low-value resistor ($< 1\ \Omega$) required to sustain the high AC currents would exhibit a small (but finite) reactance, giving rise to a parasitic phase-lag. In our experiment, the reference signal is the emf across a reference coil whose position is discussed later; this emf is phase shifted by exactly 90° with the applied AC magnetic field.

(2) by a data acquisition card (National Instruments CompactDAQ - NI9215) working at a high sampling rate (100 kHz). The low level of the induced emf's imposes us to use instrumentation amplifiers (INA 128 - gain of 10 000 and bandwidth of 10kHz) in front of the acquisition card. Such a system is able to record simultaneously the signal coming from 16 different microcoils, while the first technique allows us to only measure a single microcoil at a time. This automatic acquisition procedure can be used either with AC magnetic fields or with pulsed fields.
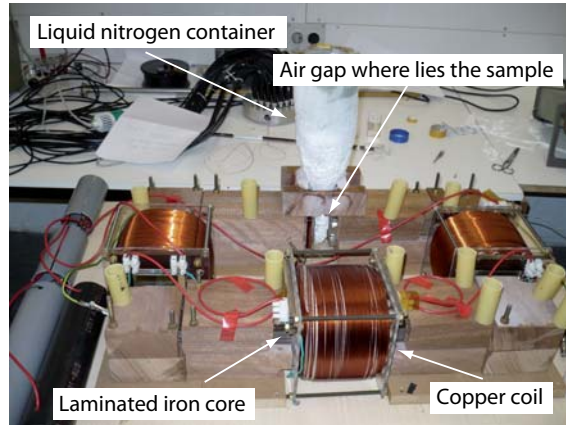
Figure 4.2: *Photograph of the AC electromagnet used for the measurement of the magnetic field inside the holes of a drilled sample subjected to an AC magnetic field whose amplitude reaches up to 130 mT.*

Whatever is the type of excitation, the sample is immersed in liquid nitrogen ($T = 77$ K) and the cooling procedure is always performed in zero field. Once cooled, the sample is subjected to a uniform AC or pulsed magnetic field, applied parallel to its c-axis (i.e. parallel to the axis of the holes). The inductive emf appearing across each microcoil is recorded to determine the magnetic flux density threading the corresponding hole.

4.1.1   Setup for the measurements with AC magnetic fields

In order to record a measurable electromotive force in most holes, the amplitude of the AC magnetic fields must be sufficiently large, so as to penetrate at least the peripheral holes of the sample. To this aim, we build a specifically designed experimental set-up with which we can generate AC magnetic fields with an amplitude larger than 100 mT. Several home-made systems use an air coil for generating AC fields with an amplitude up to 100 mT [203, 204, 205, 206, 207]. In our experiment, we use an iron-core electromagnet in order to generate magnetic fields with an amplitude larger than 100 mT. Three 1000-turns coils are wound around a 'C-shape' laminated core, consisting of a stack of Si-doped thin iron sheets (0.3 mm thickness) which are isolated from one another in order to reduce eddy currents [208]. The core has a cross section of 7 cm × 8 cm. The sample holder is inserted in a pyrex cryogenic vessel placed in the air gap of the electromagnet (width of 2.4 cm). The large size of the core cross section guarantees an excellent homogeneity of the applied magnetic field over the sample volume. In our system, the field inhomogeneity over the volume of the sample was measured to be less than 1 %. A picture of the electromagnet is shown in Figure 4.2. A 50-turn coil that is used as reference for the lock-in amplifier is wound around the iron core.

The windings are realized on a Plexiglas structure with a varnish insulated cooper wire having a diameter of 1.8 mm. Capacitors are placed in series with the coils in order to compensate their inductance (the
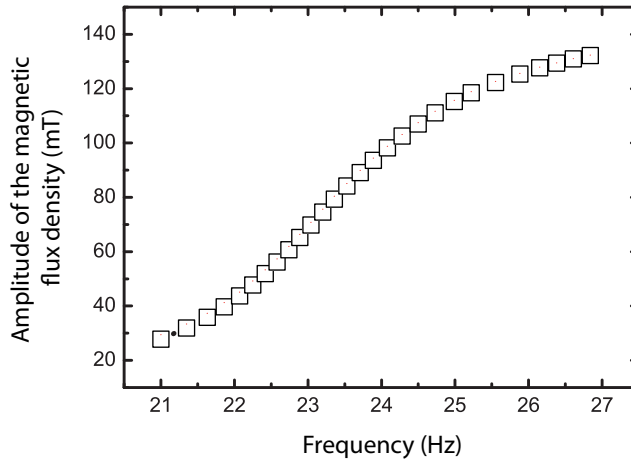
Figure 4.3: *Magnetic flux density (RMS value) measured by a Hall probe located in the air gap of the electromagnet with no HTS sample as a function of the frequency of the input signal.*

inductance of the electromagnet is measured to be $L \sim 5$ H). The AC current is delivered to the coils via a 3200W audio amplifier (Crown XTI 2000). A voltage source (HP 33120A) provides a low frequency signal with a constant amplitude of $2\, V - RMS$[2]. The audio amplifier rises up that voltage to ~ 80V. Due to the non-linearity of the RLC circuit, preliminary tests have shown that, instead of varying the amplitude of the applied field, tuning the frequency is recommended in order to guarantee a smooth control of the amplitude of the applied field. In fact, the variation of the frequency modifies the impedance of the RLC circuit and, hence, the current flowing in the coils. A variation of frequency from 21 Hz to 27 Hz induces a variation of the magnetic flux density in the air gap ranging from 30 mT to 130 mT, as measured by a Hall probe placed in the air gap in the absence of the sample. The measured flux density is reproduced in Figure 4.3.

Prior to every measurement sequence, a calibration procedure of the microcoils is performed at room temperature: the microcoils are positioned in the holes, the sample is placed in the cryogenic vessel inside the air gap of the electromagnet, and is subjected to a known magnetic field (RMS value B, frequency f) while keeping the sample in the non-superconducting state. The RMS value of the emf of the coil (N turns), $V = 2\pi N f B A$, is recorded to determine the effective cross section A of each microcoil. The effective cross section is found to match the geometric cross section of the Teflon holder within 80 %. The difference can be attributed to the finite diameter of the wire and to a slight tilting of the winding with respect to the applied field. The effective cross section determined from the calibration procedure is then used to convert the measured emf at 77 K into a magnetic flux density.

4.1.2   Setup for the measurements with pulsed magnetic fields

The measurements involving pulsed fields are carried out at the high magnetic field facilities of the "Laboratoire National des Champs Magnétiques Intenses" (LNCMI) on the Toulouse site (France).

---

[2]Except when explicitly stated, the AC quantities are expressed in RMS values.
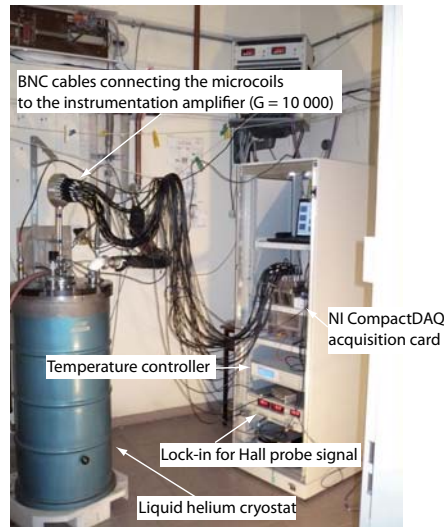
Figure 4.4: *Photograph of the experimental chamber used for pulsed field experiments. Indicated on this picture are: the liquid helium cryostat containing the sample, the 32 BNC cables connecting the microcoils to the instrumentation amplifier, the NI CompactDAQ acquisition card, the temperature controller and the lock-in amplifier for measuring the Hall probe signal.*

A picture of the experimental chamber is shown in Figure 4.4. Pulsed fields with an amplitude of 3 T, a rising time of 60 ms, and a duration of 370 ms were applied to the sample, initially cooled down to 77 K in the absence of magnetic field.

The pulse of magnetic field is generated by a fast discharge current flowing through a copper coil placed in the liquid helium cryostat. The current is produced by the discharge of a bench of capacitors (470 mF) initially loaded at 1 kV. The shape of the magnetic pulse is determined with a Hall sensor (Arepoc LHP-MU) placed in the experimental chamber inside the cryostat in the absence of the sample. The pulse is represented in Figure 4.5-(a). It starts with a sharp increase of the magnetic flux density B, at a rate of $dB/dt \sim 100$ T/s. The magnetic field then reaches a maximum after 60 ms, decays, and vanishes at $t^* = 370$ ms when the electric circuit is open.

The sample is inserted in the cryostat with the help of a glass fiber rod terminated by a sample holder (also in glass fiber). The temperature of the sample (77 K) is monitored by a LakeShore 340 temperature controller.

16 microcoil holders are inserted at the same time in the holes belonging to a quarter of a drilled sample, as represented in Figure 4.5-(b). Each holder contains two microcoils consisting each of 10 turns of 50 μm of isolated copper wire, yielding a coil height of 1 mm. For each hole, one coil is placed in the median plane of the sample — the centre coil — ; the other coil is put close to the sample surface — the surface coil —[3].

---

[3]During the measurement campaign, we had not been able to change the position of the microcoils. After the first series of pulses during which the position of the microcoils remained unchanged, the sample holder pulled away from the rod and all the twisted wires connecting the coils to the head of the rod were broken. It was then impossible to repair the setup before the end of the allocated time slot for our measurements. Note however that measurements with an
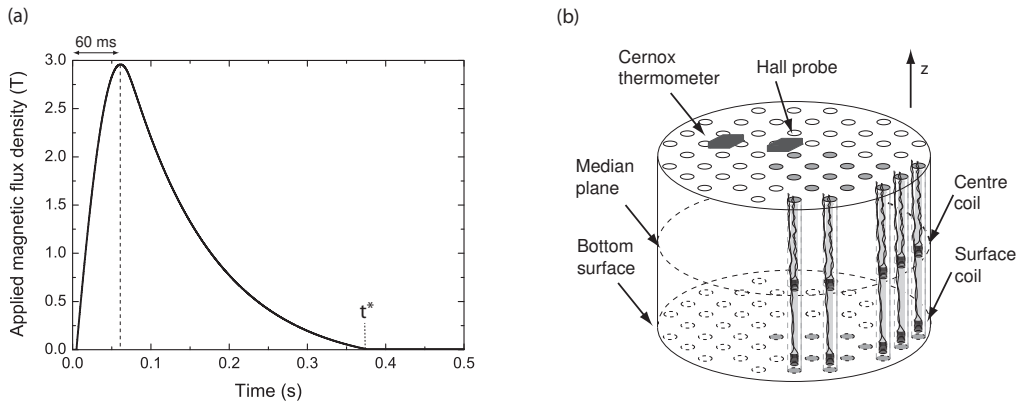
Figure 4.5: *(a)- Applied magnetic pulse, as measured by a Hall probe in the cryostat containing no HTS sample. (b)- Schematic illustration of the drilled sample considered for the experiments involving a pulsed-field. The 16 holes (grey) where the magnetic flux density is measured are highlighted. The coil holders, containing each two microcoils (a centre coil and a surface coil), are also represented in five peripheral holes.*

In order to measure the pulse of applied magnetic field, a coil with 100 turns of 150 μm diameter wire is placed on the main rod at 1 cm above the sample holder, where the magnetic influence of the sample can be neglected. A temperature sensor (Cernox probe) and a Hall probe (Arepoc LHP-MU) are also placed against the sample surface (as in Figure 4.5-(b)). These three additional signals are acquired simultaneously with the microcoil signals at 100 kHz. The Hall probe signal is measured using a lock-in amplifier in order to increase the sensitivity. The reference signal is delivered by the lock-in and serves as the current input for the Hall probe.

The microcoils and the reference coil are calibrated by applying a magnetic pulse with the sample in its normal state ($T = 100$ K). The coil pick-up signals are then acquired simultaneously with the Hall probe signal during the application of the pulse; the Hall probe is used as a reference for the calibration.

4.2 Drilled bulk superconducting samples used for the experiments

Two drilled samples are considered in this chapter. The first sample, sample A, is only characterized in the case of an AC magnetic field excitation. The second sample, sample B, is used both with AC and pulsed magnetic field excitations.

AC magnetic field excitation performed on the same drilled sample showed that this particular quarter of the sample is representative of the full sample.

1 cm

Figure 4.6: *Photograph of the YBCO drilled Sample A. The white line delimits the quarter of the sample under consideration in this chapter.*

4.2.1   Sample A

Sample A consists of a $YBa_2Cu_3O_{7-\delta}$ drilled cylinder containing 68 artificially patterned holes. It was produced at CRISMAT (Caen, France) by the top-seeded melt-textured growth process from a drilled preform. The details of the sample preparation can be foun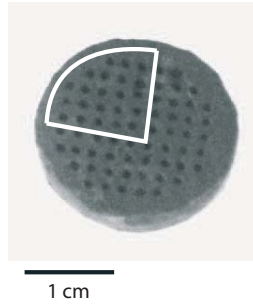d in Ref. [9]. The sample has a diameter of 20 mm and a height of 8 mm. The holes are parallel to the c-axis and are arranged on a regular square pattern; the macroscopic holes have a diameter of 0.7 mm and are separated by a distance of ~ 1.5 mm. A picture of Sample A is shown in Figure 4.6. The critical current density of the YBCO material is $J_c \approx 1000$ A/cm^2 at $T = 77$ K and $B = 100$ mT. In order to reduce the number of thermal cycles, we have only analyzed the field in the holes belonging to the quarter of the sample delimited by the white lines.

The magnetic properties of the sample are characterized first with Hall probe scans over both surfaces, with the method described in Section 3.5.2. In view of comparing the Hall probe mapping with measurements of the AC magnetic field inside the holes, we measure the penetration of the DC magnetic field (100 mT) applied after a zero-field cooled process (down to 77 K) and kept constant during the Hall probe mapping experiment.

The distributions of the c-axis component of the DC magnetic flux density at the top (a) and the bottom (b) surfaces of the sample are represented in Figure 4.7-(a,b). The dark areas correspond to low magnetic flux densities while the bright areas are related to a high magnetic flux. Although we have measured the distributions of the magnetic flux density at the whole top and bottom surfaces, we only show it above the quarter of the sample where we have performed the measurements of the magnetic flux inside the holes.

First it can be observed that the Hall probe mapping does not resolve spatially the positions of the holes. Their positions are superimposed on the mappings for clarity. Second, noticeable differences appear between the bottom and the top surfaces. Not only the values of the magnetic flux density differ in magnitude (as commonly observed with top-seeded melt-grown YBCO, see e.g. Ref [184]), but also the distribution of the magnetic flux density varies between the top and bottom surfaces. In particular, one can distinguish, at the top surface, a $\supset$-shaped shielded area with low magnetic flux density, whereas the low-field area at the bottom surface exhibits a more regular (circular) shape.
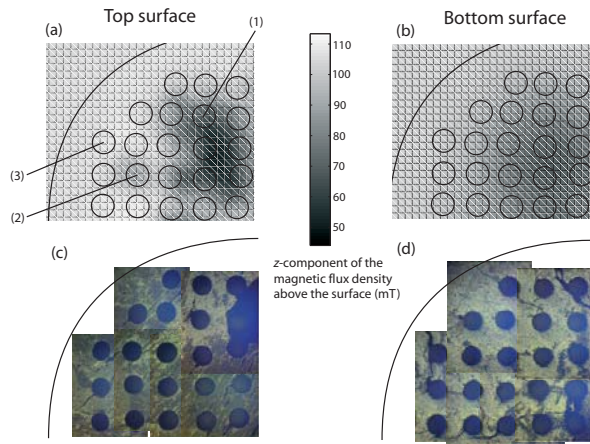
Figure 4.7: *(a,b)- DC magnetic flux density distribution measured in a Hall probe mapping experiment at 0.2 mm above the top (a) and bottom (b) surface of the quarter of the sample under consideration. The sample is subjected to a DC uniform magnetic flux density of 100 mT during the measurement. A grid showing the position of the holes is superimposed. (c,d)- Picture of the top (c) and bottom (d) surface of the quarter of sample acquired with a micrograph taken under polarized light.*

The distribution of the magnetic field at both surfaces is different from what would be expected in a sample without defects [133]. The peculiar distribution observed at both surfaces most likely arises from cracks, defects or disoriented grains [193, 209]. In order to further characterize the sample, we have performed optical polarized light micrographs that are reproduced in Figure 4.7-(c,d) for the quarter of the top (c) and bottom (d) surfaces. These micrographs do not underline the presence of multiple superconducting grains with different orientations, but indicate the presence of cracks on the bottom surface (especially at the top right corner and at the bottom of the picture). However, the micrographs do not clearly point to either cracks or multiple superconducting grains that could explain the observed distribution of the magnetic flux density. Moreover, it is impossible to know from such surface characterization techniques (Hall probe mapping and microscopy) whether these inhomogeneities extend or not inside the bulk of the sample. The signals from coils placed inside the holes, as reported in the next sections, can then be used to gain further information on the presence of invisible inhomogeneities in the sample.

4.2.2 Sample B

Sample B is a top-seeded melt-grown single domain of $YBa_2Cu_3O_{7-\delta}$, synthesized at CRETA (Grenoble-France). The sample is a cylinder with a diameter of 16 mm and a thickness of 10 mm. It contains 55 holes that have been drilled before the synthesis of the sample. The diameter of the holes in the sample after the synthesis is 0.8 mm. A picture of Sample B is shown in Figure 4.8-(a).

The magnetic properties of the sample are first investigated after a field-cooled magnetization at 77 K in a magnetic flux density of 2 T provided by a superconducting coil. Once permanently magnetized,
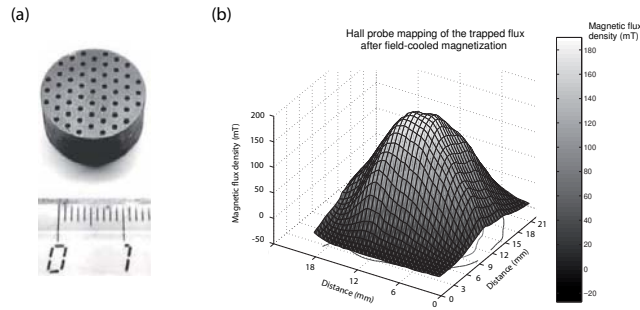
Figure 4.8: *(a)- Picture of Sample B. (b)- Hall probe mapping of the trapped magnetic flux density above the top surface of the drilled sample. The mapping is carried out 20 min after a field-cooling process at 77 K in a uniform magnetic flux density of 2 T.*

a two-dimensional mapping of the trapped magnetic flux density is performed about 20 minutes after magnetization so as to reduce the effects of magnetic relaxation. The distribution of the trapped magnetic flux density, B, as measured above the surface, is shown in Figure 4.8-(b). The axisymmetric trapped flux profile exhibits a single maximum, $B_{max} = 190$ mT, and does not indicate the presence of macrocracks on the sample surface, unlike in sample A. Because of the distance between the probe and the sample surface, the flux distribution is smooth and the holes cannot be identified in the flux profile. The distribution observed in Figure 4.8-(b) is similar to distributions observed previously in other drilled samples [61, 76, 85].

4.3   Application to the characterization of the penetration of an AC magnetic field

4.3.1   *Bean model analysis of the magnetic flux in the holes of a sample of infinite height*

As an introduction to the measurements of the AC magnetic field inside the holes of a drilled sample, we consider a very simple model to predict the types of signal expected across the microcoils. To this aim, we calculate the magnetic field in the holes of a HTS drilled cylinder with an infinite length and uniform superconducting properties. The calculations are carried out with the help of the numerical Bean model. One could have also used the finite-element method in order to refine that simple model by taking into account flux creep and demagnetizing effects. However, the numerical Bean model applied to a sample of infinite height allows us to already set up the problem of the penetration of an AC magnetic field in the holes of a drilled sample, from which qualitative conclusions may be drawn. Besides, FEM requires very long calculation times in order to simulate a complete cycle of the applied field.

We consider thus an infinitely extended cylinder drilled by a single hole. The cylinder has a radius a, the hole has a radius $R = 0.05\ a$ and its centre is located at a distance d from the border of the cylinder (see Figure 4.9-(a)) . We assume that the critical current density, J_c, has a constant amplitude in the sample cross section. The drilled cylinder is subjected to a uniform AC applied magnetic field parallel

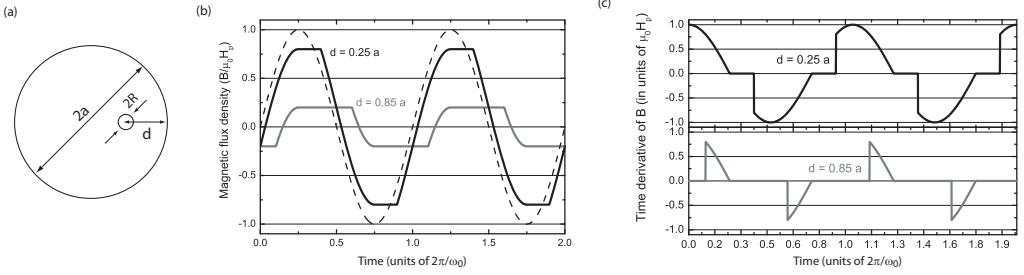**Figure 4.9**: *(a)- Cross section of a cylinder (radius a) with an infinite height and a single hole (radius R) whose centre is located at a distance d from the border. (b)- Magnetic flux density as a function of time inside a hole located at d =0.25 a (black line) and at d =0.85 a (grey line) in a sample containing a single hole. The applied magnetic flux density of amplitude B_a is represented by a dotted line. The magnetic flux density is calculated in units of $\mu_0 H_p$. The calculations are performed with the numerical Bean model. (c)- Time derivative of the magnetic flux density inside the hole located at d =0.25 a (black line) and at d =0.85 a (grey line).*

to its axis, $B_a(t)$, with a pulsation ω_0.

The critical state of the drilled cylinder with an infinitely long extension is calculated numerically with the numerical Bean model, as described in Chapter 2. In Figure 4.9-(b), we reproduce the time evolution of the magnetic flux density inside the hole located at two different positions $d = 0.25\ a$ (black line) and $d = 0.85\ a$ (grey line). The applied magnetic flux density is represented by the dotted line. It has an amplitude $B_a = \mu_0 H_p$, where H_p is the full penetration field of the plain sample, $H_p = \mu_0 J_c a$. The corresponding time derivative of the magnetic flux density are reproduced in Figure 4.9-(c).

The magnetic flux density in the hole exhibits a clipped sinus shape, that saturates at $B = B_{\text{clipped}}$. Note that if the amplitude of the applied magnetic flux density is too small for penetrating the hole, the magnetic flux density inside the hole remains null.

The clipping plateau arises from the bulk pinning in the HTS sample. The high (resp. low) clipping plateau starts when the applied magnetic field is at its maximum (resp. minimum) value. The constant magnetic flux density on the clipping plateau is given by

$$B_{\text{clipped}} = B_a - \mu_0 J_c (d - R). \qquad (4.1)$$

When the applied magnetic field starts to decrease (resp. increase), the magnetic flux in the sample is first modified in a shell surrounding the external boundary, while the magnetic flux crossing the rest of the sample is conserved over time. The modification front then gradually penetrates toward the sample centre as the applied field continues to decrease (resp. increase). Thus, the magnetic flux density remains constant in a given hole until the perturbation front reaches this hole, *i.e.* when the applied magnetic flux density is such that $|B_a - B(t)| = 2\mu_0 J_c (d - R)$. The magnetic field in the holes then decreases (resp. increases) with the applied field until the applied field reaches its next extremum.
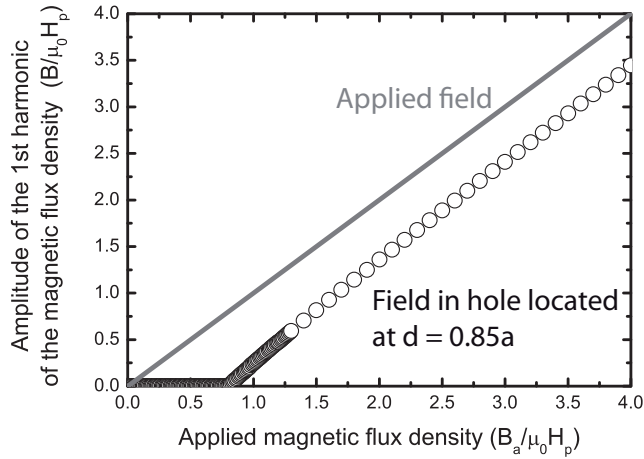
Figure 4.10: *Amplitude of the first harmonic of the magnetic field inside a hole located at a distance d =0.85 a from the border, as a function of the amplitude of the applied field. The calculations are based on the numerical Bean model.*

The amplitude of the clipping plateau corresponds to the DC magnetic flux density that would be measured inside the hole if the sample were subjected to a DC magnetic flux density with an amplitude B_a. For a given amplitude of the applied magnetic flux density, the width and the height of the clipping plateau in a hole only depends on the distance of the hole from the border, d. In a sample containing several holes, the magnetic flux density inside a given hole exhibits the same shape as in Figure 4.9, provided the amplitude of the applied magnetic flux density is such that the hole is penetrated. However, in samples containing several holes, the height and the width of the clipping plateau are no longer related to only the distance d. The clipping plateau is given by $B_{clipped} = B_a - \mu_0 J_c \ell$ where ℓ stands for the total penetration distance for reaching the hole, taking into account the presence of the other holes.

The time derivatives of the magnetic flux density (represented in Figure 4.9-(c)) contain a succession of peaks that are separated by steps of zero amplitude corresponding to the clipping plateau in Figure 4.9-(b).

From the time-derivative of the magnetic flux density in the hole located at a distance $d = 0.85\ a$ from the border, we can calculate the amplitude of the first harmonic of the signal, as measured by the lock-in amplifier. Figure 4.10 reproduces that amplitude as a function of the amplitude of the applied field. We clearly observe that the hole is not penetrated when $B_a < 0.8\ \mu_0 H_p$. For $B_a > 0.8\ \mu_0 H_p$, the amplitude of the first harmonic increases with that of the applied field, with an initial slope larger than 1 and tends asymptotically to $B = B_a$ with a unit slope. Note that the amplitude of the first harmonic of the magnetic field in the hole never exceeds the applied field.

4.3.2 Measurements in Sample A

Now that the AC magnetic field penetration in a drilled sample has been introduced with the help of a simple model, we discuss the results of the microcoil measurements. We start with Sample A.

Time evolution of the emf across the microcoils

The time evolution of the induced emf inside the holes of Sample A is recorded by the digitizing oscilloscope. Figures 4.11 shows the time evolution of the inductive emf, together with the resulting magnetic flux densities, as measured by three microcoils inserted inside hole (1), (2), and (3), of Figure 4.7-(a). These holes are located in a low, intermediate, and high magnetic flux region, respectively. The microcoils are centered in their corresponding hole. The applied magnetic flux density is 120 mT and has a frequency of 24.73 Hz. The upper halves of Figures 4.11 (a), (b) and (c) show the time evolution of the inductive emf (V_1, V_2, V_3 - solid line) in holes (1), (2) and (3). For the sake of clarity, the inductive emf's are shown after amplification by the low-noise preamplifier, the gain being indicated in parentheses. The reference emf (V_{ref} - dashed lines) corresponds to the inductive emf across the 50-turn coil wound around the iron core.

Three different waveforms can be distinguished in the holes (1), (2), and (3), respectively.

1. In hole (1) located in a low field region, the inductive emf across the microcoil is a sine wave.
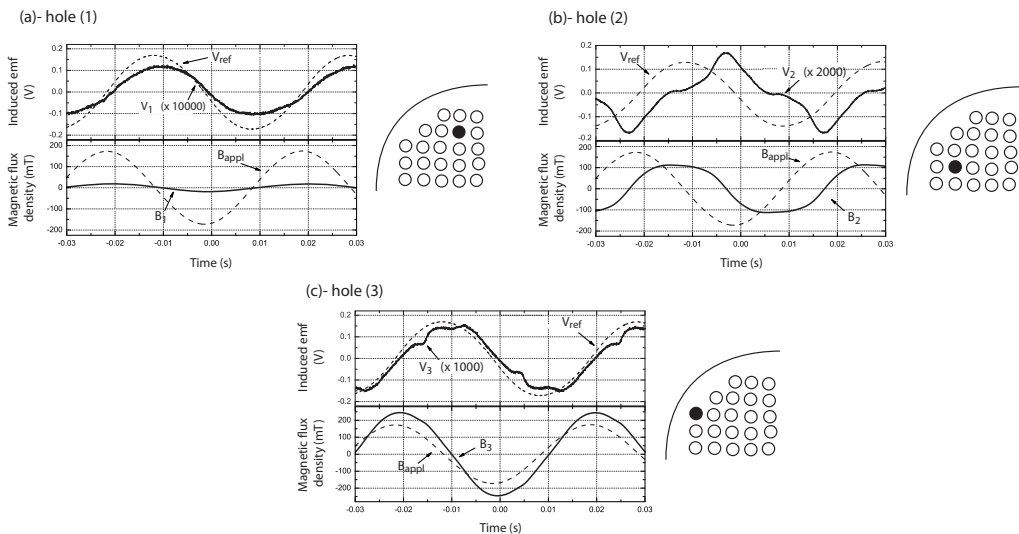
Figure 4.11: *(i) Top half of each graph: emf (V_1, V_2, and V_3 - solid line) vs. time as measured with a microcoil inserted (in the central position) inside hole (1) , (2) and (3), respectively (see Figure 4.7-(a)). The reference emf (dashed line) is at 90° with respect to the sinusoidal applied field (120 mT at 24.73 Hz). (ii) Bottom half of each graph: magnetic flux density vs. time as obtained by a numerical integration of the inductive emf inside the holes (B_1, B_2 and B_3 - solid line). The applied magnetic flux density is shown with a dashed line.*

There is a negligible phase-shift of V_1 with respect to the reference signal V_{ref}. The emf in this case is to be attributed to parasitic emf's produced by the applied field that cross closed loops of wires connecting the coil and have a larger amplitude than the signal from the microcoil itself.

2. In hole (2) located in a region of fields with an intermediate amplitude, the inductive emf is strongly distorted, and exhibits a succession of positive and negative peaks, reminiscent of those observed with a pick-up coil inserted inside a HTS tube made of polycrystalline Bi-2223 subjected to an axial AC magnetic field [210].

3. The inductive emf produced by the microcoil inserted inside hole (3), located in a region of high field, exhibits a weakly distorted sine shape with almost no phase-shift with respect to the reference emf.

Let us now focus on the magnetic flux density inside the hole. The flux densities are determined by a numerical integration of the inductive emf's shown in the top panels of Figure 4.11. In practice, the pick-up voltage is biased by an unavoidable parasitic DC offset arising from the output of the preamplifier. The offset can be considered as remaining constant during the acquisition time. It is evaluated as the average value of the induced emf on an integer numbers of periods. The offset is then subtracted from the raw data.

The bottom panels of Figures 4.11 show the time evolution of the magnetic flux density (B_1, B_2, B_3 - black line) crossing the median section of the hole. The applied magnetic flux density (B_{appl} - dashed line) is also shown for comparison.

One can clearly distinguish three different time dependences which are correlated to the respective emf waveforms measured inside holes (1), (2), and (3).

1. In hole (1), the magnetic flux density is a sine wave whose amplitude is much smaller than the applied one (by a factor of ≈ 10).

2. The magnetic flux density corresponding to the strongly distorted emf in hole (2) is a clipped sine wave that lags behind the applied field. Such characteristics are the consequence of strong pinning in the sample which leads to a hysteresis between the applied field and the local induction in the hole. Such a behaviour is qualitatively consistent with the Bean model description in Section 4.3.1.

3. In hole (3), the magnetic flux density is almost sinusoidal and has a larger amplitude than the applied magnetic flux density (by a factor of ≈ 1.5).

It is emphasized that the signals measured in the other holes, although not discussed in this section, are similar to those presented in Figure 4.11.

Classification of three different penetration regimes

We now analyze the magnetic flux density inside holes (1), (2) and (3) (as indicated in Figure 4.11) as a function of the applied magnetic flux density. The applied magnetic flux density varies from 30 to 130 mT. The microcoil is placed in each case as carefully as possible in a central position.
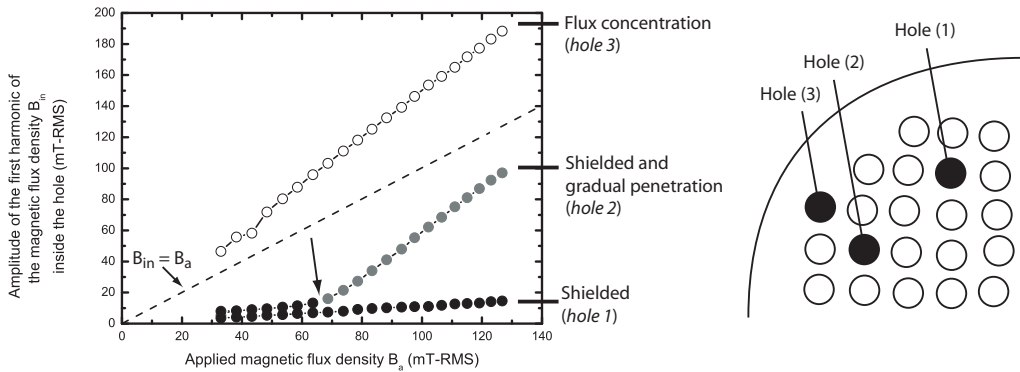
Figure 4.12: *Amplitude of the fundamental harmonic of the magnetic flux density inside hole (1), (2), and (3) (their position in the sample is reminded in the right panel) as a function of the applied magnetic flux density varying from 30 to 130 mT. The arrow shows the transition between the shielded regime and the gradual penetration regime.*

Figure 4.12 shows the amplitude of the fundamental harmonic of the magnetic flux density inside the holes (symbols + solid lines), as a function of the applied magnetic flux density (dashed lines), as measured by the lock-in amplifier. Quite similarly to the waveform pattern, we can distinguish three different behaviours (that are further referred to as "penetration regimes"), as a function of the hole location in the sample:

1. *the shielded regime*, for which the magnetic flux inside the hole is negligible with respect to the applied one (attenuated by a factor of ≈ 10). The magnetic flux increases almost linearly with the applied field. Hole (1) is in this regime over the range of applied fields, while hole (2) is in the shielded regime for the lower fields (black circles). The waveform of the emf in this regime is similar to what is observed in Figure 4.11-(a).

2. *the gradual penetration regime*: the hole is penetrated by the magnetic flux, with a density that is smaller than the applied one and that is not so strongly attenuated than in the shielded regime. The magnetic flux density in the hole increases almost linearly with the applied one but with a large slope (≈ 1.5 mT/mT; the slope is ≈ 10 times larger than in the shielded regime). The observable kink (see arrow in Figure 4.12) due to the change of slope in hole (2) defines the transition from the shielded regime to the gradual penetration one (grey circles).

3. *the flux concentration regime*: the hole is also penetrated by the magnetic flux, but now with a density that significantly exceeds the applied one (≈ 1.5 times larger). There is thus a flux concentration in the hole, as shown in hole (3) (white circles).

In the other holes, the behaviour of the fundamental component of the magnetic flux density as a function of the applied field was found consistent with the regimes described above.

Distribution of the penetration regimes of the holes

Based on the observations presented in the above paragraphs, we now determine the penetration regimes of the holes located in the quarter of sample under consideration (see Figure 4.6) at a given applied field. An interesting question is to determine how the distribution of the penetration regimes is modified when the coil is placed in the median plane of the sample and close to the top and bottom surfaces.

The distribution of the penetration regimes is shown in Figure 4.13 for an applied magnetic flux density of 100 mT. The microcoils are located close to the top surface in Figure 4.13-(a), in the centre position in Figure 4.13-(b), and close to the bottom position in Figure 4.13-(c). The black holes are in the shielded regime, the grey holes in the gradual penetration regime, and the white holes in the flux concentration regime.

Independent of the vertical position of the coil inside the hole, it is observed that the magnetic field
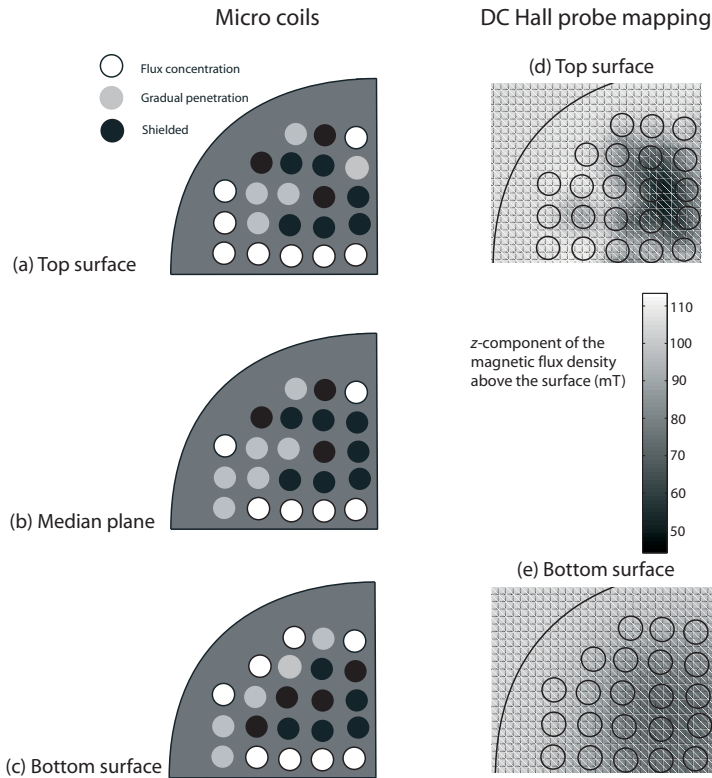
Figure 4.13: *(i)- Left panels: distribution of the penetration regimes inside the holes of the quarter of the sample for an applied magnetic field of $B_a = 100$ mT and for microcoils located close to the top surface (a), symmetrically around the median plane (b), and close to the bottom surface (c). (ii)- Right panels: distribution of the magnetic flux density at the sample surfaces (d,e) obtained with the Hall probe mappings discussed in Figure 4.7-(a,b).*

does not penetrate in the same way the holes that are located at a given radial distance from the border. The holes that are shielded at their top surface or in their centre form a ⊃-shape which is localized at the right corner of the picture. In a homogeneous sample, one would expect the shielded holes to lie in a circular region having the same centre as the sample cross section, whose radius decreases as the applied field increases, until the sample is fully penetrated. The holes outside that shielded region would be in the gradual penetration regime. In a non-homogeneous sample, as studied here, the situation is quite different.

The distribution of the penetration regimes of the holes is correlated with the distribution of the magnetic flux density at the sample surfaces, as shown on the right panels of Figure 4.13. As a reminder, the Hall probe mapping is performed under an applied 100 mT DC field. In view of a fair comparison, the distributions of the penetration regimes of the holes are measured under an AC magnetic field with the same magnitude, equal to 100 mT − RMS.

A comparison of AC and DC measurements brings out three pieces of information. First, from the Hall probe mapping, we observe that the holes in the shielded regime lie at the surface in a low magnetic flux density region. In particular, the ⊃-shape of low magnetic field at the top surface corresponds in the AC measurements to a region of shielded holes. Second, the holes in the gradual penetration regime (AC experiment) are located in regions of intermediate magnetic flux densities in the surface (DC experiment). Third, it can be observed that the smooth distribution of the penetration regimes of the holes close to the bottom surface (AC experiment) is consistent with the distribution of the magnetic flux at that surface (DC experiment).

This comparison illustrates the interest of probing the field in the bulk. The Hall probe mapping technique by itself does not bring enough information to infer the penetration pattern in the volume of the sample. Only the microcoil technique allows one to understand how the magnetic flux penetrates the bulk of the sample. For instance, Figure 4.13 shows that the field distribution in the median plane is more similar to the one observed close to the top surface than close to the bottom surface. These results are related to the detailed microstructure of the bulk of the sample.

The flux concentration regime is not observed in either of the Hall probe mappings. In these experiments, the probe, which measures the vertical component of the magnetic field, is located at a fixed distance from the surface, in a region where the magnetic field lines that are concentrated inside the hole are spreading out. The flux concentration can only be observed when the flux is probed inside the holes. Interestingly, the holes with a flux concentration (especially close to the top surface) surround more efficiently shielded regions. Combined with the fact that such a regime is not predicted in a sample of infinite height, these observations suggest that the flux concentration results from demagnetization effects associated with the microstructure of the sample. Cracks or defects represent obstacles for the current flow in the sample. These obstacles cause an irregular distribution of the magnetic flux, with an apparition of shielded regions that are not necessarily located in the centre of the sample. The return path for the demagnetizing field coming from a given shielded region crosses the neighbouring holes and the demagnetizing field increases locally the magnetic flux density inside these holes. Such demagnetizing effects are also responsible for the flux concentration inside natural or artifical grain boundaries [193, 211].

4.3.3   Measurements in Sample B

Magnetic flux density inside the holes

We now turn to the description of the magnetic flux density in the holes of Sample B. The measurements of the magnetic flux density in the holes of Sample B subjected to an AC magnetic field are carried out in the same conditions as those used for Sample A, except that the induced emf's are recorded simultaneously in 16 holes by the National Instruments acquisition card.

From these measurements, one can observe that the holes of Sample B are also penetrated according to one of the three aforementioned penetration regimes: the shielded, the gradual penetration or the flux concentration regime. In particular, when the amplitude of the applied field increases, some holes cross all these regimes. Figure 4.14 investigates such a situation.

Figure 4.14-(a) shows the amplitude of the first harmonic of the magnetic flux density measured in the median plane of a particular hole (represented in black on the sketch of the sample) as a function of the amplitude of the applied field. The emf signals (plotted with the DC offset of the output of the instrumentation amplifier) at (1) $B_a = 33$ mT, (2) $B_a = 85$ mT, and (3) $B_a = 130$ mT are reproduced in Figure 4.14-(b), together with the reference emf.
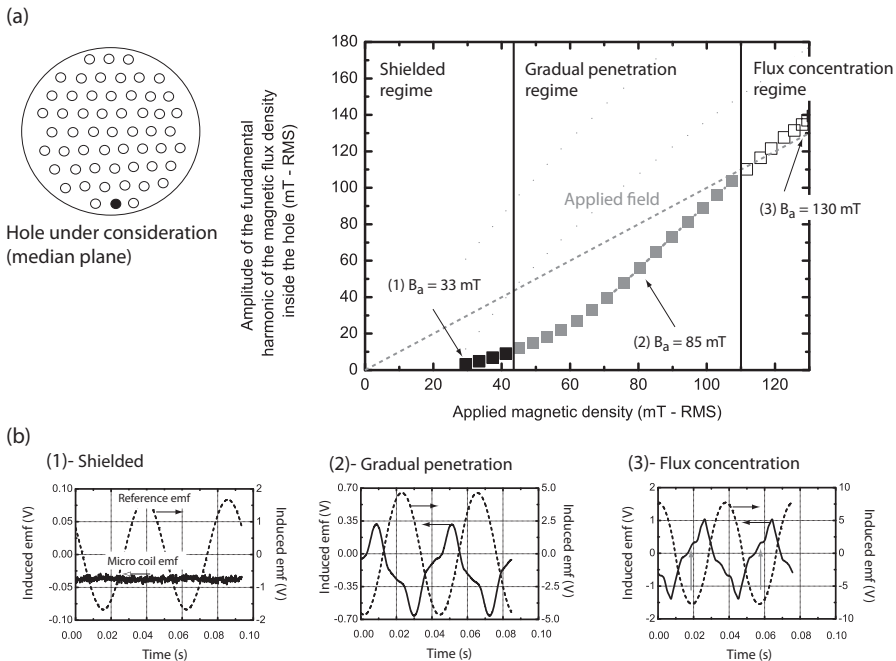
Figure 4.14: (a)- Amplitude of the first harmonic of the magnetic flux density inside the median plane of a particular hole (as represented in grey on the sketch of Sample B) as a function of the amplitude of the applied field. The three penetration regimes are highlighted. (b)- Time signal of the inductive emf measured across the microcoil, for (1) $B_a = 33$ mT, (2) $B_a = 85$ mT, and (3) $B_a = 130$ mT.

For $B_a < 45$ mT, the amplitude of the magnetic flux in the hole is much smaller than that of the applied field. The emf in the hole is noisy and almost constant. The median plane of this particular hole is not penetrated by the applied field, it is in the shielded regime. For 45 mT $< B_a < 110$ mT, the amplitude of the field in the hole increases with the applied field, while remaining smaller than B_a, and the emf time signal consists of a succession of alternating positive and negative peaks that are associated with the gradual penetration regime. The transition from the shielded to the gradual penetration regime (when $B_a = 45$ mT) is not clearly defined when only examining the B_{in}-vs-B_a curve. In that situation, we recommend to combine the curve analysis to the emf time signal, this latter one must exhibit a succession of peaks as soon as the holes enter the gradual penetration regime.

For $B_a > 110$ mT, the amplitude of the magnetic flux density in the hole exceeds that of the applied field, which is the main feature of the flux concentration regime. The emf time signal is still composed of a succession of main peaks that are separated by intermediate peaks with a smaller amplitude (preceding the main peak, as indicated by the grey arrows).

Distribution of the penetration regimes

The distribution of the penetration regimes in the median plane and in the top and bottom surfaces of the holes of Sample B is reproduced in Figure 4.15-(a), for an amplitude of the applied magnetic flux density of $B_a = 33$ mT, $B_a = 85$ mT, and $B_a = 130$ mT. Figure 4.15-(b) reproduces the Hall probe mapping above the top and bottom surfaces of Sample B subjected to a magnetic flux density that remains fixed at $B_a = 100$ mT during the experiment.

Figure 4.15: *(a)- Penetration regimes in the median plane and on the top and bottom surfaces of the holes when $B_a = 33$ mT, $B_a = 85$ mT, and $B_a = 130$ mT. (b)- Hall probe mappings above the top and bottom surfaces of Sample B subjected to a DC magnetic flux density of 100 mT.*

At a given applied field, the distribution of the penetration regimes is almost radial. The holes located close to the sample centre are shielded while the periphe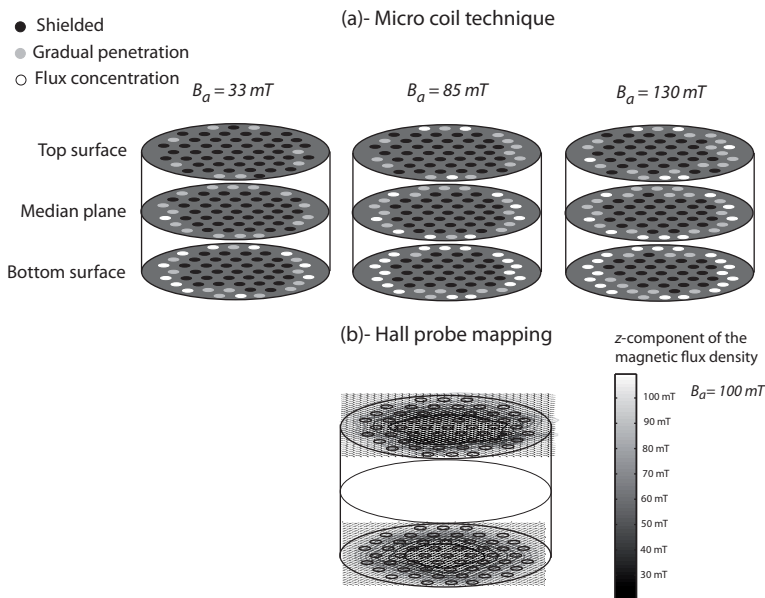ral holes are either in a gradual penetration or in a flux concentration regime. That situation differs from what is observed in Sample A, where the holes close to the sample centre are not necessarily shielded. Sample B, as already observed with Hall probe mapping, exhibits more uniform superconducting properties than Sample A where macrocracks are observed on the surfaces. The microcoil technique reveals that the uniformity of the superconducting properties extends up to the median plane in Sample B, a result which could not be observed with the Hall probe mappings of Figure 4.8 and Figure 4.15-(b).

A further inspection on the distribution of the penetration regimes at both sample surfaces suggests that the penetration front proceeds lower on the top surface than on the bottom surface. Indeed, the extent of the circumferential shell in which the holes are penetrated is larger on the bottom surface than on the top surface. This result is in agreement with the Hall probe mappings of both surfaces shown in Figure 4.15-(b).

While the distributions of the magnetic flux density and of the penetration regimes are almost regular in Sample B, several holes are also in the flux concentration regime. These holes are located close to the sample border, unlike in Sample A where this regime is associated with holes surrounding efficiently shielded regions. The relative increase of the magnetic flux density in the holes with respect to the applied field is however smaller than in Sample B. The occurrence of the flux concentration regime is likely associated with the return field lines of the demagnetizing field. The demagnetizing field may either originate from the supercurrent flowing around the entire sample, like in Sample B, or from smaller shielded regions, like in Sample A.

4.4   Application to the characterization of the penetration of a pulsed field

4.4.1   Bean model analysis of the magnetic flux in the holes of a sample of infinite height

Similarly to what is performed to introduce the measurements with the AC magnetic field excitation, we first consider a sample with an infinite height and a single hole; the sample is subjected to a pulsed magnetic field and we calculate the magnetic flux density inside that hole as a function of time, with the help of the numerical Bean model. The sample has a radius a, the hole is located at a distance d from the border, and has a radius R. The applied magnetic pulse has an amplitude of $B_{\max} = 2\mu_0 H_p$ (where H_p is the penetration field of the sample having no hole, $H_p = J_c a$) that is reached after 20 ms. The applied field (grey line), together with the magnetic flux density in the hole (black line), is reproduced as a function of time in Figure 4.16.

At the beginning of the pulse, the external field does not reach the hole. There is no magnetic flux density in the hole until $B_a = \mu_0 J_c(d - R)$. As soon as that threshold field is reached, the time evolution of the magnetic field in the hole follows that of the applied field with a negative offset. In particular, when the applied pulse reaches its maximum value, the magnetic flux in the hole is maximum and saturates at a constant value, B_s, as it has been already observed with an AC
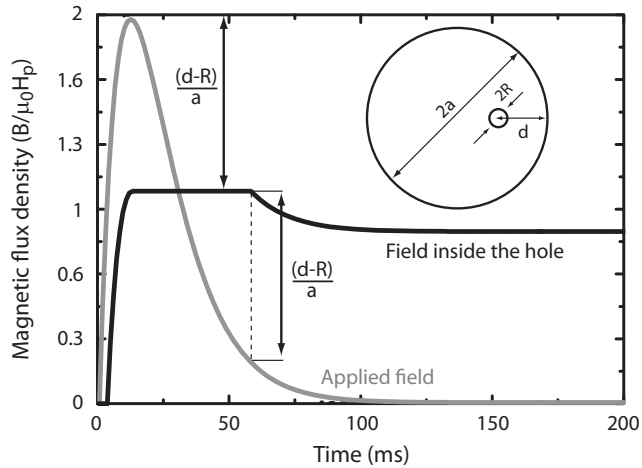
Figure 4.16: *Magnetic flux density (black line) as a function of time in a hole of radius R located at a distance d from the border of a cylinder with an infinite height, subjected to a pulse of magnetic field (grey line).*

excitation in Section 4.3.1. The saturation value is given by

$$B_{max} - B_s \;\; = \;\; \mu_0 J_c (d - R).$$ (4.2)

The magnetic flux density in the hole remains unchanged, until the applied field is such that

$$B_{max} - B_a \;\; = \;\; 2\mu_0 J_c (d - R).$$ (4.3)

At larger times, the magnetic field evolution in the hole follows that of the applied field. When the applied pulse is over, there remains a trapped magnetic flux density in the hole, $B_{trapped}$, whose value reads

$$B_{trapped} = \mu_0 J_c (d - R).$$ (4.4)

From this analysis based on a very simple model, we get a first insight on the shape of the signals to be expected from the measurements. As is also the case with the AC excitation, the Bean model analysis will certainly not be able to explain all the measured signals, as for instance demagnetizing effects have not been taken into account. Unlike in the AC case, it is expected that the flux creep phenomena will have a non negligible influence on the results since pulse excitations induce much larger electric fields than those obtained with the low-frequency AC excitation.

4.4.2   Measurements in Sample B

We now address the description of the experimental results obtained with Sample B subjected to a pulsed magnetic field. We first discuss the time evolution of the magnetic flux density in the median plane of four given holes. On this basis, we compare the characteristics of the flux front diffusion in the median plane and on the surface of the sample. We finally compare the trapped magnetic flux density in the median plane with that on the surface of the sample.

Time evolution of the magnetic flux density in the hole

We first consider the time evolution of the magnetic flux density in the median plane of the sample, *i.e.* for microcoils that are placed at an equal distance from the top and bottom surfaces. Four representative holes are investigated (cf. Figure 4.17). The magnetic flux density in a given hole is calculated by integrating the pick-up voltage induced across the microcoils (which is proportional to dB/dt). In practice, the pick-up voltage is biased by an unavoidable parasitic DC offset arising from the output of the instrumentation amplifier. The offset can be considered as remaining constant during the pulse (< 500 ms). To estimate this offset, the acquisition starts 5 ms before the pulse is applied and the voltages recorded prior to the beginning of the pulse are averaged. The result is then subtracted from the raw data.

Figure 4.17 shows the time evolution of the magnetic flux density, $B(t)$, in the median plane of the four representative holes (black and grey lines), together with the applied magnetic pulse (dashed line). Hole (a) is located at the centre of the sample, hole (b) is located at a half radius from the centre, and holes (c) and (d) are the closest to the sample outer edge as sketched on the right panel of Figure 4.17.

The time-dependence of the magnetic flux density in the holes has an overall pulse shape similar to that of the applied field, but however with a few different features. In hole (a), which joins the centres of the top and bottom faces, the pulse of flux density is preceded by a time interval during which $B(t)$ decreases slightly and is negative, *i.e.* the magnetic field in hole (a) is oriented in the opposite direction to the applied field. Then, the $B(t)$ pulse is shifted in time with respect to the applied field
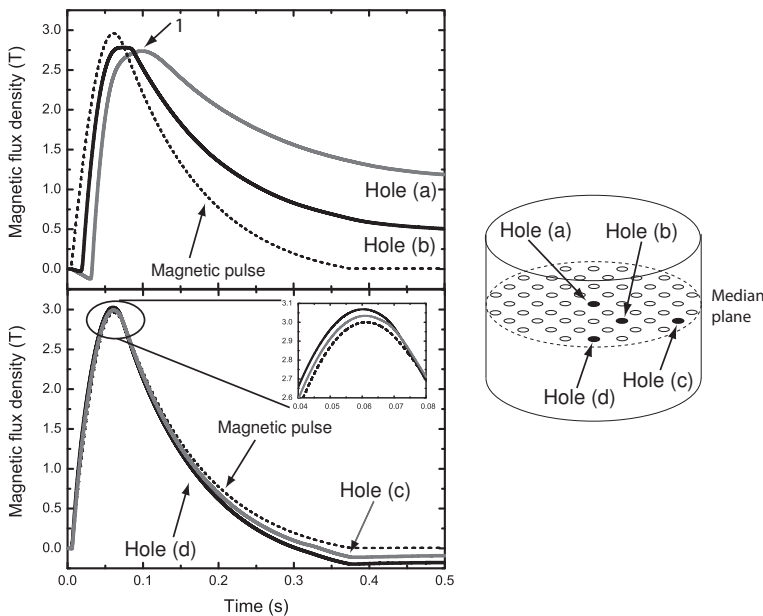

Figure 4.17: *Time evolution of the magnetic flux density in the median plane of holes (a), (b), (c), and (d). The applied magnetic flux density is shown with a dashed line.*

and the magnetic flux density reaches a maximum after the applied field has already started to decay (see arrow 1 in Figure 4.17). Moreover, when the applied field vanishes, a positive trapped magnetic flux density remains in the hole.

In hole (b), during a short time-interval preceding the pulse, the magnetic flux density is also negative and thus oriented in the opposite direction to the applied field. After a time delay that is shorter than for hole (a), the magnetic flux density in hole (b) increases with the applied field and reaches a maximum value when the applied field is maximum. Afterwards, it decreases with time and — similarly to the situation in hole (a) – a positive trapped magnetic flux density is measured in hole (b) at the end of the pulse.

In holes (c) and (d), located close to the sample edge, the behaviours of the magnetic flux density during the pulse are similar to each other. As soon as the applied field starts to increase, the magnetic flux density increases and reaches a maximum that exceeds the applied field (see inset of Figure 4.17). This behaviour is a reminder of the flux concentration regime observed with the AC excitation and it is carefully checked not to be due to a calibration artefact. The magnetic flux density in holes (c) and (d) remains larger than the applied flux density until the applied pulse starts decreasing. Then, it becomes smaller than the applied flux density. In particular, when the applied pulse vanishes, a negative trapped magnetic flux density is measured.

The simple Bean model, which is discussed as an introduction to the measurements in Section 4.4.1, only explains the time signal for hole (b), expect at the very beginning of the pulse. In the other holes, data clearly show deviations from the Bean picture. The Bean model fails reproducing, (i), the negative magnetic flux density at the beginning of the pulse in holes (a) and (b), (ii), the time delay between the maximum of the applied field and that of the field in hole (a), and (iii), the flux concentration and the negative trapped flux density in holes (c) and (d).

We suggest that these discrepancies may be attributed to demagnetizing effects appearing in short superconducting samples.

(i) As the magnetic flux starts penetrating the sample from the edges, the magnetic field is found to be negative in holes (a) and (b). The sample being only partly penetrated, supercurrents flow in its outer region so as to screen its bulk from the applied magnetic flux. The net negative induction which is observed in data suggests the occurrence of an *overscreening* mechanism, where the induced field exceeds the applied one. Such mechanism results from the demagnetizing effects that are associated with the geometry of the supercurrent trajectories. Overscreening has already been observed in flat rings, near their inner edge [212], or in superconducting tubes, close to the inner wall [126]. In the present case, the overscreening mechanism is likely to be strengthened by the rather complex trajectories of the supercurrents, which must flow around the holes.

(ii) Right after the applied field has reached its maximum amplitude and starts decreasing, the magnetic field in hole (a) keeps increasing. A plausible explanation of this effect can be elaborated by thinking along the lines of a critical model to which one adds demagnetizing effects. According to the Bean model, at the instant the applied field starts decreasing, the supercurrents flowing
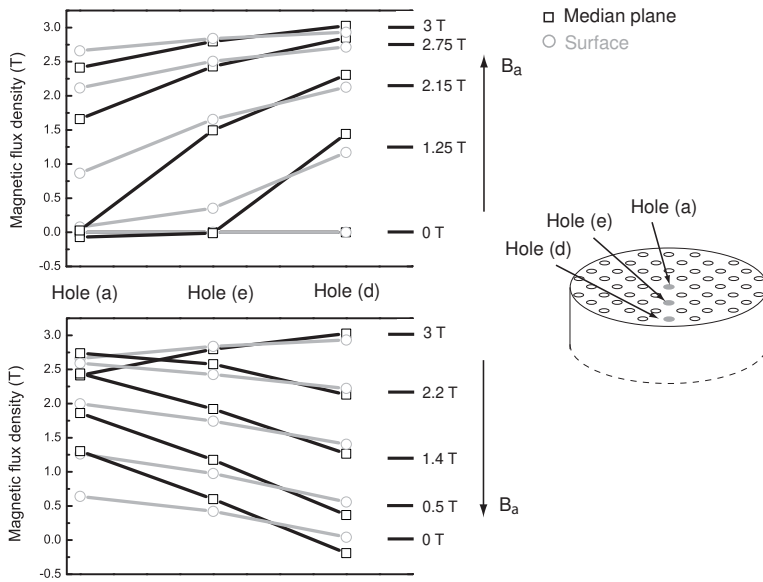
Figure 4.18: *Magnetic flux density in holes (a), (e), and (d), whose positions are represented on the right panel. The flux density is shown in the median plane (black squares) and on the sample surface (grey circles), for both the increasing part (top panel) and the decreasing part of the pulse (bottom panel).*

in the outer part of the sample reverse their direction with respect to that of the supercurrents flowing in the remaining part of the sample. The resulting demagnetizing field through hole (a) is now oriented in the same direction as the applied field and thus reinforces the flux density in that hole. As a result, the occurrence of the maximum in the magnetic flux threading hole (a) is delayed.

(iii) During the increasing part of the applied pulse, a flux concentration is observed in holes (c) and (d). As mentioned above, the demagnetizing field produced in the central hole during that time is oriented in the direction opposite to the applied field. The returning lines of the demagnetizing field, however, are oriented in the same direction as the applied field. It is therefore likely that the periphery of the sample is crossed by the returning lines of that demagnetizing field; in particular, holes (c) and (d) intercept such lines. Since these lines remain after the applied field has vanished, the remnant magnetic flux density in the holes located near the lateral surface of the sample is negative, as indeed observed in Figure 4.17.

In order to study whether the demagnetizing field influences the magnetic flux density in the same manner on the surface and in the bulk, let us consider three successive holes along a given radial line. We reproduce in Figure 4.18 the magnetic flux density in the median plane and on the surface of these holes, namely (a), (e), and (d), at several consecutive times during the pulse. During the increasing part of the pulse (Figure 4.18 - top panel), the magnetic flux density is larger at the sample periphery than near the sample centre. The spatial decay of the magnetic flux density along the radial line is stronger in the median plane than at the sample surface, due to demagnetizing effects. For hole (d),

which is the closest to the sample edge, we observe a flux concentration in the median plane. This behaviour is not observed near the surface. Similarly, for hole (a), the magnetic flux density is found to be negative at the beginning of the pulse in the median plane, whereas it is always positive near the surface.

As the pulse starts decreasing (Figure 4.18 - bottom panel), the magnetic flux density in the median plane of the central hole (a) first increases before decreasing, whereas the flux density on the surface is found to decrease monotonically. Once the applied field vanishes, the trapped flux density in the centre of the sample is always larger in the median plane than near the surface. Moreover, the spatial variation of the magnetic flux density along the radial line is also smaller near the surface than in the median plane, because of the demagnetizing field. In particular, the magnetic flux density is found negative in the median plane of the peripheral hole, whereas it remains positive at the sample surface.

It is therefore observed that the effects attributed to the demagnetizing field are different on the surface than in the median plane. Near the surface, the demagnetizing field cause the spatial variations of B_z along the radial line to differ from that in the median plane. In the median plane of the sample, it is responsible for the effects (i), (ii), and (iii) which were described above. These effects are not observed on the surface.

Characterization of the diffusion of the flux front in the sample

On the basis of the time evolution of the magnetic flux density in each of the 16 holes, we now characterize the diffusion of the flux front during the pulse in both the median plane and on the surface. The flux front is defined as the boundary between the regions that are already penetrated by the magnetic flux and those that are not. In practice, the characterization of that boundary requires defining a threshold for the magnetic flux density above which a given location can be considered as being penetrated. In the following, we consider a given hole as penetrated if

$$B_{in} \geq \frac{B_a}{10}, \tag{4.5}$$

where B_{in} stands for the magnetic flux density in the hole and B_a is the applied magnetic flux density. Accordingly, we define for each hole a penetration time, t_{pen}, as the time $t = t_{pen}$ at which $B_{in}(t_{pen}) = B_a(t_{pen})/10$.

The penetration times of holes belonging to two different sample radial lines are shown in Figure 4.19. The penetration time of a given hole is reported in the median plane and on the surface; the shortest penetration time is underlined. Along the radial line (1), the flux front first penetrates the peripheral hole in its median plane ($t_{pen} = 5.4$ ms) before reaching its surface ($t_{pen} = 5.7$ ms). In the other holes along that line, the situation is reversed: the flux penetration first occurs on the surface. Along the radial line (2), we observe a similar behaviour. The peripheral hole is penetrated in its median plane first whereas we observe the opposite situation in the other holes.

Two observations may be drawn from the results presented in Figure 4.19:

  (1) close to the sample edge, the flux front moves faster in the median plane than on the surface,

Penetration time (ms)

Centre

(1)			Centre
Median plane	5.4	20.9	34
Surface	5.7	15.3	22

(2)				Centre
Median plane	8.5	20.9	24	34
Surface	9.4	14	17	22

(2)

(1)
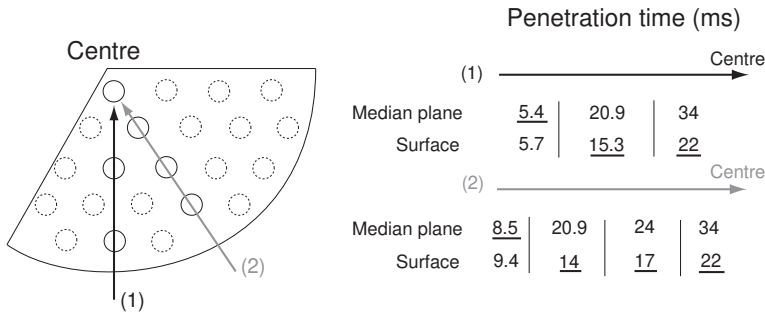
Figure 4.19: *Penetration times of the flux front in the median plane and on the surface of 6 holes belonging to one of the radial lines (1) and (2). For each hole, the shortest penetration time (median plane or surface) is underlined.*

(2) as the flux front moves further toward the sample centre, it proceeds at a higher speed on the surface than in the bulk.

Figure 4.20-(a) shows a sketch of the flux front at different times in the (r, z) plane, for two situations: (a) - left panel - a sample with a uniform critical current density flowing along the azimuthal direction, and (b) - right panel - the sample considered in this paper, on the basis of the above results. The qualitative description of the flux front diffusion in panel (a) is based on the results of Brandt in Ref. [135] for a cylindrical sample with the same aspect ratio as that of sample (b). In sample (a), the flux front systematically moves faster on the surface than in the median plane. By contrast, in the sample considered in the paper, the flux front proceeds at a faster pace in the median plane for the largest radial positions, whereas it is faster on the surface for the lowest radial positions.

The properties of the flux front diffusion are closely related to the detailed distribution of the critical current density in the sample. A large critical current density — a strong pinning — hampers the penetration of the flux. Thus, Figure 4.20 suggests that the critical current density is not uniform in the sample. In particular, it has a lower value in the median plane, close to the sample edge where the flux front moves faster than on the surface. Such non-uniformities in the critical current density may arise either (i) from intrinsic superconducting properties, $J_c(r, z)$ [59, 213], or (ii), from a non-uniform

(a) Homogeneous J_c (b) Sample B
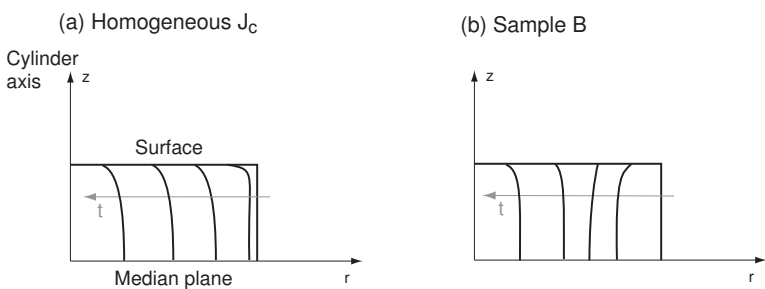
Figure 4.20: *Sketch of the diffusion of the flux front in the (r, z) plane of a cylindrical sample, at different times during the ascending part of the pulse. Two situations are depicted: (a) a sample having a uniform critical current density, and (b), the sample considered in the present work.*

heat production in the sample and a non-uniform surface heat exchange coefficient, $J_c(T)$ [214].

Trapped magnetic flux in the volume of the sample

We now turn to the analysis of the spatial distribution of the trapped field in the median plane and on the surface of the sample.

Figure 4.21 shows the magnetic flux density in the median plane of the 16 holes considered in this section, measured shortly after the end of the pulse, $t = 500$ ms. The holes are represented by a square tower whose height is proportional to the trapped flux density. The trapped flux density is found to be maximum at the centre of the sample, $B_{\text{trapped}}^{\text{median plane}} = 1.2$ T, and is smaller in holes that are located further from the centre. It is also observed that the peripheral holes have a negative trapped flux density in their median plane.

The maximum trapped flux density measured in the median plane of the sample allows us to estimate an average critical current density, $\tilde{J}_c$, flowing in the sample. If we consider as a first approximation that the holes are negligible obstacles for the current flow, the trapped magnetic flux density at the centre of the median plane of a cylinder with a radius R and a height L is given by [183],

$$B_{\text{trapped,max}} = \mu_0 \tilde{J}_c \frac{L}{2} \ln \frac{R + \sqrt{R^2 + L^2/4}}{L/2}. \tag{4.6}$$

From the field density values of Figure 4.21, we thus find

$$\tilde{J}_c \sim 1.5 \ 10^8 \ \text{A/m}^2 \tag{4.7}$$

as a first approximation.

Figure 4.21: *Distribution of the trapped magnetic flux density in the median plane of the holes shortly after the end of the pulse, at $t = 0.5$ s.*

However, the neglect of the holes may lead to non-negligible errors, as shown in Chapter 3. Following the same analysis as that used in Chapter 3, we find that the maximum trapped flux density in the drilled sample is expected to be about 40 % smaller than that in a sample without holes, assuming the same uniform critical current density. Taking this corrective factor into account yields

$$\tilde{J}_c \sim 2.5 \ 10^8 \ \mathrm{A/m^2} \tag{4.8}$$

as a better estimate.

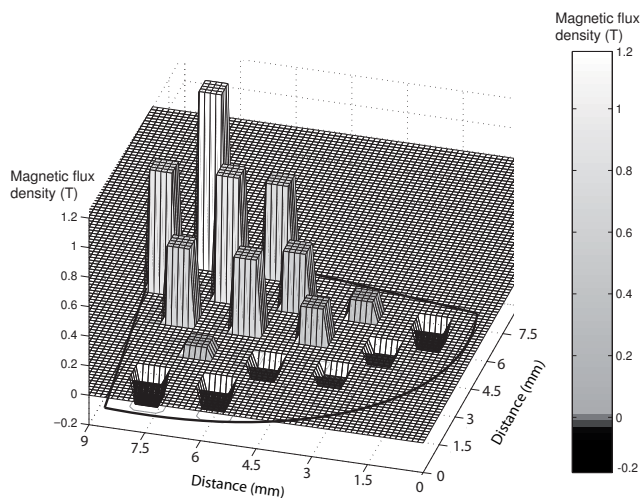The trapped magnetic flux density measured on the surface of the hole differs from that measured in the median plane. At the central hole, we measured $B_\mathrm{trapped}^\mathrm{surface} = 545$ mT (data shown in Figure 4.18). This value is smaller than that in the median plane by a factor $B_\mathrm{trapped}^\mathrm{median\ plane}/B_\mathrm{trapped}^\mathrm{surface} \approx 1.18/0.545 \approx 2.17$.

This value can be compared to elementary models. An analytical expression of the magnetic flux density along the central axis of the sample has been calculated in the case of a cylindrical sample without holes, see Ref. [183]. Given a radius, R, and a height, L, and assuming a uniform critical current density, J_c, the magnetic flux density along the axis of the cylinder is given as

$$
\begin{aligned}
B_z(z) \;=\; &\frac{1}{2}\mu_0 J_c \left\{ \left(z + \frac{L}{2}\right) \ln\left(\frac{R + \sqrt{R^2 + (z + L/2)^2}}{|z + L/2|} \right) \right. \\
&\left. - \left(z - \frac{L}{2}\right) \ln\left(\frac{R + \sqrt{R^2 + (z - L/2)^2}}{|z - L/2|} \right) \right\},
\end{aligned}
\tag{4.9}
$$

where z denotes the elevation from the centre. According to this relation, for a plain sample (i.e. containing no holes) with the dimensions of the sample described in Section 4.2.2 ($L = 10$ mm and $R = 8$ mm), the ratio between the maximum trapped flux in the median plane and on the surface is equal to

$$\lim_{z \to L/2} \left.\frac{B_z(0)}{B_z(L/2)}\right|_{L/R=1.25} = 1.7 \ . \tag{4.10}$$

Since the holes modify the current stream lines, there is *a priori* no reason that equation (4.9) remains valid for a drilled sample. To better understand the influence of the holes on the magnetic induction along the axis of the sample, we performed a 3D numerical simulation with the finite-element method described in Chapter 3 and calculated the trapped flux density for the drilled sample considered in this section. The two-time step method is used, one step for increasing the applied field from 0 to 3 T at a sweep rate of 10 mT/s and another one for decreasing the applied field from 3 T to 0 at the same sweep rate. According to our previous estimate for the critical density, Eq. (4.8), we assume a uniform and field-independent critical current density $J_c = 2.5 \ 10^8 \ \mathrm{A/m^2}$. The resulting magnetic flux density is shown as a function of the vertical position from the median plane in Figure 4.22, for the central hole of the sample. The analytical expression for $B_z(z)$, Eq. (4.9), is shown with a dashed line. It can be seen that the dependence of $B_z(z)$ of the drilled sample is very close to that of the plain sample. In particular, the ratio between the maximum trapped flux in the median plane and on the surface is found to be equal to ≈ 1.74 in both cases.

This simulated ratio, obtained for a sample with a uniform critical current density, is different from the ratio measured in our drilled sample (for which we found 2.17). The difference may result from
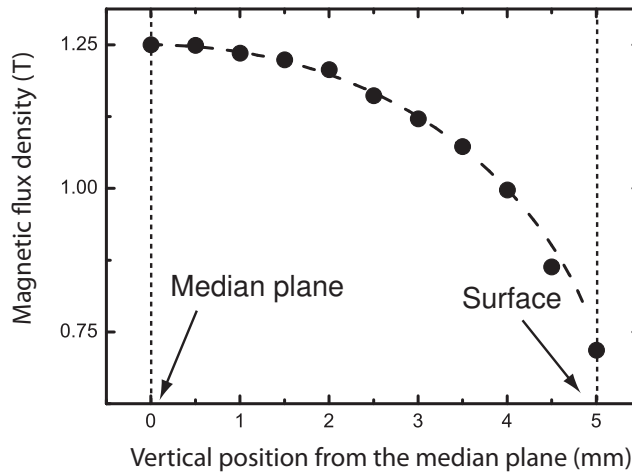
Figure 4.22: *3D finite-element simulation of the vertical component of the magnetic flux density as a function of the vertical coordinate, $B_z(z)$, in the central hole of the drilled sample considered in the paper (filled circles). The analytical expression of $B_z(z)$ at the centre of a sample without holes is shown with a dashed line.*

two causes. First, the position of the microcoil inside the hole is not perfectly known and the data is obtained from an average over the microcoil volume. As a small variation in z close to the surface of the sample leads to a large change in $B(z)$ (as observed in Figure 4.22), the measured ratio can easily differ from the simulated one. Second, the sample may exhibit a non-uniform distribution of its critical current density, such effect was not taken into account in the numerical model.

4.5   Summary of Chapter 4

In this chapter, we present a novel experimental technique for characterizing the magnetic properties of drilled samples. It is based on the local probing of the time-variations of the magnetic field inside the holes with microcoils. This microcoil measurement technique is appropriate for a local characterization of the magnetic properties of drilled samples, in the median plane, and on the surface of the sample as well. This technique enables us, for the first time, to characterize the flux diffusion in the bulk of the sample, instead of a few millimeters above its surface as is the case with conventional field mapping techniques.

Two types of magnetic excitations are investigated in this chapter: a low frequency AC magnetic field ranging from 30 to 130 mT produced by a bespoke electromagnet, and a magnetic pulse with an amplitude of 3 T and a duration of few hundreds of ms. The AC magnetic field excitation enables for an accurate assessment of the microstructure and of the local superconducting properties on the top and bottom surfaces, as well as in the median plane of drilled samples. During a pulsed-field excitation, the microcoil technique reveals the local diffusion of the pulse in the bulk and on the surfaces of the drilled samples.

Independent of the type of excitations, a simple analysis based on the Bean model applied to a drilled sample with an infinite height fails in describing particular features that are observed with the microcoil technique. The results suggest that some holes may serve as a returning path for the demagnetizing field, yielding a different behaviour from what is predicted by the Bean model, in particular a magnetic flux density in some holes that is larger than the applied one.

Different results are obtained with each type of excitations:

1. **AC magnetic field**

   For a given amplitude of the AC applied field, three penetration regimes are observed: (i)- the shielded regime, for which the magnetic flux does not penetrate the hole and its time evolution exhibits a sine shape of very small amplitude; (ii)- the gradual penetration regime, for which the magnetic flux density in the hole exhibits a clipped sine shape and the amplitude of its fundamental harmonic increases linearly with the applied field, the pick-up signal in this case contains a succession of peaks; (iii)- the flux concentration regime, for which the magnetic flux density in the hole is larger than the applied one and the pick-up voltage is almost a sine-wave.

   The distribution of the penetration regimes is closely related to the magnetic flux density measured at the surfaces by a DC Hall probe mapping. The local probing of the magnetic flux density inside the holes brings pieces of information that are impossible to obtain with usual surface characterization techniques. The analysis of the signals from the coils placed inside the holes allows one to know how a flux distribution at the surface is modified in the bulk and to measure the flux concentration appearing in the volume of the sample.

2. **Pulsed magnetic field**

   When the sample is subjected to a pulse of magnetic field, we analyze the time evolution of the magnetic flux density in the holes (median plane and surface) and we observe that the demagnetizing effects modify significantly the predictions based on the Bean model. In particular, during the ascending part of the pulse, they induce a flux concentration inside the holes that are close to the sample edge and a negative magnetic flux density in the holes near the centre of the sample. Moreover, when the pulse is over, the trapped magnetic flux density is negative in the holes that are close to the sample edge whereas it is positive at the centre of the sample. These effects, generated by the return lines of the demagnetizing field, are found to be stronger in the median plane than on the surface of the sample.

   In order to further characterize the flux diffusion in the sample, we define in each hole the required time for the external flux to reach this hole. We find that the holes located at the sample edge are penetrated in their median plane sooner than on their surface, while the opposite is found in the other holes. These observations may arise from either non-uniform superconducting properties in the sample or from particular thermal boundary conditions at the surface of the sample.

   For the first time, we show experimentally that the trapped flux density is larger in the median plane than on the surface. This finding is confirmed by modelling results. Moreover, the measured trapped magnetic flux density in the centre of the median plane of the sample allows us to directly estimate the critical current density in the volume of the sample. With the help of numerical modelling, we compare the magnetic flux density in the median plane and on the

surface of the sample. In particular, we show that the measured ratio between the maximum trapped flux in the median plane and that on the surface slightly differs from the ratio predicted by numerical results.

5

Magnetic properties of drilled samples containing a ferromagnetic powder in the holes

As already pointed out, creating holes in superconducting samples primarily aims at enhancing the synthesis of bulk HTS [6]. Soon after the first tests, the drilled structures also proved to be useful to strengthen other properties of the samples: in particular, the thermal stability [9] and the mechanical resistance [81, 85] could benefit from the presence of the holes, as the empty space cleared by the holes improves the thermal exchange with the cryofluid and allows the sample to be mechanically reinforced by filling the holes with a resin.

This latter example suggests that the holes may serve as a container for any type of material, provided they do not strongly alter the cooling of the superconducting material. Keeping that philosophy in mind, one could look for an appropriate filling material in view of enhancing the magnetic properties of drilled samples as well. With its tendency to concentrate the field lines inside its volume, a ferromagnetic material might increase efficiently the bulk magnetization. In particular, it would be interesting to study whether the magnetization drop, as discussed in Chapter 3, could be reduced or suppressed by inserting a ferromagnetic material inside the holes of the sample.

The combination of ferromagnetic and HTS materials in view of enhancing the performances of HTS is not a completely novel concept. Macroscopic hybrid ferromagnetic/superconductor (F/S) structures have already been considered in various applications. When used for transporting large currents, HTS tapes can be surrounded by ferromagnetic sheets in order to increase the critical current and to reduce the AC losses [148, 215, 216, 217, 218, 219]. In shielding applications, the placing of a hollow ferromagnetic cylinder around a superconducting tube enables one to substantially improve the shielding properties of each separated structure [220, 221, 222]. Last, an YBCO ring containing a concentric soft iron yoke has been shown to exhibit a larger and more stable trapped magnetic flux

density than that obtained with the ring alone [223].

In this chapter, we propose to characterize drilled YBCO samples whose holes are filled with a ferro-magnetic material. To this aim, we experimentally investigate the modifications of the magnetization curve and of the trapped flux density induced by the ferromagnetic material, as well as that of the levitation force between the HTS sample and a permanent magnet. Then, we develop further the study of these *impregnated* samples with the help of a numerical modelling that is based on the three-dimensional finite-element method described in Chapter 2.

5.1   Measurements of the magnetic properties of drilled samples impregnated with ferromagnetic powder

The study of impregnated samples starts with the description of few experimental results in order to reveal their main features and their main differences with respect to the non-impregnated samples. It will help us focusing the numerical study on the main modifications that are relevant for applications.

5.1.1   Drilled samples and impregnation

The experiments are carried out on two drilled $YBa_2Cu_3O_{7-\delta}$ bulk high-temperature superconductors (HTS). These were processed at CRETA (Grenoble, France) by the top-seeded melt-grown technique in the shape of cylinders with a diameter of 16 mm and a height of 10 mm. Artificial holes are drilled in the preform, in the direction parallel to the *c*-axis of the sample. Sample (1) contains 55 holes with an initial diameter of 1 mm that is reduced to 0.8 mm during the synthesis, and Sample (2)
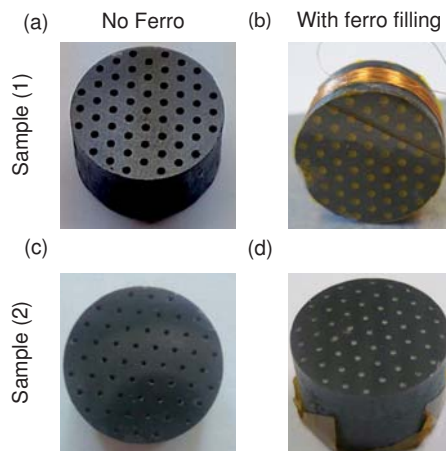

Figure 5.1: *(a)- Picture of Sample (1) before impregnation. (b)- Picture of Sample (1) after impregnation. (c)- Picture of Sample (2) before impregnation. (d)- Picture of Sample (2) after impregnation.*

contains 55 holes with an initial diameter of 0.5 mm that is reduced to 0.35 mm. These samples are impregnated by filling the holes with a ferromagnetic material.

The ferromagnetic material consists of a powder of stainless steel AISI 410 (Fe/Cr$_{12.5}$) [224] whose particles have a typical size of 45 μm. The use of a powder does not restrict the impregnation method to specific hole geometries, since the powder adjusts itself to the hole dimensions. During the filling of the holes, the powder is pressed, so as to reduce the total reluctance of the magnetic circuit crossing the holes. The powder is maintained in the holes by two polyimide films (Kapton) stuck on both sample surfaces. Figure 5.1 shows a photograph of Sample (1) and (2) before and after the filling of the holes with the ferromagnetic powder.

The relative magnetic permeability of the powder is measured at low fields and is found to be equal to $\mu_r = 24$ and $\mu_r = 28$, respectively at $T = 300$ K and $T = 77$ K. Details of the experimental procedure can be found in Appendix B.

5.1.2   Experimental results

Three types of measurements allow one to assess the influence of the ferromagnetic powder on the magnetic properties of the drilled sample: the characterization of the bulk magnetization, of the trapped magnetic flux above the surface, and of the levitation force. For each type of measurements, a comparison is made between the impregnated and the non-impregnated samples.

Measurement of the bulk magnetization

The bulk magnetization of the drilled samples is measured in a Physical Property Measurement System (PPMS - Quantum Design). Forty turns of 80μm-diameter wire are wound around the sample. This coil is centered around the median plane and extends up to 3 mm off the bottom and top surfaces. The sample is inserted in the experimental chamber of the PPMS and is cooled down to 77 K in the absence of magnetic field. Then, a linearly increasing magnetic flux density B_a is applied around the sample, in the direction parallel to its c-axis. It starts from 0 T and increased to 1.5 T at a sweep rate of 5 mT/s, and then cycles between -1.5 T and 1.5 T at the same sweep rate. The induced electromotive force (emf) across the sample coil is recorded by a nanovoltmeter (HP 34420A) controlled by a GPIB interface. The sample coil is calibrated by running a measurement sequence at a temperature of 100 K, at which the sample is in the normal state.

The induced emf is integrated numerically in order to obtain the average flux density inside the sample, $< B >$. The magnetization of the sample is then given by

$$\mu_0 M = < B > - B_a. \tag{5.1}$$

During the integration procedure, the constant offset of the voltmeter is carefully subtracted from the measured data, so that the magnetization curves superimpose on itself after a complete cycle.

The bulk magnetization curves of Sample (1) and (2) with (grey circles) and without (black triangles) the ferromagnetic powder in the holes are shown in Figure 5.2-(a,b). The magnetization curves form
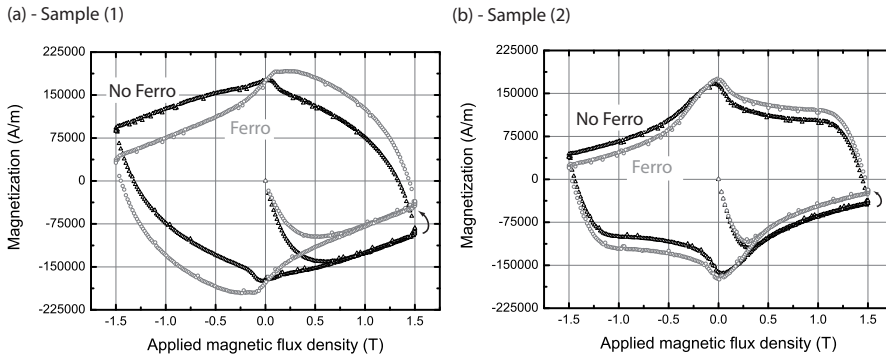
(a) - Sample (1)   (b) - Sample (2)

Figure 5.2: *Volume magnetization as a function of the applied flux density of the non-impregnated (black triangles) and the impregnated (grey circles) samples (Sample (1) and (2)).*

a hysteresis loop. In Sample (1), the impregnation of the holes strongly modifies the hysteresis loop which undergoes a counter-clockwise rotation of few degrees with respect to its centre (see arrow). Such a rotation has already been observed when measuring the magnetization curve of a YBCO ring having an iron yoke in its centre [223]. It arises from the interplay between the ferromagnetic material and the superconductor that is discussed in more details in the following section. The magnetization under large fields of Sample (1) is strongly modified after impregnation. In particular, when $B_a = 1.5$ T, the bulk magnetization of the impregnated sample is reduced by a factor slightly larger than 2 with respect to that of the non-impregnated sample. The bulk trapped magnetization (that is when $B_a = 0$ T) remains almost unchanged after the impregnation in Sample (1). In Sample (2), the magnetization curve of the sample with the ferromagnetic powder is similarly modified, but the amplitude of the counter-clockwise rotation is smaller than in Sample (1), since the volume proportion of the ferromagnetic material in Sample (2) (3%) is smaller than in Sample (1) (16%).

Characterization of the trapped magnetic flux

The trapped magnetic flux density above the sample surfaces is characterized in a Hall probe mapping experiment, with the same experimental procedure as that described in Section 3.5.2.

The distribution of the vertical component of the trapped magnetic flux density above the sample top and bottom surfaces is reproduced in Figure 5.3-(a,b). Figure 5.3-(a) shows the distribution of the trapped field above both surfaces of Sample (1), and Figure 5.3-(b) shows its distribution above both surfaces of Sample (2). The left panels correspond to the mappings of the top and bottom surfaces of the non-impregnated samples, while the right ones correspond to the samples with a ferromagnetic filling. As usual with this field mapping technique, the moderate distance between the probe and the surface does not allow one to resolve the positions of the holes [82, 85, 176, 177].

As observed in Figure 5.3, filling the holes with the ferromagnetic powder leads to modifications of the trapped flux profiles. When there is no ferromagnetic material inside the holes, Sample (1) and (2) exhibit an axisymmetric flux profile with a single maximum for both surfaces, indicating that there is no macrocrack close to the surfaces. In Sample (1), when the holes are filled with the powder, the
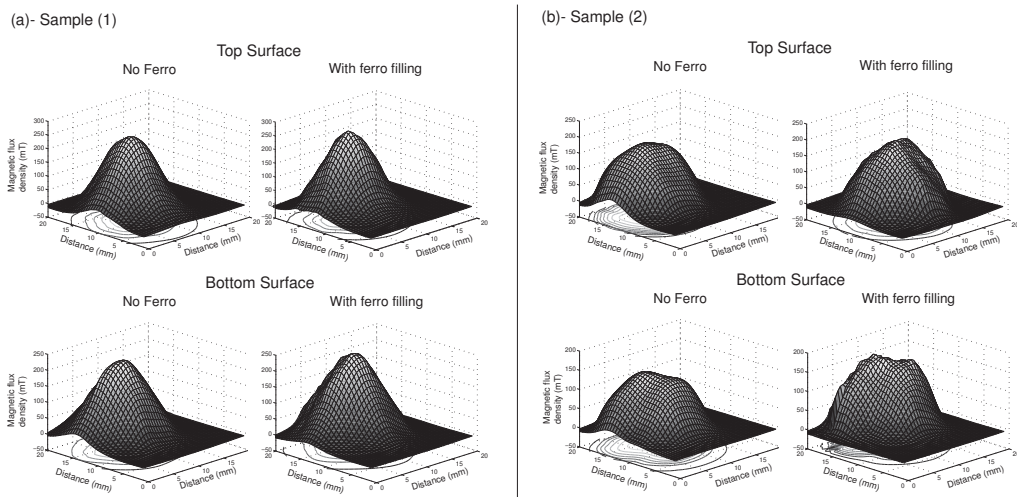
Figure 5.3: *Hall probe mappings of the trapped flux density after a field-cooled magnetization ($B_a = 450$ mT) at 0.5 mm above the surface of the non-impregnated (left column) and impregnated (right column) samples. In each case, the first row corresponds to the top surface, and the second one to the bottom surface.*

maximum trapped flux that is measured at 0.5 mm above the surface is larger while the flux profile remains almost unchanged. In Sample (2), the impregnation of the holes involves a similar increase of the maximum trapped flux, but causes the flux distribution to be slightly irregular, with the appearance of some bumps around the maximum.

In order to further investigate the increase of trapped flux observed in Figure 5.3, we report in Table 5.1 the maximum vertical component of the trapped flux density, B_{max}, that is measured when the Hall probe is brought in contact with the surface. The impregnation of the holes in Sample (1) yields the largest increase of trapped flux, with a relative increase of ≈ 34 % measured on the top surface. By contrast, the maximum trapped flux density of Sample (2) rises up to ≈ 10 %.

Table 5.1: *Maximum trapped magnetic flux density on the top and bottom surfaces of Sample (1) and (2)*

	Sample (1)		Sample (2)	
	No Ferro	Ferro	No Ferro	Ferro
Top Surface	303 mT	406 mT	209 mT	244 mT
Bottom Surface	282 mT	350 mT	176 mT	194 mT

Measurement of the levitation force

The levitation force between the drilled sample and a permanent Nb-Fe-B magnet is measured by a home-made system. It consists of a stand on which is clamped a micrometer screw connected to a liquid nitrogen container used as a sample holder. A cylindrical permanent magnet is fixed to a heavy ferromagnetic cylinder resting on a weighing scale. A picture of the experimental setup is shown in Figure 5.4. When the HTS sample (with a temperature of 77 K) lies above the magnet, a repulsive (*resp.* attractive) magnetic force is created between the HTS and the magnet; as a result, the weight of the magnet is increased (*resp.* decreased) with respect to its weight when there is no HTS sample above it.

The drilled sample, connected to the micrometer screw is initially positioned at 1 cm from the permanent magnet. The container is then filled with liquid nitrogen. After 5 min, the temperature of the sample is uniform, $T = 77$ K, and we start the following measurement sequence: (i) the drilled sample is brought close to the permanent magnet by turning the screw with a step size of 500 μm, (ii) once the sample container becomes in close contact with the permanent magnet, the sample is brought back step-by-step to its initial position, and (iii) the sample is again brought close to the magnet, as in step (i). After each 500 μm motion, the apparent weight of the magnet is recorded and the levitation force is determined.

The levitation force measured above the top surface of Sample (1) is shown in Figure 5.5, which shows the situations of the non-impregnated holes (a) and of the impregnated ones (b). The three consecutive steps of the measurement sequence are indicated by arrows. When the distance between the sample and the magnet is sufficiently small, a repulsive levitation force is measured between the two materials. The curves corresponding to the steps (ii) and (iii) form a hysteresis loop due to the pinning of the vortices inside the sample.

The non-impregnated sample is found to produce a larger levitation force than that measured above the impregnated one. In particular when the sample is close to the magnet, the repulsive levitation force is larger above the non-impregnated sample than above the impregnated one. This behaviour is attributed to the attractive force existing between the ferromagnetic material and the magnet, which reduces the repulsive levitation force. In particular, we observe that the force between the impregnated
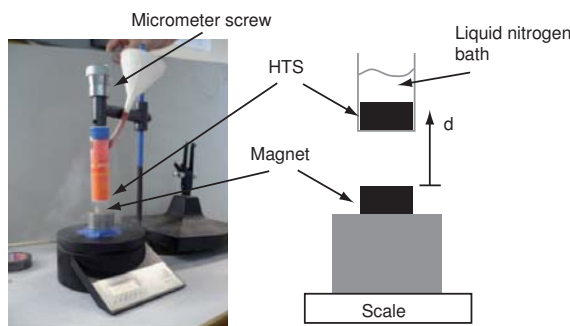
Figure 5.4: *Picture and schematic illustration of the experimental setup used for measuring the levitation force between a HTS sample and a permanent magnet.*
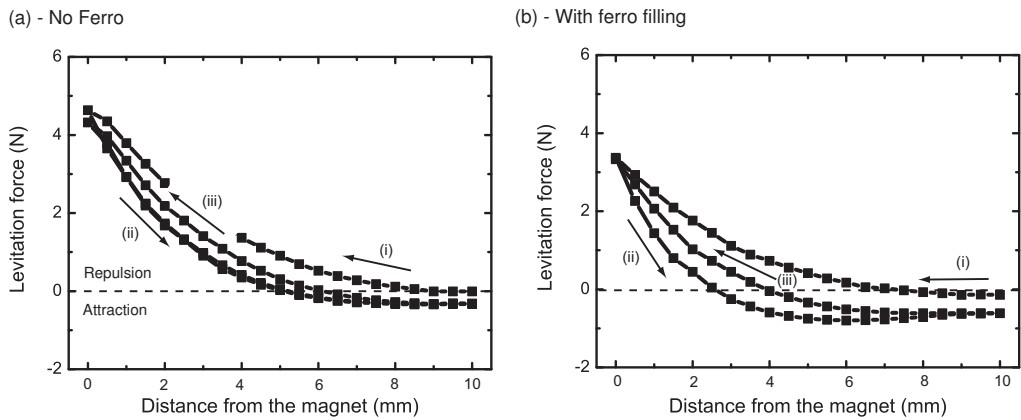
Figure 5.5: *Levitation force as a function of the distance between the permanent magnet and Sample (1), either non-impregnated (a) or impregnated (b).*

sample and the magnet when they are separated by 10 mm is attractive when the holes are filled with the ferromagnetic powder.

5.1.3 Summary

Following the experimental results reported above, the effects of the ferromagnetic powder in the holes may be summarized as follows. The impregnation of the ferromagnetic material in the hole leads to:

(i) a modification of the shape of the magnetization curve of the HTS sample. In particular, a counter-clockwise rotation of the hysteresis loop is observed;

(ii) an increase of the maximum trapped magnetic flux density;

(iii) a decrease (resp. increase) of the repulsive (resp. attractive) levitation force acting between an HTS sample and a permanent magnet.

The effects (i) and (ii) tend to enhance the magnetic properties of the drilled samples. However, the third consequence of the impregnation, that is associated to the levitation between the sample and a magnet, has a harmful character since it reduces the levitation efficiency.

5.2 Modelling of the magnetic properties of impregnated samples

The experimental results presented in Section 5.1.2 enable one to get some insights of the effects of the ferromagnetic material on the properties of the drilled superconductor, as summarized in Section 5.1.3. We now proceed a step further in the study of impregnated samples by using modelling and simulations in order to assess in more details the influence of the ferromagnetic material on the hybrid structure.

In view of stating the problem, we first consider the simple model of a drilled sample with an infinite height, in the limit of very strong pinning (Bean model). We assume that the powder which is inserted
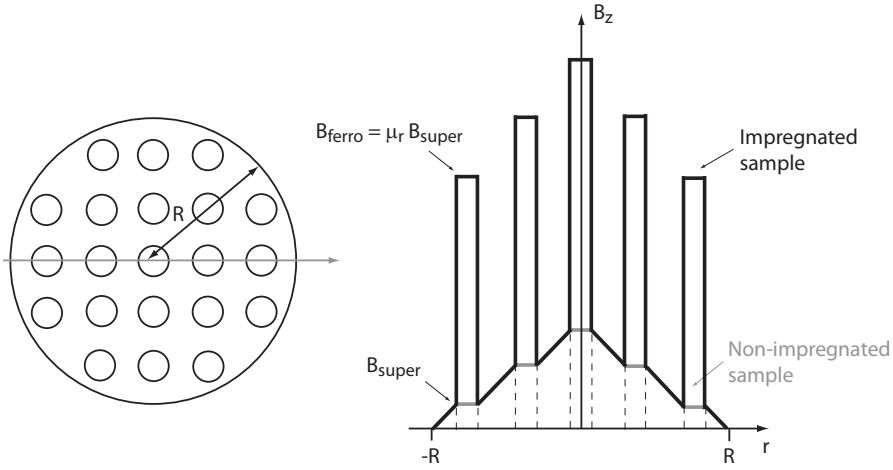
Figure 5.6: *Trapped flux profile along a diameter of a drilled cylinder of infinite height that is either impregnated (black line) or not (grey line). The profile is calculated according to the Bean critical state model.*

inside the holes is a continuous and homogeneous material, and that the relative magnetic permeability of the powder, μ_r, is constant. The symmetry of the sample with infinite height involves that the magnetic field **H** has a single non-vanishing component, H_z, that is oriented along the vertical direction in the cross section. At the superconductor/ferromagnetic interface, the Maxwell equations impose H_z to be continuous. The magnetic field thus remains uniform in the powder where it assumes the same value as at the edge of the hole. Therefore, the distribution of the trapped magnetic field in the impregnated sample assumes the same shape as in a non-impregnated one. Now, since $\mathbf{B} = \mu_0 \mu_r \mathbf{H}$, the flux profile undergoes a discontinuity at the superconductor/powder interfaces. The ratio between the magnetic flux density in the hole, B_{ferro}, and that in the superconductor at the interface, B_{super}, is equal to μ_r. The profile of trapped flux in the superconducting region does not change when the holes are impregnated, as schematically represented in Figure 5.6.

To sum up, the net effect of filling the holes with the ferromagnetic powder in a sample with an infinite height is to increase the magnetic flux density in the holes, while its profile inside the superconductor is not altered. That situation is no longer valid in samples of finite heights, where the demagnetizing effects induced by the ferromagnetic material are expected to strongly modify the magnetic field distribution in the superconductor.

In order to model the effects of the ferromagnetic powder in a superconducting sample with a finite height, we use the 3D finite-element model described in Section 2.3, to which we add a specific magnetic constitutive law in order to take into account the ferromagnetic material inside the hole. The magnetic permeability of the simulation domain Ω is defined piecewise and is discontinuous at the superconductor/powder interface. Eqs. (2.19)-(2.20) are modified consequently, and the corresponding weak form of the magneto-quasistatic Maxwell equations reads

$$(\frac{1}{\mu_0 \mu_r} \nabla \times \mathbf{A}, \nabla \times \mathbf{A}_i) - < \mathbf{B}_{\mathrm{self}} \times \mathbf{n}, \mathbf{A}_i > + \left(\sigma(\dot{\mathbf{A}} + \dot{\mathbf{A}}_a + \nabla \phi), \mathbf{A}_i \right) = 0, \tag{5.2}$$

$$(\sigma \dot{\mathbf{A}}, \nabla \phi_j) + (\sigma \dot{\mathbf{A}}_a, \nabla \phi_j) + (\sigma \nabla \phi, \nabla \phi_j) + < \mathbf{n} \cdot \mathbf{J}, \phi_j > = 0, \tag{5.3}$$

where $(a, b) = \int_\Omega ab \, d^3\mathbf{r}$ and $< a, b >= \int_\Gamma ab \, d\mathcal{C}$ with Γ being the external surface of the simulation domain Ω.

In practice, the relative magnetic permeability of the soft ferromagnetic powder depends on **H**, due to the magnetic saturation. However, incorporating the non-linearity of the ferromagnetic constitutive law in the 3D finite-element formulation yields very long calculation times. For instance, a non-linear magnetic permeability has already been successfully integrated in GetDP when modelling F/S hybrid structures, for the specific case of two-dimensional axisymmetric geometries that we discuss in Ref. [222]. In such a geometry, the meshing comprises less than 5000 nodes and the treatment of the non-linearity of the magnetic material requires a calculation time that is 20 times as large as that required if the material is linear. Such a time cost is not affordable in 3D meshings with over 150000 nodes. From the observations reported in [222], we believe that modelling the ferromagnetic powder with a field-independent magnetic permeability brings already very valuable results from which generic conclusions can be drawn on the behaviour of impregnated samples. In fact, the saturation of the ferromagnetic material is accompanied with a decrease of its relative magnetic permeability, since it asymptotically tends to $\mu_r = 1$ when $H \to \infty$. As a first approximation, the effect of the saturation may be roughly taken into account by considering a uniform magnetic permeability that is smaller than that measured at low fields. To this aim, three different values of magnetic permeability are adopted — in a given simulation, a unique value of μ_r is associated to the ferromagnetic region —: (i) $\mu_r = 20$, which is close to the measured permeability of the ferromagnetic powder at low fields (see Appendix B), (ii) $\mu_r = 2$, and (iii) $\mu_r = 1.5$. The last two values of the magnetic permeability are representative of situations when the powder is saturated.

Note however, that the magnetic flux density in the ferromagnetic powder is a function of the radial position of the hole, as suggested by the Bean model in Figure 5.6. It implies that the magnetic permeability of the powder may also depend on the position of the hole. By using a uniform magnetic permeability, we neglect these variations and consider limiting cases of the magnetic permeability.

Since only slowly varying magnetic fields ($dB/dt = 10$ mT/s) are considered, effects associated with eddy currents induced in the ferromagnetic materials are ignored and the conductivity of the ferromagnetic powder is taken to be 0. Moreover, the magnetic behaviour of the ferromagnetic powder subjected to a given applied flux density, B_a, does not depend on the way B_a is established (we neglect the hysteresis of the soft ferromagnetic material). In particular, in the case of a linearly varying applied field, the simulation of the magnetic properties of the powder subjected to B_a may

Table 5.2: *Parameters used for the finite-element simulations*

Critical exponent	n	21
Critical current density	J_{c0}	2.10^8 A/m^2
Critical field	E_c	10^{-4} V/m
Maximum applied field	$B_{\max}$	3 T
Sweep rate	$\dot{B}_a$	10 mT/s

be carried out with an arbitrary number of time steps. When associated to a HTS sample, single time-step simulations, as discussed in Section 2.3, are thus possible.

We consider the same sample geometry as that of Sample (1), on which the experiments reported in Section 5.1.2 are carried out. The cylindrical sample has a height of 10 mm and a diameter of 16 mm. It contains 55 holes with a diameter of 0.8 mm. The material parameters and the applied fields used in the simulations are summarized in Table 5.2.

5.2.1   Magnetization of impregnated samples

The bulk magnetization of the impregnated samples is calculated with the help of FEM simulations. The applied field increases linearly with time, from 0 to $B_{\max}$, at a sweep rate of $\dot{B}_a = 10$ mT/s. The calculated magnetization M of the non-impregnated sample ($\mu_r = 1$ - black line) and of the impregnated one, with $\mu_r = 1.5$ (dark grey line), $\mu_r = 2$ (grey line), and $\mu_r = 20$ are plotted as a function of the applied field B_a in Figure 5.7. Each calculated point on the magnetization curve is obtained with a single time-step FEM simulation. Note that the magnetizations corresponding to applied fields smaller than 600 mT suffer from bad convergence and are not reproduced in Figure 5.7.

The first part of the magnetization curve of the non-impregnated sample saturates when $B_a > 800$ mT, and the calculated magnetization slightly fluctuates around a constant value. The small fluctuations arise from small numerical errors in the simulations. The saturation of the magnetization is expected from the critical state description of a superconductor sample having a constant critical current density.

In the impregnated samples, the magnetization no longer saturates at a constant value, but rather increases linearly with the applied field when $B_a > 800$ mT. The slope of the curve is proportional to the relative permeability of the powder. Figure 5.7 therefore suggests that the magnetization curve of a drilled sample undergoes a counter-clockwise rotation when the holes are filled with a ferromagnetic
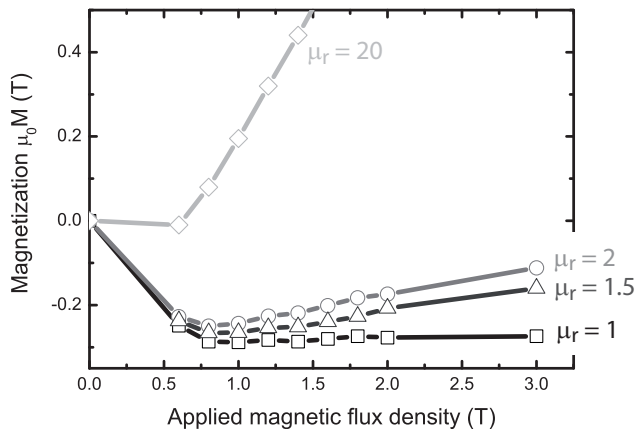

Figure 5.7: *Initial magnetization curve of a drilled sample whose holes are either non-impregnated (black line) or impregnated with a ferromagnetic powder with $\mu_r =1.5$ (dark grey line), $\mu_r =2$ (grey line), and $\mu_r = 20$ (soft grey line). The magnetization is calculated with single time-step FEM simulation.*

material. This tendency is consistent with the measured magnetization curve of the impregnated samples shown in Figure 5.2. The increase of magnetization with the applied field that leads to the rotation of the magnetization curve results from the interplay between the diamagnetic behaviour of the superconductor and the ferromagnetic behaviour of the powder. The powder 'attracts' the flux lines inside the holes and makes the average flux density in the volume of the sample larger than that in the non-impregnated sample. The magnetic flux density that is concentrated inside the holes increases linearly with the applied field, as indicated by the increase of the magnetization with the applied field.

5.2.2 Trapped flux profile in impregnated samples

The FEM simulations can also be used to calculate the trapped flux of impregnated samples in two time-steps, one for increasing the applied flux density to $B_a = 3$ T at a sweep rate of 10 mT/s, and another one for reducing the applied flux density to 0 at the same sweep rate.

The trapped flux profile along a diameter in the median plane of the drilled sample is represented in Figure 5.8. The relative permeability of the ferromagnetic material is respectively $\mu_r = 1$ (non impregnated sample - black lines), $\mu_r = 2$ (dark grey lines), and $\mu_r = 20$ (grey lines). The hole positions are highlighted with a grey background. Note that, when $\mu_r = 20$, the magnetic flux density in several holes is in fact out of the range of the left axis.

As already observed in samples with an infinite height, the trapped flux profiles of impregnated samples exhibit discontinuities at the interface between the superconductor and the ferromagnetic material. In particular, the ratio between the magnetic flux density at the ferromagnetic side (with a relative permeability μ_r) at the interface B_{ferro}, and that at the superconducting side B_{super} is given by $B_{\text{ferro}}/B_{\text{super}} = \mu_r$. The magnetic flux density in the hole of the impregnated sample is thus larger
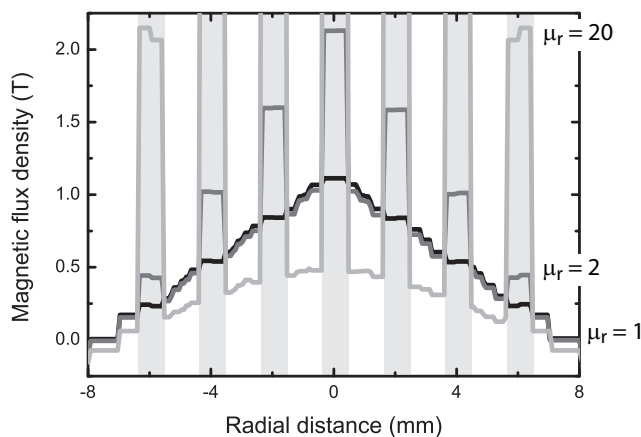

Figure 5.8: *Trapped magnetic flux profile along a diameter in the median plane of a drilled sample calculated with two time-steps FEM simulations. The drilled sample is either non-impregnated (black line) or impregnated with a ferromagnetic powder of $\mu_r = 1.5$ (dark grey line) and $\mu_r = 20$ (grey line). The positions of the holes along the diameter are highlighted.*
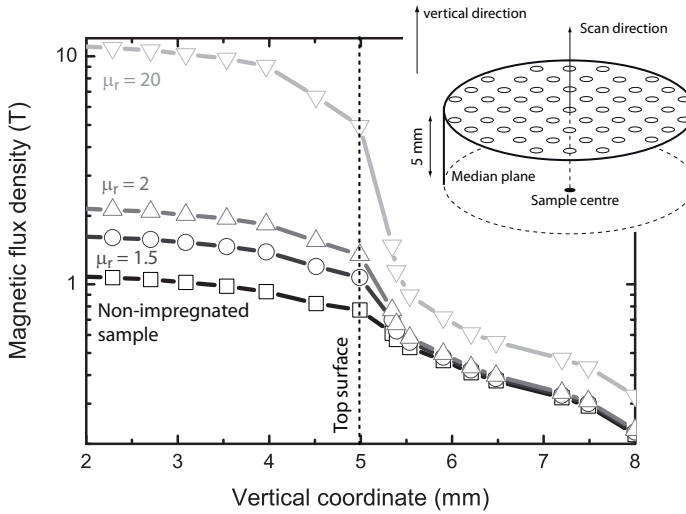
Figure 5.9: *Vertical component of the trapped magnetic flux density as a function of the coordinate z, in a non-impregnated sample (black line) and in an impregnated sample with $\mu_r = 1.5$ (dark grey line), $\mu_r = 2$ (grey line), and $\mu_r = 20$ (soft grey line).*

than when the holes are not filled by the ferromagnetic powder. The increase of trapped magnetic flux density is proportional to the relative permeability of the ferromagnetic powder.

However, by contrast to what occurs in a sample with an infinite height, the trapped magnetic flux profile in the superconductor is reshaped due to the presence of the ferromagnetic material inside the holes. The slope of the distribution of B between two neighbouring holes is reduced in the impregnated samples and varies with position[1]. In particular, the slope is smaller around the sample centre. A similar modification of the slope of the flux profile induced by the presence of a ferromagnetic material in the vicinity of the sample has already been observed in hybrid structures consisting of a ferromagnetic hollow cylinder inserted inside a superconducting tube of larger diameter that are used for magnetic shielding, as described in Ref. [222]. The profile adjustment is believed to stem from an interplay between the ferromagnetic material that 'attracts' the magnetic field lines and the superconducting material that rather 'traps' these lines.

Figure 5.8 shows that the maximum trapped flux density is strongly enhanced in the median plane of the impregnated sample. However, such a large increase has not been observed on the surface with the Hall probe mapping experiments reported in Section 5.1.2. Let us analyze the trapped flux density as one gets further from the median plane.

In Figure 5.9, the vertical component of the magnetic flux density in the centre hole of the impregnated sample, B_z, is plotted as a function of the vertical distance from the median plane, z. The ferromagnetic material is assumed to be characterized by a constant relative permeability of $\mu_r = 1$ (non-impregnated sample - black line), $\mu_r = 1.5$ (dark grey line), $\mu_r = 2$ (grey line), and $\mu_r = 20$ (soft grey line).

---

[1]In the non-impregnated sample, the slope is the same between all the nodes because the critical current density is assumed to be field-independent.

Table 5.3: *Maximum trapped flux density in impregnated and non-impregnated samples*

	Plain sample	Drilled sample	Impregnated sample		
			$\mu_r = 1.5$	$\mu_r = 2$	$\mu_r = 20$
Median plane	1.6 T	1.1 T	1.6 T	2.1 T	9 T
Top surface	0.85 T	0.61 T	0.7 T	0.77 T	1.34 T
500 μm above	0.72 T	0.56 T	0.6 T	0.64 T	1.07 T

While the magnetic flux density remains almost constant (and equal to its value calculated in the median plane) in the volume of the ferromagnetic material, it decays as one comes closer to the surface, suddenly drops above the sample surface ($z > 5$ mm), and is close to the value of the non-impregnated sample. The drop increases with μ_r. As a result, the increase of trapped flux measured on the surface of the impregnated sample, with respect to that of the non-impregnated one, is lower than that calculated in the median plane. This explains the discrepancy between the increase of trapped flux density calculated in the median plane after impregnation, and that measured experimentally above the surface. The maximum magnetic flux density calculated in the impregnated sample and in the non-impregnated one are listed in Table 5.3, for fields in the median plane, on the surface (vertical distance equals to 5 mm), and 0.5 mm above the surface. While the maximum magnetic flux density in the median plane increases by 45%, 90%, and by a factor 7 when the relative magnetic permeability is respectively $\mu_r = 1.5$, $\mu_r = 2$, and $\mu_r = 20$, the corresponding increases on the surface drops to 15%, 26%, and to a factor 1.2. A comparison of these calculated increases of maximum trapped flux density and the measurements indicates us that the ferromagnetic powder should exhibit a relative permeability that is on average close to $\mu_r = 2$, since the maximum trapped flux density was measured to be enhanced by 30% on the surface.

Table 5.3 also shows the maximum magnetic flux density in a sample having the same characteristics and no hole. In the median plane, we observe that the drop of maximum trapped flux density induced by the presence of the holes is totally compensated by impregnating the holes with the ferromagnetic powder, even with a relatively low magnetic permeability of $\mu_r = 1.5$. On the top surface, the compensation is obtained for $\mu_r > 2$. These results suggest that the impregnation of a drilled sample with a ferromagnetic powder allows one to reduce the inherent drop of trapped flux that is calculated in Chapter 3. The trapped flux enhancement depends on the value of the relative magnetic permeability of the ferromagnetic powder used for the impregnation: the largest is μ_r, the largest is the gain of trapped flux.

5.2.3   Influence of the volume of impregnated ferromagnetic material

In the above simulation results, only a single sample geometry has been considered. However, in the experiments reported in Section 5.1.2, two samples having a different hole diameter are used. The powder impregnation in Sample (2), with the smallest hole diameter, yields smaller modifications of

Maximum trapped flux calculated at 500 μm above the top surface

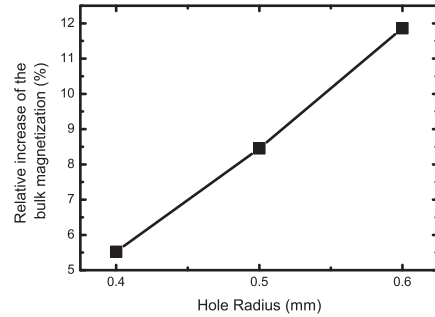| Hole radius (mm)	0.4	0.5	0.6
Non-impregnated sample	560 mT	488 mT	420 mT
Impregnated sample (μ_r=2)	644 mT	574 mT	500 mT
Relative increase	15%	18%	19%

Figure 5.10: *(a)- Maximum trapped magnetic flux density calculated 500 μm above the surface of a non impregnated sample and an impregnated sample ($\mu_r = 2$). The hole radius is respectively 0.4 mm, 0.5 mm and 0.6 mm. (b)- Relative increase of the trapped magnetization (with respect to that of a non-impregnated sample) as a function of the hole radius.*

the magnetic properties than those obtained with Sample (1). In order to discuss this observation on the basis of modelling results, we consider three drilled samples with different hole radii[2]: (i) $r = 0.4$ mm – the same sample as that considered in the previous sections –, (ii) $r = 0.5$ mm, and (iii) $r = 0.6$ mm.

The maximum trapped flux density calculated 500 μm above the top surface is reported in Figure 5.10-(a). The samples are either impregnated (with $\mu_r = 2$) or not. The relative increase with respect to a non-impregnated sample is also indicated. Figure 5.10-(b) shows the relative increase of trapped magnetization in the impregnated samples (with respect to that of the non impregnated ones) as a function of the hole radius. In both situations, we observe that the increase of trapped flux or magnetization depends on the volume of ferromagnetic powder inside the holes. The larger is the hole radius, the larger is that relative increase. Nevertheless, the increase of the hole radius is accompanied by a decay of the maximum magnetic flux density that is trapped in the sample, since the volume of superconducting material is reduced.

5.3   Summary of Chapter 5

Throughout this chapter, we discuss the modifications of the magnetic properties of drilled samples obtained by filling the holes with a ferromagnetic powder. The discussion is based on several experiments and on modelling results obtained with a 3D FEM model. The experimental and simulation results provide qualitative complementary observations that are in good agreement with each other (although the non-linearity of the ferromagnetic material is approximated in the model). We put forward two major advantages to impregnating the holes with a ferromagnetic powder:

1. The magnetization curve of impregnated samples undergoes a counter-clockwise rotation with respect to that of a non-impregnated sample. The concentration of the flux lines inside the hole

---

[2]Note that the modelling of a sample having a smaller radius than $r = 0.4$ mm (such as Sample (2)) is not affordable because the size of the meshing exceeds the largest available computer capacity.

increases the average magnetic flux density in the sample and results in an increase of the bulk magnetization.

2. The trapped flux of impregnated samples is enhanced as compared to that of the non-impregnated ones. The increase of trapped flux has been shown to be larger in the median plane than on the sample surface. The gain of maximum trapped flux and on magnetization obtained in impregnated samples could even be used for reducing the inherent magnetization drop resulting from drilling holes that is discussed in Chapter 3.

We show that the enhancement of the trapping properties of drilled samples by ferromagnetic powder impregnation depends on the relative permeability of the powder. The larger is the relative permeability, the larger is the relative increase of trapped magnetization. In practice, since the magnetization of the ferromagnetic material saturates, it is recommended to choose a material having the largest relative permeability at low fields. Using such a material allows one to still get a quite high value of μ_r when the material is saturated.

Similarly, the effects of the ferromagnetic material on the trapping properties of the drilled samples are larger when the volume ratio of ferromagnetic material increases. Using holes of large diameters allows one to get a larger relative increase of maximum trapped flux. However, there is a compromise to resolve as the samples with large hole diameters are not able to trap a large magnetic flux. The combination of the results presented in Chapter 3 (influence of the hole on the magnetization drop) and in this Chapter should help the designer of a trapped flux magnet to find the optimal hole diameter.

6

Conclusions and outlook

Drilling holes in bulk superconductors primarily aims at facilitating the oxygen annealing process in view of obtaining a high oxygen content, as well as a low density of defects. As a result, both the critical current density and the maximum trapped flux density are enhanced in the sample.

Beside improving the oxygen annealing in bulk samples, the holes are also beneficial for the thermal stability and the mechanical resistance, as the empty space cleared by the holes improves the thermal exchange with the cryofluid and allows the sample to be mechanically reinforced by filling the holes with a resin. However, the holes also modify the magnetic properties of the samples, as they impede the current stream lines and modify the magnetic flux distribution in the drilled sample with respect to that of a plain sample.

Drilled samples were already studied at the time we started the research reported in this manuscript. However, the magnetic properties of these samples were not fully understood. Only few studies reported the modifications of the trapped magnetic flux induced by the holes [61, 89]. They put forward the influence of the size and of the number of holes in the sample, but neither described precisely the modifications of the current stream lines, nor investigated the impact of the mutual position of the holes. These opened questions triggered our thesis work.

Our dissertation aims at a better understanding of the magnetic properties of drilled samples, by considering several methods. We follow two main directions: the numerical modelling and the experimental characterization. In both domains, we develop novel and original methods for gaining access to information that was out of reach with other existing techniques.

The numerical approach to the magnetic properties of drilled samples relies on a home-made algorithm for solving the Bean critical-state model in infinitely extended samples with an arbitrary cross

section, and on a three-dimensional finite-element method using large time steps in the case of samples assuming a power law conductivity that are subjected to linearly varying applied fields. For the experimental characterization, we use classical Hall probe mapping techniques, volume magnetization measurements, and a novel characterizing method that takes advantage of drilled structures so as to probe locally the magnetic field inside the holes with the help of microcoils.

The lessons that may be learned from this study appear at two levels: (1) understanding and enhancing the magnetic properties of drilled samples, and (2) providing indications for an efficient use of the numerical methods applied to bulk HTS samples.

6.1   On the magnetic properties of drilled samples

6.1.1   Influence of the hole lattice on the magnetic properties

The influence of the hole lattice on the magnetic properties of the samples is investigated numerically, starting from the simplest situation from which complexity is gradually added, so as to eventually reproduce the experimental results.

In an infinite sample with a semi-infinite cross section, the presence of a single circular hole placed at a given distance from the interface causes the current stream lines to be modified in a region located beyond that hole in the direction of magnetic flux diffusion. This region of influence is delimited by a parabolic discontinuity line where the direction of the current density changes abruptly, from a region where it flows parallel to the sample border to a region where it flows along circular lines that are concentric with the hole. This modification of the current stream lines leads to an increase of the penetration depth of the applied magnetic flux density in the region of influence of the hole, and causes a decay of the magnetization of the sample. This drop of magnetization scales neither with the surface of the hole ($\propto R^2$, where R is the hole radius), nor with the surface of its parabolic region of influence ($\propto \sqrt{R}$), but as a surface of intermediate size, scaling as $R^{3/2}$.

When two or three holes are involved, the magnetization drop can be minimized by placing the holes along a discontinuity line of their closest neighbour. This rule remains valid in situations involving several holes, whether the sample is of finite or infinite height. Independent of the sample cross section, the arrangement where the holes are placed on the discontinuity lines leads to the smallest magnetization drop with respect to a plain sample having the same dimension and critical current density. The best magnetic properties are achieved with a centered rectangular hole lattice for samples with a rectangular cross section, and with a polar triangular lattice for samples with a circular cross section.

The influence of the hole lattice on the magnetic properties of drilled samples is investigated experimentally on two parallelepipedic YBCO single domains; each of them is drilled after its synthesis by 6 holes that are arranged on two different lattices. The comparison of the trapped flux profile before and after the drilling of the holes reveals that the sample with the centered rectangular hole pattern shows better magnetic properties.

Although the experimental results are in agreement with those predicted by the theory, they must be considered with care. These results are based on the assumption that the critical current density remains unchanged in drilled and plain samples. However, the drilling process routinely takes place before the synthesis of the single domain so as to facilitate the oxygen annealing step. As a result, the current density of the drilled samples has been reported in many cases to exceed that of plain samples synthesized with the same process [6, 84]. Since plain and drilled samples do not have the same J_c, our analysis should be completed by a delicate assessment of the increase of critical current density resulting from the oxygen annealing step. Despite this remark, the results presented in this thesis on the influence of the hole lattice suggest that the magnetization of drilled samples can however be enhanced by adopting the optimal hole arrangement corresponding to the geometry of the sample cross section, whether or not the current density remains constant after the drilling.

6.1.2 Magnetic field inside the holes

Drilled samples offer a unique opportunity to probe locally the magnetic field inside the bulk of the samples with a non-destructive technique. This novel experimental method consists in inserting sensing microcoils inside the holes of a drilled sample subjected to a time-varying magnetic field. The objectives of the method are twofold: (1) to study how the magnetic flux diffuses through the holes, and (2) to determine whether the local magnetic properties measured on the surface (e.g. by Hall probe mapping) are indicative of those in the bulk of the sample.

The magnetic field inside the holes is characterized with two types of magnetic excitations: a low frequency AC field and a pulsed field. The microcoil technique with an AC excitation is used for a local characterization of the bulk magnetic properties of the sample, whereas the technique with a pulsed field excitation reveals features associated with the diffusion of a magnetic pulse in the bulk of the sample.

For an AC applied field of a given amplitude, three regimes of penetration of the magnetic flux inside the holes are observed: (i)- the shielded regime, for which the magnetic flux does not penetrate the hole; (ii)- the gradual penetration regime, for which the magnetic flux density in the hole is measurable and smaller than the applied field; and (iii)- the flux concentration regime, for which the magnetic flux density in the hole is larger than the applied one. The spatial distribution of these penetration regimes is directly associated with the microstructure of the sample. In particular, it is in good agreement with the magnetic properties at the surface, as measured with Hall probe mappings.

The flux concentration regime cannot be predicted with the Bean model analysis in a sample with an infinite height. It occurs in holes that are located at the periphery of efficiently shielded islands and is attributed to the demagnetizing field of these particular islands. The holes offer a return path for the demagnetizing field lines which causes the flux concentration.

Moreover, the characterization of the diffusion of a magnetic pulse inside the holes of a drilled YBCO sample leads to three observations. First, some holes also act as return paths for the demagnetizing field and the magnetic flux density measured in their median plane exhibits features (e.g. flux concentration) that are not predicted by models considering infinitely extended samples. Then, holes located

at the sample edges are found to be penetrated in their median plane sooner than at their surface, while the opposite is found for the other holes. This behaviour may arise from either non-uniform superconducting properties in the sample or from particular thermal boundary conditions at the surface of the sample. Finally, the trapped flux density is measured to be larger in the median plane than on the surface (by a factor of about 2, which depends on the size of the sample), and it allows us to directly estimate the critical current density in the volume of the sample.

6.1.3   Improvement of the trapped flux with ferromagnetic powder inside the holes

In the same manner as a resin impregnation in the holes reinforces mechanically the drilled samples, filling the holes with a ferromagnetic powder improves their magnetic properties. Due to its high magnetic permeability, the ferromagnetic powder modifies the distribution of the trapped magnetic flux density in the sample. In the median plane, the magnetic flux density is concentrated in the impregnated holes where it exceeds the flux density in the superconductor by a factor proportional to the relative permeability of the powder. On the surfaces, the differences between the flux in the superconducting material and in the ferromagnetic powder are smaller than in the bulk. However, the trapped flux on the surface of an impregnated sample is measured and calculated to be larger than that above a drilled sample that is not impregnated.

A modelling of drilled superconductors containing ferromagnetic powder shows that the increase of trapped flux on the sample surface may even compensate the magnetization drop arising from the presence of the holes in the sample. Starting from a synthesized sample, the drilling of the holes reduces its maximum trapped flux, provided the critical current density is not modified by the drilling process. Filling the holes with ferromagnetic powder may help compensating this drop of trapped flux. However, since that finding is only based on simulation results, a further experimental investigation should be carried out in order to confirm it.

6.1.4   General prospects

In previous works related to drilled samples [6, 10, 77, 78], the holes were drilled in the preform without taking into account the influence of their arrangement on the magnetic properties of the samples. The chosen hole arrangement has always arisen from a compromise between the need to have small diameters in order not to impede the growth front and the requirement for a simple regular pattern to be implemented easily on the drilling machine. The results presented in this thesis show that a third parameter should be involved when designing the hole array: the holes should be ideally placed so that they lie on the discontinuity lines of their neighbours.

Since the presence of a hole lattice induces a magnetization drop, the design of the optimal hole lattice should therefore be focused on finding a balance between the increase of critical current obtained with the holes drilled in the preform and the diminution of the magnetization induced by the holes with respect to an ideal sample having the same critical current density and no hole. However, the results obtained by filling the holes with a ferromagnetic powder suggest that the magnetization drop might be suppressed in the impregnated samples. In such a beneficial situation, the compromise for the

design of the hole lattice would be greatly simplified. Further experimental investigations are however needed to confirm these results.

The hole filling with a ferromagnetic powder has nevertheless to be confronted with the results concerning the thermal stability of the drilled structures that are presented in the thesis of P. Laurent [7]. The question that obviously needs to be raised concerns the influence of the powder on the cooling rate of the sample. It would be detrimental to reduce the heat exchange with the cryogenic fluid because of the powder. However, in a non-impregnated sample, the cooling in the holes that results from heat losses in the sample may induce liquid nitrogen to locally boil and form a gas phase in the holes. The cooling efficiency might be affected by the presence of this phase. If it were the case, the presence of the powder would not be so detrimental, provided it exhibits a good thermal conductivity. Filling the hole with a ferromagnetic powder of good thermal conductivity might thus be an advantageous solution.

In the present work, we investigate several features associated with drilled samples, but others also deserve to be considered in a near future. In particular, the study of the thermal stability of the non-impregnated drilled structure presented in the thesis of P. Laurent [7] could also be extended to the case of a pulsed-field activation, where it is well known that a large amount of heat is created by the fast motion of vortices. Our work could serve as a basis for that investigation. A thermal model could be easily introduced in the 3D FEM simulations so as to predict the maximum temperature rise in the drilled sample subjected to a given pulse.

Finally, the measurements of the magnetic field inside the holes reveal that the holes are not penetrated in the same manner. Some specific applications could take advantage of the empty space cleared by the holes. One could imagine inserting small devices that are sensitive to the magnetic noise in the shielded holes so as to reduce the perturbation, or using the flux concentration to increase the magnetic flux applied to the devices.

6.2   On the use of the numerical methods

The study of the magnetic properties of the drilled sample is accompanied by the development of specific numerical models that allow us to successfully conduct the research. While specifically used for assessing the magnetic properties of the drilled samples, these methods are not strictly restricted to this case and possess a wider range of applications.

Moreover, we often consider the specific issue of finding an appropriate numerical method for obtaining an answer to a given question. Thanks to the experience gained through this study, several recommendations may be given with regards to the relevance, advantages and drawbacks of each method.

Three methods of increasing complexity are considered: the numerical Bean model, a two-dimensional, and a three-dimensional finite-element method. The choice of a given numerical method depends on the type of information that is expected from the simulation.

The Bean model is applied with infinite samples of arbitrary cross section where a very strong pinning is

assumed (the flux creep is neglected). This model is solved very fast, but its implementation depends on the sample geometry. An adjustment of the numerical code is required each time the cross section geometry is changed. Even though the demagnetizing effects are neglected, the model provides an accurate estimate for the relative magnetization drop induced by the presence of holes. When the sample height is well larger than the width of its cross section, the Bean model even gives a satisfactory estimate for the local magnetic flux density in the median plane. In the other situations where the height of the sample is comparable to the width of its cross section, the Bean model analysis could only provide a first glimpse of the magnetic properties of a HTS sample.

The 2D FEM is used with the same sample geometries as those used with the Bean model, but with a power law conductivity that takes into account flux creep phenomena. Finite-elements are robust when dealing with the highly non-linear $E - J$ power law, they can be used for any sample geometry, and they are relatively easy to implement in existing software environments. The simulations with the power law conductivity are mandatory as soon as the modelling focuses on the effects related to the electric field dependence of the current density, such as those associated with the sweep rate of the applied magnetic flux density or with the temporal decay of the trapped magnetization. 2D geometries still suffer from the same drawbacks as those observed with the numerical Bean model. Thus, 2D FEM simulations are recommended when the main interest lies in finding the general trend of the modifications of the magnetic properties induced by flux creep related phenomena.

In the situations where the cross section does not exhibit an axial symmetry, the resort to 3D FEM modelling is essential when demagnetizing effects have to be modelled. Such a situation occurs in particular when one looks for an accurate estimate of the local flux density on the surface and in the median plane of a drilled sample, or when the effects of a ferromagnetic material in the holes have to be simulated in that sample. The 3D FEM simulations require large meshing sizes and are time-consuming.

In order to speed up the 3D simulations so as to be carried out in a reasonable calculation time, we propose a method with very large time-steps. In the limit of a linearly increasing field from 0 to B_{max}, the flux distribution inside a 3D HTS superconductor is calculated with a single time-step (two time-steps if the field returns back to zero, so as to simulate the trapped flux distribution). The major drawbacks of the method are that it cannot be used (i), with a HTS sample subjected to an AC or a pulsed magnetic field, and (ii), for calculating the decay of the magnetization due to the flux creep.

When recalling the need of accurate simulations, it is important to keep in mind that the accuracy of the results does not entirely rely on the simulation method. Independent of the method (the numerical Bean model, the 2D FEM, or the 3D FEM), the agreement with the measurements strongly depends on the knowledge of the material parameters (mainly the critical current density). When dealing with HTS bulk melt-textured samples, this may turn out to be a major issue. Besides the fact that the bulk material may exhibit a polycrystalline behaviour for which it is very difficult to extract the material parameters, single domains of YBCO may also exhibit a non-uniform distribution of critical current density that is difficult to simulate.

The 3D numerical method presented in this dissertation fits in line with the current development of the 3D modelling of HTS [140, 225]. It prepares the ground for a more complete model that would

incorporate the effects associated with the current parallel to the magnetic field lines. In particular, one could already use our 3D model to check whether or not the current may have a component parallel to the magnetic field in drilled structures. It would then be interesting to estimate the magnitude of the corrections that would be brought by a model taking longitudinal components into account [136].

6.3 General conclusion

In addition to facilitate the oxygen annealing and the thermal stability of the sample, the presence of holes in bulk HTS suggests several other ways for enhancing the performance of HTS trapped field magnets. The maximum trapped field in the magnet may be significantly increased thanks to an optimal hole arrangement and/or an impregnation of the holes with ferromagnetic powder. The microcoil technique for probing the magnetic field inside the holes provides a better knowledge of the propagation of a magnetic pulse inside the bulk of the sample, so as to better control the pulsed field activation of the magnet. The results of this thesis aim at reinforcing the interests of drilled samples for trapped field magnet applications and are believed to encourage other scientists to proceed with these structures.

<div style="text-align: right; font-size: 4em; color: gray; font-weight: bold;">A</div>

Brandt method for the magnetic field penetration into hollow cylinders of finite height

In this Appendix, we present a numerical method based on the Green's functions for solving the magnetic field penetration in superconducting samples with an axial symmetry and whose conductivity is modelled by an $E(J)$ power law. The method has been developped by E.H. Brandt [135] and the results obtained with tubular geometries have been validated experimentally by S. Denis [126].

We consider a superconducting cylinder with a finite height and a centered hole, i.e. a superconducting tube, that is subjected to a magnetic field parallel to its z-axis, $\mathbf{B}_a = B_a \mathbf{e}_z$ (see Figure A.1). The cylinder radius is a and its height is h. The inner diameter of the tube is denoted by r_{int}.

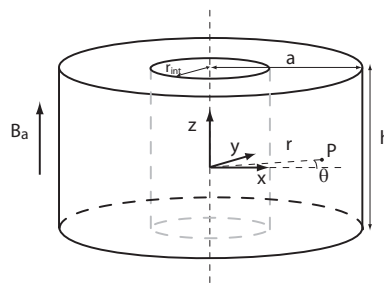Because of the axial symmetry, the current is flowing along the azimuthal direction parallel to the

Figure A.1: *Sketch of the cylindrical tube of radius a and height h. The inner radius is r_{int}. The applied magnetic field is parallel to the cylinder axis. A point P in the tube is localized by its cylindrical coordinates (r, θ, z).*

electric field and does not depend on the angular coordinate θ. The current and the electric field are written as

$$\mathbf{J} = J(r, z)\mathbf{e}_\theta \quad \text{and} \quad \mathbf{E} = E(r, z)\mathbf{e}_\theta, \tag{A.1}$$

where $\mathbf{e}_\theta$ is the unit vector parallel to the azimuthal direction.

As usual, the magnetic field is split into two contributions: the applied magnetic field $\mathbf{B}_a$ and the self-field induced by the currents in the superconductor, $\mathbf{B}_{self}$, which is identically null far from the sample. The total magnetic field is given by

$$\mathbf{B}(r, z) \;=\; B_a\mathbf{e}_z + \mathbf{B}_{self}. \tag{A.2}$$

According to symmetry, the self induced magnetic field does not depend on the angular coordinate and has no azimuthal component, that is

$$\mathbf{B}_{self}(r, z) \;=\; B_r(r, z)\mathbf{e}_r + B_z(r, z)\mathbf{e}_z. \tag{A.3}$$

We introduce the vector potential $\mathbf{A}$ such that

$$\nabla \times \mathbf{A} \;=\; \mathbf{B}_{self} \quad \text{and} \quad \nabla \cdot \mathbf{A} = 0. \tag{A.4}$$

$\mathbf{B}_{self} = 0$ infinitely far from the sample and the vector potential $\mathbf{A}$ is assumed to be also identically null on this region. Again, the axial symmetry implies that $\mathbf{A}$ has only an azimuthal component which does not depend on the angular coordinate,

$$\mathbf{A} \;=\; A(r, z)\mathbf{e}_\theta. \tag{A.5}$$

The vector potential related to the applied magnetic field assumes the following form in the Coulomb gauge

$$\nabla \times \mathbf{A}_a \;=\; B_a\mathbf{e}_z \quad \Rightarrow \quad \mathbf{A}_a = -\frac{r}{2}B_a\mathbf{e}_\theta. \tag{A.6}$$

Assuming the constitutive law $\mathbf{B} = \mu_0\mathbf{H}$ (which boils down to neglect H_{c1}, see [174]), the substitution of the vector potential into the Ampere's equation, $\nabla \times \mathbf{H} = \mathbf{J}$, yields

$$
\begin{aligned}
\mu_0 J(r, z)\mathbf{e}_\theta \;&=\; \nabla \times \mathbf{B} \\
&=\; \nabla \times (B_a\mathbf{e}_z + \mathbf{B}_{self}) \\
&=\; \nabla \times \mathbf{B}_{self} \\
&=\; \nabla \times \nabla \times \mathbf{A} \\
&=\; \nabla(\nabla \cdot \mathbf{A}) - \Delta\,\mathbf{A} \\
&=\; -\Delta\,\mathbf{A}.
\end{aligned}
\tag{A.7}
$$

$$\Rightarrow \quad \boxed{\Delta\mathbf{A}(r, z) = -\mu_0\mathbf{J}(r, z)} \tag{A.8}$$

The elliptic equation (A.8) can be solved using a Green's functions approach. The Green function corresponding to the Laplacian equation in a three-dimensional geometry with the above boundary conditions reads

$$G(\mathbf{r}_1, \mathbf{r}_2) \quad = \quad -1/(4\pi|\mathbf{r}_1 - \mathbf{r}_2|). \tag{A.9}$$

The solution corresponding to Equation (A.8) is then given by

$$\mathbf{A}(r, z) \quad = \quad -\mu_0 \int_{r_{int}}^{a} \int_{-h/2}^{h/2} \int_{0}^{2\pi} G(r, \theta, z, r', \theta', z') \mathbf{J}(r', z') dr' d\theta' dz' \tag{A.10}$$

The integral domain is limited to the support of the current density, i.e. the superconducting region. We project the vector equation (A.10) onto the azimuthal direction $\mathbf{e}_\theta$ corresponding to the point (r,z). For the sake of convenience, we introduce a new variable $\varphi = \theta - \theta'$.

$$A(r, z) \quad = \quad -\mu_0 \int_{r_{int}}^{a} \int_{-h/2}^{h/2} \int_{0}^{2\pi} \frac{-1}{4\pi} \frac{r' \cos\varphi J(r', z')}{(z'^2 + r^2 + r'^2 - 2rr' \cos\varphi)^{1/2}} d\varphi dz' dr' \tag{A.11}$$

The kernel integral $Q(r, z, r'z')$, defined as

$$Q(r, z, r', z') \quad = \quad \int_{0}^{2\pi} \frac{-1}{4\pi} \frac{r' \cos\varphi}{(z'^2 + r^2 + r'^2 - 2rr' \cos\varphi)^{1/2}} d\varphi, \tag{A.12}$$

can be evaluated numerically for each pairs (r, z, r', z') of points belonging to the grid formed in the $r - z$ plane of the tube

Substituting (A.12) into (A.11), it yields

$$A(r, z) \quad = \quad -\mu_0 \int_{r_{int}}^{a} \int_{-h/2}^{h/2} Q(r, z, r', z') J(r', z') dz' dr'. \tag{A.13}$$

We now introduce the Faraday's law for obtaining a second relationship between $\mathbf{A}$ and $\mathbf{J}$

$$\nabla \times \mathbf{E} \quad = \quad -\dot{\mathbf{B}} = -\nabla \times \left(\dot{\mathbf{A}} + \dot{\mathbf{A}}_a \right), \tag{A.14}$$

and we express it in the form

$$E(r, z) = -\dot{A}(r, z) + \frac{r}{2} \dot{B}_a. \tag{A.15}$$

Since, the electric field depends on the current with the non-linear power law

$$E[J(r, z, t)] \quad = \quad E_c \left(\frac{J(r, z, t)}{J_c} \right)^n, \tag{A.16}$$

we thus obtain a relationship between $\dot{\mathbf{A}}$ and $\mathbf{J}$. Let us introduce it into Eq. (A.13), it yields

$$E[J(r, z, t)] \quad = \quad \mu_0 \int_{r_{int}}^{a} \int_{-h/2}^{h/2} Q(r, z, r', z') \dot{J}(r', z', t) dz' dr' + \frac{r}{2} \dot{B}_a(t). \tag{A.17}$$

In order to have an explicit expression for the time evolution of the current density, we need to invert this latter equation. For this purpose, Eq. (A.17) is discretized on the two-dimensional grid with spatial steps Δr and Δz, yielding

$$E[J_i(t)] \quad = \quad \mu_0 \Delta r \Delta z \sum_j Q_{ij} \dot{J}_j(t) + \frac{r_i}{2} \dot{B}_a(t), \tag{A.18}$$

where indices i, j run over all the points of the two-dimensional grid. By inverting directly this matrix equation, we get

$$\boxed{J_i(t) = \frac{1}{\mu_0 \Delta r \Delta z} \sum_j Q_{ij}^{-1} \left\{ E[J_j(t)] - \frac{r_j}{2} \dot{B}_a(t) \right\}.} \tag{A.19}$$

We obtain therefore an explicit time equation governing the time evolution of the supercurrents in the superconducting tube. Imposing the initial condition $J_i|_{t=0} = 0$, the current density is numerically integrated in the time domain using

$$J_i(t + \Delta t) \quad \cong \quad J_i(t) + \dot{J}_i(t) \Delta t \tag{A.20}$$

The choice of the time step is crucial for the convergence of the method. An adaptative time step procedure is described in Ref [135] and makes the algorithm converge toward a solution that reproduces well the experimental data.

B

Characterization of the ferromagnetic powder

The magnetic permeability of the ferromagnetic powder that is used as a filling material for impregnating the drilled samples, as discussed in Chapter 5, is measured with a bespoke setup. A closed magnetic circuit, consisting of an empty electric cable sheath that is shaped as a torus, with an opening end perpendicular to the torus, is filled with the ferromagnetic powder. The opening end is used for pressing the powder in the magnetic circuit, so as to prevent from the formation of an air gap. The magnetic circuit has a total length of $\ell = 20$ cm. Two coils are turned around the sheath: one with $N_1 = 800$ turns for inducing an AC magnetic field in the closed magnetic circuit, we will refer to it as coil 1, and another one, referred as coil 2, with $N_2 = 100$ turns for probing that magnetic field. Figure B.1 shows (a) a photograph of the permeameter, with the toroïdal magnetic core and both coils and (b) the schematic illustration of that setup.
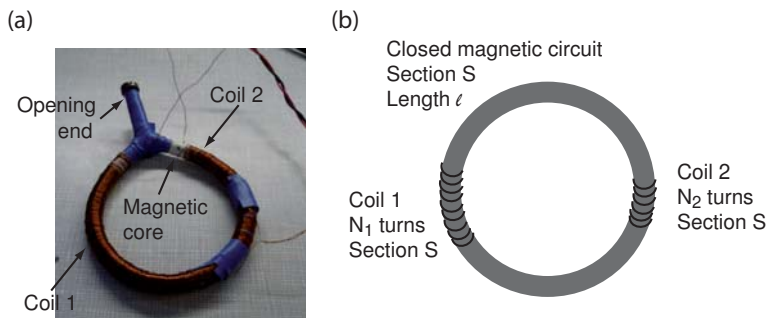

Figure B.1: (a)- Picture of the closed magnetic circuit made of the ferromagnetic powder inserted via the opening end in a plastic sheath. Two coils are wound around the sheath. (b)- Schematic illustration of the magnetic circuit.
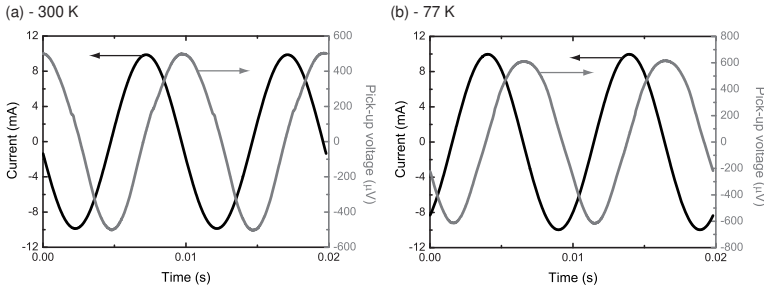
Figure B.2: *Time signal of the applied current in the primary coil (black line) and of the pick-up voltage across the secondary coil (grey line) at* 300 K *(a), and* 77 K *(b).*

According to Hopkinson's law, coil 1 that carries an AC current with an amplitude I induces a magnetic flux ϕ in the magnetic core that reads

$$N_1 I \;\; = \;\; \frac{\ell}{\mu S}\phi.$$

(B.1)

The electromotive force across coil 2, V, is proportional to the time derivative of the magnetic flux inside the core. We thus differentiate Equation (B.1) with respect to time,

$$N_1 \frac{dI}{dt} \;\; = \;\; \frac{\ell}{\mu S}\frac{V}{N_2}.$$

(B.2)

The relative magnetic permeability, $\mu_r = \mu/\mu_0$, is then given by,

$$\mu_r \;\; = \;\; \frac{V\ell}{\mu_0 \omega I N_1 N_2 S},$$

(B.3)

where ω is the pulsation of the exciting current I.

The induced emf across coil 2 is reproduced in Figure B.2 together with the current flowing through the exciting coil, at a temperature of 300 K (a) and of 77 K (b). The frequency of the excitation is 101 Hz. We extract the relative permeability from these data, and we find that $\mu_r = 23$ and $\mu_r = 28$ at $T = 300$ K and $T = 77$ K, respectively.

The magnetic permeabilty of the powder may also be extracted from the measurement of the inductance of the coils. Actually, the inductance L of the coil 1 (or, similarly, of the coil 2) is given by

$$L \;\; = \;\; \frac{N_1^2 \mu S}{\ell}.$$

(B.4)

We measure the inductance of coil 1 at 101 Hz, and we find a relative permeability of $\mu_r = 25$ and $\mu_r = 28$ at $T = 300$ K and $T = 77$ K, respectively. Both experimental techniques provide matching results.

Bibliography

[1] H. Kamerlingh-Onnes, "The superconductivity of mercury," *Comm. Phys. Lab. Univ. Leiden*, vol. 124, 1911.

[2] G. Krabbes, G. Fuchs, W.-R. Canders, H. May, and R. Palka, *High temperature superconductor bulk materials*. Wiley-VCH, 2006.

[3] B. Oswald, K.-J. Best, M. Setzer, M. Söll, W. Gawalek, A. Gutt, L. Kovalev, G. Krabbes, L. Fisher, and H. Freyhardt, "Reluctance motors with bulk HTS material," *Supercond. Sci. Technol.*, vol. 18, p. S24, 2005.

[4] S. Earnshaw, "On the nature of the molecular forces which regulate the constitution of the luminiferous ether," *Trans. Camb. Phil. Soc.*, vol. 7, p. 97, 1842.

[5] Z. Deng, J. Wang, J. Zheng, Q. Lin, Y. Zhang, and S. Wang, "Maglev performance of a double-layer bulk high temperature superconductor above a permanent magnet guideway," *Supercond. Sci. Technol.*, vol. 22, p. 055003, 2009.

[6] X. Chaud, D. Bourgault, D. Chateigner, P. Diko, L. Porcar, A. Villaume, A. Sulpice, and R. Tournier, "Fabrication and characterization of thin-wall YBCO single-domain samples," *Supercond. Sci.Technol.*, vol. 19, p. S590, 2006.

[7] P. Laurent, *Thermal effects in bulk high-temperature superconductors subjected to AC magnetic fields*. PhD thesis, University of Liege, 2009.

[8] M. Morita, S. Takebayashi, M. Tanaka, K. Kimura, K. Miyamoto, and K. Sawano, *Processing Advances in Superconductivity*. 1990.

[9] P. Laurent, J.-P. Mathieu, B. Mattivi, J.-F. Fagnard, S. Meslin, J. Noudem, M. Ausloos, R. Cloots, and P. Vanderbemden, "Study by Hall probe mapping of the trapped flux modification produced by local heating in YBCO HTS bulks for different surface/volume ratios," *Supercond. Sci. Technol.*, vol. 18, p. 1047, 2005.

[10] X. Chaud, D. Isfort, L. Porcar, and R. Tournier, "Growth of YBCO single domains through an array of holes for FCL c-axis superconducting elements," *J. E. Ceram. Soc.*, vol. 25, p. 2955, 2005.

[11] A. Campbell and J. Evetts, "Flux vortices and transport currents in type II superconductors," *Adv. Phys.*, vol. 21, p. 199, 1972.

[12] J. D. Doss, *Engineer's guide to high-temperature superconductivity*. Wiley-Interscience, 1989.

[13] G. Aschermann, E. Friederich, E. Justi, and J. Kramer *Physik. Z.*, vol. 42, p. 349, 1941.

[14] V. Kovachev, *Energy dissipation in superconducting materials*. Oxford University Press, 1991.

[15] J. G. Bednorz and K. A. Müller, "Possible high-Tc superconductivity in the Ba-La-Cu-O system," *Z. Phys. B*, vol. 64, p. 189, 1986.

[16] M. K. Wu, J. R. Ashburn, C. J. Torng, P. H. Hor, R. L. Meng, L. Gao, Z. J. Huang, Y. Q. Wang, and C. W. Chu, "Superconductivity at 93 K in a new mixed-phase Y-Ba-Cu-O compound system at ambient pressure," *Phys. Rev. Lett.*, vol. 58, p. 908, 1987.

[17] A. Schilling, M. Cautoni, J. D. Gao, and H. R. Hott, "Superconductivity above 130K in the Hg-Ba-Ca-Cu-O system," *Nature*, vol. 363, p. 56, 1993.

[18] J. Nagamatsu, N. Nakagawa, T. Muranaka, Y. Zenitani, and J. Akimitsu, "Superconductivity at 39 K in magnesium diboride," *Nature*, vol. 63, p. 410, 2001.

[19] A. P. Malozemoff, D. T. Verebelyi, S. Fleshler, D. Aized, and D. Yu, "HTS wire: status and prospects," *Physica C*, vol. 386, p. 424, 2003.

[20] R. M. Scanlan, A. P. Malozemoff, and D. C. Larbalestier, "Superconducting materials for large scale applications," *Proceedings of IEEE*, vol. 92, p. 1639, 2004.

[21] P. M. Grant, "Superconductivity: Prospecting for an iron age," *Nature*, vol. 453, p. 1000, 2008.

[22] Y. Kamihara, T. Watanabe, M. Hirano, and H. Hosono, "Iron-based layered superconductor La($O_{1-x}F_x$)FeAs ($x = 0.05 - 0.12$) with $T_c = 26$ K," *J. Am. Chem. Soc.*, vol. 130, p. 3296, 2008.

[23] R. H. Liu, G. Wu, T. Wu, D. F. Fang, H. Chen, S. Y. Li, K. Liu, Y. L. Xie, X. F. Wang, R. L. Yang, L. Ding, C. He, D. L. Feng, and X. H. Chen, "Anomalous transport properties and phase diagram of the FeAs-based SmFeAs$O_{1-x}F_x$ superconductors," *Phys. Rev. Lett.*, vol. 101, p. 087001, 2008.

[24] W. Meissner and R. Ochsenfeld, "Ein neuer Effekt bei Eintritt der Supraleitfhigkeit," *Naturwissenschaften*, vol. 21, p. 787, 1933.

[25] T. Orlando and K. Delin, *Foundations of Applied Superconductivity*. Addison-Wesley, 1991.

[26] F. London and H. London, "The electromagnetic equations of the superconductor," *Proc. Roy. Soc.*, vol. A149, p. 71, 1935.

[27] C. Gorter and H. B. G. Casimir, "The thermodynamics of the superconducting state," *Phys. Z.*, vol. 35, p. 963, 1934.

[28] J. Bardeen, L. N. Cooper, and J. R. Schrieffer, "Microscopic theory of superconductivity," *Phys. Rev.*, vol. 106, p. 162, 1957.

[29] J. W. Rohlf, *Modern Physics from A to Z*. Wiley, 1994.

[30] T. Akune, R. Maeda, N. Sakamoto, and K. Funaki, "AC susceptibilities in NbTi multifilamentary wires with Cu and CuMn matrices," *IEEE Trans. Appl. Supercond.*, vol. 11, p. 2764, 2001.

[31] C. Böhmer, G. Brandsttter, and H. W. Weber, "The lower critical field of high-temperature superconductors," *Supercond. Sci. Technol.*, vol. 10, p. A1, 1997.

[32] H. F. Hess, R. B. Robinson, R. C. Dynes, J. M. Valles, and J. V. Waszczak, "Scanning-tunneling-microscope observation of the Abrikosov flux lattice and the density of states near and inside a fluxoid," *Phys. Rev. Lett.*, vol. 62, p. 214, 1989.

[33] P. L. Gammel, D. J. Bishop, G. J. Dolan, J. R. Kwo, C. A. Murray, L. F. Schneemeyer, and J. V. Waszczak, "Observation of hexagonally correlated flux quanta in $YBa_2Cu_3O_7$," *Phys. Rev. Lett.*, vol. 59, p. 2592, 1987.

[34] A. Abrikosov, "On the magnetic properties of superconductors of the second group," *Sov. Phys. JETP*, vol. 5, p. 1174, 1957.

[35] M. Cyrot and D. Pavuna, *Introduction to superconductivity and high-T_c materials*. World Scientific, 1992.

[36] V. Ginzburg and L. Landau, "On the theory of superconductivity," *Zh. Eksp. Teor. Fiz.*, vol. 20, p. 1064, 1950.

[37] A. R. Strnad, C. F. Hempstead, and Y. B. Kim, "Dissipative mechanism in type-II supercon-ductors," *Phys. Rev. Lett.*, vol. 13, p. 794, 1964.

[38] C. P. Bean, "Magnetization of hard superconductors," *Phys. Rev. Lett.*, vol. 8, p. 250, 1962.

[39] C. P. Bean, "Magnetization of high-field superconductors," *Rev. Mod. Phys.*, vol. 36, p. 31, 1964.

[40] Y. Kim, C. Hempstead, and A. Strnad, "Flux creep in hard superconductors," *Phys. Rev.*, vol. 131, p. 2486, Sept. 1963.

[41] H. Küpfer, S. N. Gordeev, W. Jahn, R. Kresse, R. Meier-Hirmer, T. Wolf, A. A. Zhukov, K. Salama, and D. Lee, "Phase diagram of flux creep in melt-textured and single-crystalline $YBa_2Cu_3O_{7-\delta}$," *Phys. Rev. B*, vol. 50, p. 7016, 1994.

[42] M. V. Feigel'man, V. B. Geshkenbein, A. I. Larkin, and V. M. Vinokur, "Theory of collective flux creep," *Phys. Rev. Lett.*, vol. 63, p. 2303, 1989.

[43] Y. Yeshurun, A. P. Malozemoff, and A. Shaulov, "Magnetic relaxation in high-temperature superconductors," *Rev. Mod. Phys.*, vol. 68, p. 911, 1996.

[44] T. Nattermann, "Scaling approach to pinning: Charge density waves and giant flux creep in superconductors," *Phys. Rev. Lett.*, vol. 64, p. 2454, 1990.

[45] G. Blatter, M. V. Feigel'man, V. B. Geshkenbein, A. I. Larkin, and V. M. Vinokur, "Vortices in high-temperature superconductors," *Rev. Mod. Phys.*, vol. 66, p. 1125, 1994.

[46] J. Gilchrist, "Penetration of time-varying fields into high-temperature superconductors," *Supercond. Sci. Technol.*, vol. 3, p. 1993, 1990.

[47] J. Z. Sun, C. B. Eom, B. Lairson, J. C. Bravman, and T. H. Geballe, "Magnetic relaxation, current-voltage characteristics, and possible dissipation mechanisms for high-Tc superconducting thin films of Y-Ba-Cu-O," *Phys. Rev. B*, vol. 43, p. 3002, 1991.

[48] J. Rhyner, "Magnetic properties and AC-losses of superconductors with power law current-voltage characteristics," *Physica C*, vol. 212, p. 292, 1993.

[49] E. Talantsev, N. Strickland, P. Hoefakker, J. Xia, and N. Long, "Critical current anisotropy for second generation HTS wires," *Current Applied Physics*, vol. 8, p. 388, 2008.

[50] H. Yamasaki and Y. Mawatari, "Current-voltage characteristics and flux creep in melt-textured $YBa_2Cu_3O_{7-\delta}$," *Supercond. Sci. Technol.*, vol. 13, p. 202, 2000.

[51] J.-F. Fagnard, M. Dirickx, M. Ausloos, G. Lousberg, B. Vanderheyden, and P. Vanderbemden, "Magnetic shielding properties of high-Tc superconducting hollow cylinders: Experimental and modelling results in axial and transverse magnetic field configurations," *Supercond. Sci. Technol.*, vol. 22, p. 105002, 2009.

[52] D. Zola, M. Polichetti, C. Senatore, T. Di Matteo, and S. Pace, "Hysteresis losses in BSCCO(2223)/Ag multifilamentary tapes," *Physica C*, vol. 372-376, p. 1823, 2002.

[53] A. Malozemoff, S. Fleshler, M. Rupich, C. Thieme, X. Li, W. Zhang, A. Otto, J. Maguire, D. Folts, J. Yuan, H.-P. Kraemer, W. Schmidt, M. Wohlfart, and H.-W. Neumueller, "Progress in high temperature superconductor coated conductors and their applications," *Supercond. Sci. Technol.*, vol. 21, p. 034005, 2008.

[54] Y. Iye, "How anisotropic are the cuprate high T_c superconductors ?," *Comments Cond. Mat. Phys.*, vol. 16, p. 89, 1992.

[55] A. Campbell and D. Cardwell, "Bulk high temperature superconductors for magnet applications," *Cryogenics*, vol. 37, p. 567, 1997.

[56] P. Vanderbemden, *Determination of critical current in bulk high-temperature superconductors by magnetic flux profile measuring methods*. PhD thesis, University of Liege, 1999.

[57] M. Tomita, M. Murakami, K. Sawa, and Y. Tachi, "Effect of resin impregnation on trapped field and levitation force of large-grain bulk YBaCuO superconductors," *Physica C*, vol. 357-360, p. 690, 2001.

[58] M. Sawamura, M. Morita, and H. Hirano, "A new method for multiseeding REBaCuO superconductor," *Supercond. Sci. Technol.*, vol. 17, p. S418, 2004.

[59] W. Lo, C. Dewhurst, D. Cardwell, P. Vanderbemden, R. Doyle, and D. Astill, "Growth features and intergranular connectivity of melt processed YBCO," *Applied Superconductivity*, vol. 4, p. 507, 1996.

[60] R. Cloots, A. Dang, P. Vanderbemden, A. Vanderschueren, H. Bougrine, H. Vander-schueren, A. Rulmont, and M. Ausloos, "Field percolation and high current density in 80/20 $DyBa_2Cu_3O_{7-x}$/$DyBaCuO_5$ bulk magnetically textured composite ceramics," *Z. Phys. B*, vol. 100, p. 551, 1996.

[61] S. Haindl, F. Hengstberger, H. Weber, S. Meslin, J. Noudem, and X. Chaud, "Hall probe mapping of melt processed superconductors with artificial holes," *Supercond. Sci. Technol.*, vol. 19, p. 108, 2006.

[62] R. Tournier, E. Beaugnon, O. Belmont, X. Chaud, D. Bourgault, D. Isfort, L. Porcar, and P. Tixador, "Processing of large $YBa_2Cu_3O_{7-x}$ single domains for current-limiting applications," *Supercond. Sci. Technol.*, vol. 13, p. 886, 2000.

[63] T. Aselage and K. Keefer, "Liquidus relations in Y-Ba-Cu oxides," *J. Mater. Res.*, vol. 6, p. 1279, 1988.

[64] S. Jin, T. Tiefel, R. Sherwood, M. Davis, R. van Dover, G. Kammlott, R. Fastnacht, and H. Keith, "High critical currents in Y-Ba-Cu-O superconductors," *Appl. Phys. Lett.*, vol. 52, p. 2074, 1988.

[65] K. Salama, V. Selvamanickam, L. Gao, and K. Sun, "High current density in bulk $YBa_2Cu_3O_x$ superconductor," *Appl. Phys. Lett.*, vol. 54, p. 2352, 1989.

[66] P. McGinn, W. Chen, N. Zhu, M. Lanagan, and U. Balachandran, "Microstructure and critical current density of zone melt textured $YBa_2Cu_3O_{6+x}$," *Appl. Phys. Lett.*, vol. 57, p. 1455, 1990.

[67] S. Meslin, *Infiltration et croissance des céramiques $YBa_2Cu_3O_{7-\delta}$ texturées à structure per-forée : relations microstructures et propriétés supraconductrices.* PhD thesis, University of Caen (France), 2006.

[68] S. Marinel, J. Wang, I. Monot, M. Delamare, J. Provost, and G. Desgardin, "Top-seeding melt texture growth of single-domain superconducting $YBa_2Cu_3O_{7-\delta}$ pellets," *Supercond. Sci. Technol.*, vol. 10, p. 147, 1997.

[69] D. Lee, V. Selvamanickam, and K. Salama, "Influences of Y_2BaCuO_5 particle size and content on the transport critical current density of $YBa_2Cu_3O_x$ superconductor," *Physica C*, vol. 202, p. 83, 1992.

[70] E. Reddy, N. Hari Babu, Y. Shi, and D. Cardwell, "Effect of size, morphology and crystallinity of seed crystal on the nucleation and growth of single grain YBaCuO," *J. Euro. Ceram. Soc.*, vol. 25, p. 2935, 2005.

[71] P. Diko, N. Pelerin, and P. Odier, "Microstructure analysis of melt-textured $YBa_2Cu_3O_{7-x}$ ceramics by polarized light microscopy," *Physica C*, vol. 247, p. 169, 1995.

[72] P. Diko and G. Krabbes, "Formation of c-macrocracks during oxygenation of TSMG $YBa_2Cu_3O_7$/Y_2BaCuO_5 single-grain superconductors," *Physica C*, vol. 399, p. 151, 2003.

[73] P. Diko, "Growth-related microstructure of melt-grown $REBa_2Cu_3O_y$ bulk superconductors," *Supercond. Sci. Technol.*, vol. 13, p. 1202, 2000.

[74] P. Diko and G. Krabbes, "Macro-cracking in melt-grown YBaCuO superconductor induced by surface oxygenation," *Supercond. Sci. Technol.*, vol. 16, p. 90, 2003.

[75] D. Isfort, X. Chaud, R. Tournier, and G. Kapelski, "Cracking and oxygenation of YBaCuO bulk superconductors: application to c-axis elements for current limitation," *Physica C*, vol. 390, p. 341, 2003.

[76] J. G. Noudem, S. Meslin, C. Harnois, D. Chateigner, and X. Chaud, "Melt textured $YBa_2Cu_3O_y$ bulks with artificially patterned holes: a new way of processing c-axis fault current limiter meanders," *Supercond. Sci. Technol.*, vol. 17, p. 931, 2004.

[77] C. Harnois, S. Meslin, J. Noudem, D. Chateigner, B. Ouladdiaf, and X. Chaud, "Shaping of melt textured samples for fault current limiters," *IEEE Trans. Appl. Supercond.*, vol. 15, p. 3094, 2005.

[78] X. Chaud, S. Meslin, J. Noudem, C. Harnois, L. Porcar, D. Chateigner, and R. Tournier, "Isothermal growth of large YBaCuO single domains through an artificial array of holes," *J. Crystal Growth*, vol. 275, p. e855, 2005.

[79] P. Diko, S. Kracunovska, L. Ceniga, J. Bierlich, M. Zeisberger, and W. Gawalek, "Microstructure of top seeded melt-grown YBCO bulks with holes," *Supercond. Sci. Technol.*, vol. 18, p. 1400, 2005.

[80] G. Krabbes, W. Bieger, U. Wiesner, M. Ritschel, J. Hauck, and H. Altenburg, "Representative sections in the T-x phase diagram of the system Y-Ba-Cu-O," *Physica C*, vol. 185-189, p. 503, 1991.

[81] M. Tomita and M. Murakami, "High-temperature superconductor bulk magnets that can trap magnetic fields of over 17 T at 29 K," *Nature*, vol. 421, p. 517, 2003.

[82] G. P. Lousberg, J.-F. Fagnard, M. Ausloos, P. Vanderbemden, and B. Vanderheyden, "Modification of the trapped field in bulk HTS as a result of the drilling of a pattern of artificial holes," *accepted in J. Phys.: Conf. Series*, 2009.

[83] X. Chaud, Y. Savchuk, N. Sergienko, T. Prikhna, and P. Diko, "High-pressure oxygenation of thin-wall YBCO single-domain samples," *J. Phys.: Conf. Ser.*, vol. 97, p. 012043, 2008.

[84] C. Zhang, X. Chaud, E. Beaugnon, and L. Zhou, "Bulk YBCO growth monitored by in situ high-temperature magnetic susceptibility," *J. Phys.: Conf. Ser.*, vol. 97, p. 012040, 2008.

[85] S. Meslin, C. Harnois, C. Chubilleau, D. Horvath, D. Grossin, E. Suddhakar, and J. Noudem, "Shaping and reinforcement of melt textured $YBa_2Cu_3O_{7-\delta}$ superconductors," *Supercond. Sci. Technol.*, vol. 19, p. S585, 2006.

[86] M. Tomita, M. Murakami, and K. Katagiri, "Reliability of mechanical properties for bulk superconductors with resin impregnation," *Physica C*, vol. 378-381, p. 783, 2002.

[87] H. Yong and Y.-H. Zhou, "Elliptical hole in a bulk superconductor under electromagnetic forces," *Supercond. Sci. Technol.*, vol. 22, p. 025018, 2009.

[88] T. H. Johansen, C. Wang, Q. Y. Chen, and W.-K. Chu, "Enhancement of tensile stress near a hole in superconducting trapped-field magnets," *J. Appl. Phys.*, vol. 88, p. 2730, 2000.

[89] E. Bartolomé, X. Granados, T. Puig, X. Obradors, E. Reddy, and S. Kracunovska, "Critical state of YBCO superconductors with artificially patterned holes," *IEEE Trans. Appl. Supercond.*, vol. 15, p. 2775, 2005.

[90] N. Lee, G. Jang, C. Kim, T. Sung, Y. Han, and S. Jung, "The effects of artificial holes with different diameters on the surface magnetic properties in YBCO superconductor," *Physica C*, vol. 463, p. 320, 2007.

[91] C. Joos, J. Albrecht, H. Kuhn, S. Leonhardt, and H. Kronmüller, "Magneto-optical studies of current distributions in high-Tc superconductors," *Rep. Prog. Phys.*, vol. 65, p. 651, 2002.

[92] T. Schuster, H. Kuhn, E. Brandt, M. Indenbom, M. Koblischka, and M. Konczykowski, "Flux motion in thin superconductors with inhomogeneous pinning," *Phys. Rev. B*, vol. 50, p. 16684, 1994.

[93] A. Goya, D. F. Lee, F. A. List, E. D. Specht, R. Feenstra, M. Paranthaman, X. Cui, S. Lu, P. M. Martin, D. M. Kroeger, D. K. Christen, B. W. Kang, D. P. Norton, C. Park, D. T. Verebelyi, J. R. Thompson, R. K. Williams, T. Aytug, and C. Cantoni, "Recent progress in the fabrication of high-J_c tapes by epitaxial deposition of YBCO on RABiTS," *Physica C*, vol. 357-360, p. 903, 2001.

[94] K. Ohmatsu, K. Muranaka, S. Hahakura, T. Taneda, K. Fujino, H. Takei, Y. Sato, K. Matsuo, and Y. Takahashi, "Development of in-plane aligned YBCO tapes fabricated by inclined substrate deposition," *Physica C*, vol. 357-360, p. 946, 2001.

[95] R. Hott, *High temperature superconductivity, 2. Engineering applications*. Springer, 2004.

[96] T. Masuda, H. Yumura, M. Watanabe, H. Takigawa, Y. Ashibe, C. Suzawa, H. Ito, M. Hirose, K. Sato, S. Isojima, C. Weber, R. Lee, and J. Moscovic, "Fabrication and installation results for Albany HTS cable," *IEEE Trans. Appl. Supercond.*, vol. 17, p. 1648, 2007.

[97] T. Masuda, H. Yumura, and M. Watanabe, "Recent progress of HTS cable project," *Physica C*, vol. 468, p. 2014, 2008.

[98] J. Demko, I. Sauer, D. James, M. Gouge, D. Lindsay, M. Roden, J. Tolbert, D. Willen, C. Traeholt, and C. Nielsen, "Triaxial HTS cable for the AEP bixby project," *IEEE Trans. Appl. Supercond.*, vol. 17, p. 2047, 2007.

[99] J.-F. Maguire, F. Schmidt, S. Bratt, T. Welsh, J. Yuan, A. Allais, and F. Hamber, "Development and demonstration of a HTS power cable to operate in the Long Island power authority transmission grid," *IEEE Trans. Appl. Supercond.*, vol. 17, p. 1529, 2007.

[100] Y. Li, J. Reeves, X. Xiong, Y. Qiao, Y. Xie, P. Hou, A. Knoll, K. Lenseth, and V. Selvamanickam, "Fast growth process of long-length YBCO coated conductor with high critical current density," *IEEE Trans. Appl. Supercond.*, vol. 15, p. 2771, 2005.

[101] M. Ahn, D. Bae, S. Yang, D. Park, T. Ko, C. Lee, B.-Y. Seok, and H.-M. Chang, "Manufacture and test of small-scale superconducting fault current limiter by using the bifilar winding of coated conductor," *IEEE Trans. Appl. Supercond.*, vol. 16, p. 646, 2006.

[102] A. Ballarino, "HTS current leads for the LHC magnet powering system," *Physica C*, vol. 372-376, p. 1413, 2002.

[103] J. Miller, "The NHMFL 45-T hybrid magnet system: past, present, and future," *IEEE Trans. Appl. Supercond.*, vol. 13, p. 1385, 2003.

[104] S. Gourlay, G. Sabbi, F. Kircher, N. Martovetsky, and D. Ketchen, "Superconducting magnets and their applications," *Proc. IEEE*, vol. 92, p. 1675, 2004.

[105] D. Hazelton, V. Selvamanickam, J. Duval, D. Larbalestier, W. Markiewicz, H. Weijers, and R. Holtz, "Recent developments in 2G HTS coil technology," *IEEE Trans. Appl. Supercond.*, vol. 19, p. 2218, 2009.

[106] "New mag lab record promises more to come." NHMFL Press Release, August 7 2007. Contact: D. Larbalestier, S. Ray, Available: http://www.magnet.fsu.edu/mediacenter/news/pressreleases/2007august7.html.

[107] K. Seong, H. Kim, S. Kim, K. Sim, M. Sohn, E. Lee, S. Park, S. Hahn, and M. Park, "Development of a 600 kJ HTS SMES," *Physica C*, vol. 468, p. 2091, 2008.

[108] J.-F. Fagnard, D. Crate, J.-F. Jamoye, P. Laurent, B. Mattivi, R. Cloots, M. Ausloos, A. Genon, and P. Vanderbemden, "Use of a high-temperature superconducting coil for magnetic energy storage," *J. Phys.: Conf. Ser.*, vol. 43, p. 829, 2006.

[109] P. Tixador, M. Deleglise, A. Badel, K. Berger, B. Bellin, J. Vallier, A. Allais, and C. Bruzek, "First tests of a 800 kJ HTS SMES," *IEEE Trans. Appl. Supercond.*, vol. 18, p. 774, 2008.

[110] M. Gouge, "2002 DOE Wire Workshop, St. Petersburg, FL," January 2002.

[111] J. Cloyd, "2002 DOE Wire Workshop, St. Petersburg, FL," January 2002. http://www.eren.doe.gov/superconductivity/docs/10mil_perspective_cloyd.ppt.

[112] M. Meinert, M. Leghissa, R. Schlosser, and H. Schmidt, "System test of a 1-MVA-HTS-transformer connected to a converter-fed drive for rail vehicles," *IEEE Trans. Appl. Supercond.*, vol. 13, p. 2348, 2003.

[113] A. Klushin, R. Behr, K. Numssen, M. Siegel, and J. Niemeyer, "Accurate measurements of quantum voltage steps on arrays of bicrystal Josephson junctions," *Appl. Phys. Lett.*, vol. 80, p. 1972, 2002.

[114] G. Tsuzuki, M. Suzuki, N. Sakakibara, and Y. Ueno, "Novel superconducting ring filter," in *IEEE MTT-S Int. Microwave Symp. Dig.*, p. 379, June 1998.

[115] B. Willemsen, "HTS filter subsystems for wireless telecommunications," *IEEE Trans. Appl. Supercond.*, vol. 11, p. 60, 2001.

[116] S. R. K'doah, "Gravity Probe B: Exploring Einstein's Universe with Gyroscopes.." NASA, 2004. http://einstein.stanford.edu/content/education/GP-B_T-Guide4-2008.pdf.

[117] T. Schurig, D. Drung, S. Bechstein, J. Beyer, and F. Ludwig, "High-Tc superconductor DC SQUIDs for unshielded operation and their applications," *Physica C*, vol. 378-381, p. 1378, 2002.

[118] C. Foley, D. Tilbrook, K. Leslie, R. Binks, G. Donaldson, J. Du, S. Lam, P. Schmidt, and D. Clark, "Geophysical exploration using magnetic gradiometry based on HTS SQUIDs," *IEEE Trans. Appl. Supercond.*, vol. 11, p. 1375, 2001.

[119] M. Hidaka, M. Maruyama, and T. Satoh, "A Josephson transmission line buffer for reducing leak current in a high-T_c superconductor sampler," *Physica C*, vol. 378-381, p. 1435, 2002.

[120] Q. He, J. Wang, S. Wang, J. Wang, H. Dong, Y. Wang, and S. Shao, "Levitation force relaxation under reloading in a HTS Maglev system," *Physica C*, vol. 469, p. 91, 2009.

[121] F. Guo, Y. Tang, L. Ren, and J. Li, "A novel permanent magnetic rail for HTS levitation propulsion system," *Physica C*, vol. 469, p. 1825, 2009.

[122] T. Oka, H. Kanayama, K. Tanaka, S. Fukui, J. Ogawa, T. Sato, M. Ooizumi, T. Terasawa, Y. Itoh, and R. Yabuno, "Waste water purification by magnetic separation technique using HTS bulk magnet system," *Physica C*, vol. 469, p. 1849, 2009.

[123] F. Werfel, U. Floegel-Delor, T. Riedel, R. Rothfeld, D. Wippich, B. Goebel, G. Reiner, and N. Wehlau, "250 kW flywheel with HTS magnetic bearing for industrial use," *J. Phys.: Conf. Ser.*, vol. 97, p. 012206, 2008.

[124] S. Siems, W.-R. Canders, H. Walter, and J. Bock, "Superconducting magnetic bearings for a 2 MW/10 kWh class energy storage flywheel system," *Supercond. Sci. Technol.*, vol. 17, p. S229, 2004.

[125] M. Strasik, P. Johnson, A. Day, J. Mittleider, M. Higgins, J. Edwards, J. Schindler, K. McCrary, C. McIver, D. Carlson, J. Gonder, and J. Hull, "Design, fabrication, and test of a 5-kWh/100-kW flywheel energy storage utilizing a high-temperature superconducting bearing," *IEEE Trans. Appl. Supercond.*, vol. 17, p. 2133, 2007.

[126] S. Denis, L. Dusoulier, M. Dirickx, P. Vanderbemden, R. Cloots, M. Ausloos, and B. Vanderheyden, "Magnetic shielding properties of high-temperature superconducting tubes subjected to axial fields," *Supercond. Sci. Technol.*, vol. 20, p. 192, 2007.

[127] S. Denis, M. Dirickx, P. Vanderbemden, M. Ausloos, and B. Vanderheyden, "Field penetration into hard type-II superconducting tubes: effects of a cap, a non-superconducting joint, and non-uniform superconducting properties," *Supercond. Sci. Technol.*, vol. 20, p. 418, 2007.

[128] A. Havenhill, K. Wong, and C. Fan, "Magnetic flux diffusion through HTS shields," *IEEE Trans. Appl. Supercond.*, vol. 8, p. 62, 1998.

[129] S. Denis, G. Grenci, L. Dusoulier, R. Cloots, P. Vanderbemden, B. Vanderheyden, M. Dirickx, and M. Ausloos, "Characterisation of the magnetic shielding properties of YBaCuO thick films prepared by electrophoretic deposition on silver substrates," *J. Phys.: Conf. Ser.*, vol. 43, p. 509, 2006.

[130] E. Maher, J. S. Abell, R. I. Chakalova, Y. L. Cheung, T. W. Button, and P. Tixador, "Multi-layer coated conductor cylinders – an alternative approach to superconducting coil fabrication," *Supercond. Sci. Technol.*, vol. 17, pp. 1440–1445, 2004.

[131] M. McCulloch and D. Dew-Hughes, "Brushless AC machines with high temperature superconducting rotors," *Mat. Sci. Eng. B*, vol. 53, p. 211, 1998.

[132] T. Ohyama, H. Shimizu, M. Tsuda, and A. Ishiyama, "Trapped field characteristics of Y-Ba-Cu-O bulk in time-varying external magnetic field," *IEEE Trans. Appl. Supercond.*, vol. 11, p. 1988, 2001.

[133] G. P. Lousberg, M. Ausloos, P. Vanderbemden, and B. Vanderheyden, "Bulk high-Tc superconductors with drilled holes: how to arrange the holes to maximize the trapped magnetic flux?," *Supercond. Sci. Technol.*, vol. 21, p. 025010, 2008.

[134] G. P. Lousberg, M. Ausloos, C. Geuzaine, P. Dular, P. Vanderbemden, and B. Vanderheyden, "Numerical simulation of the magnetization of high-temperature superconductors: a 3D finite element method using a single time-step iteration," *Supercond. Sci. Technol.*, vol. 22, p. 055005, 2009.

[135] E. H. Brandt, "Determination of currents in flat superconductors," *Phys. Rev. B*, vol. 46, p. 8628, 1992.

[136] E. H. Brandt and G. P. Mikitik, "Unusual critical states in type-II superconductors," *Phys. Rev. B*, vol. 76, p. 064526, 2007.

[137] Y. R. Sun, J. R. Thompson, D. K. Christen, J. G. Ossandon, Y. J. Chen, and A. Goyal, "Effects of field sweep rate on the magnetization of melt-textured $YBa_2Cu_3O_{7-\delta}$," *Phys. Rev. B*, vol. 46, p. 8480, 1992.

[138] A. Gurevich and H. Kupfer, "Time scales of the flux creep in superconductors," *Phys. Rev. B*, vol. 48, p. 6477, 1993.

[139] A. Campbell, "A new method of determining the critical state in superconductors," *Supercond. Sci. Technol.*, vol. 20, p. 292, 2007.

[140] A. M. Wolsky and A. M. Campbell, "A new method for determining the critical state of three-dimensional superconductors: explanation and examples," *Supercond. Sci. Technol.*, vol. 21, p. 075021, 2008.

[141] A. M. Campbell, "A direct method for obtaining the critical state in two and three dimensions," *Supercond. Sci. Technol.*, vol. 22, p. 034005, 2009.

[142] F. Gömöry, M. Vojenciak, E. Pardo, and J. Souc, "Magnetic flux penetration and AC loss in a composite superconducting wire with ferromagnetic parts," *Supercond. Sci. Technol.*, vol. 22, p. 034017, 2009.

[143] A. Sanchez and C. Navau, "Magnetic properties of finite superconducting cylinders. I. uniform applied field," *Phys. Rev. B*, vol. 64, p. 214506, 2001.

[144] F. Gömöry, R. Tebano, A. Sanchez, E. Pardo, C. Navau, I. Husek, F. Strycek, and P. Kovac, "Current profiles and AC losses of a superconducting strip with an elliptic cross-section in a perpendicular magnetic field," *Supercond. Sci. Technol.*, vol. 15, p. 1311, 2002.

[145] K. Berger, J. Levêque, D. Netter, B. Douine, and A. Rezzoug, "AC transport losses calculation in a Bi-2223 current lead using thermal coupling with an analytical formula," *IEEE Trans. Appl. Supercond.*, vol. 15, p. 1508, 2005.

[146] D. Ruiz-Alonso, T. Coombs, and A. M. Campbell, "Computer modelling of high-temperature superconductors using an *A-V* formulation," *Supercond. Sci. Technol.*, vol. 17, p. S305, 2004.

[147] F. Grilli, S. Stavrev, Y. Le Floch, M. Costa-Bouzo, E. Vinot, I. Klutsch, G. Meunier, P. Tixador, and B. Dutoit, "Finite-element method modeling of superconductors: from 2-D to 3-D," *IEEE Trans. Appl. Supercond.*, vol. 15, p. 17, 2005.

[148] N. Amemiya and M. Nakahata, "Numerical study on AC loss characteristics of superconducting power transmission cables comprising coated conductors with magnetic substrates," *Physica C*, vol. 463–465, p. 775, 2007.

[149] P. Tixador, G. David, T. Chevalier, G. Meunier, and K. Berger, "Thermal-electromagnetic modeling of superconductors," *Cryogenics*, vol. 47, p. 539, 2007.

[150] Z. Hong, A. M. Campbell, and T. A. Coombs, "Numerical solution of critical state in super-conductivity by finite element software," *Supercond. Sci. Technol.*, vol. 19, p. 1246, 2006.

[151] R. Pecher, M. D. McCulloch, S. Chapman, L. Prigozhin, and C. M. Elliott, "3D-modelling of bulk type-II superconductors using unconstrained *H*-formulation," *EUCAS 2003: 6th European Conf. on Applied Superconductivity*, 2003.

[152] P. Dular and C. Geuzaine, *GetDP reference manual: the documentation for GetDP, a general environment for the treatment of discrete problems.* 2006. http://www.geuz.org/getdp/doc/texinfo/getdp.html.

[153] P. Dular, C. Geuzaine, A. Genon, and W. Legros, "An evolutive software environment for teaching the finite element method in electromagnetism," *IEEE Trans. Magn.*, vol. 35, p. 1682, 1999.

[154] P. Dular, C. Geuzaine, F. Henrotte, and W. Legros, "A general environment for the treatment of discrete problems and its application to the finite element method," *IEEE Trans. Magn.*, vol. 34, p. 3395, 1998.

[155] A. Narlikar, *Studies of high temperature superconductors: advances in research and applications Volume 11*. Nova Publishers, 1993.

[156] E. M. Gyorgy, R. B. van Dover, K. A. Jackson, L. F. Schneemeyer, and J. V. Waszczak, "Anisotropic critical currents in $Ba_2YCu_3O_7$ analyzed using an extended bean model," *Appl. Phys. Lett.*, vol. 55, p. 283, 1989.

[157] J. D. Jackson, *Classical electrodynamics*. John Wiley and Sons, 1998.

[158] A. Bossavit, "Numerical modelling of superconductors in three dimensions: a model and a finite element method," *IEEE Trans. Magn.*, vol. 30, p. 3363, 1994.

[159] T. Coombs, A. Campbell, A. Murphy, and M. Emmens, "A fast algorithm for calculating the critical state in superconductors," *COMPEL: The Int. J. Comput. Math. Electr. Electron. Eng.*, vol. 20, p. 240, 2001.

[160] P. Lousberg, *Analyse avancée*. Derouaux, 2007.

[161] P. Dular, *Modélisation du champ magnétique et des courants induits dans des systèmes tridimensionnels non linéaires*. PhD thesis, University of Liege, 1996.

[162] R. Brambilla, F. Grilli, and L. Martini, "Development of an edge-element model for AC loss computation of high-temperature superconductors," *Supercond. Sci. Technol.*, vol. 20, p. 16, 2007.

[163] M. Slodicka and A. Janikova, "Convergence of the backward Euler method for type-II superconductors," *J. Math. Anal. Appl.*, vol. 342, p. 1026, 2008.

[164] F. Henrotte, B. Meys, H. Hedia, P. Dular, and W. Legros, "Finite element modelling with transformation techniques," *IEEE Trans. Magn.*, vol. 35, p. 1434, 1999.

[165] C. Geuzaine and J.-F. Remacle, *Gmsh: a three-dimensional finite element mesh generator with built-in pre- and post-processing facilities*. 2009. http://www.geuz.org/gmsh/doc/texinfo/gmsh.html.

[166] C. Geuzaine, *High-order hybrid finite element schemes for Maxwell's equations taking thin structures and global quantities into account*. PhD thesis, University of Liege, 2002.

[167] R. Albanese and G. Rubinacci, "Magnetostatic field computations in terms of two-component vector potentials," *Int. J. Numer. Methods*, vol. 29, p. 515, 1990.

[168] M. Brown *IEE Proc.*, vol. 129A, p. 46, 1982.

[169] K. Morton and D. Mayers, *Numerical solution of partial differential equations*. Cambridge University Press, 2005.

[170] D. A. Knoll, W. J. Rider, and G. L. Olson, "An efficient nonlinear solution method for non-equilibrium radiation diffusion," *J. Quant. Spectros. Radiat. Transfer*, vol. 63, p. 15, 1999.

[171] Y. Saad and M. Schultz, "GMRES: a generalized minimal residual algorithm for solving non-symetric linear systems," *J. Sci. Stat. Comput.*, vol. 7, p. 856, 1986.

[172] E. Janikova and M. Slodicka, "Fully discrete linear approximation scheme for electric field diffusion in type-II superconductors," in *ACOMEN 2008, Liège, Belgium*, 2008.

[173] Y. S. Cha, "Magnetic diffusion in high-T_c superconductors," *Physica C*, vol. 330, p. 1, 2000.

[174] E. Brandt, "Superconductor disks and cylinders in an axial magnetic field. I. Flux penetration and magnetization curves," *Phys. Rev. B*, vol. 58, p. 6506, 1998.

[175] K. Berger, J. Levêque, D. Netter, B. Douine, and A. Rezzoug, "Influence of temperature and/or field dependences of the E-J power law on trapped magnetic field in bulk YBaCuO," *IEEE Trans. Appl. Supercond.*, vol. 17, p. 3028, 2007.

[176] G. P. Lousberg, J.-F. Fagnard, E. Haanappel, X. Chaud, M. Ausloos, B. Vanderheyden, and P. Vanderbemden, "Pulsed-field magnetization of drilled bulk high-temperature superconductors: flux front propagation in the volume and on the surface," *Supercond. Sci. Technol.*, vol. 22, p. 125026, 2009.

[177] G. P. Lousberg, J.-F. Fagnard, J. Noudem, M. Ausloos, B. Vanderheyden, and P. Vanderbemden, "Measurement of the magnetic field inside the holes of a drilled bulk high-Tc superconductor," *Supercond. Sci. Technol.*, vol. 22, p. 045009, 2009.

[178] A. M. Campbell, *Magnetic susceptibility of superconductors and other spin systems*. Plenum press, 1991.

[179] P. Vanderbemden, Z. Hong, T. A. Coombs, S. Denis, M. Ausloos, I. Rutel, J. Schwartz, N. Hari Babu, D. Cardwell, and A. M. Campbell, "Behavior of bulk high-temperature superconductors of finite thickness subjected to crossed magnetic fields: Experiment and model," *Phys. Rev. B*, vol. 75, p. 174515, 2007.

[180] K. Yamagishi, J. Ogawa, S. Sekizawa, and O. Tsukamoto, "Measurement methods of AC losses in HTS bulk," *Physica C*, vol. 445, p. 395, 2006.

[181] D.-X. Chen, A. Sanchez, C. Navau, Y.-H. Shi, and D. Cardwell, "Critical-current density of melt-grown single-grain Y-Ba-Cu-O disks determined by AC susceptibility measurements," *Supercond. Sci. Technol.*, vol. 21, p. 085013, 2008.

[182] P. Laurent, J.-F. Fagnard, B. Vanderheyden, H. Hari Babu, D. Cardwell, M. Ausloos, and P. Vanderbemden, "An AC susceptometer for the characterization of large, bulk superconducting samples," *Meas. Sci. Technol.*, vol. 19, p. 085705, 2008.

[183] I.-G. Chen, J. Liu, R. Weinstein, and K. Lau, "Characterization of $YBa_2Cu_3O_7$, including critical current density J_c, by trapped magnetic field," *J. Appl. Phys.*, vol. 72, p. 1013, 1992.

[184] D. Cardwell, M. Murakami, M. Zeisberger, W. Gawalek, R. Gonzalez-Arrabal, M. Eisterer, H. Weber, G. Fuchs, G. Krabbes, A. Leenders, H. C. Freyhardt, and N. H. Babu, "Round robin tests on large grain melt processed Sm-Ba-Cu-O bulk superconductors," *Supercond. Sci. Technol.*, vol. 18, p. S173, 2005.

[185] M. Zeisberger, T. Habisreuther, D. Litzkendorf, O. Surzhenko, R. Muller, and W. Gawalek, "A fast method of characterizing HTSC bulk material," *IEEE Trans. Appl. Supercond.*, vol. 13, p. 3706, 2003.

[186] M. Eisterer, S. Haindl, T. Wojcik, and H. W. Weber, "'Magnetoscan': a modified Hall probe scanning technique for the detection of inhomogeneities in bulk high temperature superconductors," *Supercond. Sci. Technol.*, vol. 16, p. 1282, 2003.

[187] M. Zeisberger, T. Habisreuther, D. Litzkendorf, A. Surzhenko, and W. Gawalek, "Investigation of the structure of melt-textured YBCO by magnetic measurements," *Supercond. Sci. Technol.*, vol. 18, p. S90, 2005.

[188] S. Haindl, M. Eisterer, H. W. Weber, L. Shlyk, and G. Krabbes, "Magnetic flux penetration into melt-textured superconductors," *Supercond. Sci. Technol.*, vol. 18, p. S164, 2005.

[189] M. Zeisberger, A. M. Campbell, W. Lo, and D. A. Cardwell, "Characterization of YBCO bulk samples by local AC-susceptometry," *IEEE Trans. Appl. Supercond.*, vol. 17, p. 1065, 1997.

[190] S. Nariki, N. Sakai, M. Kita, M. Fujikura, M. Murakami, and I. Hirabayashi, "Advances in enlargement of melt-textured Gd-Ba-Cu-O superconductors," *Supercond. Sci. Technol.*, vol. 19, p. S500, 2006.

[191] D. Cardwell and N. Hari Babu, "Processing and properties of single grain (RE)-Ba-Cu-O bulk superconductors," *Physica C*, vol. 445-448, p. 1, 2006.

[192] B. Lehndorff, H. G. Kurschner, and H. Piel, "Mapping of magnetic force and field distribution of melt-textured Y-Ba-Cu-O," *IEEE Trans. Appl. Supercond.*, vol. 5, p. 1814, 1995.

[193] P. Vanderbemden, A. D. Bradley, R. A. Doyle, W. Lo, D. M. Astill, D. A. Cardwell, and A. M. Campbell, "Superconducting properties of natural and artificial grain boundaries in bulk melt-textured YBCO," *Physica C*, vol. 302, p. 257, 1998.

[194] P. Temple, "An introduction to phase-sensitive amplifiers: An inexpensive student instrument," *Am. J. Phys.*, vol. 43, p. 801, 1975.

[195] P. A. Probst and B. Collet, "Low-frequency digital lock-in amplifier," *Rev. Sci. Instrum.*, vol. 56, p. 466, 1985.

[196] X. Chaud, E. Haanappel, J. Noudem, and D. Horvath, "Trapped field of YBCO single-domain samples using pulse magnetization from 77K to 20K," *J. Phys. : Conf. Series*, vol. 97, p. 012047, 2008.

[197] H. Huo, M. Qiu, and D. Xia, "Analysis of HTS bulk during pulsed field magnetization with experimental and numerical methods," *IEEE Trans. Appl. Supercond.*, vol. 14, p. 1082, 2004.

[198] M. Tokuyama, Y. Yanagi, and H. Ikuta, "Local measurement of the pulsed field magnetization process of melt-processed bulk superconductor," *Physica C*, vol. 463-465, p. 405, 2007.

[199] K. Yokoyama, T. Oka, H. Fujishiro, and K. Noto, "Evaluation of current distribution in bulk superconductors magnetized by pulsed-fields," *Physica C*, vol. 463-465, p. 410, 2007.

[200] M. Tsuchimoto, H. Waki, Y. Itoh, Y. Yanagi, M. Yoshikawa, T. Oka, Y. Yamada, and U. Mizutani, "Numerical evaluation of pulsed field magnetization of a bulk high T_c superconductor," *Cryogenics*, vol. 37, p. 43, 1997.

[201] F. Gömöry, "Characterization of high-temperature superconductors by AC susceptibility measurements," *Supercond. Sci. Technol.*, vol. 10, p. 523, 1997.

[202] M. Raven and M. Salim, "Design aspects of a differential magnetic susceptometer for high temperature superconductors," *Meas. Sci. Technol.*, vol. 12, p. 744, 2001.

[203] P. Laurent, P. Vanderbemden, S. Meslin, J. Noudem, J.-P. Mathieu, R. Cloots, and M. Ausloos, "Measurements of thermal effects in a bulk YBCO single domain superconductor submitted to a variable magnetic field," *IEEE Trans. Appl. Supercond.*, vol. 17, p. 3036, 2007.

[204] F. Gömöry, P. Lobotka, and K. Frohlich, "Variable temperature insert for AC susceptibility measurements at AC field amplitudes up to 0.1 T," *Cryogenics*, vol. 34, p. 837, 1994.

[205] J. Ogawa, M. Iwamoto, K. Yamagishi, O. Tsukamoto, M. Murakami, and M. Tomita, "Influence of AC external magnetic field perturbation on trapped magnetic field in HTS bulk," *Physica C*, vol. 386, p. 26, 2003.

[206] O. Tsukamoto, M. Liu, S. Odaka, D. Miyagi, and K. Ohmatsu, "AC magnetization loss characteristics of HTS coated-conductors with magnetic substrates," *Physica C*, vol. 463-465, p. 766, 2007.

[207] S. Trojanowski and M. Ciszek, "Race-track coils for measurements of AC energy losses in high temperature superconducting tapes," *Przeglad Elektrotechniczny*, vol. 83, p. 26, 2007.

[208] P. Vanderbemden, "Design of an AC susceptometer based on a cryocooler," *Cryogenics*, vol. 38, p. 839, 1998.

[209] X. Jiang, D. Astill, W. Lo, D. Cardwell, T. Coombs, A. Campbell, and J. Larsen, "Experimental analysis of the magnetic field shielding and trapping properties of bulk melt-processed $YBa_2Cu_3O_{7-\delta}$," *Physica C*, vol. 249, p. 171, 1994.

[210] Q. Chen, *Magnetic Susceptibility of Superconductors and Other Spin Systems*. Plenum Press, 1991.

[211] D. Lopez and F. de la Cruz, "Anisotropic energy dissipation in high-Tc ceramic superconductors: local-field effects," *Phys. Rev. B*, vol. 43, p. 11480, 1991.

[212] E. H. Brandt, "Susceptibility of superconductor disks and rings with and without flux creep," *Phys. Rev. B*, vol. 55, p. 14513, 1997.

[213] J. Chow, W. Lo, H.-T. Leung, C. Dewhurst, and D. Cardwell, "Processing, Y_2BaCuO_5 distribution and critical current density in large grain Pt-doped YBCO," *Mat. Sci. Eng. B*, vol. 53, no. 1-2, p. 79, 1998.

[214] H. Fujishiro, K. Yokoyama, M. Kaneyama, T. Oka, and K. Noto, "Estimation of generated heat in pulse field magnetizing for SmBaCuO bulk superconductor," *Physica C: Superconductivity*, vol. 412-414, p. 646, 2004.

[215] F. Gömöry, "Improvement of the self-field critical current of a high-T_c superconducting tape by the edge cover from soft ferromagnetic material," *Appl. Phys. Lett.*, vol. 89, p. 072506, 2006.

[216] Y. Mawatari, "Magnetic field distributions around superconducting strips on ferromagnetic substrates," *Phys. Rev. B*, vol. 77, p. 104505, 2008.

[217] M. Majoros, B. A. Glowacki, and A. Campbell, "Magnetic screening as a possible way to decrease transport AC losses in multifilamentary superconductors – basic theoretical considerations," *Physica C*, vol. 334, p. 129, 2000.

[218] A. Caplin, L. Cohen, G. Perkins, and A. Zhukov, "The electric field within high-temperature superconductors : mapping the E-J-B surface," *Supercond. Sci. Technol.*, vol. 7, p. 412, 1994.

[219] F. Grilli, S. P. Ashworth, and L. Civale, "Interaction of magnetic field and magnetic history in high-temperature superconductors," *J. Appl. Phys.*, vol. 102, p. 073909, 2007.

[220] M. Itoh, T. Ohyama, K. Hoshino, H. Ishigaki, and T. Minemoto, "Improvement in magnetic shielding by the superposition of a magnetic cylinder over a copper-oxide superconducting cylinder," *IEEE Trans. Appl. Supercond.*, vol. 3, p. 181, 1993.

[221] K. Mori, T. Minemoto, and M. Itoh, "Magnetic shielding of the superposition of a hybrid ferromagnetic cylinder over a BPSCCO cylinders," *IEEE Trans. Appl. Supercond.*, vol. 7, p. 378, 1997.

[222] G. P. Lousberg, J.-F. Fagnard, M. Ausloos, P. Vanderbemden, and B. Vanderheyden, "Numerical study of the shielding properties of macroscopic hybrid ferromagnetic/superconductor hollow cylinders," *IEEE Trans. Appl. Supercond., in press*, 2010.

[223] X. Granados, M. Torner, T. Puig, and X. Obradors, "Magnetization of ferromagnetic-SC heterostructures for trapped field low power motors," *IEEE Trans. Appl. Supercond.*, vol. 17, p. 1629, 2007.

[224] S. S. M. Tavares, M. R. da Silva, J. M. Neto, S. Miraglia, and D. Fruchart, "Ferromagnetic properties of cold rolled AISI 304L steel," *J. Magn. Magn. Mater.*, vol. 242-245, p. 1391, 2002.

[225] T. Famakinwa, Q. M. Chen, and S. Yamaguchi, "3D finite element analysis of eddy current loss of HTS tapes - External field analysis," *Physica C*, vol. 459, no. 1-2, p. 18, 2007.